

Dissertation zur Erlangung des Doktorgrades
der Fakultät für Chemie und Pharmazie
der Ludwig-Maximilians-Universität München

Iron pnictide superconductors

Marcus Christian Tegel
aus
Backnang

2011

Erklärung

Diese Dissertation wurde im Sinne von § 13 Abs. 3 bzw. 4 der Promotionsordnung vom 29. Januar 1998 (in der Fassung der vierten Änderungssatzung vom 26. November 2004) von Herrn Prof. Dr. Dirk Johrendt betreut.

Ehrenwörtliche Versicherung

Diese Dissertation wurde selbständig, ohne unerlaubte Hilfe erarbeitet.

München, 04.02.2011


Marcus Tegel

Dissertation eingereicht am 08.02.2011

1. Gutachter: Prof. Dr. Dirk Johrendt

2. Gutachter: Prof. Dr. Wolfgang Schnick

Mündliche Prüfung am 22.03.2011

Danksagung

Herrn Prof. Dr. Dirk Johrendt danke ich herzlich für die Aufnahme in seinen Arbeitskreis, für die äußerst interessante Themenstellung, für viel forschersche Freiheit und dennoch stetige und engagierte Unterstützung bei der Durchführung dieser Doktorarbeit. Herrn Prof. Dr. Wolfgang Schnick danke ich herzlich für die Übernahme des Zweitgutachtens und für sein immer offenes Ohr bezüglich Wünschen und Vorschlägen für den Arbeitskreis. Auch meinen weiteren Prüfern danke ich für ihre Bereitschaft, an meinem Rigorosum teilzunehmen.

Ein sehr großer Dank gilt allen Arbeitskreismitgliedern für ihre Hilfsbereitschaft, das unglaublich tolle Arbeitsklima und einfach eine fantastische Zeit. Ich werde euch total vermissen! Besonderen Dank geht natürlich an meinen Chef und Frau Marianne Rotter für die tolle Zusammenarbeit in der „heißen Phase“ dieser Promotion. Sehr möchte ich mich auch für spannende, hilfreiche und horizonterweiternde Diskussionen vor allem bei Herrn Daniel Bichler und Frau Franziska Hummel und für Hilfe bei vielen organisatorischen Problemen bei Frau Catrin Löhnert bedanken. Herrn Daniel Bichler, Frau Bele Boeddinghaus, Frau Katharina Förg, Herrn Rainer Frankovsky, Frau Gina Friederichs, Herrn Christoph Höller, Frau Franziska Hummel, Frau Petra Jakubcová, Frau Marianne Rotter, Herrn Sebastian Schneider, Herrn Erwin Wiesemayer und Frau Veronika Zinth danke ich für unendlich viel Motivation, die mir unsere gemeinsame Arbeits- und Freizeit gegeben hat. Auch bei allen anderen Mitarbeitern der Schwester-AKs Müller-Buschbaum, Schnick, Oeckler, Lotsch und Schmedt auf der Günne möchte ich mich für die schöne gemeinsame Zeit bedanken.

Herrn Prof. Dr. Klaus Müller-Buschbaum danke ich herzlich für die kollegiale Atmosphäre, die er mit nach München gebracht hat und für eine tolle Zusammenarbeit. Herrn PD Dr. Oliver Oeckler danke ich für sein Engagement im kristallographischen Bereich und für viele interessante Diskussionen fachlicher und privater Natur. Ein herzliches Dankeschön gilt Herrn Christian Minke für seine Geduld bei der Anfertigung zahlreicher EDX-Spektren und Herrn Wolfgang Wünschheim für seinen Aufwand und seine Geduld mit meinen vielen Wünschen für die IT im Arbeitskreis.

Besonderen Dank geht auch an Daniel Lopez-Diaz und seine Kollegen vom Fraunhofer IAF in Freiburg für das Fräsen der Leitfähigkeits-Probenträger. Viel Dank ge-

bührt Herrn Prof. Dr. Thomas Fässler für fast drei Jahre Mitbenutzungsmöglichkeit des SQUID an der TU München. In diesem Zuge möchte ich mich auch ganz herzlich bei Frau Bele Boeddinghaus für die tolle Zusammenarbeit und die vielen Hilfen bedanken. Bei Herrn Dr. Rudi Hackl bedanke ich mich besonders herzlich für Rat, Tat, Engagement und tollen Kaffee beim Bau des AC-Suszeptometers.

Ein ganz herzliches Dankeschön geht auch an Herrn Rainer Frankovsky, Frau Franziska Hummel und Herrn Erwin Wiesenmayer für das Korrekturlesen dieser Arbeit und an Frau Isabell Staub für wichtige Impulse für meinen Dissertationsvortrag. Mein besonderer Dank gilt meinen Eltern. Sie haben mir die Freiheit ermöglicht, das tun zu dürfen, was mich fasziniert und begeistert.

Meinen ganz speziellen und herzlichen Dank möchte ich jedoch all meinen ehemaligen Forschungspraktikanten und Bacheloranden aussprechen: Marinus Auracher, Masamitsu Egawa, Sabine Frohnappel, Franziska Hummel, Sebastian Johansson, Sebastian Lackner, Tanja Schmid, Tobias Stürzer, Veronika Weiß und Simon Welz-miller – ohne euer Engagement wäre ein Gelingen dieser Arbeit in dieser Form niemals möglich gewesen!

“The meaning of things lies not in the things themselves, but in our attitude towards them.”

(Antoine de Saint-Exupéry)

Contents

1. Introduction	1
1.1 Electronic properties of the <i>FePn</i> superconductors	7
1.1.1 General considerations.....	7
1.1.2 Proposed superconducting mechanism	11
1.2 Overview and motivation.....	18
2. Methods	20
2.1 Density functional theory.....	20
2.2 Powder diffraction	21
2.2.1 X-ray powder diffraction	21
2.2.2 Neutron powder diffraction (elastic scattering).....	22
2.2.3 Simulation of powder patterns	23
2.2.4 Rietveld refinements (general)	24
2.2.5 TOPAS Academic launch mode control files (.inp templates).....	24
Diffractometer specific templates	25
2.2.6 TOPAS Academic, special implementations	31
HUBER G670 imaging plate intensity correction	31
<i>Le Bail-Jouanneaux</i> anisotropy correction.....	32
Robust refinements	34
2.3 Single crystal diffraction	35
2.4 Inelastic neutron scattering	36
2.4.1 General	36
2.4.2 Measurement details	38
2.5 Scanning electron microscopy, EDX.....	39
2.6 Magnetic measurements.....	39
2.6.1 SQUID magnetometer	40
2.6.2 AC susceptometer	41
2.7 Resistivity measurements	41
2.7.1 High vacuum refrigerator	42
2.7.2 ⁴ He exchange gas refrigerator	42

2.8	Mössbauer spectroscopy	42
2.9	Specific heat	43
2.10	Synthesis methods.....	44
2.10.1	Starting materials.....	44
2.10.2	Synthesis equipment and conditions	46
2.10.3	Standard synthesis method	46
2.10.4	Tin flux	47
2.10.5	NaCl / KCl flux	47
3.	La(Co_xFe_{1-x})PO	49
3.1	Synthesis	50
3.2	Mössbauer study of undoped LaFePO.....	51
3.3	Influence of Co-doping	53
3.4	Electronic structure.....	57
4.	SrFeAsF	60
4.1	Synthesis	60
4.2	Crystal structure	61
4.3	Magnetic ordering.....	66
4.4	Resistivity, susceptibility and specific heat	69
4.5	DFT calculations	70
5.	EuMnPF	75
5.1	Synthesis	76
5.2	Crystal structure	76
5.3	Magnetism	78
6.	REZnPO	80
6.1	Computational details.....	81
6.2	Electronic structure.....	82
6.3	Volume optimisations	87
7.	Ba_{1-x}K_xFe₂As₂	89
7.1	Undoped BaFe ₂ As ₂	90
7.1.1	Crystal structure.....	90

7.1.2	Magnetic ordering	94
7.1.3	Resistivity, susceptibility and specific heat	95
7.2	Optimally doped $\text{Ba}_{0.6}\text{K}_{0.4}\text{Fe}_2\text{As}_2$	97
7.2.1	Crystal structure	98
7.2.2	Resistivity and magnetism.....	100
7.3	The solid solution series $\text{Ba}_{1-x}\text{K}_x\text{Fe}_2\text{As}_2$ ($x = 0 - 1$)	104
7.4	Underdoped $\text{Ba}_{1-x}\text{K}_x\text{Fe}_2\text{As}_2$ ($x = 0.1 - 0.3$).....	106
7.4.1	Crystal structures and phase transitions.....	109
7.4.2	Superconductivity and antiferromagnetic ordering	111
8.	$M\text{Fe}_2\text{As}_2$ ($M = \text{Sr}, \text{Eu}$)	115
8.1	Synthesis.....	115
8.2	Crystal structure.....	116
8.3	Magnetic ordering	122
9.	$\text{Sr}_{1-x}\text{K}_x\text{Fe}_2\text{As}_2$ and $\text{Ca}_{1-x}\text{Na}_x\text{Fe}_2\text{As}_2$.....	126
9.1	Synthesis.....	127
9.2	Crystal structures	127
9.3	Superconductivity	131
9.4	Inelastic neutron scattering.....	132
10.	$\text{FeSe}_{1-x}\text{Te}_x$.....	139
10.1	Experimental.....	141
10.2	Single crystal refinement	142
10.3	Crystal structure	143
11.	$\text{Sr}_3\text{Sc}_2\text{O}_5\text{Fe}_2\text{As}_2$	147
11.1	Synthesis	149
11.2	Crystal structure	149
11.3	Structural relationships.....	153
11.4	Magnetism and Mössbauer spectroscopy	154
11.5	DFT calculations	156
12.	$\text{Ba}_2\text{ScO}_3\text{FeAs}$.....	160
12.1	Synthesis	161

12.2	Crystal structure.....	161
12.3	Magnetism, resistivity and Mössbauer spectroscopy.....	164
12.4	Electronic structure	167
13.	Sr₂CrO₃FeAs	170
13.1	Synthesis (I).....	170
13.2	Crystal structure.....	170
13.3	Magnetic susceptibility and resistivity	173
13.4	Mössbauer spectroscopy	174
13.5	Absence of superconductivity.....	176
13.6	Synthesis (II).....	177
13.7	Neutron diffraction, refinement details.....	177
13.8	Redetermined crystal structure.....	178
13.9	Neutron diffraction, antiferromagnetic ordering	180
14.	Sr₂VO₃FeAs	186
14.1	Synthesis.....	187
14.2	Resistivity and susceptibility	188
14.3	Crystal structure.....	189
14.4	Magnetic ordering	192
15.	Summary and outlook.....	194
15.1	Summary.....	194
15.2	Outlook.....	201
16.	AC susceptometer.....	204
16.1	Overview	205
16.2	Coil design	206
16.3	Coil holder, wiring	209
16.4	Sample transport.....	209
16.5	AC susceptometer control software	212
16.5.1	User interface	212
16.5.2	Centring dialog	222
16.5.3	Other dialogs	225

17. Four-terminal conductometer	227
17.1 Overview	227
17.2 Sample holder design.....	228
17.3 Sample rod, wiring.....	230
17.4 Conductivity control software.....	231
18. HConvert	234
19. SQUID Processor	236
20. Molar weight calculator	238
21. Appendix	239
21.1 Superconducting order parameters.....	239
21.2 WIEN2k compiler and linker options for Mac OS X.....	239
21.3 Additional Rietveld refinements.....	240
21.3.1 $\text{Sr}_2\text{CrO}_3\text{FeAs}$ (Sample II, X-ray)	240
21.4 Magnetic ordering types.....	242
21.5 $C_{2v}mma'$ colour group.....	243
21.6 Susceptometer sample transport circuit and wiring diagrams.....	244
22. Abbreviations and glossary	249
22.1 Abbreviations.....	249
22.2 Quantities.....	251
22.3 Glossary.....	255
23. Publications and talks.....	258
23.1 Publications in peer-reviewed journals.....	258
23.2 Conference contributions	260
23.3 LMU talks and methodology seminars.....	261
24. Curriculum Vitae.....	263
25. Bibliography	264

1. Introduction

The discovery of high-temperature superconductivity in the cuprates in 1986^[1] has given a strong impetus to the natural sciences at the end of the 20th century. There are many reasons for this enthusiasm. At first, it can be explained by the fascination to overcome a physical barrier, which had seemed insuperable for decades and such discoveries always induce the wish for a deeper understanding of the underlying physics. Furthermore, the multitude of possible applications of these materials is obvious even to the amateur:^[2] The thought of superconductivity often sparks visions of application in lossless power supplies, ultra-strong permanent electromagnets or maybe even highly efficient superconducting magnetic railways. Such public attention promotes the required support and funding to carry out the necessary but sometimes lengthy research into new physical fundamentals but also the quest for materials, which are suitable for application. However, difficulties to overcome certain application specific problems and the limitation to exactly one class of materials for more than 20 years had also led to a slowly declining interest in high-temperature superconductivity fundamental research (Figure 1.1).^[3]

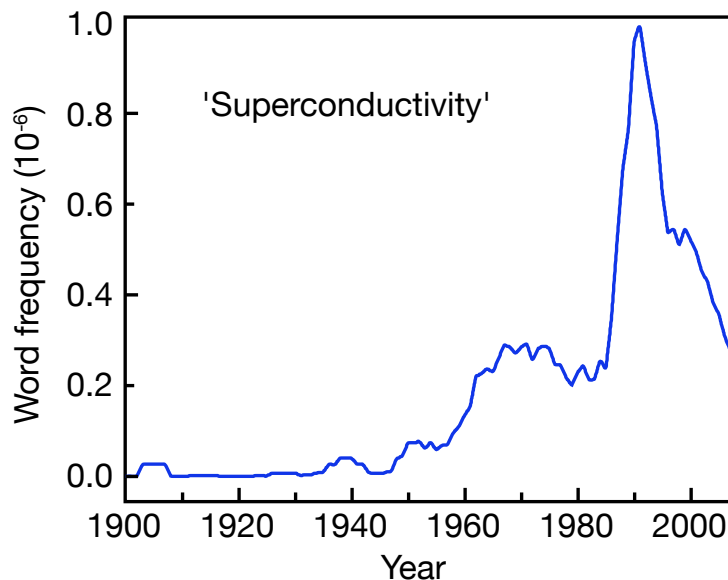


Figure 1.1: Prevalence of the word 'superconductivity' in textbooks.

Chapter 1: Introduction

The vast majority of commercially used superconductors today are superconducting alloys like (NbTi)^[4] or intermetallic compounds like Nb₃Sn,^[5] the so-called 'A15 phases'. (NbTi) possesses a critical temperature (T_C) at only around 9 K and Nb₃Sn a T_C of 18 K. These compounds therefore have to be cooled with liquid helium in order to work. The magnetic flux densities, which safely can be achieved in real applications of superconducting magnets are about 8 T in (NbTi), e.g. employed in the tremendous magnets of the Large Hadron Collider.^[6] In Nb₃Sn, magnetic flux densities of up to 23.5 T can currently be achieved, as for example in the BRUKER AVANCE 1 GHz NMR spectrometer.^[7]

The use of low-temperature superconductors in such special applications is well established and relatively easy fabrication of these materials is a particular advantage here. Despite of this, the necessity of cooling with liquid helium can be considered a major drawback, as it prevents the use of low-temperature superconductors in more price-sensitive applications, such as in the energy sector. In this area, the cost of liquid helium as a coolant would eat up any potential savings. Cuprate high-temperature superconductors can be efficiently cooled either with liquid nitrogen or with closed-cycle refrigerators.^[8] High-temperature superconductors are therefore not only of academic interest, but there are ongoing efforts to employ them in the following energy applications: In power generators and superconducting motors, superconducting rotors can produce higher magnetic flux densities than conventional magnets, leading to both a weight and size reduction of such devices of up to 50 %.^[9] In power transformers, superconducting wires can reduce ohmic losses by up to 90 %.^[10] A further, very recent application is the experimental use of high-temperature superconductors in frictionless bearings for high-performance energy storage flywheels.^[11] Such flywheels can be employed to cover peak loads in the electricity grid, which is of growing importance considering the steadily increasing use of renewable energy sources causing such peaks.

All current cuprate superconductors however exhibit certain material specific disadvantages, which impose serious restrictions for applications on a wider basis. One aspect is the price of cuprate high-temperature superconductors due to costly starting materials. Besides, complicated fabrication of superconducting wires or tapes of the brittle, polycrystalline substances makes these materials even more expensive.

But also intergranular non-zero resistance arising from crystallite misalignments in the bulk substance in combination with the special superconducting properties of the cuprate superconductors are critical issues.^[12]

In short, one could say that while there is interest in high-temperature superconductors for commercial applications, they still have niche status.

It was therefore not until 2008, that another gold rush has hit the area of high-temperature superconductivity research. For the first time, high-temperature superconductivity has been discovered in a different class of materials – the class of iron arsenide superconductors.

These compounds are metals and as such relatively good conductors even in their normal state. Yet, such metallic compounds had always been predicted to exhibit – if at all – only conventional superconductivity. It should be clear that the magnetic properties of any element such as iron in its body-centred modification cannot simply be related to any other modification of the same element or even a chemical compound containing this element. Nevertheless, iron had been ruled out as a possible candidate for superconductors for a long time as a matter of principle.^[13] All these predictions have proved completely wrong, which probably has been the most intriguing insight in superconductivity research for a long time.

The first iron-based high-temperature superconductor, $\text{LaFeAsO}_{1-x}\text{F}_x$, which becomes superconducting below 26 K has been discovered by *Kamihara*.^[14] Soon after this discovery, the critical temperature could be increased to 55 K in the closely related compound $\text{SmFeAsO}_{1-x}\text{F}_x$.^[15] The crystal structure is depicted in Figure 1.2.^[16]

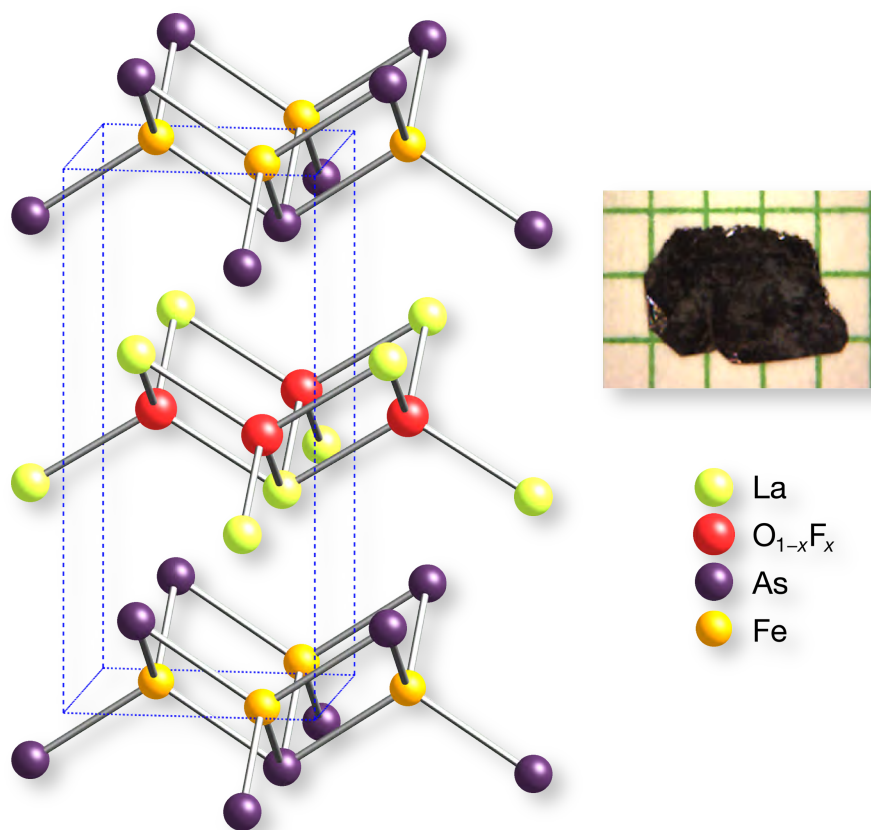


Figure 1.2: Left: Crystal structure of $\text{LaFeAs}(\text{O}_{1-x}\text{F}_x)$. Right: $\text{LaFeAs}(\text{O}_{1-x}\text{F}_x)$ single crystal on millimetre grid paper.

$\text{LaFeAsO}_{1-x}\text{F}_x$ crystallises in the ZrCuSiAs -type structure in the tetragonal space group $P4/nmm$. According to its chemical stoichiometry, this structure type is also referred to as 1111-type. The structure consists of lanthanum oxide (OLa)⁺-layers, which alternate with iron arsenide (FeAs)⁻-layers. In $\text{LaFeAsO}_{1-x}\text{F}_x$, some of the oxide ions are exchanged for fluoride ions. Both the iron atoms as well as the oxide ions are tetrahedrally coordinated by arsenide and lanthanum ions, respectively and these tetrahedra are connected to two-dimensional layers via their edges. Due to the edge-sharing tetrahedral layers, the nearest neighbour iron–iron distance is only about 285 pm in $\text{LaFeAsO}_{1-x}\text{F}_x$ which leads to metallic bonds between adjacent iron atoms. It is this two-dimensional layered structure in general and the iron–iron and iron–pnictogen interactions in particular, which dominate several macroscopic properties of the whole class of substances. All iron pnictides of the 1111 or similar structure types form black, tetragonal platelet crystals, which have a metallic lustre. The normal state resistivities of these compounds are some orders of magnitude

larger than those of good metals like copper or silver, which is referred to as poor metal behaviour.

In order to understand the phenomenon of superconductivity, it is mandatory to realise, why normal metals exhibit a certain resistance even at zero temperature. On applying a voltage to a metal, electrons begin to flow and because charge neutrality must be conserved, a hole is dragged behind, whenever an electron is moved. Both electrons and holes are scattered by impurities or crystal defects and thus contribute to the electric resistance. Another contribution is made by electron–phonon interactions, which make up the majority of the resistance, especially at elevated temperatures. This phenomenon would even be present in a perfect crystal.

In a conventional superconductor however, a special kind of electron–phonon interaction occurs at very low temperatures: According to the BCS theory^[17] the Coulomb repulsion of electrons at the Fermi level can be overcome by this interaction and two electrons each form a Cooper pair. Qualitatively, this formation can be explained as follows: When an electron moves through the solid, it creates a deformation or depression in the atomic lattice via phonons. If this depression of the lattice is strong enough, another electron can ‘fall’ into it and a Cooper pair is formed. The formation of Cooper pairs is then favoured over the creation of electron–hole pairs. All this is of course only possible if the total energy of the system with Cooper pairs is lower in the superconducting than in the normal state. The energy difference of the system between normal and superconducting state at $T = 0$ K is proportional to the binding energy of the Cooper pairs, which in turn is proportional to the critical temperature of the superconductor¹. Thus, the Cooper pairs are separated from the normal electrons by this superconducting energy gap at zero temperature. Unlike normal electrons, which are fermions and therefore have to obey Pauli’s principle, all Cooper pairs exhibit the same quantum state. This also means that a single Cooper pair cannot gain energy in comparison with the others, which implies that single Cooper pairs cannot be scattered by the crystal lattice any more. As a result, the resistance of the compound is zero.^[2, 18]

¹ According to the BCS theory, the binding energy of the Cooper pairs is two times the superconducting energy gap, which is defined at zero temperature as $\Delta_{(T=0\text{ K})} = 1.76 \cdot k_B \cdot T_C$.

Chapter 1: Introduction

However, this only holds true up to a critical temperature T_C (i.e. if the energy of the phonons in the crystal is smaller than the binding energy of the Cooper pairs). In a similar fashion, there is a critical current density (i.e. the kinetic energy of the Cooper pairs has to be smaller than their binding energy) or a critical magnetic field. Within the BCS theory, one can show that in so-called conventional, i.e. exclusively phonon-mediated superconductors, critical temperatures of above ~ 40 K are impossible and for a long time one had thought that this is a hard limit, which cannot be overcome.

The situation has radically changed with the discovery of superconductivity in the cuprates (which possess critical temperatures of up to 133 K in $\text{HgBa}_2\text{CaCu}_2\text{O}_{6+x}$)^[19]. It was found that their electronic properties are dominated by electronic correlations rather than electron–phonon interactions. Such electronic correlations are also capable of inducing superconductivity in a surprisingly effective way, but the mechanism of the formation of Cooper pairs differs from the just discussed phonon-mediated one. In these so-called unconventional superconductors, the role of phonons is replaced by spin-density waves.ⁱⁱ^[20] Cuprate superconductors are strong spin-density wave systems^[21] which are within close vicinity of a magnetic transition to, for example, an antiferromagnet. When an electron moves in such a superconductor, this electron's spin creates a spin-density wave around it. This spin-density wave in turn causes a nearby electron to fall into the spin-depression created by the first electron and hence, again, a Cooper pair is formed. This mechanism is called either d-wave or s_{\pm} -wave pairing according to the symmetry of the superconducting order parameter. As these systems are magnetic systems due to the Coulomb interaction, there is a strong Coulomb repulsion between electrons. As will be discussed in Chapter 1.1.2, this Coulomb repulsion prevents the formation of Cooper pairs on the same lattice site and the pairing therefore occurs at near-neighbour lattice sites.

ⁱⁱ A spin-density wave (SDW) is a periodic modulation of the electron spin with a characteristic spatial periodicity, which mostly is incommensurate with the crystal structure. It often occurs as ground state in materials of low dimensionality, metals with a high DOS at E_F or because of the existence of Fermi surface nesting vectors, as it is the case in the iron pnictides. Similar to superconductivity, the occurrence of a SDW causes the formation of an energy gap that lowers the system's total energy.

The discovery of superconductivity in iron-based compounds such as $\text{SmFeAsO}_{1-x}\text{F}_x$ immediately suggested a pairing mechanism by electronic interactions rather than by phonon–electron interactions because a transition temperature of 55 K is well above the BCS limit of 40 K. A more detailed analysis of the electronic situation in the iron-based superconductors and its implication on superconductivity will be part of the next chapter.

1.1 Electronic properties of the *FePn* superconductors

All calculations in this chapter were performed with LMTO (Chapter 2.1) and crystallographic data had been taken from [22]. Generally, all iron pnictide superconductors and their non-superconducting parent compounds exhibit a similar electronic situation. Thus most considerations in this chapter, which are based on calculations for LaFeAsO , are valid for other iron pnictides likewise.

1.1.1 General considerations

As a first approach to the chemical bonding situation in LaFeAsO , an ionic formula according to $[\text{La}^{3+}\text{O}^{2-}]\text{Fe}^{2+}\text{As}^{3-}$ might be useful. But this description is not really accurate, because a considerable amount of covalent bonding occurs between Fe and As. While the La–O interactions are predominantly ionic in nature, this holds true to a smaller extent for the interlayer La–As bonds. LaFeAsO on the whole therefore is far from being a purely ionic solid, but rather a polar compound. In addition to the abovementioned bonds, there is also a significant contribution of Fe–Fe interactions in LaFeAsO and in all other iron pnictides.^{III} Both the Fe–As as well as the Fe–Fe bonds cause metallic bands at the Fermi level and as a result, LaFeAsO is a metal in its normal state.

^{III}Due to their similar lattice parameters a , all iron pnictides have similar Fe–Fe bond lengths (ranging from ~ 267 pm in LiFeAs to ~ 285 pm in LaFeAsO). They are therefore only $\sim 8 - 15$ % longer than the iron–iron bonds in elemental iron (248 pm).

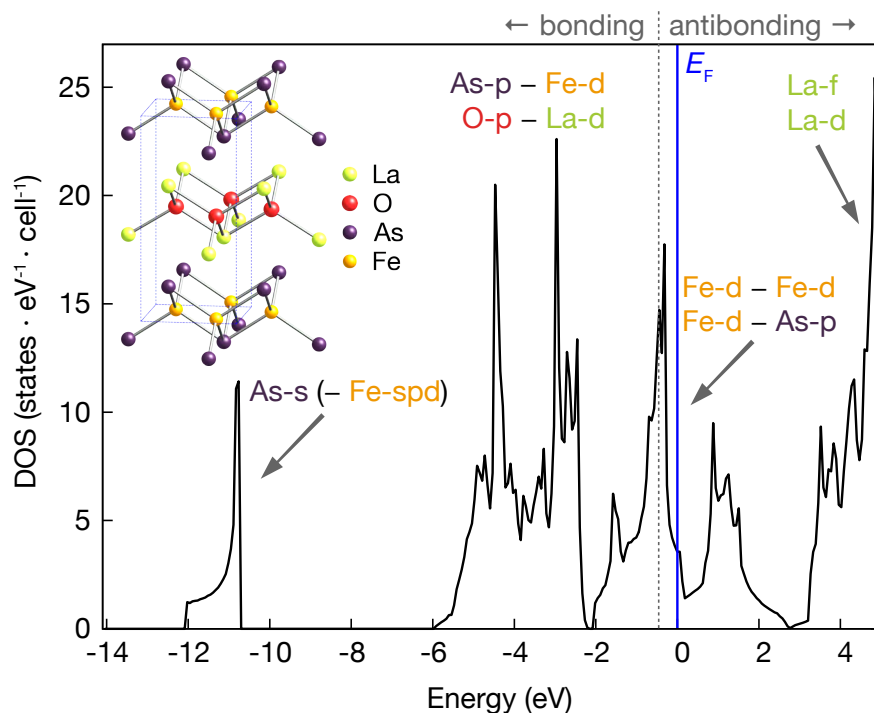


Figure 1.3: Total density of states (DOS) of LaFeAsO with character analyses of the different features. Minor contributions were omitted for clarity. Fe–Fe and Fe–As bonding and antibonding interactions are separated by the dotted line and were derived from COHP calculations (see also Figure 1.5).

This bonding situation can also be understood on the basis of density of states (DOS) calculations (Figure 1.3).

The energetically lowest valence states in LaFeAsO arise from occupied O-s orbitals, which have been treated as core states (not depicted). The feature at about -11 eV is mainly due to filled As-s orbitals, which are slightly mixed with s, p and d-states from Fe. The unoccupied states above $\sim +3$ eV arise mainly from empty La-f and La-d orbitals. The features between about -6 and -2 eV are predominantly caused by As-p – Fe-d bonding and O-p – La-d bonding interactions.

A closer look at the electronic situation near the Fermi level (between about -2 and $+3$ eV) reveals Fe–Fe interactions, which mainly possess Fe- d_{xy} and Fe- $d_{x^2-y^2}$ σ and π bonding and antibonding character (a schematic plot of these interactions is depicted in Figure 1.4). In the same energy range, also Fe–As interactions occur, which are antibonding above ~ -0.6 eV. The crystal orbital Hamilton populations (COHPs) of both the Fe–Fe and the Fe–As bonds are depicted in Figure 1.5.

Character analyses of the DOS exactly at the Fermi level ($E = 0$ eV) revealed 2.4 % La, 0.7 % O, 91.9 % Fe and 5.0 % As contributions. From a chemical point of view, the states at the Fermi level and thus the Fermi surface are dominated by Fe–Fe π^* antibonding orbitals.

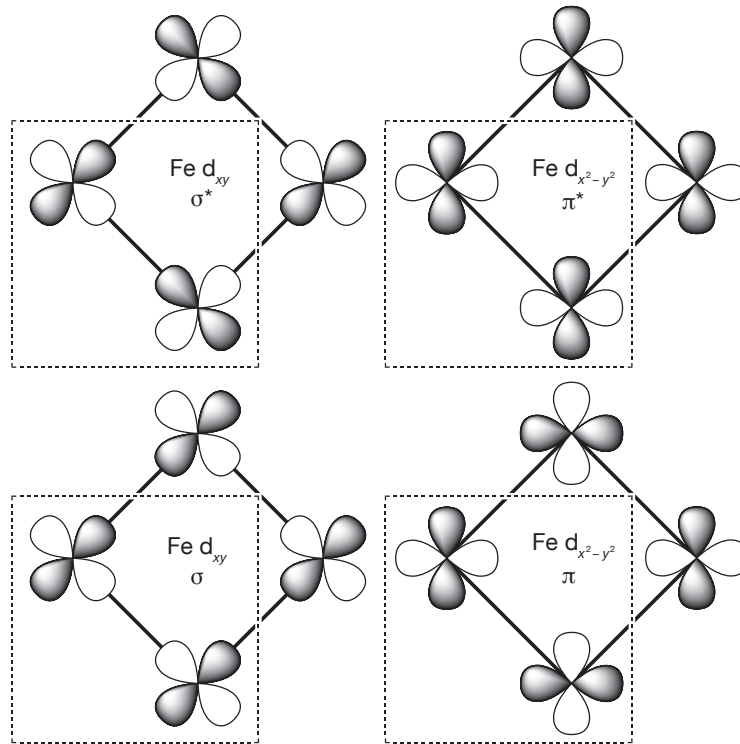


Figure 1.4: Schematic Fe–Fe interactions in LaFeAsO (the unit cells are depicted as dotted squares). The bonding σ and π and for the most part, the antibonding π^* orbitals are occupied.

The states at the Fermi level are not only responsible for the normal conductivity in LaFeAsO. Depending on the total number of valence electrons, the Fermi energy can be decreased (also referred to as hole doping) or increased (electron doping), because charge neutrality is not mandatory in metals. In this way, the non-superconducting and charge-neutral parent compound LaFeAsO can be altered in such way (e.g. by fluoride doping) that it becomes superconducting upon cooling. As will be seen in the next chapter, the exact topology of the bands at the Fermi level is crucial for superconductivity because it is at the Fermi level, where the superconducting gap occurs.

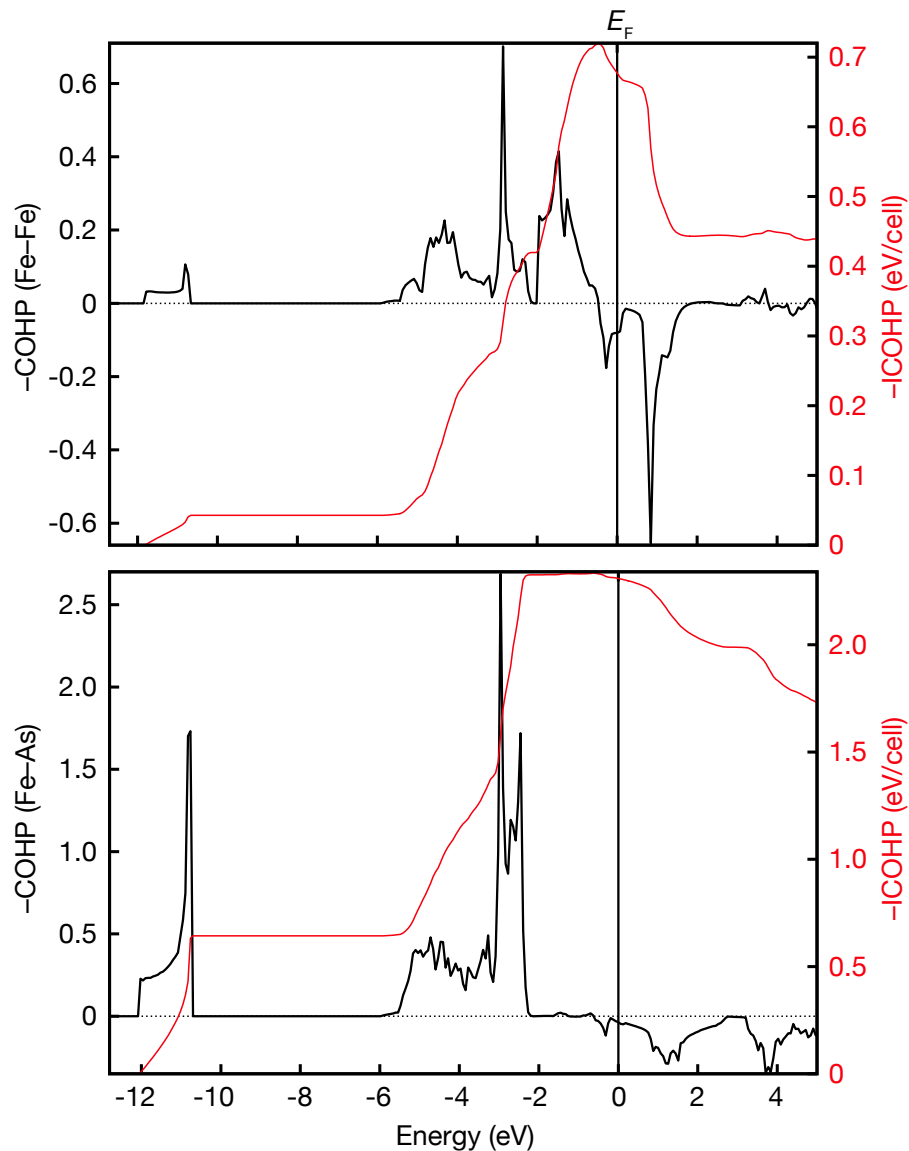


Figure 1.5: $-\text{COHP}$ and $-\text{ICOHP}$ of a Fe–Fe nearest-neighbour bond (top) and a Fe–As bond (bottom) in LaFeAsO.

Metals like LaFeAsO sometimes are also referred to as semi-metals.^[23] Semi-metals are true metals,^{iv} which can be formally derived from indirect semiconductors. This deduction is sketched for a two-dimensional solid in Figure 1.6. In Figure 1.6 (left), the situation of an indirect semiconductor is depicted, which shows a vertical separation of the conduction and valence band by an energy gap and a horizontal separation in momentum space, which results in an indirect band gap. In semi-metals

^{iv} A metal simply is defined as a material having finite conductivity at zero temperature. By means of band structures, this is the case if there are bands, which cross the Fermi level. The term ‘semi-metal’ must not be confused with the term ‘half-metal’, which also denotes a true metal, but with a completely ferromagnetic conduction band.

such as the iron pnictides (Figure 1.6, middle), these bands are still horizontally displaced, but they overlap in energy, so that electrons from the valence band flow into the conduction band. As there are ‘holes’ in the \cap -shape valence band then, this band is also denoted as a hole pocket and likewise, the U-shape conduction band as an electron pocket. In Figure 1.6 (right), the according two-dimensional Brillouin zone with the resulting Fermi cylinders (circles) is also depicted.

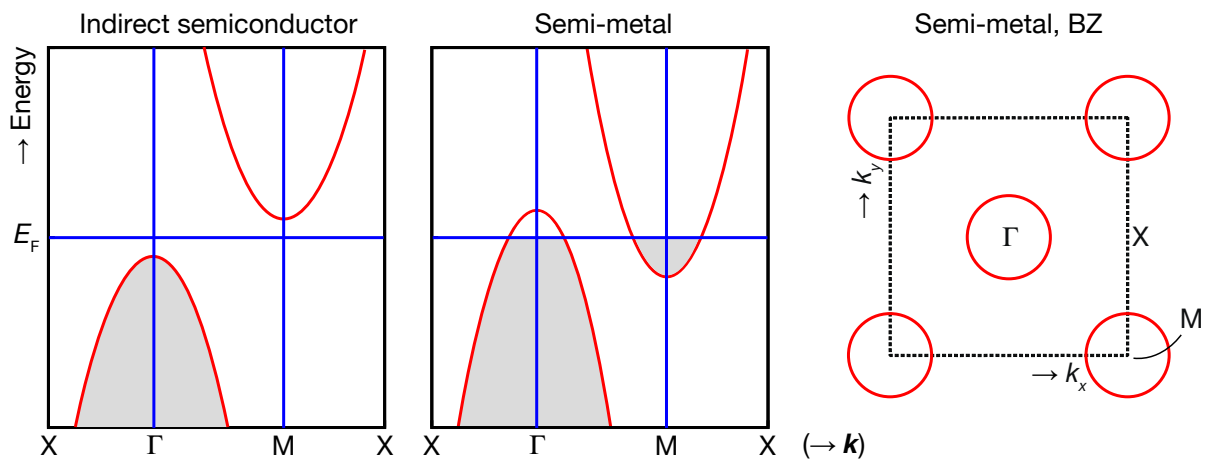


Figure 1.6: Left: Band structure of an indirect 2D-semiconductor. Middle: Band structure of a 2D-semi-metal. Right: Brillouin zone (BZ) with Fermi surface sheets of a semi-metal. The special points of the BZ were chosen to match the situation in the iron pnictides.

1.1.2 Proposed superconducting mechanism

A number of unusual properties in the iron pnictide superconductors show that superconductivity is not of BCS-type in this class of compounds. In short, one could say that in BCS superconductors, superconductivity is mediated by phonons, thus the lattice is used as ‘deformable medium’. In non-BCS superconductors like the cuprates and iron pnictides, the role of phonons is replaced by a special spin arrangement (e.g. antiferromagnetic order) and superconductivity is therefore called electron-mediated.

Chapter 1: Introduction

Indeed, superconductivity is not only electron-mediated but there is also growing evidence for the first case of multigap^{[24], v} superconductivity with a sign change of the superconducting order parameter between different sheets of the Fermi surface. This is a state, which had not been discovered in any compound previously but had been suggested to exist theoretically.^[25] The superconducting order parameter (also referred to as superconducting wavefunction) is the quantum mechanical description of the electron pairing in the superconducting state. It can be isotropic, which is then called s-wave or conventional superconductivity, because a wavefunction with spherical symmetry is an appropriate quantum mechanical description for the pairing. This is the case in all phonon-mediated BCS superconductors.

For the formation of Cooper pairs due to spin fluctuations in the so-called unconventional superconductors, the situation is more complex. The superconducting order parameter must have a sign change, which requires either d- or s_{\pm} -symmetry (see Figure 1.7 and Figure 21.1 in the appendix). The d-wave order parameter is typically of $\cos(k_x) - \cos(k_y)$ symmetry and the s_{\pm} -wave order parameter of $\cos(k_x) + \cos(k_y)$ symmetry.

^v Multigap superconductivity has first been proposed for the intermetallic s-wave (BCS) superconductor MgB_2 . As a consequence of more than one superconducting order parameters, there are also more than one superconducting energy gaps, which can be observed e.g. by tunnelling spectroscopy or by the course of the electronic contribution of C_p at the superconducting transition. Within the BCS theory, two superconducting order parameters are necessary to describe such strong electron-phonon coupling, that T_C s as high as 38 K can be reached at all. MgB_2 is therefore sometimes referred to as 'queen of BCS superconductors'.

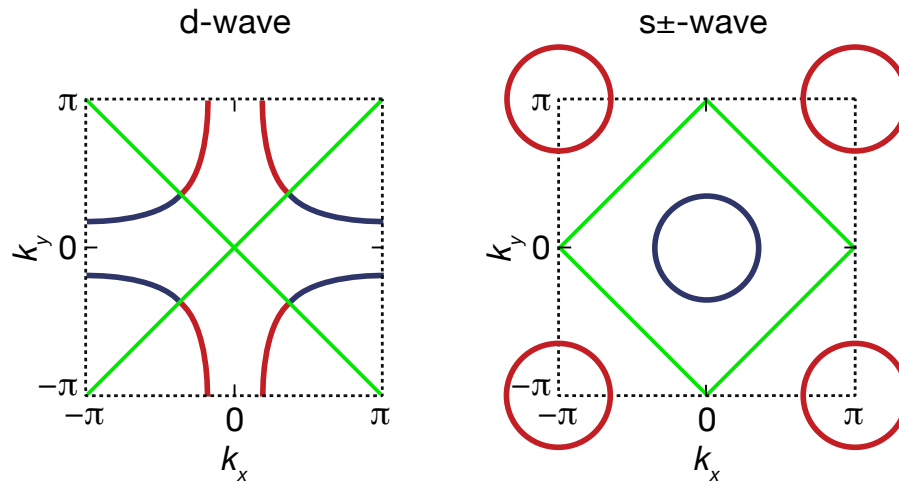


Figure 1.7: Brillouin zones and Fermi surfaces with a sign change in the superconducting order parameters. Green lines denote nodes in the superconducting order parameters.

For example in the cuprates, it is generally accepted that the superconducting order parameter is of $d_{x^2-y^2}$ symmetry and there is only one superconducting gap. The non-superconducting parent compounds of the cuprates are Mott insulators and they possess localised magnetic moments at the Cu sites, which are linked^[26] by the superexchange mechanism and form a checkerboard ordering pattern.^[27] On both electron and hole doping, the magnetic ordering disappears and the materials become metals and superconductors.^[28] But although there has been impressive progress in describing the underlying physics of the cuprates,^[29] complete understanding still has not been achieved.^[30]

Even early experiments have shown that the situation is different in the iron pnictide superconductors. Their parent compounds are semi-metals rather than Mott insulators and show weak, itinerant magnetism rather than strong, localised magnetic moments.^[31] Furthermore, many experiments have ruled out d-wave superconductivity but shown that the order parameter is nodeless and the superconducting wave function presumably has s_{\pm} -symmetry.^[32] ^{vi}

^{vi} Corner-junction experiments have shown that the superconducting order parameter cannot be of $d_{x^2-y^2}$ symmetry, as such a wavefunction would lead to a detectable destructive interference of the superconducting current between two adjacent faces of a single crystal. Additionally performed angle-resolved photoemission spectroscopy (ARPES) measurements of the magnitude of the superconducting energy gap have shown that there are no nodes in the energy gap of the observed Fermi surface sheets.

Chapter 1: Introduction

This sign-reversal s_{\pm} -symmetry also is an implication of how the band structures and thus Fermi surfaces of the iron-based superconductors look like. The two-dimensional representation of the band structure, which has been calculated for LaFeAsO, is depicted in Figure 1.8 (left): Two bands feature the characteristic \cap -shape (hole-like character) around M– Γ –Z–R and two bands around X–M– Γ exhibit the U-shape (electron-like character). The Fermi surfaces of the undoped iron pnictides (in the $P4/nmm$ space group) therefore consist of two electron-like cylinders around the tetragonal M point and two hole-like cylinders around Γ and a (π, π) -nesting vector between the electron and hole cylinders exists. A two-dimensional schematic plot of the Brillouin zone with these cylinders and the Fermi surface nesting vector is depicted in Figure 1.8 (right). This electronic situation could also be experimentally confirmed via ARPES measurements.^[32c]

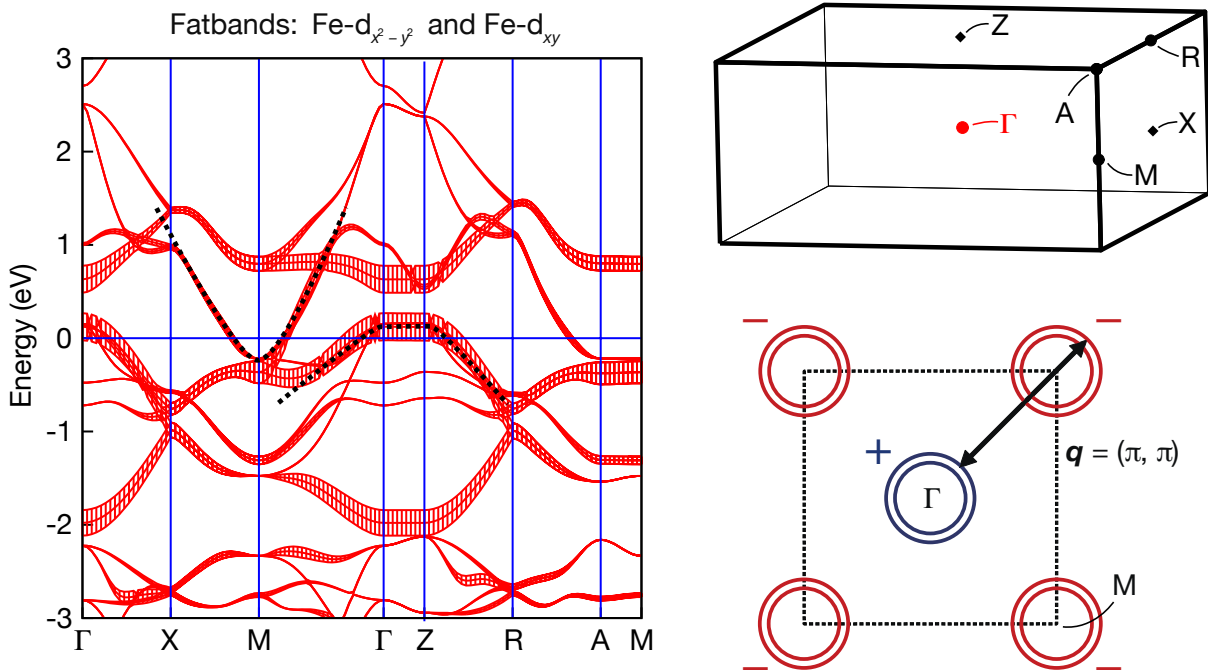


Figure 1.8: Left: Band structure of LaFeAsO (Fe- d_{xy} and Fe- $d_{x^2-y^2}$ orbitals are emphasised, dotted lines are guides for the eye). Top right: Three-dimensional Brillouin zone (BZ). Bottom right: Top view of the BZ with stylised hole and electron cylinders. The colours denote the signs of the superconducting order parameter.

This electronic situation however seems to be highly unstable. It is well established that many undoped iron pnictide superconductors experience a weak structural tetragonal-to-orthorhombic structural distortion (e.g. at ~ 150 K in LaFeAsO) followed

by the formation of a spin-density wave anomaly (SDW) at slightly lower temperatures. The measurable magnetic moment (e.g. via neutron diffraction) of this spin-density wave anomaly grows on further cooling to an ordered magnetic moment of $\sim 0.4 - 0.8 \mu_B$ per iron atom in LaFeAsO.^[31, 33] The nearest-neighbour magnetic moments are then aligned along the shorter orthorhombic direction and anti-aligned along the longer one (Figure 1.9) forming a stripe-type antiferromagnetic order:^[31, vii] Suppression of this long-range magnetic order is believed to be one condition to induce superconductivity in these compounds. This has first been achieved either by electron or by hole doping but later it could be shown that the application of pressure is another measure to realise this effect.^[34]

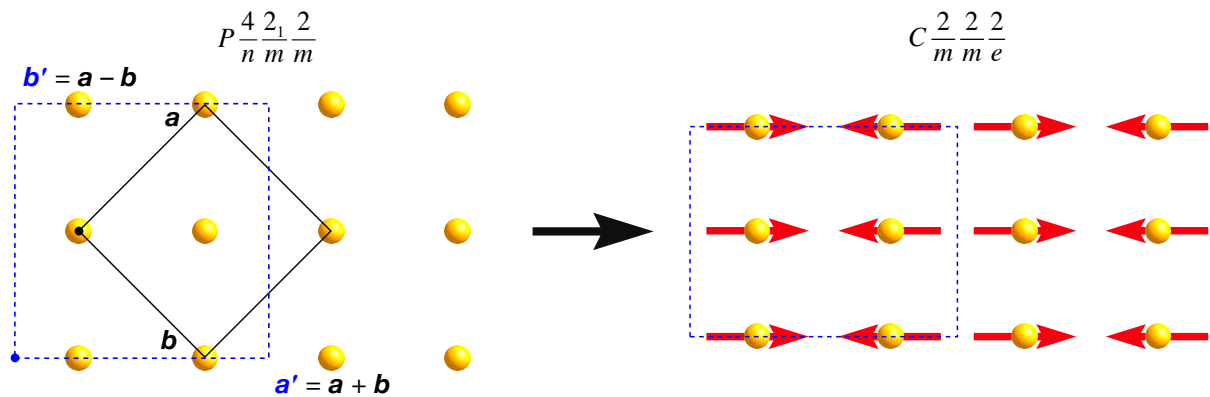


Figure 1.9: Structural distortion and magnetic ordering of LaFeAsO on cooling. The magnitude of the distortion is emphasised for clarity. The solid black lines denote the tetragonal unit cell ($o1$) and the dashed blue lines the orthorhombic cell.

What is the superconducting mechanism in these superconducting iron pnictides, then? In conventional BCS superconductors, the superconducting gap is isotropic and it has the same sign over the Fermi surface (s-wave). The formation of Cooper pairs is possible due to attractive electron–phonon interactions. But even in LaFeAsO_{1-x}F_x with a critical temperature of ‘only’ 26 K,^{viii} the calculated electron–phonon coupling constant $\lambda_{e-p} \approx 0.21$ is much too small in order to explain critical temperatures of this order of magnitude.^[35] The Cooper pairs are therefore presuma-

^{vii} The cause and effect of these phase transitions will be discussed in Chapter 4.3 in more detail.

^{viii} A T_C of 26 K would be compatible with the BCS theory.

bly mediated by spin-fluctuations (electron–electron interactions). On the one hand, it can be shown, that in order to satisfy the BCS gap equation in such spin-fluctuation mediated systems, the superconducting gap *must* change its sign.^[36] This is possible either with a $d_{x^2-y^2}$ - or a s_{\pm} -superconducting order parameter and the iron pnictide superconductors seem to exhibit the latter. There are also many experiments, which support this claim.^[32]

On the other hand, it can be shown by a spatial Fourier transform of the superconducting pairing interaction function (which is defined in momentum space), that two pairing electrons can avoid their Coulomb repulsion by arranging themselves in space in such way that the potential between them becomes attractive. This is the case on near-neighbour as well as some longer-range lattice sites^{ix} for both electrons of a cooper pair (Figure 1.10).^[32a, 36-37]

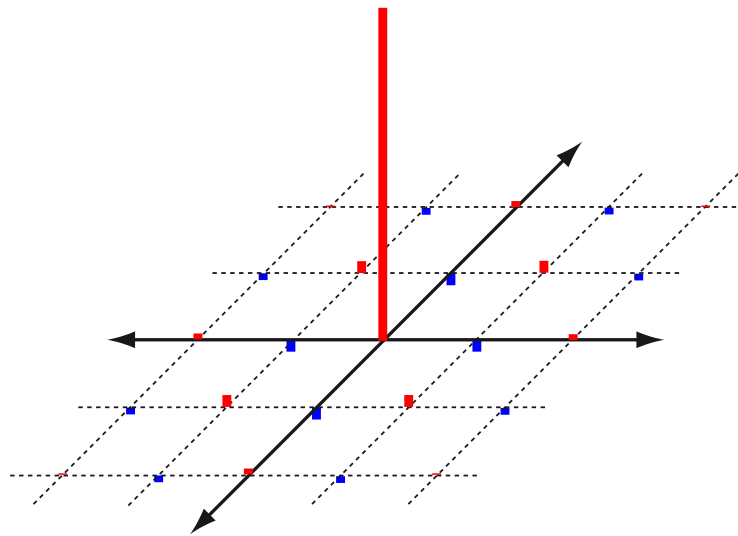


Figure 1.10: Fourier transform of the pairing interaction function for a two-dimensional system with short-range antiferromagnetic spin fluctuations. Here one member of the singlet pair is located at the origin and the other at a surrounding lattice site. The potential is strongly repulsive for both electrons on the same site, as shown by the large positive (red) bar at the origin. However, the potential is attractive on near-neighbour sites (blue bars).

^{ix} of a square lattice, as it is the case in the iron pnictides

Further insights in the superconducting mechanism however, for example the question to what extent electron–phonon coupling yet is present in the iron pnictides, are still disputed controversially.

All considerations of this chapter are not only valid for the 1111 iron pnictides in the $P4/nmm$ space group, but also for the new iron arsenide superconductors in the ThCr_2Si_2 (122) structural family. These materials crystallise in the $I4/mmm$ space group and will be discussed in Chapters 7 – 9.

In the Brillouin zone of the 122 iron arsenides, two electron cylinders are located at the tetragonal X point (Figure 1.11), which results in both the 1111 and the 122 structures sharing a (π, π) nesting vector between each electron- and hole-cylinder pair. This is also reasonable as both structure types exhibit the same local symmetry around the iron atoms and the band structures around the Fermi level depend mainly on the Fe-d and Pn -p orbitals. All known iron pnictides of other structural families (e.g. 11, 111, 21311, 32522) crystallise either in the $P4/nmm$ or in the $I4/mmm$ space group.

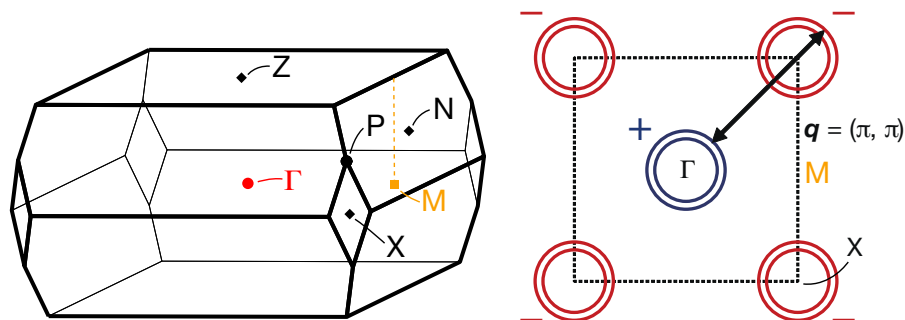


Figure 1.11: Brillouin zone and stylised Fermi surface cylinders for iron pnictides in the $I4/mmm$ space group.

1.2 Overview and motivation

Much progress has already been made regarding the physical background of the newly discovered iron pnictide superconductors since their discovery. That is due not least to the availability of suitable substances, optimised syntheses and detailed structural studies. The scope of this dissertation therefore has not only been the synthesis of various new superconducting and non-superconducting iron pnictides of several structural families but also their in-depth crystallographic and physical characterisation.

In Chapters 3 – 6, the family of the ZrCuSiAs-type (1111) compounds is subject of discussion. The solid solution series $\text{La}(\text{Co}_x\text{Fe}_{1-x})\text{PO}$ is analysed regarding magnetic and superconducting properties and the new compounds EuMnPF and REZnPO , as well as the new superconductor parent compound SrFeAsF are presented.

Chapters 7 – 9 are dedicated to the new iron arsenide superconductors of the ThCr_2Si_2 -type (122 family). Therein, also the discovery of the first superconductor in this structural family, $\text{Ba}_{0.6}\text{K}_{0.4}\text{Fe}_2\text{As}_2$, is unveiled. A detailed examination of the complete solid solution series $(\text{Ba}_{1-x}\text{K}_x)\text{Fe}_2\text{As}_2$ is presented. Moreover, the crystallographic phase transitions of the closely related compounds SrFe_2As_2 and EuFe_2As_2 are characterised and the superconductors $\text{Sr}_{1-x}\text{K}_x\text{Fe}_2\text{As}_2$ and $\text{Ca}_{1-x}\text{Na}_x\text{Fe}_2\text{As}_2$ are examined for magnetic and phononic excitations.

In Chapter 10, the redetermined crystal structure of the superconductor $\text{Fe}(\text{Se}_{1-x}\text{Te}_x)$ (11-type) is presented from a chemist's point of view.

Chapters 11 – 14 look into the superconducting and non-superconducting iron arsenides of more complex structural families (32522-type and 21311-type). Therein, crystallographic and magnetic details of $\text{Sr}_3\text{Sc}_2\text{O}_5\text{Fe}_2\text{As}_2$ are presented and $\text{Ba}_2\text{ScO}_3\text{FeAs}$ and $\text{Sr}_2\text{CrO}_3\text{FeAs}$, the first two members of the new 21311-type are portrayed. $\text{Sr}_2\text{CrO}_3\text{FeAs}$ is looked at in close detail with various methods, so e.g. the spin structure of the magnetically ordered compound is solved and a possible reason for the absence of superconductivity in this compound is given. Finally, the superconductor $\text{Sr}_2\text{VO}_3\text{FeAs}$ is scrutinised and necessary prerequisites for superconductivity in this compound are suggested.

In Chapter 15, a summary of all previous results as well as a short perspective on more recent developments are given. Therein, questions that remain unanswered are briefly discussed, too.

Last but not least, the rest of this dissertation is dedicated to the description of the methods, which were employed to synthesise and examine the compounds in this dissertation (Chapter 2) and the description of specially developed measurement equipment and data processing software (Chapters 16 – 20).

In all chapters, the focus was put on a look at the subject from a chemist's perspective. This is particularly true for details, which had been or which would have been overlooked otherwise. It is this different view on the systematic changes of material properties due to altered chemical conditions, which is the motivation for a chemist to work in the field of superconductivity research.

2. Methods

2.1 Density functional theory

Electronic structure calculations were performed either using the linear muffin-tin orbital (LMTO) method in its scalar-relativistic version (TB-LMTO-ASA)^[38] or with the WIEN2k program package^[39] using density functional theory within the full-potential LAPW method and the local spin density approximation (LSDA) or generalised gradient approximation (GGA, *Perdew, Burke and Ernzerhof*)^[40]

In case of the LMTO calculations, reciprocal space integrations were performed with the tetrahedron method. To avoid too large overlap of the atom-centred spheres for the atomic sphere approximation, interstitial spheres were introduced. The crystal orbital Hamilton population (COHP) method^[41] was used for bonding analyses. COHP yields the energy contributions of all electronic states for a selected bond. In this dissertation, energy states are plotted against $-\text{COHP}$, thus values are negative for antibonding and positive for bonding interactions.

Full-potential LAPW, which was employed for the WIEN2k calculations, is based on the muffin-tin construction of non-overlapping spheres. In the interstitial region between spheres, the potential is represented by a plane-wave expansion. The according plane-wave cut-off $r_{\text{mt}} \cdot k_{\text{max}}$ was set to 7.0 – 8.0. Because of the great flexibility and accuracy of this expansion for the potential and charge density, a very high numerical accuracy is achieved for the LAPW method. Mixed LAPW and APW + *lo* (*lo* = local orbitals) basis sets were used to increase the efficiency of the APW linearisation.^[42] Further technical details can be found in [43] and the monograph of Singh.^[44] Total energies converged to residual changes smaller than 10^{-5} Ry·cell⁻¹ and charge densities of the SCF cycles converged to changes smaller than 10^{-4} e·cell⁻¹.

To calculate the insulating ground states of non-metals, either the LDA + *U* approach^[45] with the SIC method for double counting correction^[46] or the EECE method (exact exchange of correlated electrons)^[47] were used, which both are implemented in the WIEN2k program. Values of up to 8 eV were used for the effective Hubbard *U*

($J = 0$). The LSDA (respectively GGA) treatment was retained to describe uncorrelated states. Fermi surfaces were visualised with XCrysDen.^[48]

For volume and structure optimisations, the atomic sphere radii were reduced by 8 – 15 % and fewer irreducible k -points were used. As all calculated structures are either tetragonal or rhombohedral, absolute energies were calculated as a function of the lattice parameters a and c (using the hexagonal setting for rhombohedral structures), both lattice parameters were varied independently around their experimental or estimated values (7×7 to 9×9 calculations) and the structures were allowed to relax. In order to find the absolute energy minima, Taylor's theorem for two variables was fitted numerically to the calculated energies with the computer algebra system Maple,^[49] thus permitting interpolation between the calculated values. An example Maple worksheet to calculate the absolute energy minima is available for download.^[50]

Both LMTO and WIEN2k had been compiled for MacOS 10.5 (Leopard) and both programs were run under MacOS 10.5 and 10.6 either on a Mac MINI (2×1.8 GHz Core 2 Duo) or on a Mac PRO workstation (8×3.0 GHz Xeon 5160). For WIEN2k, the Intel compiler suite (icc, ifc, mkl) was used in its 64-bit variant. The compiler and linker settings can be found in the appendix (Chapter 21.2).

2.2 Powder diffraction

2.2.1 X-ray powder diffraction

The X-ray powder diffraction patterns were recorded on the following computer controlled powder diffractometers:

- HUBER Imaging Plate Guinier Diffractometer G670 (Cu- $K\alpha_1$ radiation, Ge (111) primary monochromator, HUBER 616.2, $\lambda = 154.06$ pm, silicon dioxide and silicon as external standards, oscillating sample holder)

- STOE Stadi P (Cu-K α_1 radiation, Ge (111) primary monochromator, $\lambda = 154.06$ pm, silicon as external standard, rotating capillary 0.1 mm outer diameter or rotating flat sample holder)
- STOE Stadi P (Mo-K α_1 radiation, Ge (111) primary monochromator, $\lambda = 70.93$ pm, silicon as external standard, rotating capillary 0.2 mm outer diameter or rotating flat sample holder)

HUBER powder data were pre-processed with the HConvert program (see Chapter 18)^[51] The diffractograms were processed with WinXPOW,^[52] phase analyses were carried out either manually using Pcpdwin^[53] or DDview+^[54] or semi-automatically using the WinXPOW Search/Match algorithm, which both access either the PDF 2 or PDF 4+^[55] database. Manual and semi-automatic indexing of powder patterns was performed either with TOPAS,^[56] CMPR^[57] or DICVOL.^[58]

In powder diffraction patterns, the x -axis is either given as the scattering angle at a specific incident wavelength or the related wavelength-independent Q -value.

Q is defined as:

$$Q = \frac{2 \cdot \pi}{d} \quad (d \text{ being the interplanar spacing})$$

On inserting the *Bragg* equation $\lambda = 2 \cdot d \cdot \sin(\theta)$, Q therefore is:

$$Q = \frac{4 \cdot \pi}{\lambda} \cdot \sin(\theta)$$

2.2.2 Neutron powder diffraction (elastic scattering)

Neutron powder diffraction patterns of different compounds were recorded either at the high-flux powder diffractometer D20 at Institut Laue-Langevin (Grenoble, France) with 187 pm incident wavelength or at the SPODI diffractometer at FRM II (Garching, Germany) with incident wavelengths of 155 pm and 146 pm, respectively. The

measurements were performed at several temperatures to check for antiferromagnetic ordering.

From the antiferromagnetically ordered compound $\text{Sr}_2\text{CrO}_3\text{FeAs}$, powder diffraction patterns were also recorded using polarised neutrons (474 pm incident wavelength) on the polarised spectrometer DNS at FRM II (Garching, Germany) at various temperatures. An unambiguous separation of nuclear coherent, spin incoherent and magnetic scattering contributions simultaneously over a wide scattering angle has been achieved via neutron polarisation analysis from the xyz-method.^[59]

2.2.3 Simulation of powder patterns

Powder patterns were simulated with the CrystalDiffract^[60] tool of the CrystalMaker^[61] program package. For powder pattern simulations, Pseudo-Voigt profiles were used. The Pseudo-Voigt (pV) profiles are a linear combination of a Gaussian (G) and a Lorentzian (L) function:

$$pV(x) = \eta \cdot L(x) + (1 - \eta) \cdot G(x) \quad \text{with}$$

$$G(x) = e^{-\ln(2) \cdot \left(\frac{x-x_0}{\omega}\right)^2} \quad \text{and}$$

$$L(x) = \frac{1}{1 + \left(\frac{x-x_0}{\omega}\right)^2}$$

For the different X-ray diffractometers, the following profile parameters were used:

- HUBER Imaging Plate Guinier Diffractometer 670 (Cu- $K\alpha_1$):
 $\eta = 0.7$; $\omega = 0.175^\circ 2\theta$
- STOE Stadi P (Cu- $K\alpha_1$):
 $\eta = 0.7$; $\omega = 0.175^\circ 2\theta$
- STOE Stadi P (Mo- $K\alpha_1$):
 $\eta = 0.75$; $\omega = 0.117^\circ 2\theta$

2.2.4 Rietveld refinements (general)

Rietveld refinements^[62] of both X-ray and neutron nuclear scattering patterns were performed either with the GSAS/EXPGUI^[63] or TOPAS^[56] program package.

For GSAS X-ray refinements, a convolution of the empirical Pseudo-Voigt function by *Thompson et al.*^[64] with the asymmetry function of *Finger et al.*^[65] (GSAS CW profile function 3) was used. The profile parameters for the Gaussian and Lorentzian contributions were constrained if necessary and checked for plausibility. Asymmetry starting parameters were taken from a standard silicon sample. For GSAS DNS neutron scattering refinements, the standard Gaussian profile function with asymmetry corrections (GSAS CW profile function 1) was used.

For X-ray and neutron refinements with TOPAS, the fundamental parameters approach was used to generate the reflection profiles. This approach involves a convolution of appropriate source emission profiles with axial instrument contributions as well as crystallite microstructure effects. In order to describe small peak half width and shape anisotropy effects, a modified approach of *Le Bail and Jouanneaux*^[66] was implemented into the TOPAS program and the respective parameters were allowed to refine freely. For details about this implementation, see Chapter 2.2.5.

For both GSAS and TOPAS refinements, preferred orientation of the crystallites was described either with the March-Dollase^[67] or a spherical harmonics function. Capillary X-ray samples were corrected for absorption with estimated powder densities between 50 and 70 % of the crystallographic density and the calculated linear absorption coefficient.

2.2.5 TOPAS Academic launch mode control files (.inp templates)

For Rietveld refinements with TOPAS, several diffractometer specific templates (TOPAS launch mode .inp control files) were generated for the following powder diffractometers:

- STOE STADI P (PSD), Mo-K α_1 , Debye-Scherrer- and transmission geometry
- STOE STADI P (PSD), Cu-K α_1 , Debye-Scherrer- and transmission geometry
- HUBER G670 (imaging plate), Cu-K α_1 , Guinier geometry

-
- HUBER G670 (imaging plate), Co-K α_1 , Guinier geometry
 - BRUKER D8 Discover, Cu-K α (beta filter), Göbel mirrors, Bragg-Brentano- and transmission geometry
 - PANALYTICAL X'Pert, Cu-K α (graphite secondary monochromator), Bragg-Brentano geometry
 - ILL D20 two-axis neutron diffractometer, 187 pm wavelength (adjustable)
 - FRM II SPODI neutron diffractometer, 155 pm wavelength (adjustable)

Diffractometer specific templates

All templates are available for download^[68] and as an example, the STOE STADI P, Mo-K α_1 , Debye-Scherrer template is discussed in this chapter. For details about the definition of commands, refer to the TOPAS Academic Technical Reference.^[69] Generally, remarks are added (marked with `/*...*/` or `'`) and necessary user action is marked with the symbol `#`. For better readability, some remarks following commands were omitted in this discussion. However, they can be found in the original templates. To refine a parameter, it must be preceded either by a chosen variable name or by `@`. If the chosen variable name is preceded by `!`, the parameter will be kept fixed.

Every `.inp` template starts with the header containing information about both the diffractometer and template followed by the **general part** of the template, which consists of general commands concerning the entire refinement.

```
/* Rietveld template for
- STOE STADI P
- Mo-Ka1 radiation
- Ge111 monochromator ... */
```

This header is followed by commands to read in the observed diffractogram, the robust refinement option (see Chapter 'Robust refinements', page 34), residual values (for their definition refer to the TOPAS Technical Reference,^[69] page 18), number of convolution steps, calculation of standard deviations and convergence criteria.

```
'Powder file
xdd "#####.xy"
```

Chapter 2: Methods

```
'Robust refinement option
/* #include "robust.inc"
   prm !sigma_correction_factor 1 'must not be zero
   Robust_Refinement(sigma_correction_factor) */

'R values (only meaningful in case of non-robust refinement)
r_p           1
r_exp         1
r_p_dash      1
r_exp_dash    1
r_wp          1
r_wp_dash     1
gof           1
weighted_Durbin_Watson 0

'Calculation and convolution step size
x_calculation_step = Yobs_dx_at(Xo);
convolution_step 5

'Calculate errors
do_errors

'Convergence criteria
chi2_convergence_criteria 1e-6
```

Next is the diffractometer's emission profile, which consists of the wavelength and Lorentzian half width (in mÅ) of the emitted X-ray light. The peak area can be set to one as normalisation factor.

```
'Emission profile
lam ymin_on_ymax 0.0001
la           1.000000 'Area
lo           0.709300 'Wavelength
lh           0.2695   'Lorentzian half width in mAngstr
```

The diffractometer's constants start with the diffractometer radius (Debye-Scherrer geometry) or radii (Bragg-Brentano geometry). In case of the Guinier geometry, an averaged radius is used, as the distance between sample and detector is scattering angle-dependent. Next is the Lorentzian polarisation factor, which depends both on the monochromator and wavelength of the X-ray source.

```
'Diffractometer constants
Radius(170)
```

```
LP_Factor(!lp, 12.466)      '2th angle of Ge_111 Mo-monochromator
```

The position sensitive device divergence correction is strictly necessary only for higher divergence and greater sample lengths, like it is the case in neutron diffractometers.

```
'PSD counter correction
lpsd_th2_angular_range_degrees      6
lpsd_equitorial_divergence_degrees  0.06
lpsd_equitorial_sample_length_mm    0.18
```

In TOPAS, axial divergence is generally best described with the full axial model, which defines various lengths in mm (X-ray tube filament length, axial sample length and length of the receiving slit) and the apertures of the Soller slits (in degrees). As the latter values are strictly valid for the Bragg-Brentano geometry only but yield the best peak fit also for many other diffractometer setups, they are best refined with a known standard and one or more of these parameters should be refined to compensate displacements (see template files for details).

```
'Axial divergence
Full_Axial_Model(11, 10, 6, 1.25, 4.91)

'Zero shift
Zero_Error(@, 0) 'in degrees.
```

In the case of Debye-Scherrer capillary setup, an option to correct for linear absorption was added. It can be adjusted for both capillary diameter and the linear absorption coefficient. The latter can be calculated by TOPAS using the 'Phase_LAC_1_on_cm' or the 'Mixture_LAC_1_on_cm' macros. Usually, the true density of powders is 50 – 70 % of the crystallographic density depending on the packing density; the obtained absorption coefficients therefore have to be multiplied by 0.5 to 0.7:

```
'Capillary absorption correction.
capillary_diameter_mm          0.18
capillary_u_cm_inv             !absc  1
capillary_parallel_beam
```

Chapter 2: Methods

An option to output the calculated intensities and difference curve of the entire diffractogram and the background function variables conclude the general part of each template. It is generally recommended to adjust the number of background terms according to the refinements' needs. Care has to be taken that:

- The number of background parameters is sufficiently high to accurately describe the background of the diffractogram (best checked with the corresponding 'display background' switch in TOPAS' GUI).
- The refined background parameter values should not be higher than their standard deviations (otherwise the number of parameters may need to be reduced)
- The background function must not produce any bulges at observed reflections as this would lead to an incorrect intensity extraction (check also via 'display background' switch). If this is the case, the number of parameters has to be reduced, too.

```
'Output for whole diffractogram
'Out_Yobs_Ycalc_and_Difference("out_Yobs_Ycalc_and_Diff.txt")

'Background (Shifted Chebychev). Uncomment remarks if more
'background terms are needed.
bkg @ 0 0 0 0 0 0
      0 0 0 0 0 0...
```

The **phase specific part** of each template contains information about the different phases, which are included in the refinement. It has to be repeated for every phase but one must make sure that all variables have different names for each phase. Each phase starts with the 'STR' macro, which defines the space group and name for each phase and is followed either by macros or commands defining the lattice parameters.

```
'Phase 1 (main phase)
STR(#####, "#name#")

'###Choose appropriate symmetry###
Cubic(@ 5.54)
'Tetragonal(@ #, @ #)...
```

The peak function type, which should be used for the phase contribution convolution is next (fundamental parameters approach as default). It is followed by an option to generate output files for each phase as well as general phase information (e.g. the linear absorption coefficient and the R_{Bragg} residual value).

```
peak_type fp
```

```
'Generate output files for phase 1
/* Out_CIF_STR("phase1.cif")
   Out_F2_Details("phase1_F2.txt")
   Out_FCF("phase1_FCF.fcf")
   Create_hklm_d_Th2_Ip_file("phase1_hklm_d_Th2_Ip.txt") */

'Information on phase 1
cell_volume 0
Phase_LAC_1_on_cm(0)
Phase_Density_g_on_cm3(0)
r_bragg 1
```

Generally, all refinable site parameters and the thermal displacement factor 'beq'^x must be refined at least for the main phase(s) of the powder. Constraints, restraints or tools such as the rigid body approach can be used for more complex structures. The site parameters and phase scale factors are defined as follows.

```
'Site parameters - append :2 to space group for origin choice 2.

'###ENTER SITE PARAMETERS HERE###
site La x 0.00331 y 0.19919 z 0.25 occ La 1 beq 0.7

scale @ 1e-7
```

In the case of the Guinier geometry, the 'scale' command is followed by a Guinier geometry specific intensity correction, which has to be pasted for each phase. See Chapter 'HUBER G670 imaging plate intensity correction' on page 31 for details.

^x Alternatively, anisotropic displacement parameters can be refined with the ,ADPs' macro. Then U values instead of B values are used. The relation between both parameters is: $B = 8\pi^2 \cdot U$.

Chapter 2: Methods

Crystallite microstructure effects can be described either with the integral breadth crystallite size approach and the FWHM-based strain calculation (which is highly recommended at least for the main phase) or classical strain / crystallite size functions. Refer to the TOPAS Academic Technical Reference^[69] (page 27) for details about these functions.

```
'Integral Breadth Crystallite Size approach
LVol_FWHM_CS_G_L(1, 0, 0.89, 0, csgc, 10000, cslc, 10000)
                    '10000 = infinite size

'###FWHM-based strain calculation by a Voigt function###
e0_from_Strain( 0, sgc, 0, slc, 0) 'e0 single strain value...

'Classical Microstructure functions...
'Strain_L(@, 0)
'Strain_G(@, 0)
'CS_G(@, 0)
'CS_L(@, 0)
```

Preferred orientation of crystallites can lead to systematic intensity deviations, which can be corrected either by the March Dollase or spherical harmonics functions. The latter one is (strictly) valid for rotating samples only, but has the advantage that the orientation of the lattice plane susceptible to preferred orientation does not have to be defined. It also is the only possibility to correct complex textural behaviour.

```
'Texture - possibility A: March Dollase
'Preferred_Orientation(@, 1,, 0 0 1) 'Enter correct Value for hkl

'Texture - possibility B: Spherical Harmonics function
PO_Spherical_Harmonics(sh, 4) 'Specify number of terms
```

The phase specific part ends with an adaptation of the anisotropic peak broadening and peak shape model by *Le Bail* and *Jouanneaux*^[66] which is discussed in Chapter 'Le Bail-Jouanneaux anisotropy correction' (page 32).

```
/* Le Bail-Jouanneaux anisotropic peak broadening and shape
*****
*   USE ONLY WHEN BOTH ANISOTROPIC BROADENING AND/OR   *
*                   ANISOTROPIC PEAK SHAPE OCCUR       *
***** ... */
```

2.2.6 TOPAS Academic, special implementations

Several variants of published correction functions have been implemented into TOPAS (either directly into the corresponding .inp templates or into separate macros). In this chapter, these implementations are briefly discussed.

HUBER G670 imaging plate intensity correction

A model for a Guinier geometry imaging plate intensity correction for the HUBER G670 imaging plate diffractometer had originally been published by *Baier*^[70] in the form of a computer program. An adaptation of this model has been implemented into the corresponding HUBER G670 TOPAS template. In the general part of this template, various linear absorption coefficients (in mm^{-1}) and X-ray beam path lengths (in mm) are defined.

```
'G670 Guinier Imaging Plate Absorption coeff. and distances
prm !rDiff      90
prm !rGon       57.3
prm !dCapton    0.08
prm !dCardbox   0.2
prm !dOuter     23
prm !muInner    0.00001
prm !muCapton   0.77
prm !muCardbox  0.81
prm !muAir      0.0013
```

In addition to the model proposed by *Baier*, the thickness and linear absorption coefficient of the sample is added, as scattered X-ray beams are also absorbed by parts of the sample itself. As various tests have shown, this can be a significant contribution, especially in samples with very high absorption coefficients. However, 'dSample' does not exactly specify the real sample thickness, but as this value can be freely refined, neither the correct absorption coefficient nor the actual sample thickness is critical.

```
'Guinier Sample absorption correction
prm !dSample 0 min=0; max=0.1; 'in mm.   ###Refinable
prm !muSample 40 'in mm^-1
```

The actual intensity correction of the diffractogram is performed in the phase specific part of the template with the 'scale_pks' command and uses absorption lengths calculated for different scattering angles. The intensities of every phase have to be corrected separately.

```
'Guinier geometry intensity correction. PASTE FOR EVERY PHASE!  
prm Cosine =Cos(45/180*Pi - 2*Th);      'Th in radians  
prm !wInner=2*rDiff*Cosine-dOuter/Cosine;  
scale_pks =2*Exp(muInner*wInner + muAir*dOuter/Cosine +  
                muCardbox*dCardbox/Cosine + muCapton*dCapton/Cosine +  
                muSample*dSample/Cosine);
```

***Le Bail-Jouanneaux* anisotropy correction**

The FWHM and / or peak shape often depend on the Miller indices of the reflections. Reasons are either ill-crystallised samples (non-spherical crystallites, micro strains, stacking faults, etc.) or inhomogeneous samples, where different crystallites have (slightly) different composition. A very flexible model for the first case has been proposed by *Le Bail* and *Jouanneaux*^[66] and a slightly modified version has been implemented into all TOPAS templates in combination with separate macros. All templates and macros are available for download.^[68] Up to now, various refinements have shown that the model also yields good results in the case of samples with inhomogeneous composition. In each TOPAS template, the width anisotropy parameters 'guc*', 'gvc*' and 'gwc*' and the shape anisotropy parameters 'guv*', 'gvv*' and 'gww*' are defined and restrained to sensible values. It also has to be made sure that appropriate constraints are set for each crystal system. Refer to the original literature for details.^[66] For refinements using the *Le Bail-Jouanneaux* method, the macro 'LeBailJouanneaux' has to be invoked with these parameters.

```
/* Le Bail-Jouanneaux anisotropic peak broadening and shape  
*****  
*      USE ONLY WHEN ANISOTROPIC BROADENING AND/OR      *  
*      ANISOTROPIC PEAK SHAPE OCCUR                      *  
*****  
Adaptation for tetragonal, trigonal and hexagonal crystal  
systems. Remove symmetry constraints for orthorhombic  
monoclinic and triclinic crystal systems.  
Add 33=22=11, 23=13=12 constraints for cubic crystal system.  
ADDITIONAL CONSTRAINTS MIGHT BE NECESSARY */
```

```

#include "lbj.inc"    'Broadening ONLY (recommended)
#include "lbjs.inc"  'Broadening AND shape

'Width anisotropy:
prm guc11 0.1      min=-20; max=20;
...
prm gwc23 =gwc13;  'min=-20; max=20;

'Shape anisotropy:
prm guv11 0.1     min=-20; max=20;
...
prm gvw23 =gvw13; 'min=-20; max=20;

LeBailJouanneaux(guc11,guv11,...,gwc12,gvw12)

```

The 'lbj.inc' and 'lbjs.inc' macros perform the broadening correction as a convolution of the empirical function defined with the 'gauss_fwhm' command with the reflection profiles from the fundamental parameters approach.

```

'Broadening
prm u = (H^2 A_star A_star uc11 + K^2 B_star B_star uc22 +
        L^2 C_star C_star uc33 + 2*uc12 H K A_star B_star +
        2 * uc13 H L A_star C_star + 2*uc23 K L B_star C_star);
        min=-1; max=2;
prm v = ...

gauss_fwhm = u Tan(Th)^2 + v Tan(Th) + w; 'Broadening convolution

```

The 'lbjs.inc' macro additionally contains a variant of the peak shape correction proposed in [66] as a convolution of the empirical function defined with the 'exp_conv_const' command with the reflection profiles from the fundamental parameters approach and the peak broadening function. It yielded excellent results if shape anisotropy occurred.

```

'SHAPE
prm us = (H^2 A_star A_star uv11 + K^2 B_star B_star uv22 +
        L^2 C_star C_star uv33 + 2*uv12 H K A_star B_star +
        2*uv13 H L A_star C_star + 2*uv23 K L B_star C_star);
        min=-1; max=2;

prm vs =...
exp_conv_const = us Tan(Th)^2 + vs Tan(Th) + ws; 'Shape convltn.

```

For an exact definition of the 'gauss_fwhm' and 'exp_conv_const' convolution functions, refer to the TOPAS technical reference^[69] (pages 60 – 61). If more than one phase is present, where anisotropy corrections have to be applied, different variable names have to be chosen and the macro has to be modified accordingly.

Robust refinements

As the Rietveld method relies on least-squares minimisation for the intensity fit, refinements are generally poor, if considerable amounts of unidentifiable impurity phases are present. As such impurity phases should generate only positive outliers in the difference between observed and calculated intensities, *David*^[71] proposed an approach based on Bayesian statistics, in which he penalised such positive outliers less than negative ones. This approach is called robust refinement. *Stone* wrote an implementation of David's approach for TOPAS,^[72] which was adapted for all .inp templates in a slightly modified version. The modification involves the introduction of estimated standard deviations for measurements without experimentally obtained standard deviations. In these cases, the variable 'sigma_correction_factor' can be adjusted until the difference curve of the refinement shows only positive outliers and the intensity extraction is correct. Robust refinements can be invoked by uncommenting the robust refinement option in the general part of every template. The templates and the according 'robust.inc' macro are available for download.^[68] As the weighting scheme is altered after each iteration during a robust refinement, this renders all classical residual values meaningless. Apart from the optical fit of the calculated intensities, a residual value for robust refinements χ_{RR}^2 was proposed, the definition of which can be found in [72]. However, as this value is sensitive to the amount of impurity phase(s), it was not included into the robust refinement option.

```
#include "robust.inc"  
prm !sigma_correction_factor 1 'must not be zero  
'If x/y/sigma input file is provided, the corresponding  
'sigma will always be used. Otherwise:  
'Sigma(Y) is assumed to be sigma_correction_factor*Y^(1/2).  
Robust_Refinement(sigma_correction_factor)
```

The robust.inc macro and the implementation of the estimated standard deviations is defined as follows:

```
macro Robust_Refinement (sigmacorrection)
{
'Rescale peaks according to robust refinement algorithm
prm test = If (Get(r_exp) > 0, Get(r_exp), 10);
prm N = (1/test)^2;
prm !p0  0.40007404
prm !p1  -2.5949286
prm !p2  4.3513542
prm !p3  -1.7400101
prm !p4  3.6140845e-1
prm !p5  -4.5247609e-2
prm !p6  3.5986364e-3
prm !p7  -1.8328008e-4
prm !p8  5.7937184e-6
prm !p9  -1.035303e-7
prm !p10 7.9903166e-10
prm sigY = If (SigmaYobs > 0, SigmaYobs,
              Sqrt(Yobs)*sigmacorrection);
prm t = ((Yobs - Ycalc)/sigY);
weighting = If( t < 0.8, (1/Max(SigmaYobs^2, 1))*N, If( t < 21,
N*((((((((((p10*t + p9)*t + p8)*t + p7)*t + p6)*t + p5)*t + p4)*t
+ p3)*t + p2)*t + p1)*t + p0)/(Yobs - Ycalc)^2, N*(2.0131 * Ln(t)
+ 3.9183)/(Yobs - Ycalc)^2) );
recal_weighting_on_iter
}
```

2.3 Single crystal diffraction

Suitable single crystals were selected under a stereomicroscope and fixed to a silica fibre with super glue. The silica fibre was attached to a brass pin, which itself was mounted on the diffractometer's goniometer head. Single crystal data were collected on a STOE IPDS I diffractometer (Mo $K\alpha$ radiation, graphite monochromator, $\lambda = 71.07$ pm). An optional liquid nitrogen cryostream was available for low-temperature measurements and measurements of slightly air sensitive crystals. Indexing of crystal faces was performed with a CCD camera via the FACEIT-Video software;^[73] the miller indices of crystal faces were checked for plausibility and corrected manually, if necessary. The programs X-RED 32,^[74] X-SHAPE,^[75] XPREP^[76] and PLATON^[77] were used for data reduction, numerical absorption correction, crystal

shape optimisation (distances only), data analysis and symmetry transformation. Crystal structures were solved using SIR^[78] and SHELXS^[79] structure refinements were performed using SHELXL^[79] crystal structures were visualised with CrystalMaker.^[61] As a user interface for SHELXS, SHELXL, PLATON and CrystalMaker, the text editor TextMate in combination with suitable bundles^[80] was employed.

2.4 Inelastic neutron scattering

2.4.1 General

Scattering of cold and thermal neutrons is a powerful method to examine the structure and underlying physics of condensed matter. Neutrons are usually specified by their kinetic energy, their corresponding wavelength according to the *de Broglie* relation or the thermodynamic temperature corresponding to their most probable kinetic energy as given by the *Maxwell-Boltzmann* distribution.

The most probable energy of a neutron (or monoatomic gas) is:

$$E = k_B \cdot T \quad (k_B = 1.38065 \cdot 10^{-23} \text{ J} \cdot \text{K}^{-1})$$

The relation between neutron energy and speed and thus temperature is:

$$E = \frac{1}{2} m_n \cdot v^2 \quad \Rightarrow \quad v = \sqrt{\frac{2 \cdot E}{m_n}} = \sqrt{\frac{2 \cdot k_B \cdot T}{m_n}}$$

$$(m_n = 1.674927 \cdot 10^{-27} \text{ kg and } 1 \text{ eV} = 1.602176 \cdot 10^{-19} \text{ J})$$

The momentum of a neutron is given as:

$$p = m_n \cdot v$$

According to the *de Broglie* relation, the wavelength of a neutron therefore is:

$$\lambda = \frac{h}{p} \quad \Rightarrow \quad \lambda = \frac{h}{p} = \frac{h}{m_n \cdot v} = \frac{h}{m_n \cdot \sqrt{\frac{2 \cdot k_B \cdot T}{m_n}}}$$

The energy of cold and thermal neutrons lies in the range 0.1 – 100 meV (corresponding to wavelengths of 2900 pm – 90 pm), which enables them to interact with condensed matter via elastic or inelastic scattering. Inelastic scattering means that an additional momentum transfer between the diffracted neutron and a magnetic or vibrational excitation occurs, which results in spectra like that in Figure 2.1^[81] for each diffraction angle. As such momentum transfers can be treated like momentum transfers of particles, concepts like the conservation of momentum remain valid. This particle-analogous behaviour also is often emphasised and the abovementioned excitations are therefore called magnons and phonons. The absence of any electrical charge and a comparatively high mass makes neutrons interact with the atomic nuclei of condensed matter rather than the electron shell and as neutrons possess a magnetic moment, they can interact both with ordered magnetic moments in solids and magnetic excitations. Both magnons and phonons can play an important role in the superconducting mechanism of superconductors. In conventional BCS superconductors, the formation of cooper pairs is mediated by phonons, while in high-temperature superconductors, spin fluctuations are assumed to play a key role for the superconducting mechanism (Chapter 1.1.2). But also in the latter materials, phonons still may couple to the spin system, which then can be detected via temperature-dependent measurements of the phonon spectra of these compounds. This is why inelastic neutron scattering is a highly valuable tool to study the dynamics of both superconductors and compounds on the verge of magnetic instabilities.

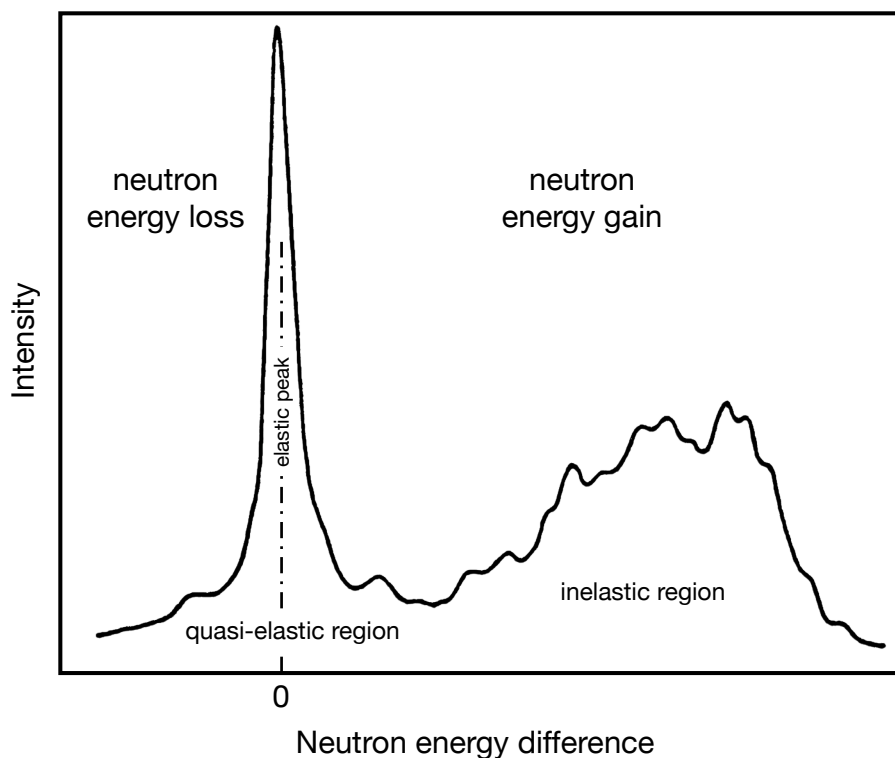


Figure 2.1: Schematic neutron spectrum (cold neutrons) with a time-of-flight spectrometer at a specific diffraction angle. The intensity of the elastic peak was scaled down for clarity.

2.4.2 Measurement details

Inelastic neutron scattering experiments on $\text{Ca}_{0.6}\text{Na}_{0.4}\text{Fe}_2\text{As}_2$ and $\text{Sr}_{0.6}\text{K}_{0.4}\text{Fe}_2\text{As}_2$ were performed using the IN4C and IN6 time-of-flight spectrometers (Institut Laue Langevin, France). Details about the spectrometer setups can be found elsewhere.^[82] The measurements were performed on 4.5 – 10 g of polycrystalline samples. On IN4C, the measurements were performed in the neutron energy loss mode using an incident neutron wavelength of 118 pm at temperatures below 2.5 K and above 50 K (the superconducting transition). In this configuration, the elastic energy resolution of the spectrometer is about 3 meV. The detector bank covered scattering angles from 13° to $120^\circ 2\theta$. For the IN6 measurements, an incident neutron wavelength of 510 pm was used. The measurements were performed in the neutron energy gain mode and the data were collected at 140 and 300 K. In this configuration the energy resolution of the spectrometer is 0.07 to 0.08 meV at elastic positions, so that a higher resolution is achieved in the low-frequency range with regard to IN4C data. The angular range of the IN4C spectrometer covers $10^\circ - 113^\circ 2\theta$. While this spec-

trometer was configured mainly to detect the presence of magnons in these experiments (thermal neutrons, 118 pm incident wavelength), the IN6 spectrometer has a higher energy resolution in the range 0 – 20 meV energy gain (cold neutrons, 510 pm incident wavelength), which allows for better resolution of low-frequency phonon modes. The scattering from a standard vanadium sample was used to calibrate the detectors both on IN4C and IN6. The relation between the phonon density of states and the measured scattering function $S(Q, E)$, as well as further details about the setup are given in the original literature.^[83]

Additional pressure-dependent measurements of $\text{Ca}_{0.6}\text{Na}_{0.4}\text{Fe}_2\text{As}_2$ were performed at ambient pressure, 30, 280 and 500 MPa at 295 K. These measurements are beyond the scope of this dissertation and can be found elsewhere.^[84]

2.5 Scanning electron microscopy, EDX

A JEOL JSM-6500F scanning electron microscope with EDX detector (model 7418, OXFORD INSTRUMENTS) was available for SEM investigations of powders and single crystals. All samples were put on double-sided adhesive conducting carbon discs (PANO, Wetzlar) on brass sample holders, which were sputtered with conductive carbon. Collections of EDX spectra were performed with the INCA software.^[85] In order to increase the accuracy of the determined compositions, measurements were recorded at different crystal positions and / or crystals, and the averaged compositions were taken. Any oxygen, as well as elements of less than 2 at% of the total composition, was disregarded. If the absence of oxygen had to be proved, freshly prepared crystal faces (under argon) were measured.

2.6 Magnetic measurements

Magnetic measurements of polycrystalline samples were either performed with a QUANTUM DESIGN MPMS XL5 SQUID magnetometer or a self-manufactured AC susceptometer. The CGS unit system was used for all magnetic measurements, as it is still more commonly used throughout the literature. The definition of the magnetic quantities used in this dissertation can be found elsewhere.^[86]

Susceptibility data could often be fitted with the Curie, Curie-Weiss or an extended Curie-Weiss law according to

$$\chi = \frac{C}{T}$$

$$\chi = \frac{C}{T - \Theta}$$

$$\chi = \frac{C}{T - \Theta} + \chi_0 \text{ , respectively.}$$

The Curie constant C is defined as:

$$C = \frac{\mu_0 \cdot N_A \cdot \mu_B \cdot n_{\text{eff}}^2}{3k_B}$$

The decision, which law was applicable and if in case of the extended Curie-Weiss law, the Weiss constant Θ had to be fitted, was derived from $\chi \cdot T$ vs. T plots according to the method described in [87].

2.6.1 SQUID magnetometer

The QUANTUM DESIGN MPMS XL5 SQUID magnetometer operates in a temperature range between 1.8 and 400 K and with magnetic fields from -50 to $+50$ kOe. The device was calibrated using a cylindrical, polycrystalline Pd sample of known mass and magnetic susceptibility at various magnetic fields. Technical details about the magnetometer and the measurement method can be found elsewhere^[88] Polycrystalline samples were thoroughly ground and filled into gelatine capsules, which were fixed in plastic drinking straws. Magnetic measurements were performed with the MPMS MultiVu software^[89] and the output data files were processed either directly in ORIGIN^[90] using semi-automated worksheets or with a self-written, fully automatic SQUID processor software (see Chapter 19), which also is available for download^[91]

2.6.2 AC susceptometer

A fully automated differential dual-coil AC susceptometer was available for measurements of the AC susceptibility in solid samples. It operates in the temperature range from 3.4 to 320 K with alternating magnetic fields of up to 8 Oe and frequencies between 100 Hz and 10 kHz. The susceptometer consists of a JANIS SHI-950 two-stage closed-cycle cryostat with ^4He exchange gas, a dual-channel temperature controller (model 332, LAKESHORE), a QUANTUM DESIGN DC transport unit for sample centring and differential measurements, as well as an EG&G (SIGNAL RECOVERY) 7260 DSP oscillator / lock-in amplifier. AC susceptometer control^[92] was used as control software. The coil assembly, stepper controller, sample holder, control software as well as various other parts are all internal developments. A detailed description of both hardware and software can be found in Chapter 16. The susceptometer was calibrated with 87.06 mg of a paramagnetic Dy_2O_3 powder sample at a primary voltage of 1.2 V (corresponding to an alternating field of 2.2 to 2.8 Oe) and a frequency of 1.333 kHz. A precision series resistor of $50\ \Omega$ was joined up in the primary coil circuit and the total impedance of the system was calibrated over the whole temperature range. Thermal expansion of the sample holder and coil were compensated via a thermal expansion calibration curve.

2.7 Resistivity measurements

Measurements of the electrical resistivity were performed on pellets of polycrystalline samples (4 or 6 mm in diameter, thickness 0.5 to 2.5 mm). The pellets were typically prepared by pressing finely ground substances with 0.9 GPa for 1 h and subsequent annealing at 800 to 1000 °C for more than 40 h in a corundum crucible in a silica ampoule under an atmosphere of purified argon. As general measurement method, the current-reversal four-terminal sensing method was employed. A KEITHLEY Source Meter 2400 was available as current source, which was used to create square waves with amplitudes of 2 μA to 5 mA and frequencies of either 2 or 0.4 Hz (1 or 5 PLC, respectively). The differential voltage drop between signal-high and signal-low was recorded with a KEITHLEY 2182 nanovoltmeter and used to calcu-

late the sample resistivity in one direction according to Ohm's law and the specific resistivity according to the Van-der-Pauw approximation.^[93]

2.7.1 High vacuum refrigerator

The pellets were fixed to an electrically insulated brass sample holder with Stycast resin (EMERSON & CUMING). Four copper wires (LAKE SHORE Quad-TwistT-Cryogenic wire 36 AWG) were attached to the surface of the pellet as terminals with silver conducting paint. The sample was measured in a CRYOPHYSICS refrigerator (CRYODYNE 22 CP closed-cycle cold head, CTI CRYOGENICS) operating between 8 and 320 K under high vacuum conditions. Leitmess^[94] was used as data acquisition software and the voltage drop data from the nanovoltmeter were processed in ORIGIN^[90] using semi-automated worksheets.

2.7.2 ⁴He exchange gas refrigerator

The pellets were fixed to special FR4 sample holders with Apiezon N grease. Each sample holder has four beryllium copper terminals, which were attached to the pellet using silver conducting paint. The sample holder was then connected to a special sample rod suitable for the JANIS SHI-950 two-stage closed-cycle refrigerator (operating between 3.4 and 320 K) with the QUANTUM DESIGN DC transport unit. The sample rod was connected to the source meter and nanovoltmeter described above and the fully automatic software Conductivity control^[95] was used for data acquisition and processing. A detailed description of the hardware and software of the conductometer can be found in Chapter 17.

2.8 Mössbauer spectroscopy

⁵⁷Fe Mössbauer spectra of various compounds were recorded by *Schellenberg* at the Westfälische Wilhelms-Universität Münster. A ⁵⁷Co/Rh source was available for these investigations. The velocity was calibrated relative to the signal of α -Fe. The samples were placed in thin-walled PVC containers at thicknesses of about 4 – 10 mg Fe·cm⁻². The measurements were run in the usual transmission geometry

at various temperatures, the source was kept at room temperature. Fitting of the spectra was performed with the NORMOS-90 program system.^[96]

2.9 Specific heat

Heat capacity (C_p) measurements between 2 and 320 K were carried out by *Hermes* at the Westfälische Wilhelms-Universität Münster on a Quantum Design Physical Property Measurement System (PPMS). The sample was fixed to the platform of a pre-calibrated heat capacity puck using Apiezon N grease.

The specific heat of a conventional solid at constant pressure and magnetic field (C_p) follows the Debye T^3 law at low temperatures ($T \ll \Theta_D$) according to:

$$C_p = \frac{12\pi^4 \cdot n \cdot k_B}{5 \cdot \Theta_D^3} \cdot T^3 = \beta \cdot T^3$$

n	: number of atoms per formula unit
$k_B = 1.38065 \cdot 10^{-23} \text{ J} \cdot \text{K}^{-1}$: Boltzmann constant
Θ_D	: Debye temperature
β	: lattice contribution to the specific heat

For metals, also conduction band electrons contribute to the specific heat. This contribution is linear near temperature zero and the Debye law can be extended as follows:

$$C_p = \frac{\pi^2 \cdot n \cdot k_B^2}{2 \cdot E_F} \cdot T + \frac{12\pi^4 \cdot n \cdot k_B}{5 \cdot \Theta_D^3} \cdot T^3 = \gamma \cdot T + \beta \cdot T^3$$

E_F	: Fermi energy
γ	: electronic contribution to the specific heat (in a normal conductor)

Chapter 2: Methods

The phase transition from the normal to the superconducting state can be understood as ordering of the conduction band electrons. This results in a change of the specific heat and measurements of C_p thus allow e.g. the determination of the superconducting volume fraction in the case of BCS superconductors.

The quotient of the difference in the specific heat ΔC_p^{XI} and the electronic contribution to the heat capacity for weakly coupling systems equals 1.43 according to the prediction of the BCS theory:^[97]

$$\frac{\Delta C_p}{\gamma \cdot T_C} = 1.43$$

This value (and thus the jump in the specific heat) can be smaller for unconventional superconductors as a result of a different superconducting order parameter.

2.10 Synthesis methods

2.10.1 Starting materials

Table 2.1 lists the starting materials used for syntheses, their purity, molar weight, manufacturer as well as their appearance.

Starting material	Purity	m.w.	Manufacturer	Appearance
As	99.999	74.9216	ALFA AESER	Pieces
As ₂ O ₃	99.5	197.8414	ACROS	Powder
Ba	99.99	137.3270	SIGMA-ALDRICH	Ingot
BaF ₂	99.999	175.3238	SIGMA-ALDRICH	Powder
Ca	99.9	40.0780	SMART ELEMENTS	Pieces
CaF ₂	99.9	78.0748	SIGMA-ALDRICH	Powder
Co	99.9	58.9332	SIGMA-ALDRICH	Pieces

^{XI} ΔC_p is the difference between the specific heat of the superconductor and hypothetical normal metal.

Co ₃ O ₄	> 95	240.7972	MERCK	Powder
Cr	99.8	51.9961	ALFA AESER	Powder
Cr ₂ O ₃	X-ray s.p.	151.9904	Unknown	Powder
Eu	99.9	151.9640	ALFA AESER	Pieces
EuF ₂	99.99	189.9608	SIGMA-ALDRICH	Powder
Fe	99.9	55.8450	CHEMPUR	Powder
Fe ₂ O ₃	> 99	159.6882	MERCK	Powder
FeO	99.9	71.8444	SIGMA-ALDRICH	Powder
FeP	X-ray s.p.	86.8188	M. Auracher	Powder
FeS	X-ray s.p.	87.9100	Unknown	Powder
Ga	99.999	69.7230	ALFA AESER	Pieces
Gd	99.99	157.2500	CHEMPUR	Pieces
In	X-ray s.p.	114.8180	Unknown	Powder
K	99.95	39.0983	SIGMA-ALDRICH	Ingot
KCl	99.999	74.5513	ALFA AESER	Powder
La	99.9	138.9055	SMART ELEMENTS	Ingot
Mg	99.8	24.3050	ALFA AESER	Chips
Mn	99.9	54.9380	SIGMA-ALDRICH	Pieces
MnO ₂	X-ray s.p.	86.9368	Unknown	Powder
Mo	99.9	95.9600	CHEMPUR	Powder
Na	99.8	22.9898	ALFA AESER	Ingot
NaCl	99.999	58.4428	ALFA AESER	Powder
Nb	99.95	92.9064	ALFA AESER	Ingot
Nd	99.99	144.2420	ALFA AESER	Pieces
Ni	99.99	58.6934	CHEMPUR	Powder
P (red)	99.999	30.9738	CHEMPUR	Powder
P ₂ O ₅	Unknown	141.9445	Unknown	Powder
S	99.99	32.0650	SIGMA-ALDRICH	Powder
Sc	99.99	44.9559	SMART ELEMENTS	Pieces
Sc ₂ O ₃	X-ray s.p.	137.9100	M. Auracher	Powder

Chapter 2: Methods

Si	99.999	28.0855	ALFA AESER	Powder
Sm	99.9	150.3600	ALFA AESER	Pieces
Sn	99.99	118.7100	ALFA AESER	Granules
Sr	99.99	87.6200	SIGMA-ALDRICH	Pieces
SrF ₂	99.99	125.6168	SIGMA-ALDRICH	Powder
SrO	X-ray s.p.	103.6194	M. Auracher	Powder
Ti	99.5	47.8670	ALFA AESER	Powder
V	99.999	50.9415	ALFA AESER	Powder
V ₂ O ₅	99.997	181.8800	SMART ELEMENTS	Powder
Y	99.9	88.9058	CHEMPUR	Pieces
Yb	99.9	173.0540	ALFA AESER	Pieces
Zn	99.999	65.380	CHEMPUR	Granules
Zr	99.97	91.2240	SMART ELEMENTS	Pieces

Table 2.1: Starting materials used for syntheses.

2.10.2 Synthesis equipment and conditions

Syntheses were usually performed by heating mixtures of starting materials in an atmosphere of purified argon. The argon gas (Argon 5.0, AIR LIQUIDE) was dried and purified through cylinders with BTS catalyst, molecular sieve and phosphorus pentoxide on substrate (Sicapent, MERCK AG). As reaction containers, alumina crucibles (FRIATEC) sealed in silica ampoules (HSQ 300, VOGELSBERGER) were used. Sample preparation and handling was generally performed in a glove box (BRAUN) in an atmosphere of purified argon ($H_2O < 1$ ppm, $O_2 < 1$ ppm). The solid-state reactions were performed in resistance furnaces with Pt/PtRh (type S) or NiCr/Ni (type K) thermocouples and programmable PID temperature controllers (model 2408, EUROTHERM).

2.10.3 Standard synthesis method

Unless otherwise stated, stoichiometric mixtures of starting materials were prepared in alumina crucibles sealed in silica ampoules under an atmosphere of purified argon. The typical batch size was 600 mg. The mixtures were normally heated to

973 – 1373 K at a rate of about $80 \text{ K}\cdot\text{h}^{-1}$, kept at this temperature for 60 h and cooled down to room temperature at $200 \text{ K}\cdot\text{h}^{-1}$. If elemental phosphorus or arsenic was present in the mixture, a smaller heating rate was chosen between 573 and 973 K in the first annealing step. The products were then homogenised in an agate mortar, pressed into pellets and sintered at the previous synthesis temperature for another 60 h. The batches were subsequently reground, checked for impurity phases via X-ray powder diffraction and, if necessary, pressed into pellets and sintered again at the previous synthesis temperatures for another 60 h. The obtained products were black polycrystalline samples, which were stable in air, unless otherwise stated.

2.10.4 Tin flux

Syntheses in tin fluxes were performed under the general synthesis conditions described in Chapter 2.10.3. However, the starting materials (typically stoichiometric mixtures with a batch size of 400 to 600 mg) were mixed with 2 to 2.5 g Sn and annealed only once, but for longer times (usually 400 h). The cooling rate from the synthesis temperature down to about 300 K below synthesis temperature was chosen very small (typically $4 \text{ K}\cdot\text{h}^{-1}$) in order to grow rather large crystals. The subsequent cooling ramp to room temperature was $200 \text{ K}\cdot\text{h}^{-1}$. The chilled alumina crucibles were smashed and the remaining tin ingots cut into small pieces and then put into half concentrated ($\sim 6 \text{ M}$) hydrochloric acid. From time to time, the suspension was decanted and the precipitated powder was separated from the remaining tin pieces by washing with distilled water over a $500 \mu\text{m}$ (~ 34 mesh) polypropylene sieve. The separated powder was filtered off and the remaining tin pieces were put into the hydrochloric acid again for further dissolution. In this way, dissolution of moderately acid-sensitive products could be avoided.

2.10.5 NaCl / KCl flux

Several syntheses were performed in a salt flux from a eutectic mixture of NaCl and KCl. Syntheses were performed under the general synthesis conditions described in Chapter 2.10.3, but the starting materials (typically 400 mg) were mixed with the salt

Chapter 2: Methods

flux in a 1:2 – 1:3 weight ratio. As salt fluxes tend to flow out of open crucibles at elevated temperatures, all syntheses were performed either directly in silica ampoules sealed under vacuum or in welded Nb or Ta tubes sealed in silica ampoules under an atmosphere of purified argon. Similar to the syntheses in tin fluxes described in Chapter 2.10.4, only one annealing step was performed. Annealing times and heating / cooling ramps were similar to those described in Chapter 2.10.4. After cooling, the silica ampoules were smashed (and the Nb crucibles opened, if applicable) and both the mixtures as well as the ampoule / crucible walls were examined for larger crystals under a stereomicroscope. If any unidentifiable crystals were found, they were separated from the mixture and analysed by X-ray single crystal diffraction. The remaining mixtures were dissolved in distilled water and quickly filtered over a paper filter disc.

3. $\text{La}(\text{Co}_x\text{Fe}_{1-x})\text{PO}$

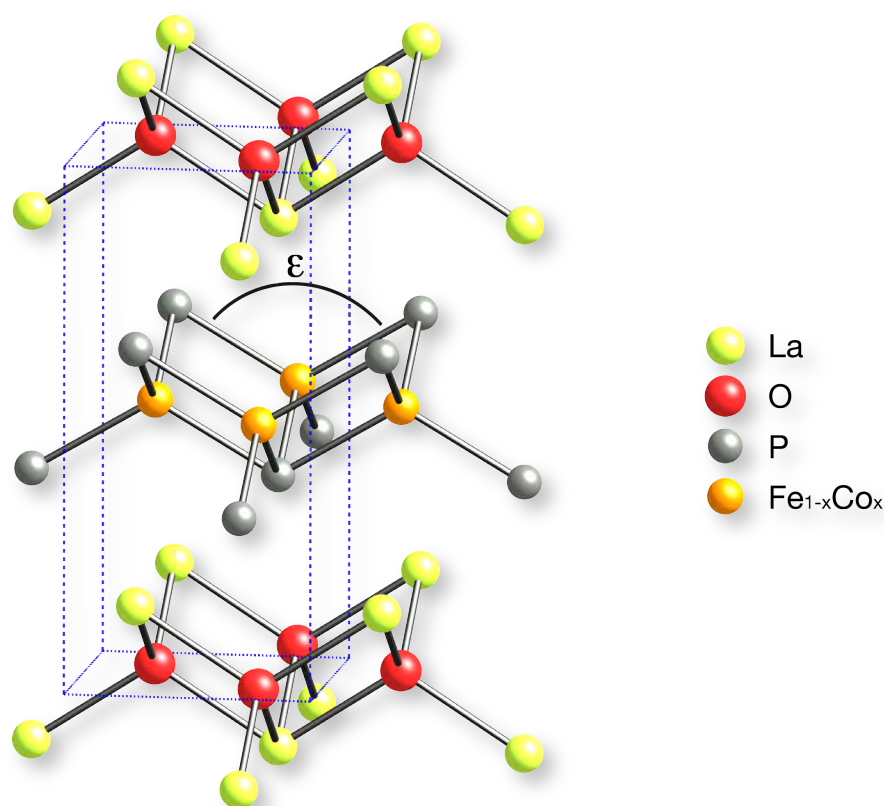


Figure 3.1: Crystal structure of $\text{La}(\text{Co}_x\text{Fe}_{1-x})\text{PO}$.

Even before high-temperature superconductivity at 26 K was discovered in $\text{LaFeAs}(\text{O}_{1-x}\text{F}_x)$, undoped LaFePO had been known to be a superconductor (since 2006) with a transition temperature of 4 – 7 K.^[86, 98] Although this had not caused a sensation at this time, as there are many intermetallic superconductors with such low critical temperatures, there had been some first signs that superconductivity is unconventional in this compound!^[99] The interest in this class of materials had intensified with the discovery of the isotypic superconductor LaNiPO in 2007!^[100] It also had been at that time, that the cobalt doping experiments of LaFePO , which are discussed in this chapter, had been started. Hence, these experiments had been carried out some time before the first successful cobalt doping in LaFeAsO !^[101] The intention of these investigations had been to try if higher T_c s could be achieved by altering the Fermi level in LaFePO and thus for very similar reasons as the later attempts to induce superconductivity in LaFeAsO .

3.1 Synthesis

Polycrystalline samples of La(Co_xFe_{1-x})PO ($T_C^{\max} = 7$ K) were synthesised according to the method described in Chapter 2.10.4 by heating 600 mg of stoichiometric mixtures of La, Fe, Fe₂O₃, Co, Co₃O₄ and red P, as well as 2.0 – 2.5 g Sn in alumina crucibles sealed in silica ampoules. The exact ratios of starting materials are given in Table 3.1. All samples were annealed only once according to the following temperature program:

RT $\xrightarrow{50 \text{ K/h}}$ 573 K $\xrightarrow{20 \text{ K/h}}$ 933 K (12 h) $\xrightarrow{40 \text{ K/h}}$ 1223 K (400 h) $\xrightarrow{3 \text{ K/h}}$ 573 K $\xrightarrow{40 \text{ K/h}}$ RT

x	La : Fe : Fe₂O₃ : Co : Co₃O₄ : P	x	La : Fe : Fe₂O₃ : Co : Co₃O₄ : P
0	3 : 1 : 1 : 0 : 0 : 3	0.6	18 : 5 : 2 : 0 : 3 : 18
0.01	900 : 299 : 296 : 3 : 900	0.6	15 : 4 : 1 : 0 : 3 : 15
0.05	180 : 59 : 56 : 0 : 3 : 180	0.7	90 : 23 : 2 : 0 : 21 : 90
0.1	90 : 29 : 26 : 0 : 3 : 90	0.8	40 : 0 : 4 : 11 : 7 : 40
0.2	45 : 14 : 11 : 0 : 3 : 45	0.9	80 : 0 : 4 : 21 : 17 : 80
0.3	10 : 3 : 2 : 0 : 1 : 10	1.0	4 : 0 : 0 : 1 : 1 : 4
0.4	45 : 13 : 7 : 0 : 6 : 45		

Table 3.1: Molar ratios of starting materials for syntheses of LaCo_xFe_{1-x}PO.

The tin ingots were dissolved in 6 M HCl at room temperature. This procedure yielded black powders consisting of platelet crystals with metallic lustre. Ferromagnetic impurities, mainly Fe₂P and Fe, were removed by stirring a suspension of the finely ground samples in liquid N₂ with a strong permanent magnet (Nd-Fe-B, 40 × 40 × 20 mm³, $H_{\text{rem}} \approx 13$ kOe).

3.2 Mössbauer study of undoped LaFePO

^{57}Fe Mössbauer spectra of the 7 K superconductor LaFePO recorded at 298, 77, 4.2, and 4 K are presented in Figure 3.2 together with transmission integral fits. The corresponding fitting parameters are listed in Table 3.2.

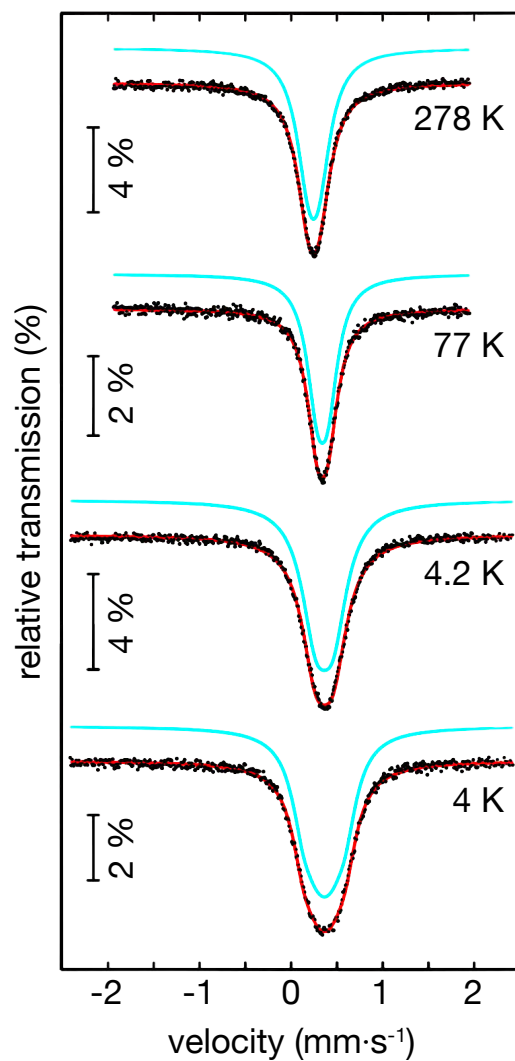


Figure 3.2: Mössbauer spectra of LaFePO .

Temperature (K)	δ (mm·s ⁻¹)	Γ (mm·s ⁻¹)	ΔE_Q (mm·s ⁻¹)
298	0.24(1)	0.32(3)	0.11(3)
77	0.34(1)	0.28(4)	0.12(3)
4.2	0.36(1)	0.37(3)	0.19(2)
4	0.36(1)	0.32(1)	0.15(1)

Table 3.2: Fitting parameters for ⁵⁷Fe Mössbauer spectroscopy data of LaFePO. δ : isomer shift; Γ : experimental line width; ΔE_Q : quadrupole splitting parameter.

In agreement with the ZrCuSiAs-type crystal structure, the spectra could be fitted with single iron sites at isomer shifts around 0.3 mm·s⁻¹, which are slightly smaller than the isomer shifts observed in LaFeAsO and LaFeAsO_{0.89}F_{0.11}.^[102] Due to the non-cubic site symmetry, the spectra are subject to weak quadrupole splitting. Similar to LaFeAsO and LaFeAsO_{0.89}F_{0.11}, a slight increase of the isomer shift with decreasing temperature was also observed in LaFePO. For iron, smaller isomer shifts are caused by higher electron densities at the nuclei.^[103] The isomer shifts observed in LaFePO are comparable with those of other iron phosphides with tetrahedrally coordinated iron.^[104] At 298 and 77 K, no magnetic hyperfine field splitting could be observed, clearly manifesting the absence of magnetic ordering, similar to the fluoride doped superconducting arsenide oxide LaFeAsO_{0.89}F_{0.11}.^[102] The 4 K spectrum shows symmetric line broadening. A reliable fit could be obtained by simultaneously applying a weak quadrupole splitting of 0.15(1) mm·s⁻¹ and a transferred magnetic hyperfine field B_{hf} of 1.15(1) T. In order to explain the symmetric spectrum with a combined hyperfine field and an electrical quadrupole interaction, the angle θ between B_{hf} and V_{zz} (the main component of the electric field gradient tensor) should be close to the magic angle of 54.7°.^{xii} Indeed, the refined θ for LaFePO was 54.7(5)°. This behaviour has also been observed for other magnetically ordered rare earth compounds.^[105] Although the experimental setup was limited to 4 K, higher transferred hyperfine fields at lower temperatures can be expected.

^{xii} $\theta_m = \cos^{-1}(1/\sqrt{3})$.

The absence of magnetic ordering in undoped LaFePO at low temperatures as well as the observed superconductivity at 7 K raise the question if the pairing mechanism in iron phosphide superconductors is generally different (e.g. an exclusively phonon-mediated mechanism is conceivable) or the same as in the iron arsenides. Scientists nowadays agree that in LaFePO, the superconducting mechanism is not completely different from that in LaFeAsO_{1-x}F_x. That means that superconductivity is probably still mediated by electronic correlations rather than by phonons.^[106] On the one hand, there are signs that these electronic correlations are only weak^[107] and thus explaining a very small ordered magnetic moment, which also corresponds to the observations of the current experiment. On the other hand, there are also signs that the measured static magnetic moment is very small due to very fast spin fluctuations.^[108] This would indeed support the hypothesis of a more unconventional superconductivity in this system.

3.3 Influence of Co-doping

While undoped LaFeAsO is not a superconductor but exhibits a structural and magnetic phase transition upon cooling, undoped LaFePO does not feature any of these transitions and becomes superconducting, albeit at a low transition temperature ($T_c \approx 7$ K for samples prepared in a tin flux). The crystal structure (both from powder and single crystal data) and magnetic properties of undoped LaFePO have already been discussed in [86] and [109]. In order to shed light on the doping behaviour of LaFePO, polycrystalline samples of the solid solution La(Co_xFe_{1-x})PO ($x = 0 - 1$) were synthesised. Unlike in the F-doped oxides, any electron doping level can be achieved by Co-doping up to one additional electron for $x = 1$. The samples were synthesised according to Chapter 2.10.4 and their crystal structures determined by Rietveld refinements of the X-ray powder diffraction patterns. A sample Rietveld fit is depicted in Figure 3.3. The course of the lattice parameters, P–Fe–P angles (ϵ) and cell volume as determined by these refinements are compiled in Figure 6.1. The actual doping levels were verified to be within ± 7 % of the nominal value by at least seven EDX measurements at each composition. Small impurities of Sn and / or SnO₂ were present in some of the samples. In order to get a more accurate course of the

lattice parameters, finely ground and sieved Si was added to all powder samples as internal standard.

As can be seen in Figure 3.4, the c lattice parameter gradually decreases on cobalt doping, while a in $\text{La}(\text{Co}_x\text{Fe}_{1-x})\text{PO}$ ($x = 0 - 1$) decreases at first up to a doping level of $x = 0.4$, but then increases again with higher doping. A similar situation was found for the vertical, twofold P–Fe–P angle (ε), which does not change linearly with increasing doping levels but exhibits a minimum at $\sim \text{LaCo}_{0.3}\text{Fe}_{0.7}\text{PO}$. This is in contrast to $(\text{K}_x\text{Ba}_{1-x})\text{Fe}_2\text{As}_2$, which shows a linear doping dependence of all parameters (refer to Chapter 7.3 for details). In $\text{La}(\text{Co}_x\text{Fe}_{1-x})\text{PO}$, the iron pnictide and lanthanum oxide layers are compressed along the c axis ($\varepsilon = 119^\circ - 122^\circ$), leaving them far from the ideal tetrahedral geometry ($\varepsilon = 109.47^\circ$).

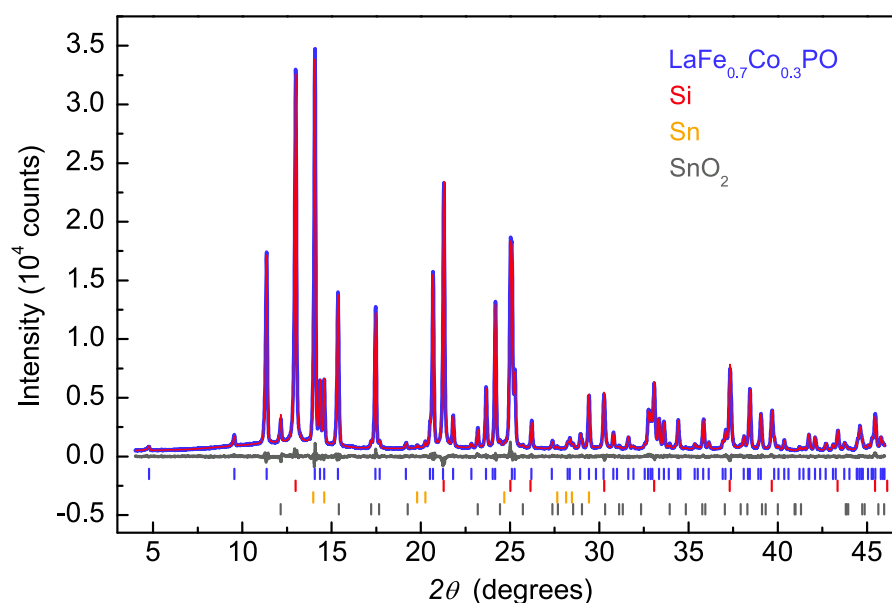


Figure 3.3: Rietveld fit of $\text{LaCo}_{0.3}\text{Fe}_{0.7}\text{PO}$ as an example.

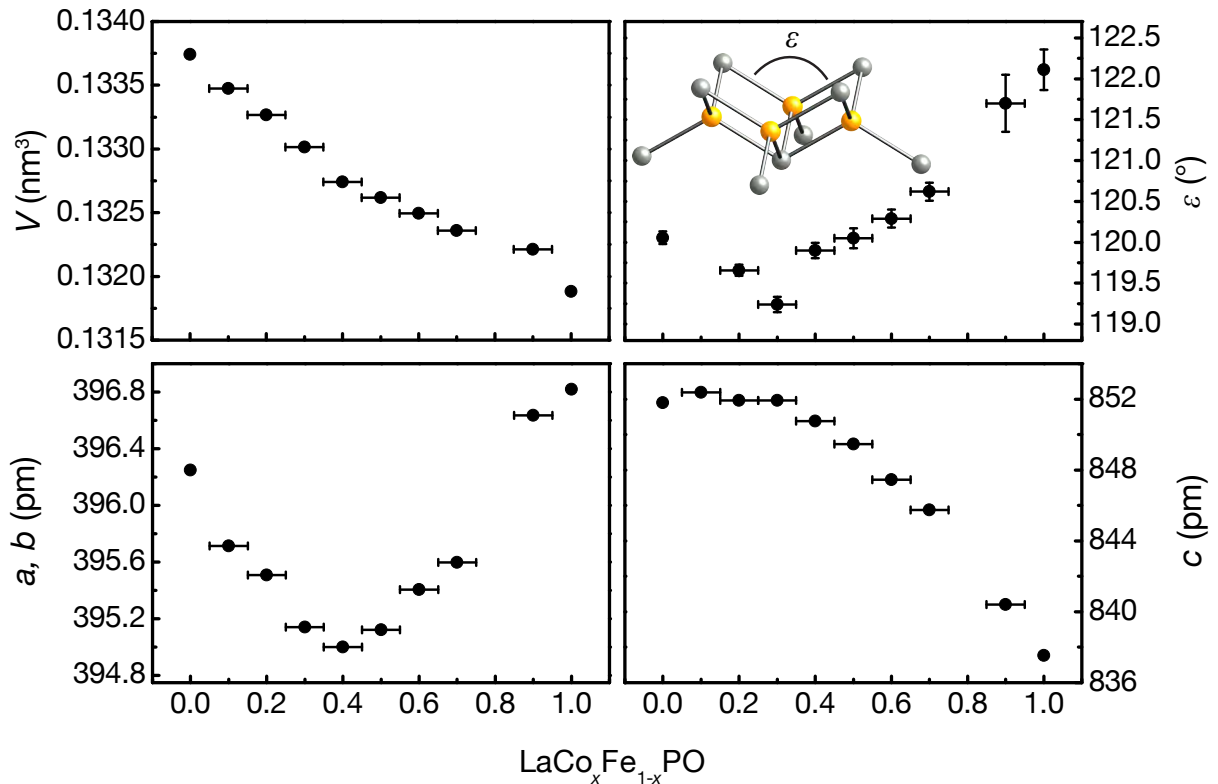


Figure 3.4: Course of the lattice parameters, cell volume and P–Fe–P angles (ε) with nominal doping level.

The compounds were also characterised magnetically. At temperatures above 7 K, all samples with $x = 0 - 0.6$ are paramagnetic. The paramagnetism is several orders of magnitude too high for Pauli-paramagnetism (Figure 3.5, middle). The samples with $x = 0.7 - 1.0$ exhibit ferromagnetic order at low temperatures (with Curie temperatures of about 40 to 50 K, Figure 3.5, bottom), similar to undoped LaCoPO.^[110] Zero-field-cooled and field-cooled measurements of La(Co_xFe_{1-x})PO show decreasing T_C s with increasing cobalt concentration (for $x < 0.1$). The highest T_C of 7 K was found for $x = 0$ (Figure 3.5, top). For $x = 0.01$, the superconducting transition temperature was only 3.6 K and for $x = 0.05$, a complete loss of superconductivity was observed (not depicted). This is in contrast to the system La(Co_xFe_{1-x})AsO, in which a maximum T_C of 14 K is attained for $x = 0.11$!^[110] In summary, 7 K still keeps the highest superconducting transition temperature in the ZrCuSiAs-type iron phosphide oxide system.

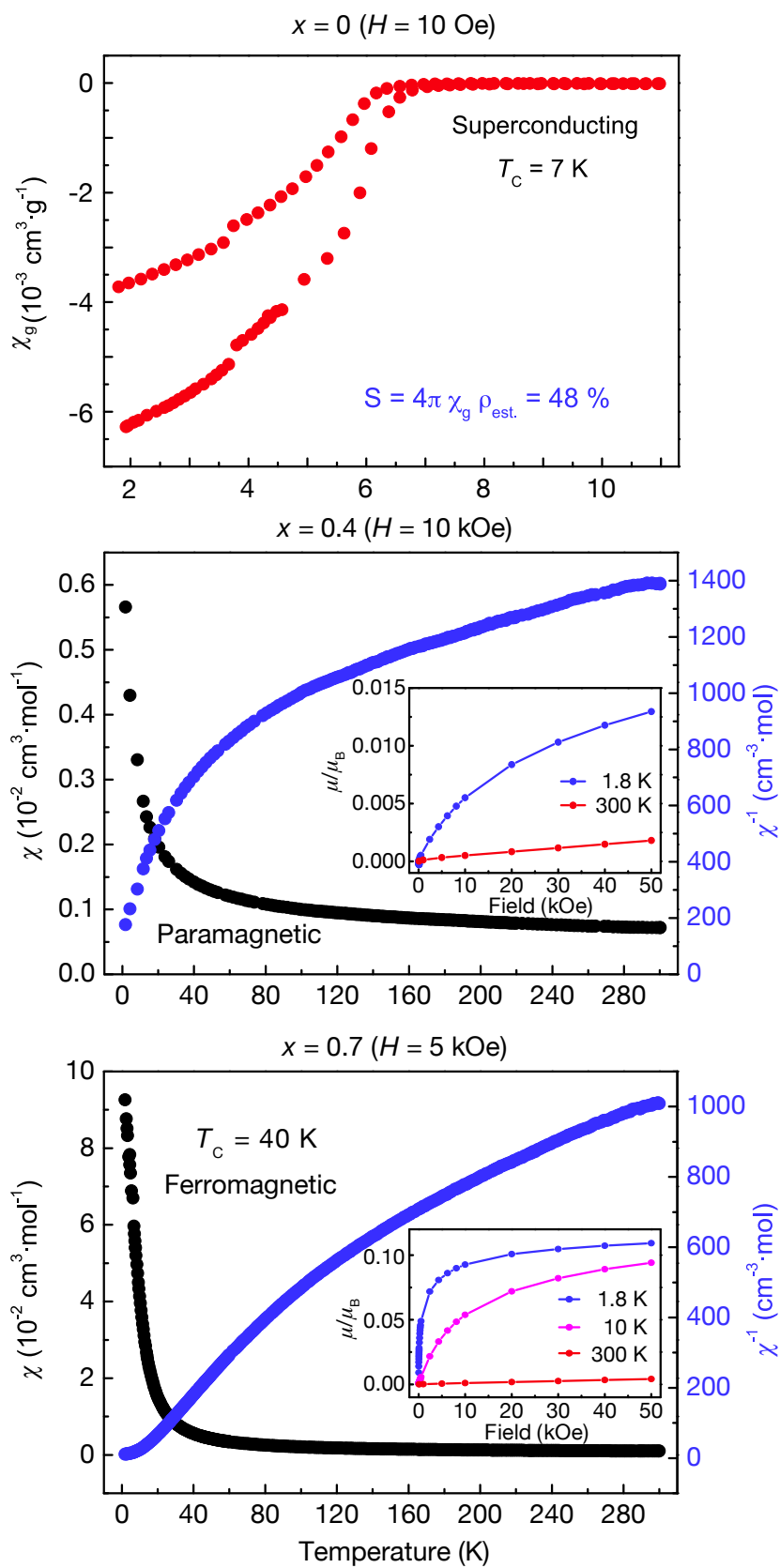


Figure 3.5: Susceptibilities and magnetisation isotherms (insets) for $\text{La}(\text{Co}_x\text{Fe}_{1-x})\text{PO}$ ($x = 0, 0.4$ and 0.7).

Undoped LaFePO prepared in a tin flux may therefore already be slightly oxygen deficient (and thus in fact electron-doped). Such a sample therefore already seems to possess the ideal doping level. This could also explain the difference in T_C observed by *Kamihara* in LaFePO prepared without any reactive flux ($T_C = 4$ K)^[98] and this sample ($T_C = 7$ K).

3.4 Electronic structure

Band structures and Fermi surfaces have been calculated for both LaFePO and LaCoPO. While the qualitative course of the bands is similar in LaFePO and LaCoPO, the Fermi level is higher in LaCoPO due to the additional valence electron (Figure 3.6). This results in huge differences in the Fermi surfaces. LaFePO displays a rather two-dimensional Fermi surface structure. It consists of nearly nested cylinders at $\mathbf{k} = (0, 0)$ [Γ] and $\mathbf{k} = (\pi, \pi)$ [M], a typical situation for all iron pnictides superconductors or parent compounds (see Chapter 1.1). In contrast to this, one of the Fermi surface sheets in LaCoPO also exhibits rather three-dimensional features and there is not any apparent Fermi surface nesting visible (Figure 3.7).

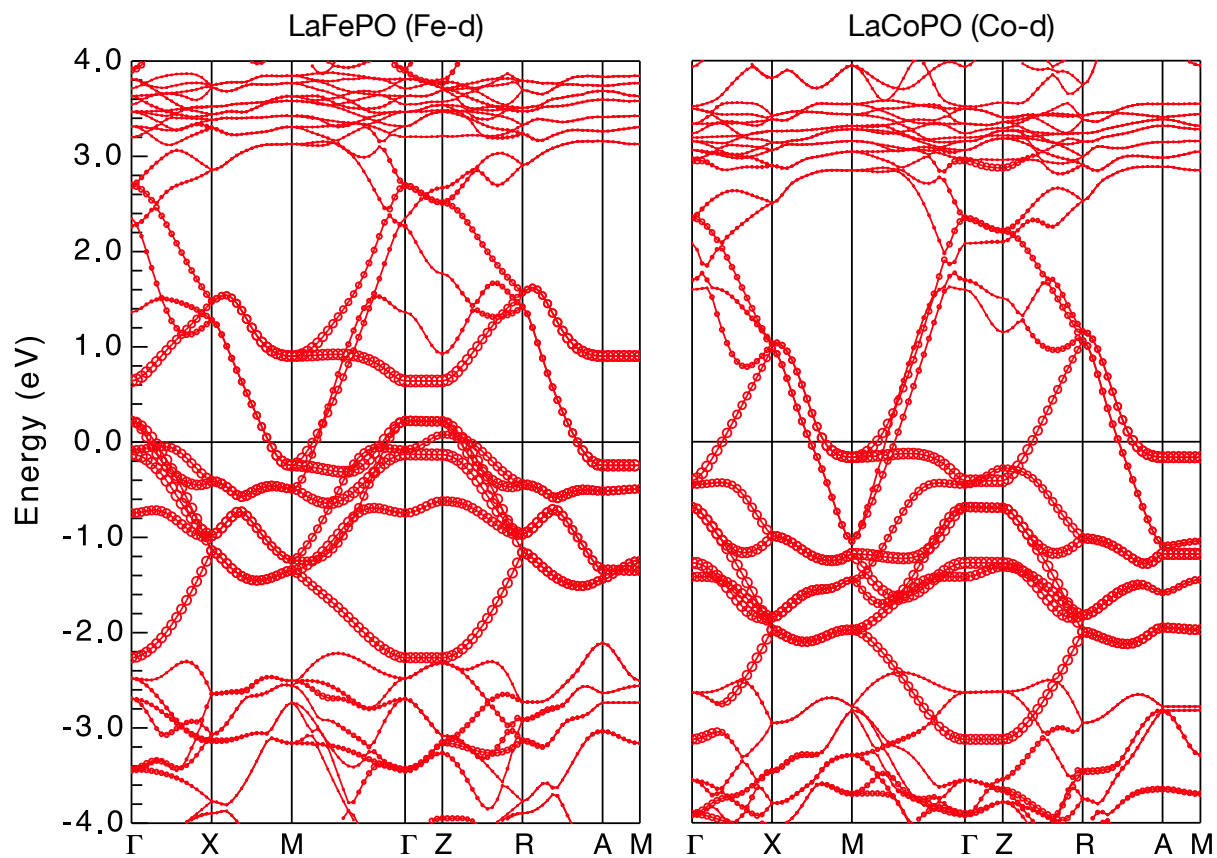


Figure 3.6: Section of the non-magnetic band structures of LaFePO and LaCoPO , calculated with the GGA method. Fat bands: TM -d contributions.

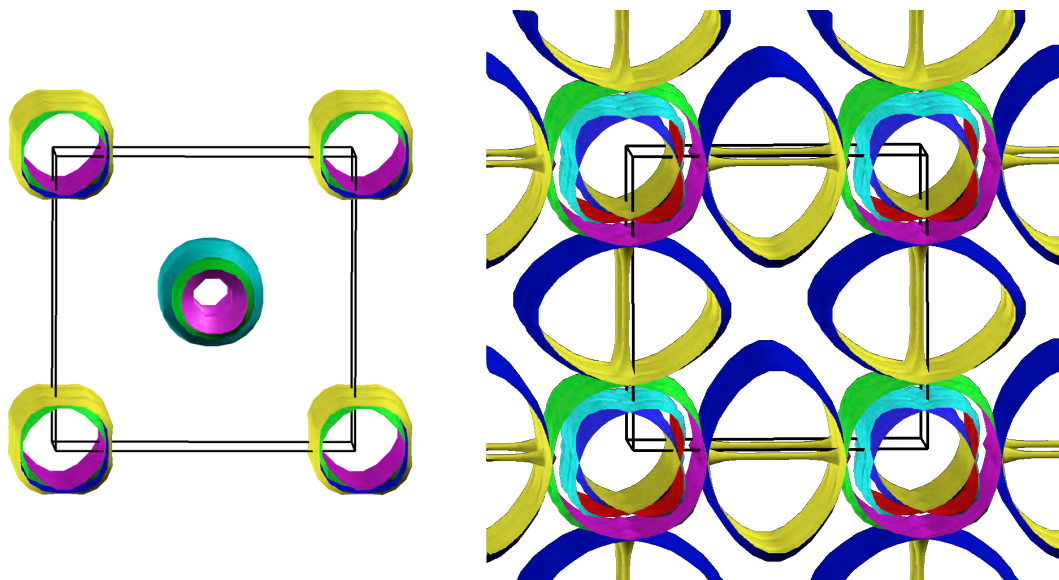


Figure 3.7: Fermi surfaces of LaFePO (left) and LaCoPO (right), calculated with the GGA method.

In summary, within the solid solution $\text{La}(\text{Co}_x\text{Fe}_{1-x})\text{PO}$, a T_C of 7 K is the highest achievable transition temperature if the samples are grown in a tin flux. This is the case already in undoped LaFePO (at $x = 0$). The reason for differences in the reported T_C s of undoped LaFePO may be due to slight oxygen deficiency (and therefore electron doping) if a tin flux was employed for synthesis. Albeit the remarkably similar electronic structure of LaFePO and LaFeAsO , the main difference between both compounds is the lack of any structural and magnetic phase transition in undoped LaFePO . The absence of magnetic ordering down to 4 K could be confirmed by Mössbauer spectroscopy. While $\text{La}(\text{Co}_x\text{Fe}_{1-x})\text{PO}$ is paramagnetic for $x = 0 - 0.6$ in the complete temperature range, ferromagnetic ordering is visible for $x = 0.7 - 1$ below Curie temperatures of 40 – 50 K.

4. SrFeAsF

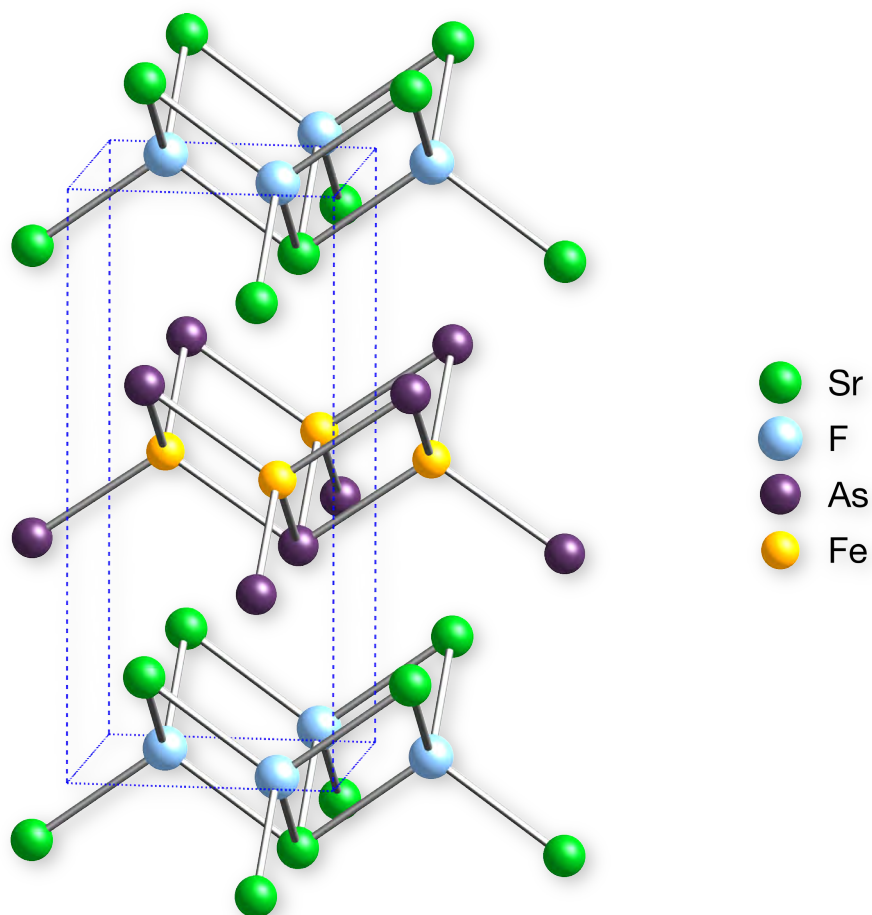


Figure 4.1: Crystal structure of SrFeAsF.

In this chapter, the iron arsenide fluoride SrFeAsF is discussed. It shares the same tetragonal ZrCuSiAs-type structure with other 1111 iron arsenides like LaFeAsO, but here, the $(\text{LaO})^+$ layers of LaFeAsO are replaced by valence isoelectronic $(\text{SrF})^+$ layers (Figure 4.1).

4.1 Synthesis

SrFeAsF was synthesised according to the method described in Chapter 2.10.3 by heating a mixture of SrF_2 , Sr, Fe and As at a ratio of 1 : 1 : 2 : 2 in a sealed niobium tube under an atmosphere of purified argon. The mixture was heated to 1173 K at a rate of $50 \text{ K}\cdot\text{h}^{-1}$, kept at this temperature for 40 h and cooled down to room temperature. The product was homogenised in an agate mortar, pressed into pellets and

sintered at 1273 K for 48 h. The synthesis could be optimised by using a corundum crucible as container material. The obtained black crystalline powder of SrFeAsF is stable in air.

4.2 Crystal structure

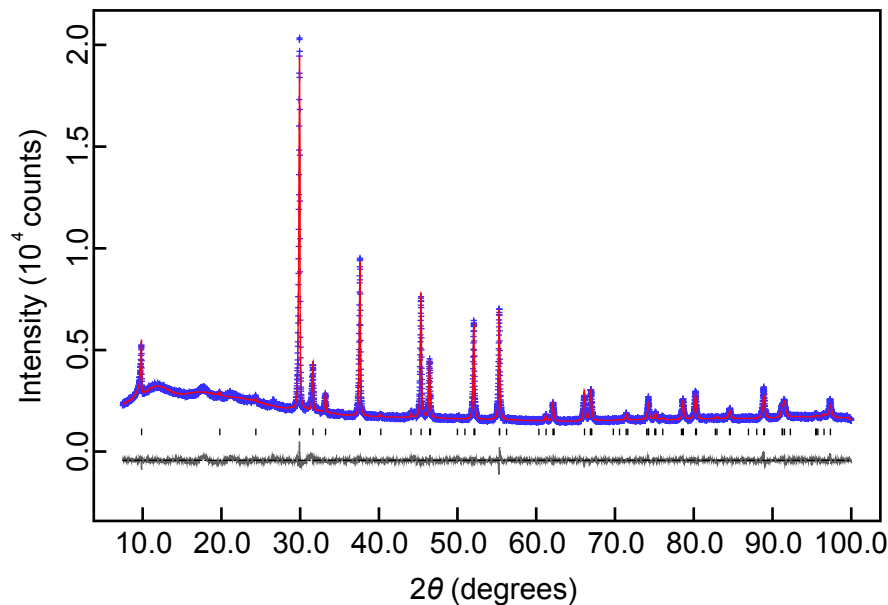


Figure 4.2: Published Rietveld fit of SrFeAsF at 297 K (space group $P4/nmm$).

Figure 4.2 shows the X-ray powder pattern of SrFeAsF, which was fitted with a single tetragonal ZrCuSiAs-type SrFeAsF phase and as it has been published in [111]. However, a more careful Rietveld analysis with powder data collected with an extended measuring time later revealed SrFe₂As₂ (5 at%) Fe (5 at%) and SrF₂ (2 at%) as impurity phases (not depicted). The synthesis was therefore optimised and a sample could be synthesised, which only contains 2 at% of SrFe₂As₂ as only impurity (Figure 4.3). The inset of Figure 4.3 depicts the (013) reflection of SrFe₂As₂ at 31.4° 2θ, which is coincidentally overlapping with the (110) reflection of SrFeAsF at 31.6° 2θ. Also other strong reflections of SrFe₂As₂ overlap with SrFeAsF reflections, which is the reason why the presence of SrFe₂As₂ had not been detected at first.

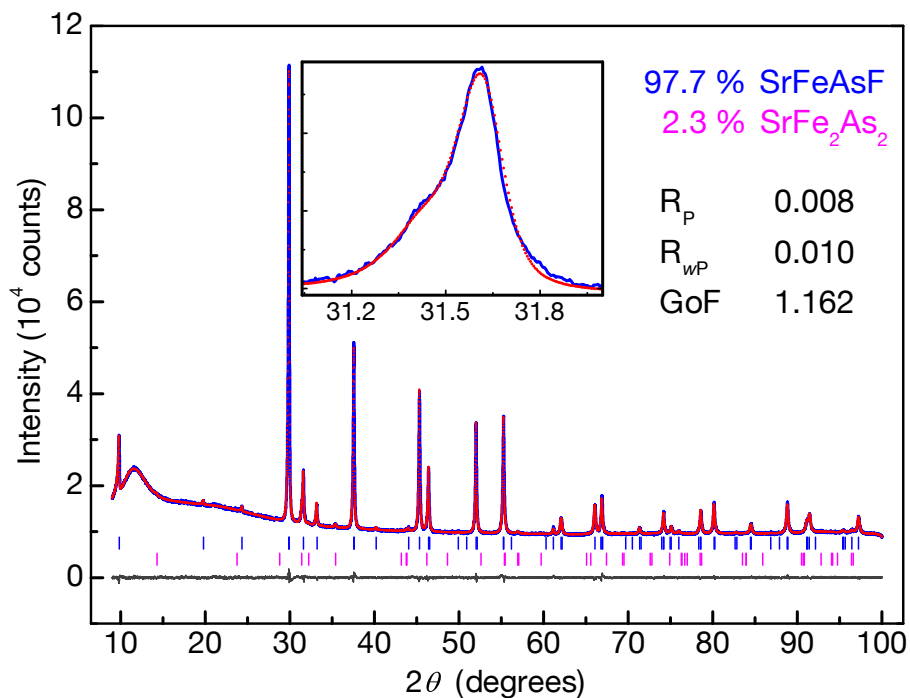


Figure 4.3: Rietveld fit of SrFeAsF at 297 K after synthesis optimisation (space group $P4/nmm$).

In order to check for a structural phase transition, patterns between 297 and 10 K were recorded. Several reflections broaden below 185 K and clearly split with further decreasing temperature. Patterns below 185 K were indexed with an orthorhombic C-centred unit cell ($a_{\text{ortho}} = \sqrt{2} \cdot a_{\text{tetra}} - \delta$; $b_{\text{ortho}} = \sqrt{2} \cdot b_{\text{tetra}} + \delta$; $c_{\text{ortho}} \approx c_{\text{tetra}}$; $\delta \approx 2.2$ pm). The low-temperature data could be refined in the space group $Cmme$. The symmetry reduction tree is depicted in Figure 4.4.

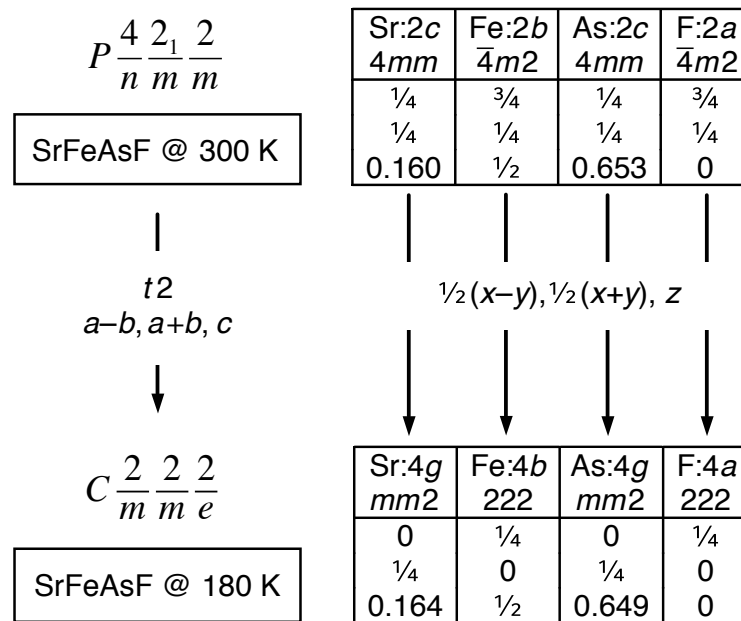
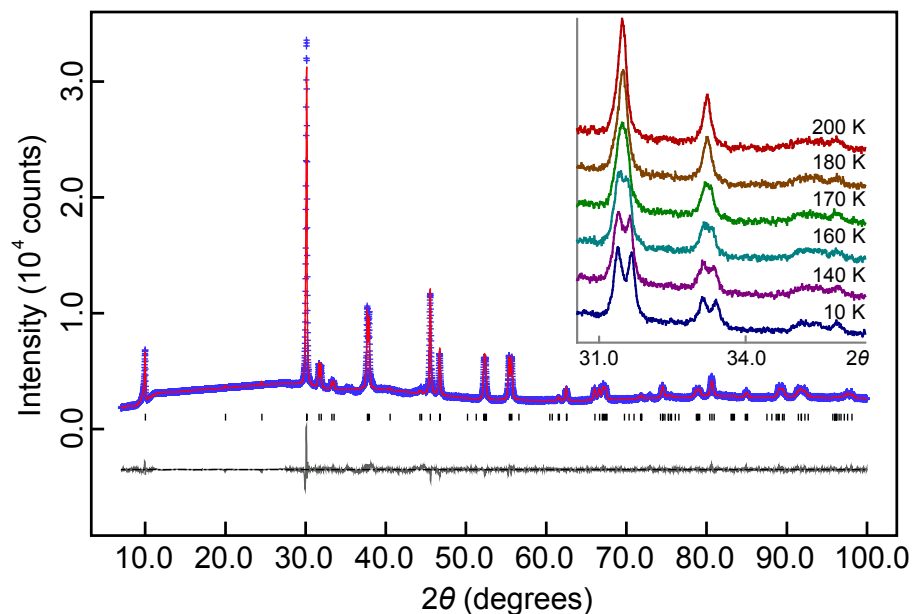


Figure 4.4: Bärnighausen tree of the structural phase transition in SrFeAsF.

Figure 4.5 shows the Rietveld fit of the data at 10 K and the continuous transition of the (200) and (201) reflections in the inset. For a better fit of the Rietveld data at 10 K, the range between $11^\circ 2\theta$ and $27.5^\circ 2\theta$ was excluded from the Rietveld refinement.

Figure 4.5: Rietveld fit of SrFeAsF at 10 K (space group $Cmme$). Inset: (200) and (201) reflections.

Chapter 4: SrFeAsF

The variation of the lattice parameters and the temperature dependence of the order parameter $P = (a-b)/(a+b)$ is depicted in Figure 4.6. All parameters have been derived from Rietveld refinements (one refinement per temperature). The lattice parameter a in the tetragonal structure has been multiplied by $\sqrt{2}$ for comparison. No signs of abrupt splitting of any reflections and also lattice parameters were found on cooling, but rather a continuous broadening. This seems to be in agreement with a second-order phase transition. The space group $Cmme$ is a maximal subgroup of $P4/nmm$ and in terms of group theory, this transition is *translationengleich* with index 2 ($P4/nmm \rightarrow Cmme$). Crystallographic data of SrFeAsF are summarised in Table 4.1. The main effect of the phase transition appears in the Fe–Fe distances, where four equal bonds of 282.3 pm length split into two pairs of 283.0 and 280.7 pm length. This supports the idea, that the Fe–Fe interactions are strongly related to the SDW anomaly and may play a certain role for the properties of SrFeAsF.

Temperature	297 K	10 K
Diffractometer	HUBER G670 (Cu-K α_1)	HUBER G670 (Cu-K α_1)
Rietveld package	GSAS	GSAS
Space group	$P4/nmm$ ($o2$)	$Cmme$
Lattice parameters	$a = 399.30(1)$ pm $c = 895.46(1)$ pm	$a = 561.55(1)$ pm $b = 566.02(1)$ pm $c = 891.73(2)$ pm
Cell volume	$V = 0.14277(1)$ nm ³	$V = 0.28343(1)$ nm ³
Z	2	4
Data points	9250	7649
Reflections	66	97
Atomic variables	4	4
d range	0.992 – 8.955	0.988 – 8.917
$R_p, R_{wp}, R_{F^2}, \chi^2$	0.0311, 0.0408, 0.0408, 1.771	0.0385, 0.0611, 0.0552, 2.860
Atomic parameters		
Sr	$2c$ ($1/4, 1/4, z$) $z = 0.1598(2)$ $U_{iso} = 185(9)$ pm ²	$4g$ ($0, 1/4, z$) $z = 0.1635(2)$ $U_{iso} = 227(12)$ pm ²
Fe	$2b$ ($3/4, 1/4, 1/2$) $U_{iso} = 75(8)$ pm ²	$4b$ ($1/4, 0, 1/2$) $U_{iso} = 142(12)$ pm ²
As	$2c$ ($1/4, 1/4, z$) $z = 0.6527(2)$ $U_{iso} = 46(8)$ pm ²	$4g$ ($0, 1/4, z$) $z = 0.6494(2)$ $U_{iso} = 60(11)$ pm ²

F	$2a$ ($\frac{3}{4}, \frac{1}{4}, 0$)	$4a$ ($\frac{1}{4}, 0, 0$)
	$U_{\text{iso}} = 210(26) \text{ pm}^2$	$U_{\text{iso}} = 114(33) \text{ pm}^2$
Bond lengths		
Sr-F	$245.7(1) \times 4$	$247.0(1) \times 4$
Fe-As	$242.0(1) \times 4$	$239.7(1) \times 4$
Fe-Fe	$282.3(1) \times 4$	$283.0(1) \times 2$ $280.7(1) \times 2$
Bond angles		
As-Fe-As	$111.2(1) \times 2$ $108.6(1) \times 4$	$112.5(1) \times 2$ $108.3(1) \times 2$ $107.7(1) \times 2$
Sr-F-Sr	$108.7(1) \times 2$ $109.8(1) \times 4$	$110.7(1) \times 2$ $110.1(1) \times 2$ $107.6(1) \times 2$

Table 4.1: Crystallographic data of SrFeAsF at 297 K and 10 K.

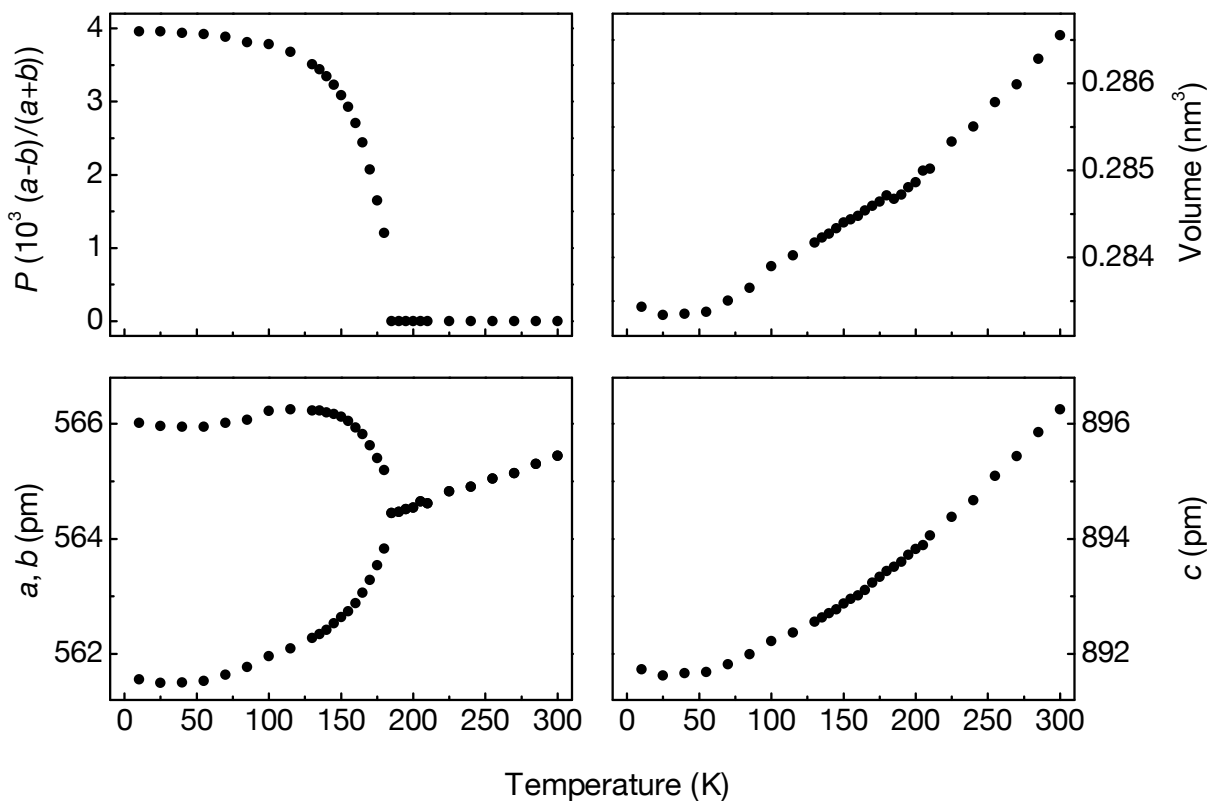


Figure 4.6: Variation of the lattice parameters and order parameter $P = (a-b)/(a+b)$ with temperature. The temperature dependence of the order parameter does not follow a simple power law. Values a and b for the tetragonal phase above 180 K are multiplied by $\sqrt{2}$ for comparability. Error bars are within data points.

4.3 Magnetic ordering

In order to check if the structural transition of SrFeAsF is connected with magnetic ordering and thus consistent with a SDW anomaly, ^{57}Fe Mössbauer spectra were recorded at various temperatures, which are shown in Figure 4.7 (left) together with transmission integral fits. In agreement with the crystal structure, a single signal was observed at room temperature at an isomer shift of $\delta = 0.33(1) \text{ mm}\cdot\text{s}^{-1}$ and with an experimental line width $\Gamma = 0.30(1) \text{ mm}\cdot\text{s}^{-1}$ subject to quadrupole splitting of $\Delta E_Q = -0.11(1) \text{ mm}\cdot\text{s}^{-1}$. The non-cubic site symmetry of the iron atoms is reflected in this quadrupole splitting value. These parameters compare well with the ^{57}Fe data of LaFeAsO ,^[102, 112] LaFePO (Chapter 3.2), SrFe_2As_2 (Chapter 8.3) and BaFe_2As_2 (Chapter 7.1.2). Below the SDW transition temperature, line broadening of the signal was observed, followed by hyperfine-field splitting due to the onset of magnetic order. As can be clearly seen, there is a large evolution of the shape of the spectra with decreasing temperature. In the magnetically ordered state, the ^{57}Fe Mössbauer spectra of the contaminated SrFeAsF sample show significant differences when compared to the related systems SrFe_2As_2 (Chapter 8.3) and BaFe_2As_2 (Chapter 7.1.2). It was not possible to reliably analyse the data with only one magnetically split component below the SDW transition temperature. However, the spectra could be effectively fitted assuming a distribution of hyperfine magnetic fields (multi-component analysis), an approach similar to the *Wivel* and *Mørup* method.^[113] The probability distribution curves $P(B_{\text{hf}})$ as a function of temperature are shown in Figure 4.7 (left). As this hyperfine field distribution is probably an artefact due to the presence of SrFe_2As_2 in the sample, the SrFeAsF sample from the optimised synthesis was also measured. These Mössbauer spectra are depicted in Figure 4.7 (right) and could be fitted without a hyperfine field distribution. The Mössbauer fitting parameters of both samples are listed in Table 4.2 and Table 4.3, respectively (δ : isomer shift; Γ : experimental line width; ΔE_Q : quadrupole splitting parameter; B_{hf} : average hyperfine field at the iron nuclei. Values marked with an asterisk were held constant).

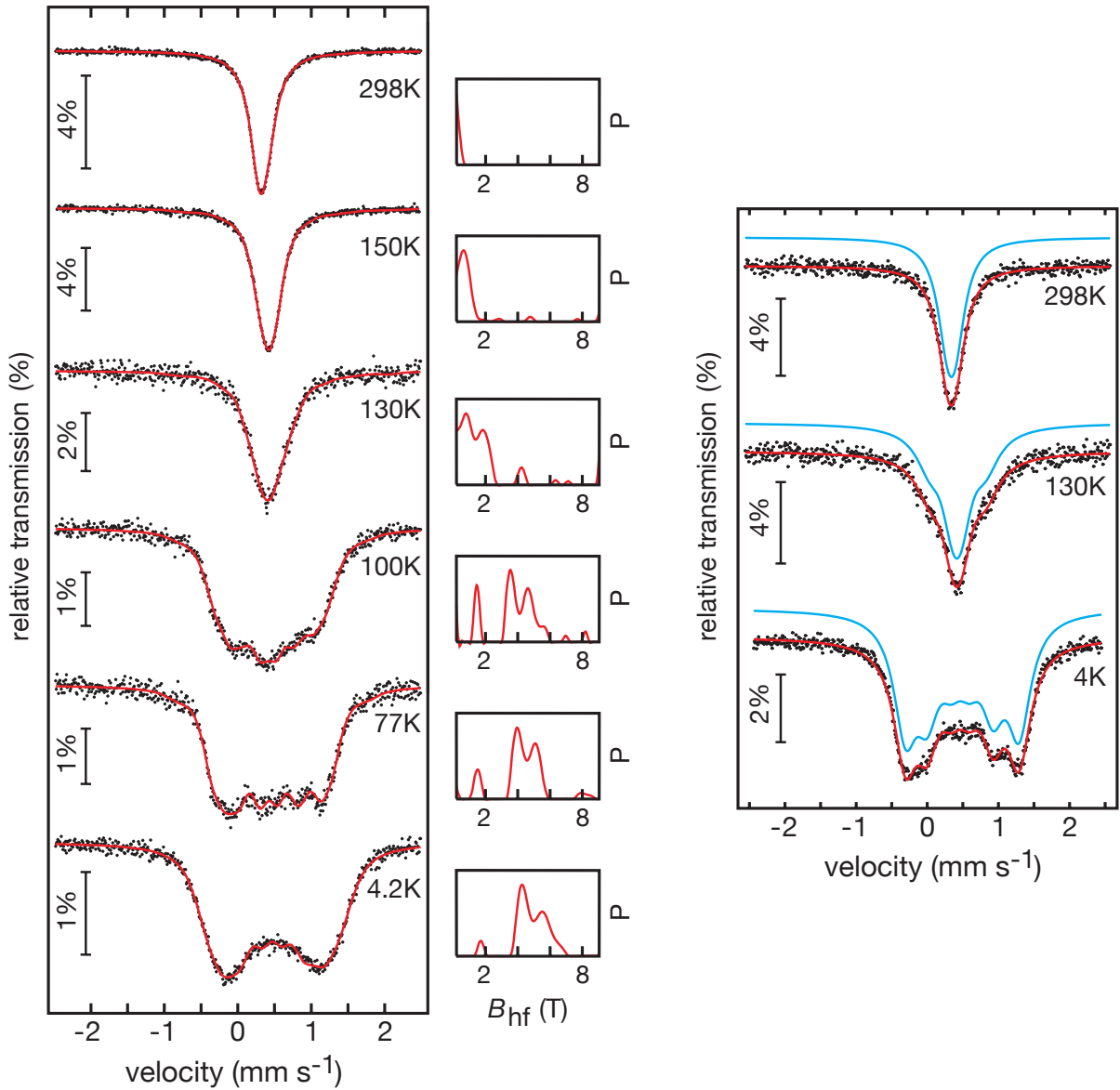


Figure 4.7: Mössbauer spectra of SrFeAsF before (left) and after (right) synthesis optimisation.

Temperature (K)	δ (mm·s ⁻¹)	Γ (mm·s ⁻¹)	ΔE_Q (mm·s ⁻¹)	B_{hf} (T)
298	0.32*	0.30*	0.08(1)	–
130	0.40*	0.26*	-0.01(1)	1.78(1)
100	0.45*	0.26*	0.03(1)	3.64(1)
77	0.45*	0.26*	0.32(1)	4.08(1)
4.2	0.40*	0.28*	0.20(1)	4.84(3)

Table 4.2: Fitting parameters for ⁵⁷Fe Mössbauer spectroscopy data of SrFeAsF *before* synthesis optimisation.

Temperature (K)	δ (mm·s ⁻¹)	Γ (mm·s ⁻¹)	ΔE_Q (mm·s ⁻¹)	B_{hf} (T)
298	0.34(1)	0.34(1)	0.11(1)	–
130	0.42(1)	0.46(3)	0.01(1)	2.39(3)
4	0.48(1)	0.39(1)	0.03(1)	4.96(1)

Table 4.3: Fitting parameters for ⁵⁷Fe Mössbauer spectroscopy data of SrFeAsF after synthesis optimisation.

These results clearly prove a structural distortion in SrFeAsF, which is connected with magnetic ordering. The nature of this effect is analogous to that in LaFeAsO!^[114] The transition is connected to a spin-density wave (SDW) instability within the iron layers and therefore causes anomalies in the electrical resistivity and magnetic susceptibility (see Chapter 4.4).

Yet, the Mössbauer spectra at 130 K of SrFeAsF do not display any *long-range* magnetic ordering – despite the structural phase transition being nearly complete at this temperature. This discovery is in line with recent neutron powder diffraction experiments on SrFeAsF, which showed the onset of a magnetic phase transition at 133 K, i.e. well below the onset of the structural phase transition (180 K)^[115] This is remarkable, as it is the largest difference between these two phenomena, which has been observed so far. In LaFeAsO, the difference between the structural and magnetic phase transition is only ~ 20 K and in BaFe₂As₂, not even *any* separation between these transition temperatures has been observed (see also Chapter 7.1.2).

Currently, there are two competing models for the cause and effect of the structural and magnetic phase transitions, which occur in several undoped iron pnictides. At first glance, it seems plausible to assume that the structural effects are primary and the antiferromagnetic order is a secondary effect, since in all compounds known so far, the temperatures of the structural phase transition T_o are higher than (or equivalent to) the Néel temperatures T_N .

However, *Fernandes* argues that magnetism is indeed the driving force for the structural distortion. In his model, the existence of spin fluctuations leads to the onset of spin-nematic ordering^{xiii} and these spins couple to the lattice. This already happens

^{xiii} Nematic ordering refers to a spontaneously broken rotational symmetry without the breaking of translational symmetry, i.e. a strong electronic anisotropy.

at temperatures above the structural phase transition and well above temperatures, where any long-range magnetic ordering is observed.^[116] Yet, this model cannot explain, why T_N is invariant to any applied uniaxial pressure^[117] and different external magnetic fields.^[118]

In a different model, Lv attributes the structural phase transition in the iron pnictide parent compounds to so-called ‘orbital ordering’ (which can be understood as a Peierls transition). Due to the anisotropy of the d_{xz} - and d_{yz} -orbitals in the ab -plane, ordering of the iron orbitals makes the orthorhombic structure energetically more favourable.^[119] While this model leads to a good description of several physical properties of the iron pnictides including the resistivity, up to now there has not been any success to support this model via DFT calculations.

4.4 Resistivity, susceptibility and specific heat

The resistivity and magnetic susceptibility of SrFeAsF were measured and a similar behaviour like in LaFeAsO was found. The temperature dependences of the magnetic susceptibility and DC electrical resistance are depicted in Figure 4.8 (left). SrFeAsF shows a relatively high resistance at room temperature. At 175 K, the resistance drops abruptly and then decreases slowly with lower temperatures. SrFeAsF shows only slightly temperature-dependent paramagnetism, which is several orders of magnitude too high for a Pauli-paramagnetic metal. At temperatures above 200 K, χ increases linearly with temperature. Below 175 K, χ drops at first but it increases again below 115 K. Similar magnetic behaviour has also been observed in other undoped iron pnictides (e.g. BaFe₂As₂). The observed linear increase of the susceptibility with temperature meanwhile is commonly attributed to itinerant electron antiferromagnetic spin fluctuations.^[120] For details, also refer to [121].

The specific heat data of SrFeAsF are shown in Figure 4.8 (right). At room temperature, the specific heat capacity reaches the value of approximately 100 J·mol⁻¹·K, in agreement with the law of *Dulong and Petit*. The phase transition of SrFeAsF becomes noticeable by an anomaly below ~ 180 K. The transition temperature has been determined as the first point right of the inflection. Thus, the C_p data are in line

with the resistivity, X-ray powder diffraction, and Mössbauer spectroscopic data. In the low-temperature region, the specific heat is of the form $C_p = \gamma \cdot T + \beta \cdot T^3$, where γ is the electronic contribution and β is the lattice contribution. The Debye temperature Θ_D can be estimated from the equation $\beta = (12\pi^4 \cdot n \cdot k_B) / (5 \cdot \Theta_D^3)$, where k_B is the Boltzmann constant and n is the number of atoms per formula unit (see also Chapter 2.9). From the plot of C_p/T vs. T^2 in the temperature range 4 – 10 K (not depicted), the electronic and lattice contributions, as well as Debye temperature were determined as $\gamma = 1.5(2) \text{ mJ} \cdot \text{K}^{-2} \cdot \text{mol}^{-1}$, $\beta = 0.2(1) \text{ mJ} \cdot \text{K}^{-4} \cdot \text{mol}^{-1}$, and $\Theta_D = 339(1) \text{ K}$.

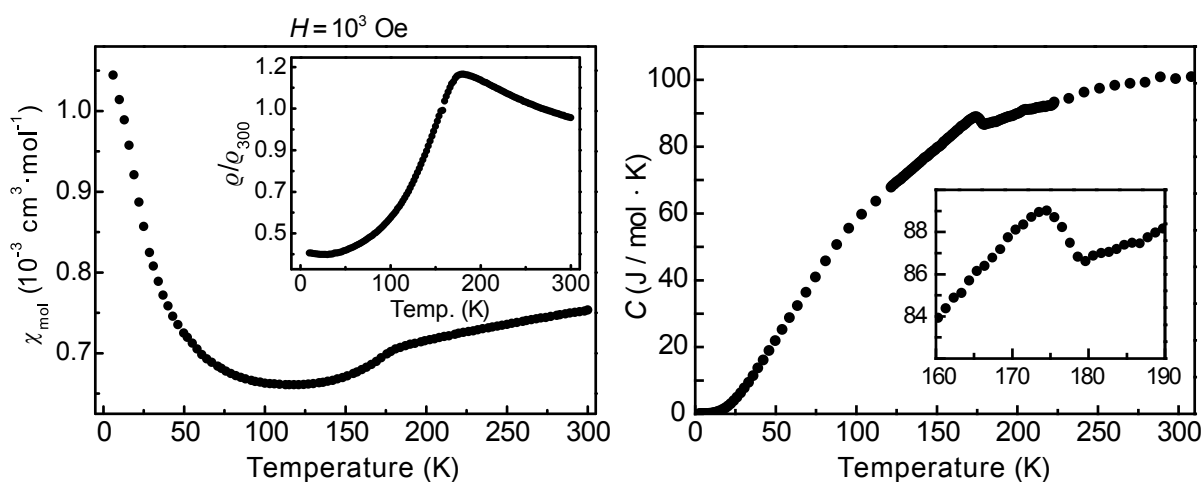


Figure 4.8: Left: Magnetic susceptibility of SrFeAsF measured at 0.1 T. Left inset: DC electrical resistance ($I = 100 \mu\text{A}$). Right: Heat capacity (C_p) vs. temperature of SrFeAsF. The right inset highlights the features between 160 and 190 K.

4.5 DFT calculations

Volume optimisations of the *EAF*FeAsF compounds CaFeAsF, SrFeAsF and BaFeAsF have been performed via DFT calculations (WIEN2k) according to the method described in Chapter 2.1. Also their band structures have been calculated with the LMTO package according to Chapter 2.1. The results of the volume optimisations are depicted in Figure 4.9. In Table 4.4, the calculated lattice parameters and cell volumes are compared with the experimentally obtained values. While the calculated cell volume for CaFeAsF lies in the same range as the experimentally obtained value, the c/a ratio differs noticeably. For SrFeAsF, both the cell volume and c/a ratio differ by $\sim 2\%$ from the corresponding experimental values. In summary, while still

acceptable, these structure optimisations are slightly inferior to similar optimisations for this structure type (for example, refer to Chapter 6.3). This may be attributed to magnetic effects (the calculations were performed non-magnetically on the tetragonal phases).

	CaFeAsF^[122]	SrFeAsF	BaFeAsF
Experimental	$a = 387.5(1) \text{ pm}$ $c = 858.4(1) \text{ pm}$ $V = 0.12888(1) \text{ nm}^3$	$a = 399.30(1) \text{ pm}$ $c = 895.46(1) \text{ pm}$ $V = 0.14277(1) \text{ nm}^3$	no data published in [123]
Calculated	$a = 392.3 \text{ pm}$ $c = 835.7 \text{ pm}$ $V = 0.12861 \text{ nm}^3$	$a = 399.2 \text{ pm}$ $c = 878.9 \text{ pm}$ $V = 0.14006 \text{ nm}^3$	$a = 406.5 \text{ pm}$ $c = 939.4 \text{ pm}$ $V = 0.15523 \text{ nm}^3$
Rel. differences	$\Delta V/V_{\text{exp}} = 0.2 \%$ $\Delta(c/a) : (c/a)_{\text{exp}}$ $= 3.8 \%$	$\Delta V/V_{\text{exp}} = 1.9 \%$ $\Delta(c/a) : (c/a)_{\text{exp}}$ $= 1.8 \%$	

Table 4.4: Comparison between calculated and experimental lattice parameters, cell volumes and c/a ratios.

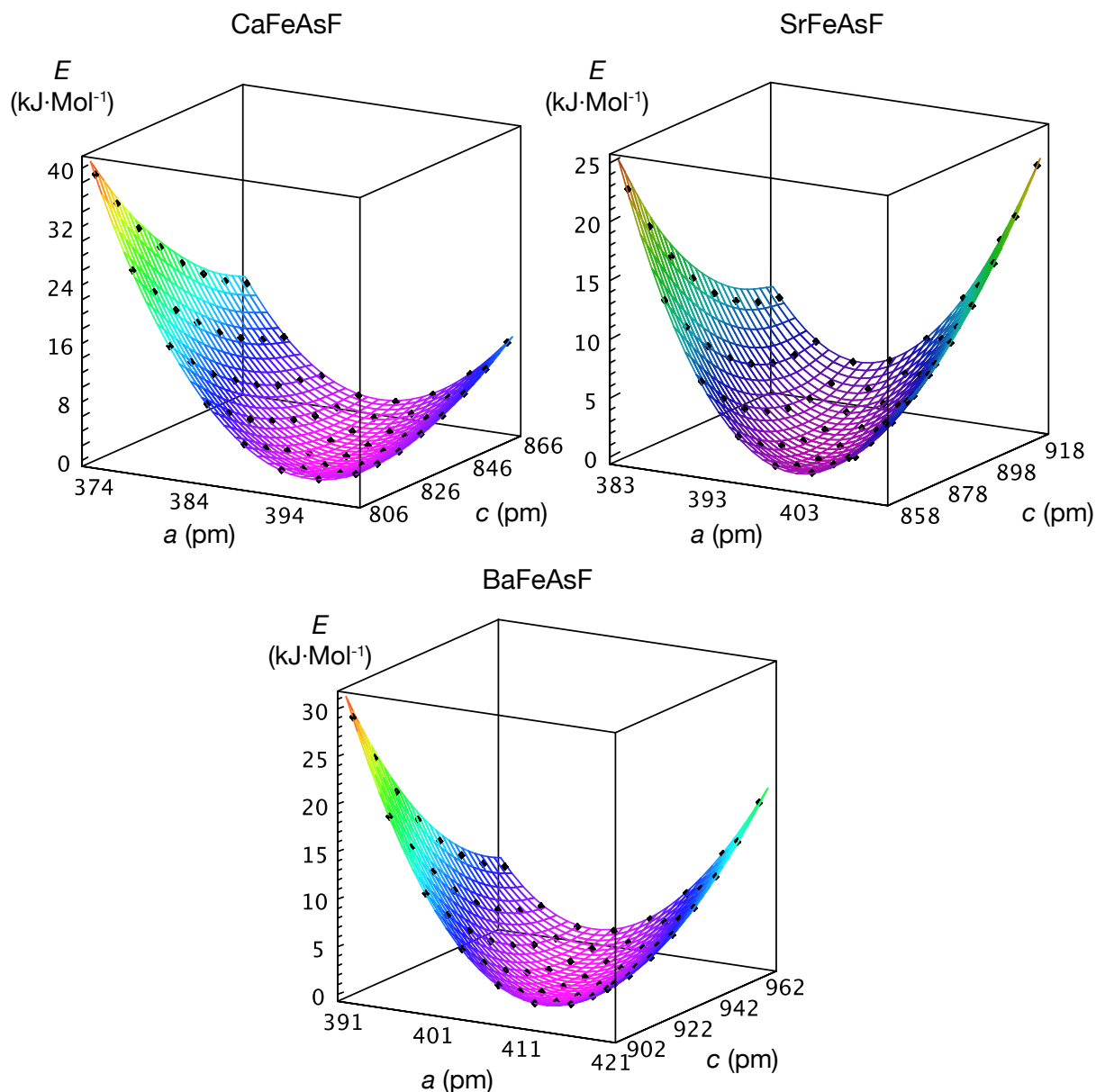


Figure 4.9: Energy dependence of the a and c lattice parameters in CaFeAsF, SrFeAsF and BaFeAsF. Black diamonds: DFT calculations.

The band structures of CaFeAsF, SrFeAsF and BaFeAsF are depicted in Figure 4.10. Apart from a slightly decreasing band dispersion in the order $EA = \text{Ca} > \text{Sr} > \text{Ba}$, all three band structures are almost identical around the Fermi level exhibiting the typical features of other iron arsenide parent compounds (see also Chapter 1.1.2). One can therefore expect these compounds to exhibit similar physical properties as for example LaFeAsO, which is also in line with the experiments of the previous chapters. Consequently, superconductivity can probably be induced in the quaternary iron arsenide fluorides upon doping.

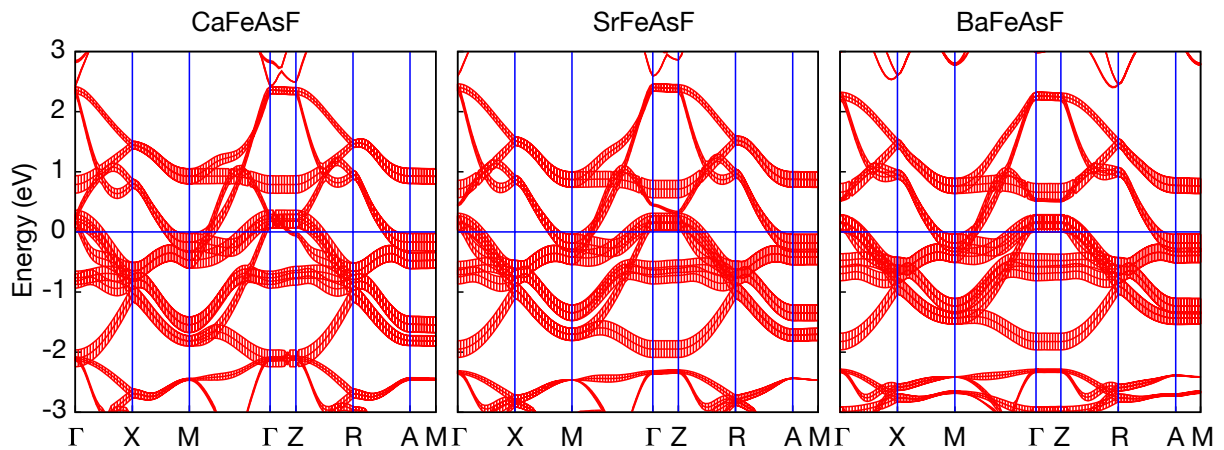


Figure 4.10: Sections of the band structures of CaFeAsF, SrFeAsF and BaFeAsF. Fe-d bands are emphasised.

In summary, the quaternary iron arsenide fluoride SrFeAsF has been successfully synthesised. The crystal structure and physical properties of SrFeAsF and LaFeAsO are very similar. Both materials are poor metals at room temperature and undergo probably second-order structural and magnetic phase transitions. The ^{57}Fe Mössbauer data of SrFeAsF show hyperfine-field splitting, which proves antiferromagnetic ordering occurring below the structural transition temperature. Consequently, SrFeAsF exhibits a similar structural distortion at 180 K as LaFeAsO at 160 K.^[33b] Magnetic ordering connected with a SDW anomaly appears at temperatures well below this structural phase transition. Because this SDW instability is thought to be an important prerequisite for high- T_c superconductivity in iron arsenides, these results suggest that SrFeAsF can serve as a parent compound for a new, oxygen-free class of iron arsenide superconductors with ZrCuSiAs-type structure. And indeed, superconductivity with critical temperatures of up to 56 K has meanwhile been successfully induced in La-,^[124] Sm-,^[125] and Nd-doped^[126] SrFeAsF. The isoelectronic compounds CaFeAsF,^[122, 127] BaFeAsF and EuFeAsF^[123] are known to exist, too and superconductivity can also be induced by Co-doping.^[127] However, to date a single-phase synthesis of these doped, fluorine-based superconducting iron arsenides is not yet possible. In order to achieve superconductivity in these compounds, electron dopants have to be employed in considerable excess, which leads to the formation of impurity phases. Although the EAF₂FeAsF materials would be very interesting for

Chapter 4: SrFeAsF

application due to their high T_c s in combination with relatively cheap starting materials (e.g. in the case of CaFeAsF), However, the preparation of clean samples is still difficult.

The large separation between the structural and magnetic phase transition temperatures make SrFeAsF an excellent model system to study the correlation between magnetism and structure. 50 K is the largest temperature difference between these phenomena in any undoped iron arsenide, which has been observed so far.

5. EuMnPF

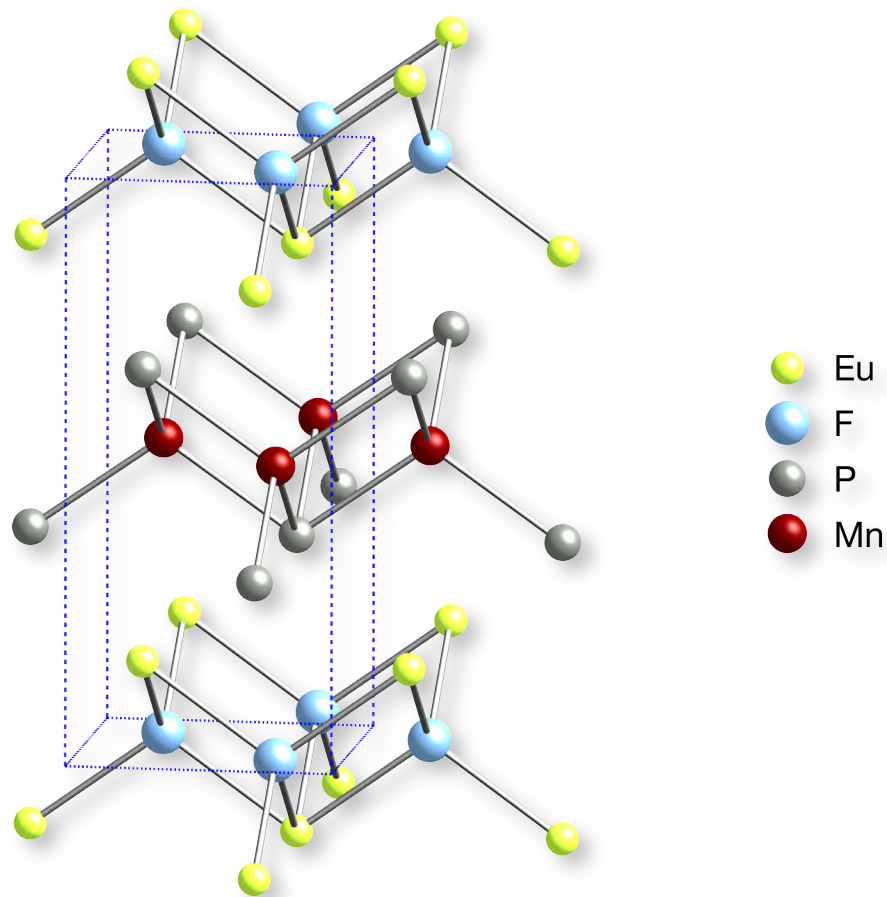


Figure 5.1: Crystal structure of EuMnPF.

The new compound EuMnPF can formally be regarded as a highly hole-doped variant of the iron phosphide superconductor LaFePO, in which not only all Fe atoms are exchanged for Mn atoms (having one electron less than Fe) but also the $(\text{OLa})^+$ -layers are replaced by $(\text{FEu})^+$ -sheets having the same nominal charge. In this chapter, the synthesis and magnetic characterisation of this compound is subject of discussion. An electron microscope image of a polycrystalline EuMnPF sample is depicted in Figure 5.2.

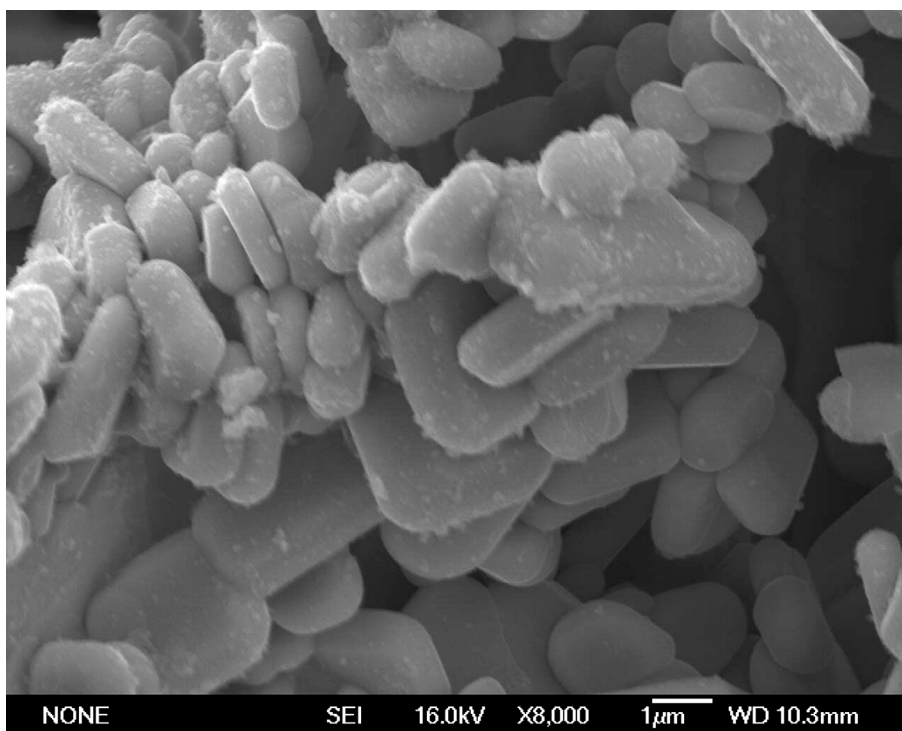


Figure 5.2: Polycrystalline sample of EuMnPF.

5.1 Synthesis

After careful synthesis optimisation, EuMnPF was synthesised according to the method described in Chapter 2.10.5 by heating EuF_3 , Eu, Mn and P in a ratio of 1.15 : 1.85 : 3 : 3 as well as NaCl / KCl as a flux to 1073 K in a sealed Ta tube and keeping at this temperature for 10 days. Lumps of polycrystalline EuMnPF were then separated from the reaction mixture under an optical microscope and washed with distilled water. Annealing temperatures of more than 1073 K were found to lead to decomposition.

5.2 Crystal structure

The crystal structure of EuMnPF was determined by X-ray powder diffraction using the Rietveld method. EuMnPF crystallises in the ZrCuSiAs-type structure. Layers of edge-sharing $\text{FEu}_{4/4}$ tetrahedra alternate with $\text{MnP}_{4/4}$ layers along [001] (Figure 5.1). The MnP_4 tetrahedra are almost undistorted as expected for the $d^5\text{-Mn}^{2+}$ ion. The powder diffractogram and Rietveld fit of EuMnPF is depicted in Figure 5.3, crystallographic details are listed in Table 5.1.

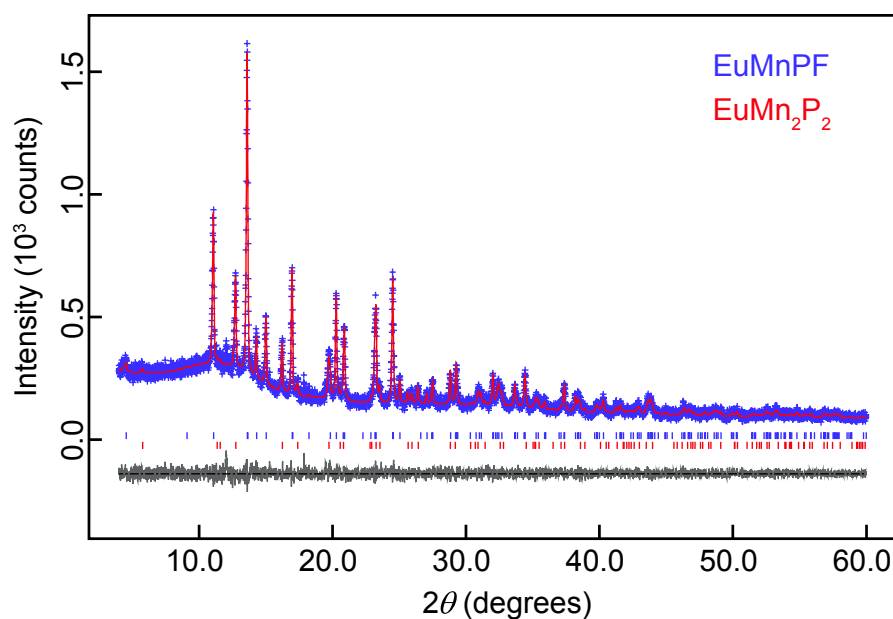


Figure 5.3: Rietveld fit of EuMnPF at 297 K.

Temperature	297 K
Diffractometer	STOE STADI P (Mo-K α_1)
Rietveld package	GSAS
Space group	<i>P4/nmm</i> (<i>o2</i>)
Lattice parameters	$a = 402.74(1)$ pm $c = 894.63(3)$ pm
Cell volume	$V = 0.1451(1)$ nm ³
Z	2
Data points	4600
Reflections	302 (total)
Atomic variables	6 (main phase)
<i>d</i> range	0.710 – 8.948
$R_p, R_{wp}, R_{F^2}, \chi^2$	0.0465, 0.0630, 0.0378, 1.757
Atomic parameters	
Eu	$2c$ ($\frac{1}{4}, \frac{1}{4}, z$) $z = 0.1608(2)$ $U_{iso} = 39(5)$ pm ²
Mn	$2b$ ($\frac{3}{4}, \frac{1}{4}, \frac{1}{2}$) $U_{iso} = 174(12)$ pm ²
P	$2c$ ($\frac{1}{4}, \frac{1}{4}, z$) $z = 0.655(1)$ $U_{iso} = 211(19)$ pm ²
F	$2a$ ($\frac{3}{4}, \frac{1}{4}, 0$) $U_{iso} = 170(40)$ pm ²

Bond lengths		
Eu–F	247.5(1) × 4	
Mn–P	244.4(6) × 4	
Mn–Mn	284.8(1) × 4	
Bond angles		
P–Mn–P	111.0(1) × 2	108.7(1) × 4
Eu–F–Eu	108.9(1) × 2	109.8(1) × 4

Table 5.1: Crystallographic data of EuMnPF at 297 K.

5.3 Magnetism

EuMnPF is paramagnetic in the temperature range between 1.8 and 380 K (Figure 5.4). A kink in the inverse susceptibility is visible at ~ 25 K, probably arising from the antiferromagnetic ordering of the EuMn₂P₂ impurity phase ($T_N = 17.5$ K, $n_{\text{eff}} = 7.87$)^[128]. The inverse susceptibility was fitted with the extended Curie-Weiss law (60 – 380 K) described in Chapter 2.6 to obtain the following parameters: $\chi_0 = 0.0046(1)$ cm³·mol⁻¹, $n_{\text{eff}} = 7.90(1)$, $\Theta = -4.6(1)$ K. The effective moment of 7.90 μ_B per formula unit is in good agreement with the expected value for Eu²⁺ (f^7) of 7.94 μ_B but lower than the moment expected for both Eu²⁺ and Mn²⁺, which is $(7.94 + 5.92)^{1/2} \mu_B = 9.90 \mu_B$. This points to an antiferromagnetic ordering of the Mn²⁺ sublattice at least below 380 K. This would also be in line with neutron powder diffraction experiments on BaMn₂P₂.^[129] BaMn₂P₂ crystallises in the ThCr₂Si₂-type structure and contains identical MnP_{4/4} tetrahedral layers as EuMnPF and also the Mn–Mn-distances of 285 pm in BaMn₂P₂ are almost identical to those in EuMnPF. In BaMn₂P₂, the Mn²⁺ atoms are ordered antiferromagnetically in a G-type pattern (Chapter 21.4) with an ordered magnetic moment of 4.2(1) μ_B per Mn²⁺ ion at 293 K. Susceptibility measurements of BaMn₂P₂ revealed antiferromagnetic ordering at least below 750 K. The closely related ZrCuSiAs-type compound LaMnPO also exhibits antiferromagnetic ordering of the Mn²⁺ ions at least up to 375 K. The magnetic ordering presumably is of the C-type with the spins aligned along **c**. The refined ordered magnetic moment is 2.26(2) μ_B per Mn²⁺ ion at room temperature.^[130]

These findings strongly suggest that also in EuMnPF, the Mn^{2+} sublattice is already antiferromagnetically ordered at room temperature, possibly with the same spin structure as in LaMnPO.

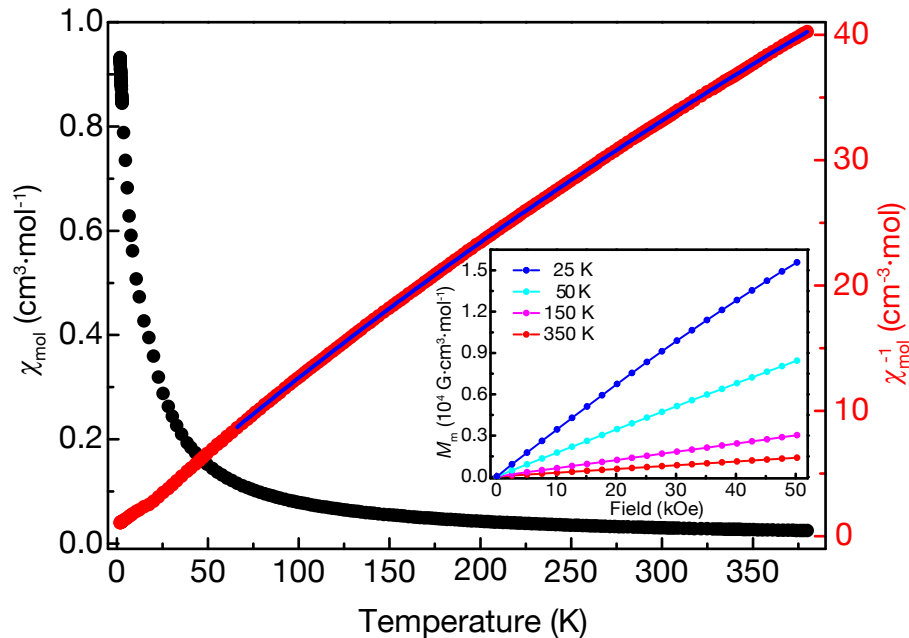


Figure 5.4: Susceptibility, inverse susceptibility and magnetisation isotherms of EuMnPF.

In summary, EuMnPF is not superconducting above 1.8 K and unlike the iron pnictides with their weak magnetism at the iron centres, the Mn^{2+} atoms of EuMnPF seem to exhibit a strong, localised magnetism. EuMnPF is a paramagnetic metal in the whole temperature range with the magnetism arising from the Eu^{2+} atoms. The spins of the Mn-atoms are probably antiferromagnetically ordered below a T_N of more than 380 K in spite of Mn–Mn bond lengths of only 285 pm, which is roughly the same as the Fe–Fe bond lengths in LaFePO (280 pm). To date, only $\text{EuFeAsF}^{[123]}$ with a SDW anomaly below 153 K is known as a ZrCuSiAs-type compound with similar $(\text{FEu})^+$ tetrahedral layers. The hypothetical compounds EuFePF and EuMnAsF, however, are not known to exist.

6. *REZnPO*

A closer look at the *REZnPO* compounds (*RE* = La, Ce, Pr) might be at first a glance beyond the main subject because these compounds are no *iron* pnictides and thus presumably no superconductors. Yet they share certain properties with the 1111 superconductors. Apart from an identical 1111 stoichiometry, the so-called α -polymorphs of *REZnPO* crystallise in the same structure type (ZrCuSiAs). Thus in α -*REZnPO*, edge-sharing, anion centred rare earth oxide tetrahedra alternate with edge-sharing zinc phosphide tetrahedra (Figure 6.1, left).

But these materials are particularly interesting because they possess four more valence electrons per formula unit than *REFePO* (assuming localised, non-participating *RE*-f electrons) and still two more valence electrons than LaNiPO. This leads to apparent differences in the physical properties of these materials: Firstly, unlike *REFePO* or LaNiPO, the *REZnPO* compounds CeZnPO and PrZnPO show a dimorphism, which means they possess β -forms that crystallise in a rhombohedral structure (Figure 6.1 right)^[131] Secondly, also their tetragonal α -forms are quite different from the pnictide oxides. That even has consequences for their appearance. While LaNiPO and *REFePO* crystallise as black platelets with metallic lustre, α -*REZnPO* forms translucent yellow to red plate-like crystals and β -*REZnPO* translucent red platelets (Figure 6.1, top). This means that while LaNiPO and *REFePO* are metals in their normal state, both α - and β -*REZnPO* appear to be optical semiconductors;^{xiv} which may be expected because they are valence compounds according to $RE^{3+}Zn^{2+}P^{3-}O^{2-}$. But there is more to it: the exact colour of α - and β -*REZnPO* obviously depends on the rare earth element. The electronic structures of α - and β -CeZnPO as well as α - and β -PrZnPO were therefore calculated, analysed and related to the physical and optical properties of these substances.

^{xiv} In the context of this dissertation, the term optical semiconductor denotes a semiconductor with a band gap between ~ 1.6 and 3.3 eV, i.e. in the region, where visible light is absorbed (~ 780 nm down to ~ 380 nm).

6.1 Computational details

DFT calculations were performed according to Chapter 2.1. In case of the LMTO calculations, reciprocal space integrations were performed with the tetrahedron method, using 1088 irreducible k -points out of 13500 ($30 \times 30 \times 15$ mesh) for tetragonal α -PrZnPO and 1469 irreducible k -points out of 15625 ($25 \times 25 \times 25$ mesh) for rhombohedral β -PrZnPO in the Brillouin zone. The basis sets consisted of Pr-6s/[6p]/5d, Zn-4s/4p/3d, P-3s/3p/[3d] and O-[3s]/2p/[3d]. Orbitals given in square brackets were downfolded. The band structure calculations of LaFePO, LaNiPO and LaZnPO were performed analogously. Pr-4f orbitals were omitted from the calculations and treated as core states because of their unsatisfactory description by LSDA. For the WIEN2k calculations, the total energies and charge densities of the SCF cycles converged to residual changes smaller than $1 \cdot 10^{-4}$ Ry·cell⁻¹. 630 k -points (α -PrZnPO, $28 \times 28 \times 12$ mesh) or 891 k -points (β -PrZnPO, $21 \times 21 \times 21$ mesh) were used in the irreducible wedges of the Brillouin zones. The basis sets consisted of 2089 or 2724 plane-waves for α -PrZnPO and β -PrZnPO, respectively, up to a cut-off $r_{\text{mt}} \cdot k_{\text{max}} \approx 8.0$. The atomic sphere radii r_{mt} were 2.32 (Pr), 2.48 (Zn), 2.2 (P) and 2.05 au (O) for α -PrZnPO and 2.35 (Pr), 2.4 (Zn), 2.13 (P) and 2.09 au (O) for β -PrZnPO.

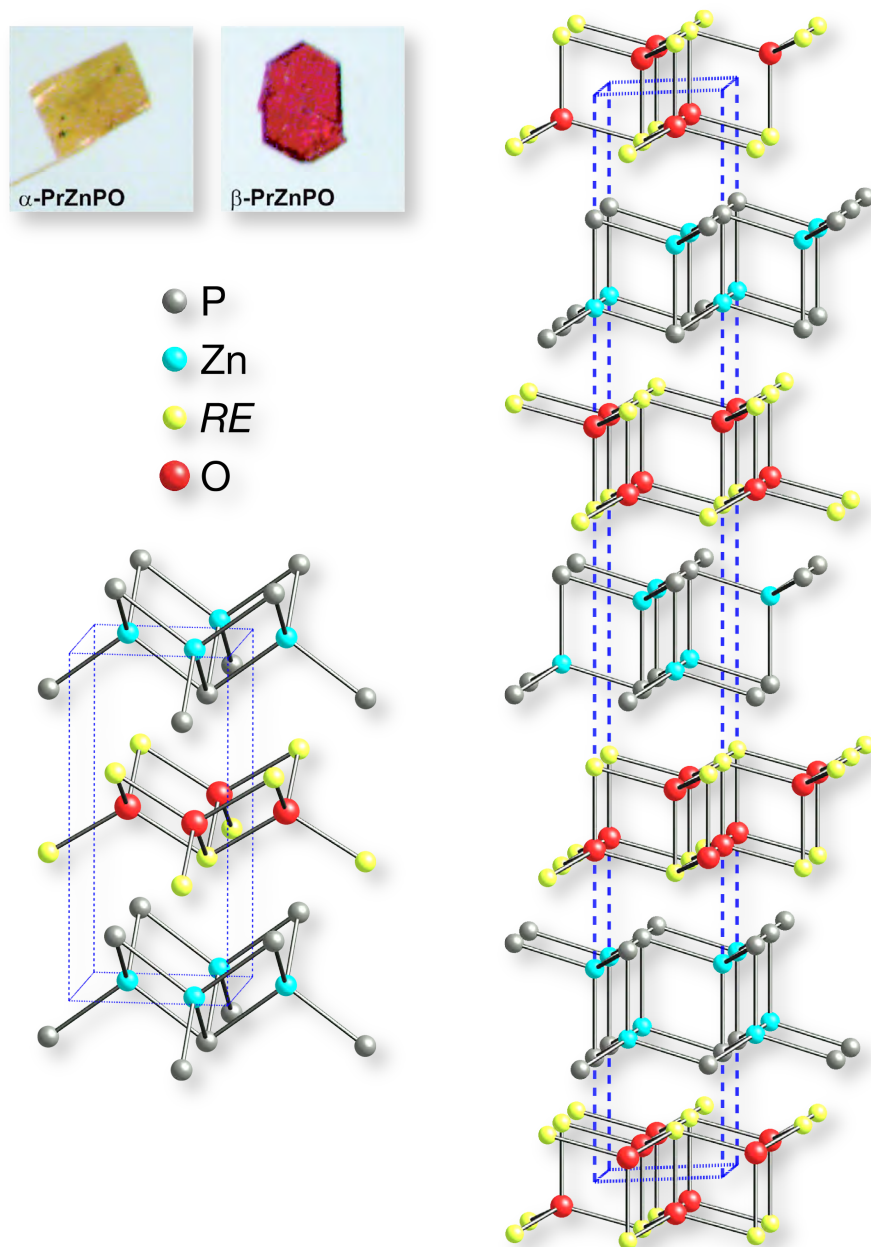


Figure 6.1: Top: α -PrZnPO and β -PrZnPO single crystals. Bottom: Crystal structures of α -*REZnPO* (left) and β -*REZnPO* (right).

6.2 Electronic structure

In comparison with the superconductors LaFePO and LaNiPO, the *REZnPO* compounds are non-metals with an optical band gap, while LaFePO and LaNiPO are metals in their normal state. This is a direct result of the higher number of valence electrons in Zn compared to Fe and Ni, which results in the Zn-3d orbitals being fully occupied and energetically far below the Fermi level. The properties of *REZnPO* are therefore dominated by the P-3p and Zn-4s orbitals and the energy gap between the

corresponding bands. Sections of the LMTO band structures of LaFePO, LaNiPO and LaZnPO in comparison are shown in Figure 6.2.

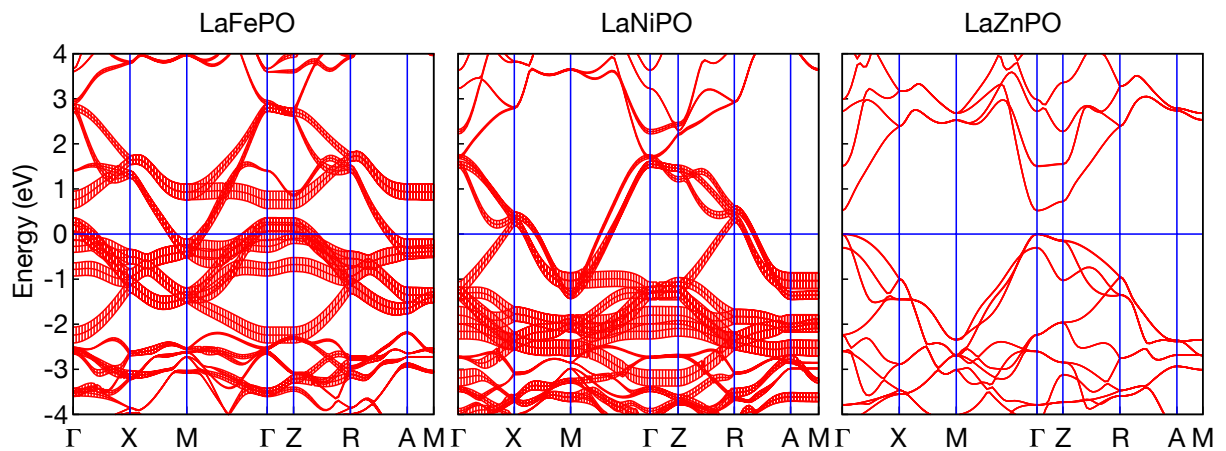


Figure 6.2: Section of the band structure of tetragonal LaFePO, LaNiPO and LaZnPO in comparison. *TM-d* bands are emphasised.

The LMTO total density of states (DOS) for α - and β -PrZnPO, as well as the COHP diagrams of selected bonds are shown in Figure 6.3. Pr-4f orbitals were excluded from the calculations for clarity. As expected from the crystal colour and also optical measurements of these compounds, there are energy gaps at the Fermi level for both polymorphs. However, the calculated gaps are much smaller than the measured ones, which is a well-known issue of DFT band structure methods.

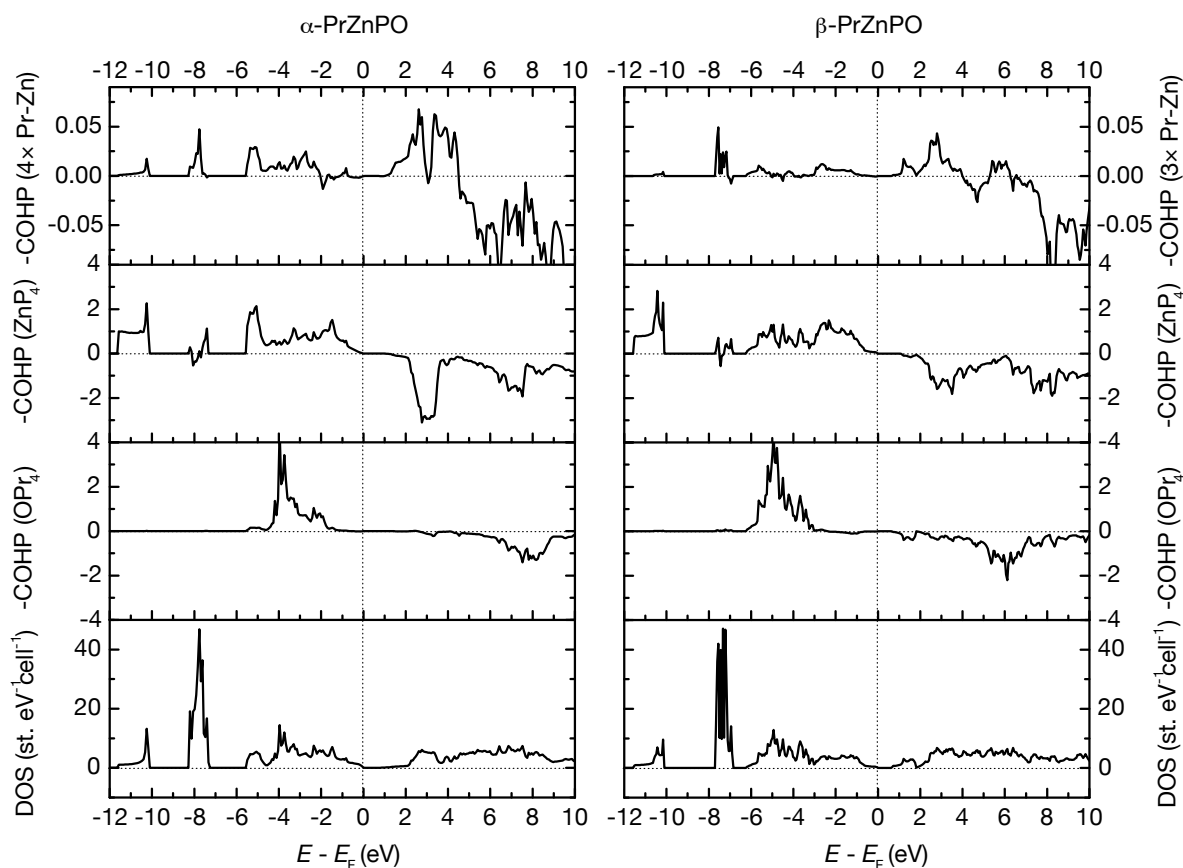


Figure 6.3: LMTO DOS and COHP diagrams of selected bonds for α - and β -PrZnPO. The Fermi level is defined as energy zero.

The magnitude of the calculated gap is smaller in the β -polymorph, which is in agreement with the observed colours. The valence bands are very similar in both α - and β -PrZnPO, which is also sensible from a chemical point of view, as these bands possess mainly P-3p (Zn–P bonding) character. But the conduction bands are remarkably different. Both bands have mainly Zn-4s character, but a significant contribution of Pr-5d occurs in β -PrZnPO, which is not the case in α -PrZnPO. As it can be recognised from the COHPs, the valence states around 1.5 eV are Pr–O antibonding and the question arises, why these states have lower energy in the case of β -PrZnPO. A detailed analysis of the eigenvectors revealed mixing of Pr-5d orbitals with the very diffuse Zn-4s orbitals to a certain extent. This interaction has bonding character and consequently decreases the energy of the Zn-4s conduction band. This effect is even more pronounced for the β -polymorph, where the Zn–Pr distance is about 15 pm shorter. As a consequence, the optical transition is P-3p \rightarrow Zn-4s + Pr-5d and differences in the Pr-5d contribution determine the mag-

nitude of the gap and therefore the colour. On the basis of these considerations, it is understandable, why the band gaps of the β -REZnPO compounds are without exception smaller than those of the α -REZnPO compounds and, as a result, why the colours are so different.

In order to get physically correct magnetic insulating ground states of α - and β -PrZnPO, spin-polarised FP-LAPW calculations with LSDA+ U or EECCE corrections for the strongly correlated 4f electrons were performed. The calculated magnetic moment corresponds to two unpaired electrons per Pr³⁺ ion in agreement with the experimental data. Also in these calculations, the obtained band gaps are much too small. Hybridisation of Zn-4s with Pr orbitals of the lowest conduction band level can also be observed here; only the difference is that the 4f orbitals of Pr contribute additionally to this band. Figure 6.4 shows sections of the band structure of α -PrZnPO. A direct optical band gap occurs at the Γ point and it is this lowest conduction band, which mainly determines the energy gap of the compound. It possesses strong Zn-4s character, but the lowering of the energy of this band along M- Γ and Z- Γ is a direct consequence of the weak mixing with Pr-5s and -4f orbitals in a bonding manner. This can be illustrated by a partial electron density map of the first unoccupied energy level at the Γ point, which is shown in Figure 6.5. The large contribution of Zn-4s orbitals is visible there, slightly mixed with Zn-3d_{z²}. Additionally, the electron density of this energy level connects the Zn- and Pr-atoms by forming a crystal orbital consisting of Zn-4s + Pr-5d + Pr-4f. This weak bonding interaction determines the exact magnitude of the band gap. Similar observations have been made for the course of the Zn-4s + Y-4d bands of YZnPO (not depicted).

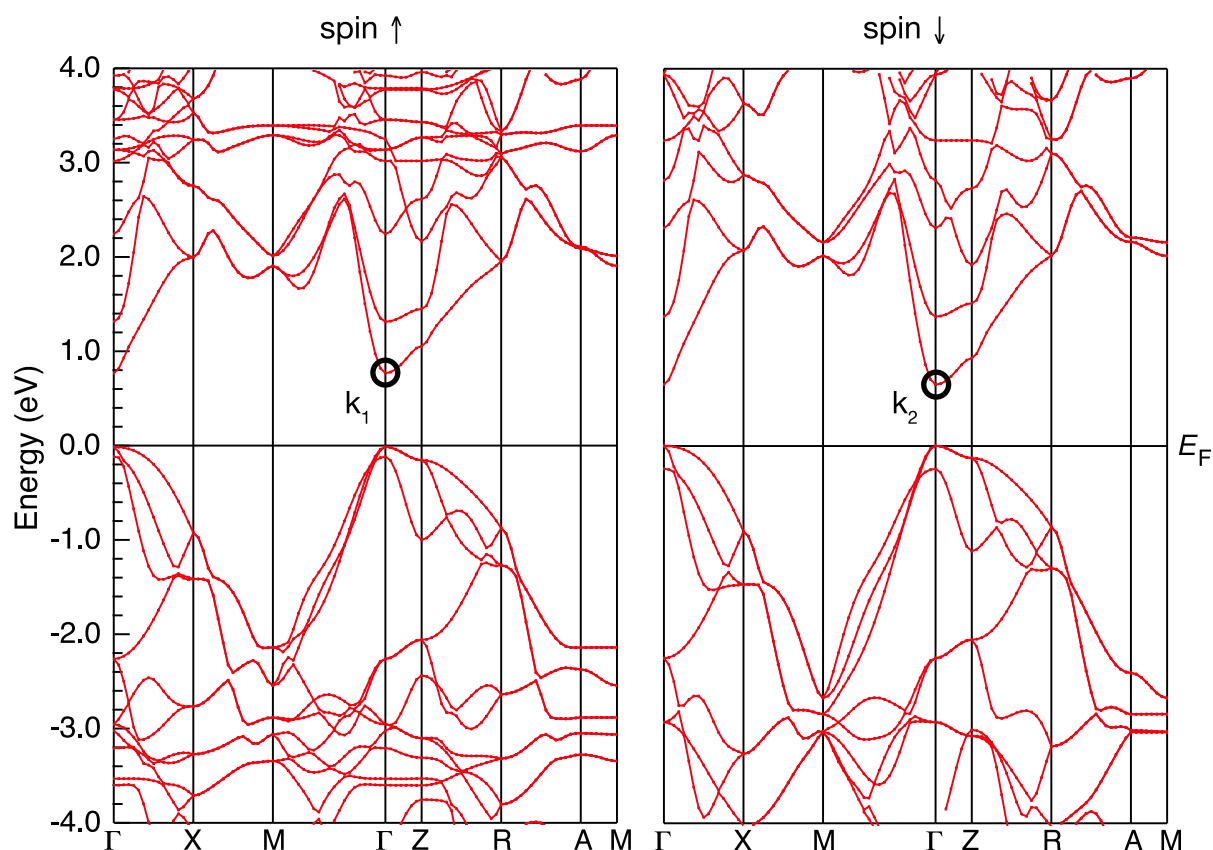


Figure 6.4: Section of the band structure of α -PrZnPO, calculated with the LSDA+ U method (WIEN2k). The direct optical gap at the Γ point is visible.

These results show how the optical gap of *REZnPO* is directly related to the rare earth component. So it can be explained qualitatively, why these gaps are so different. This would not be the case if the optical transition was only P-3p \rightarrow Zn-4s. The reason for this variance is that the diffuse Zn-4s orbitals slightly hybridise with the 5d- and 4f-orbitals of the rare earth element and thus the energy is altered according to the magnitude of this mixing. The mixing is much stronger for the rhombohedral compounds due to better *RE*-Zn overlap and consequently the optical gaps are generally smaller in β -*REZnPO*. This is in excellent agreement with the observation that the colours of all known rhombohedral compounds are darker than those of the corresponding tetragonal polymorphs, e.g. rhombohedral β -CeZnPO is dark red, whereas tetragonal α -CeZnPO is amber and β -PrZnPO is red, while α -PrZnPO is yellow.

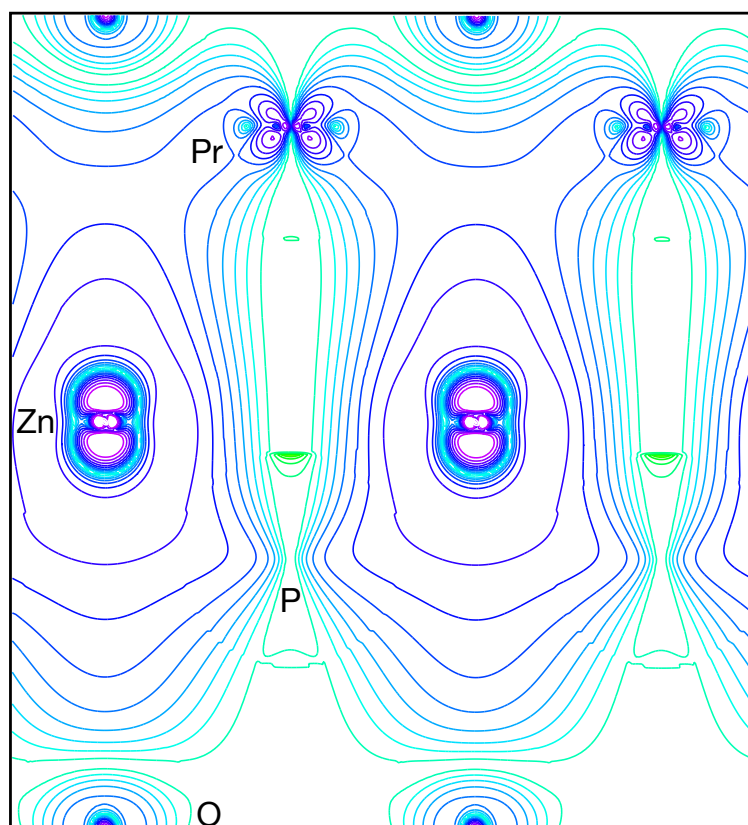


Figure 6.5: Calculated partial electron density map of α -PrZnPO, generated from the lowest conduction band level at the Γ point (marked as k_1 in Figure 6.4). The large diffuse Zn-4s orbital hybridises with the Pr-5d and 4f orbitals and generates a weak Pr-Zn bonding crystal orbital (unoccupied). The energy of Zn-4s is lowered by this hybridisation.

6.3 Volume optimisations

Volume optimisations were performed for both tetragonal α -PrZnPO and rhombohedral β -PrZnPO. The relative energy dependence of both polymorphs of the lattice parameters is depicted in Figure 6.6. The calculated energy difference between α -PrZnPO and β -PrZnPO is $10.7 \text{ kJ}\cdot\text{mol}^{-1}$, β -PrZnPO being the more stable polymorph. The calculated energy minimum of α -PrZnPO was found for the lattice parameters $a = 397.3 \text{ pm}$ and $c = 887.3 \text{ pm}$ ($V = 0.1401 \text{ nm}^3$) – lattice parameters obtained by single crystal data were $a = 399.3(2) \text{ pm}$, $c = 877.2(7) \text{ pm}$ and $V = 0.1399 \text{ nm}^3$. While the calculated cell volume differs only by 0.1 % from the experimental crystal structure for the α -polymorph, the c/a ratio difference is slightly more pronounced (1.7 %) but in the normal range for structure optimisations of this kind. The calculated energy minimum of β -PrZnPO was found for the lattice parame-

ters $a = 397.3$ pm and $c = 3111$ pm ($V = 0.4253$ nm³) – crystallographic values were $a = 399.0(2)$ pm, $c = 3108(1)$ pm and $V = 0.4285$ nm³.^[131] The relative differences in the cell volume and c/a ratio between the calculated model and experimental crystal structure are thus only 0.7 % and 0.5 %, respectively.

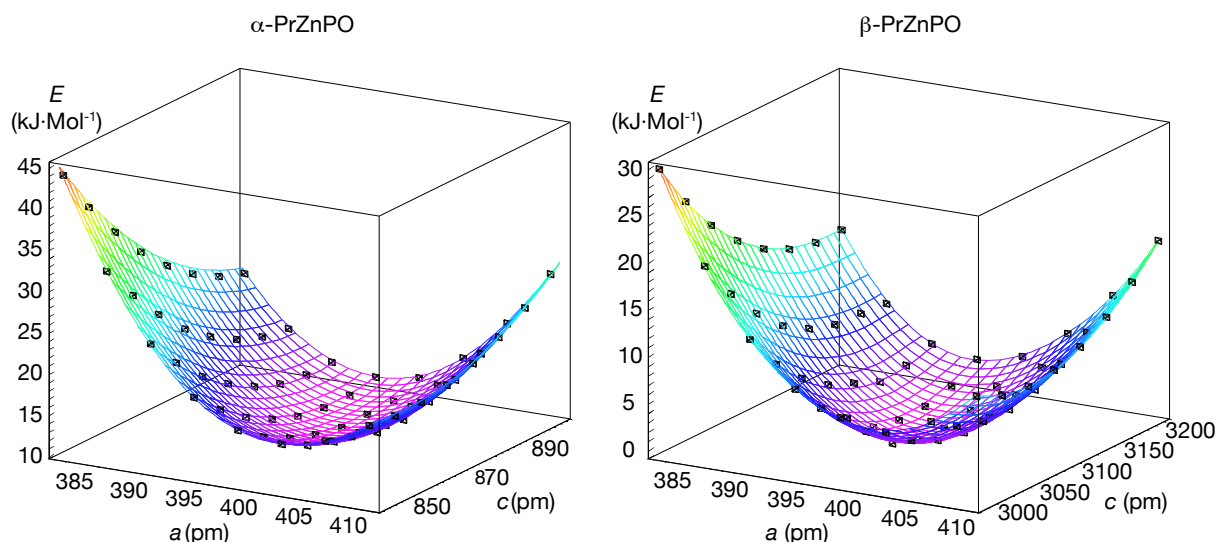


Figure 6.6: Energy dependence of α -PrZnPO (left) and β -PrZnPO (right) from the lattice parameters a and c . Black diamonds: DFT calculations.

In summary, DFT band structure calculations of *REZnPO* show a similarity between the valence bands of the tetragonal (α) and rhombohedral (β) polymorph, as they possess mainly P-3p character. In both cases, the conduction bands have mainly Zn-4s character, but a significant contribution of *RE*-5d occurs in rhombohedral *REZnPO*, which is responsible for a smaller optical band gap in these compounds. Variations of the energy gaps of tetragonal *REZnPO* can be explained by hybridisation of Zn-4s + *RE*-5d + *RE*-4f orbitals for the conduction band. DFT volume optimisations of α - and β -PrZnPO show β -PrZnPO to be more stable by 10.7 kJ·mol⁻¹.

7. Ba_{1-x}K_xFe₂As₂

At the time of the discovery of the 4 K superconductor LaFePO in 2006,^[98] *Kamihara* had proposed that the lanthanide oxide layers of this compound were a necessary prerequisite for superconductivity. Moreover, these layers should provide the charge carriers necessary for superconductivity in a similar manner as in the cuprates. However, soon after it could be shown by band structure calculations of LaFePO^[99] that the energy of both the lanthanum as well as the oxygen atoms are too far from the Fermi level and that the features around the Fermi level are therefore dominated by the iron and pnictogen atoms. This is also expected from a chemical point of view (see Chapter 1.1.1). Furthermore, in contrast to the undoped cuprates, LaFePO is a metal in its normal state.

This led to the idea, that another well-known structure type provides very similar structural and electronic conditions. The ternary iron pnictides BaFe₂P₂^[132] and BaFe₂As₂^[133] with the tetragonal ThCr₂Si₂-type (actually BaZn₂P₂-type^{[134], xv)} structures^[135] (space group *I4/mmm*) contain practically identical layers of edge-sharing FePn_{4/4} tetrahedra, but they are separated by Ba²⁺ ions instead of (OLa)⁺ sheets. Figure 7.1 shows both structures in comparison. However, in the large family of ThCr₂Si₂-type compounds, superconductivity had been known to occur scarcely and only at temperatures below 5 K.^[136] Examples are LaIr₂Ge₂, LaRu₂P₂, YIr_{2-x}Si_{2+x}, and BaNi₂P₂.^[137] BaFe₂P₂ in particular does not become superconducting (see also Chapter 4.1.1 in [86]). The whole image has changed with the discovery of superconductivity in F-doped LaFeAsO at 26 K.^[14] In contrast to LaFePO, which is superconducting even as a stoichiometric compound, undoped LaFeAsO is no superconductor but exhibits anomalies in the resistivity and magnetic susceptibility, which are linked to a spin-density wave anomaly (Chapter 1.1.2). By looking at the magnetic susceptibility data of BaFe₂As₂,^[138] which had been recorded back in 1983, remarkably similar susceptibility data to undoped LaFeAsO can be found.^[14] Both compounds show

^{xv} Despite ThCr₂Si₂ and BaZn₂P₂ being isopointal (see glossary), according to the IUCr nomenclature they are not strictly isotypic because of the presence of Si–Si bonds in ThCr₂Si₂ leading to different chemical and physical characteristics of the corresponding Si atoms.

an anomaly in their susceptibility at 140 K and 150 K, respectively. BaFe_2As_2 was therefore synthesised by Rotter^[139] and investigated in further detail.

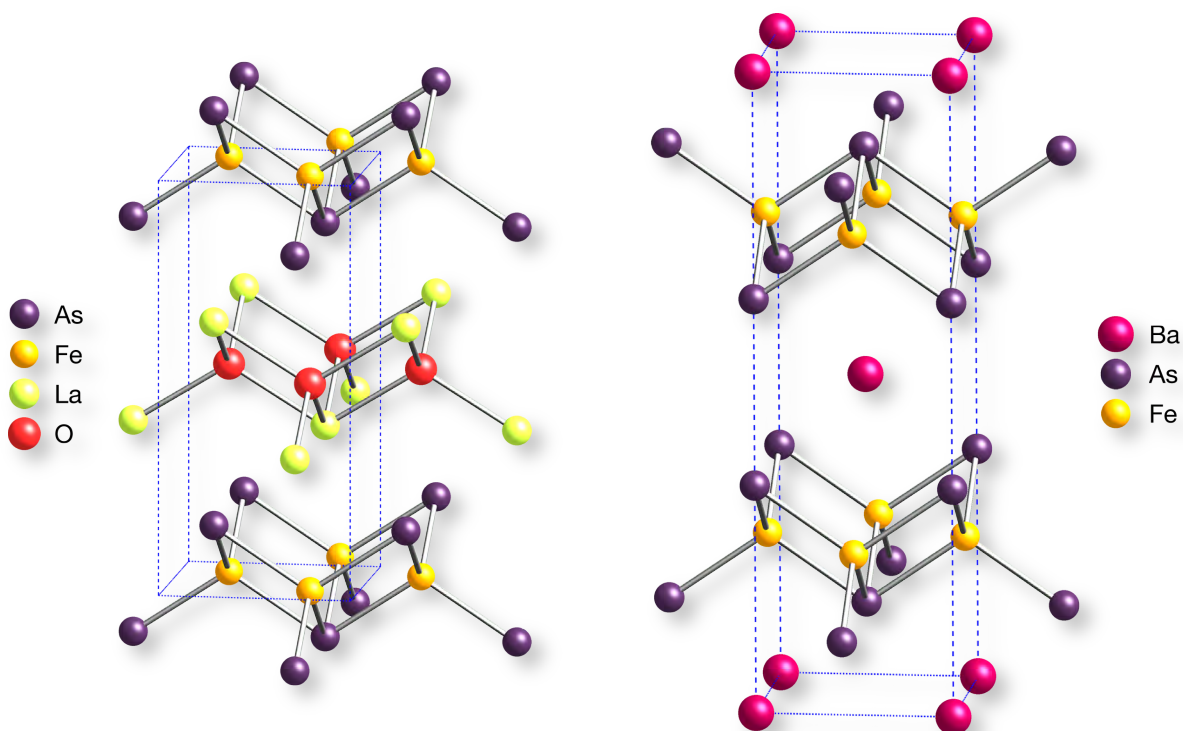


Figure 7.1: Crystal structures of LaFeAsO and BaFe_2As_2 in comparison.

7.1 Undoped BaFe_2As_2

7.1.1 Crystal structure

Figure 7.2 shows the powder pattern of BaFe_2As_2 , which could be completely fitted with a single phase. Subsequently, X-ray powder patterns of BaFe_2As_2 between 297 and 20 K were recorded. Several reflections broaden below 140 K and clearly split with further decreasing temperature. The patterns below 136 K were indexed with an orthorhombic, F -centred unit cell ($a_{\text{ortho}} = \sqrt{2} \cdot a_{\text{tetra}} - \delta$; $b_{\text{ortho}} = \sqrt{2} \cdot b_{\text{tetra}} + \delta$; $c_{\text{ortho}} \approx c_{\text{tetra}}$; $\delta \approx 5$ pm). The low-temperature data could be refined in the space group $Fmmm$. Figure 7.3 shows the Rietveld fit of the data at 20 K.

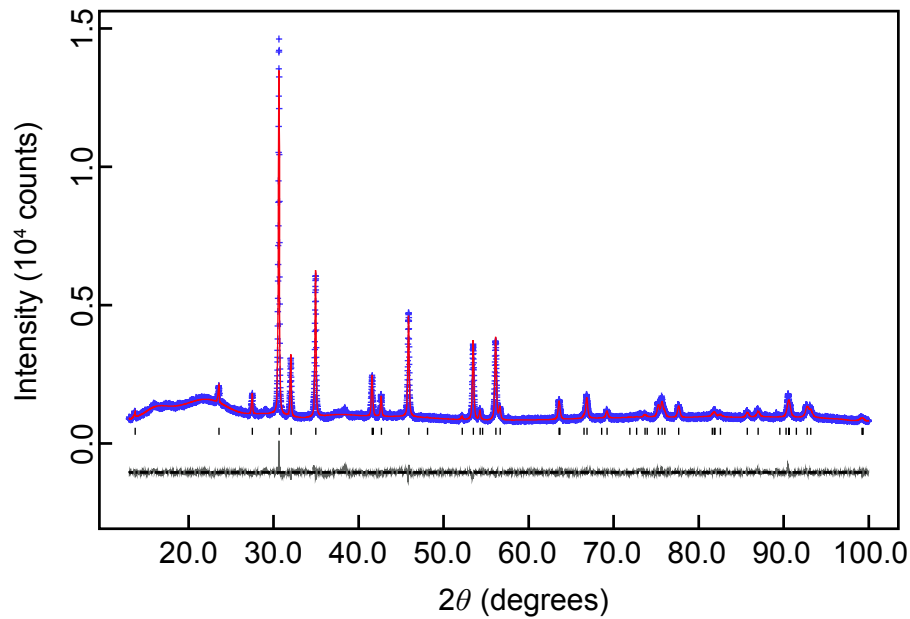


Figure 7.2: Rietveld fit of BaFe_2As_2 at 297 K (space group $I4/mmm$).

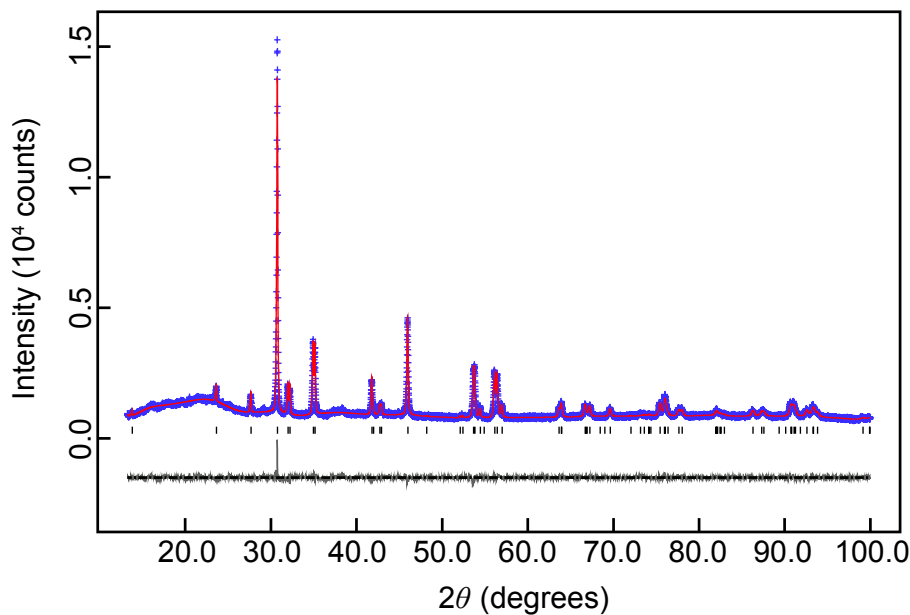


Figure 7.3: Rietveld fit of BaFe_2As_2 at 20 K (space group $Fmmm$).

The continuous transition of the (1 1 0) and (1 1 2) reflections of the diffraction pattern between 150 and 40 K as well as the variation of the lattice parameters is depicted in Figure 7.4. The space group $Fmmm$ is a maximal subgroup of $I4/mmm$, thus a second-order phase transition would be in agreement with this data (refer also to Chapter 8.2). In terms of group theory, the transition $I4/mmm \rightarrow Fmmm$ is *transla-*

tionengleich with index two. The symmetry reduction tree is depicted in Figure 7.5.

Crystallographic data are summarised in Table 7.1

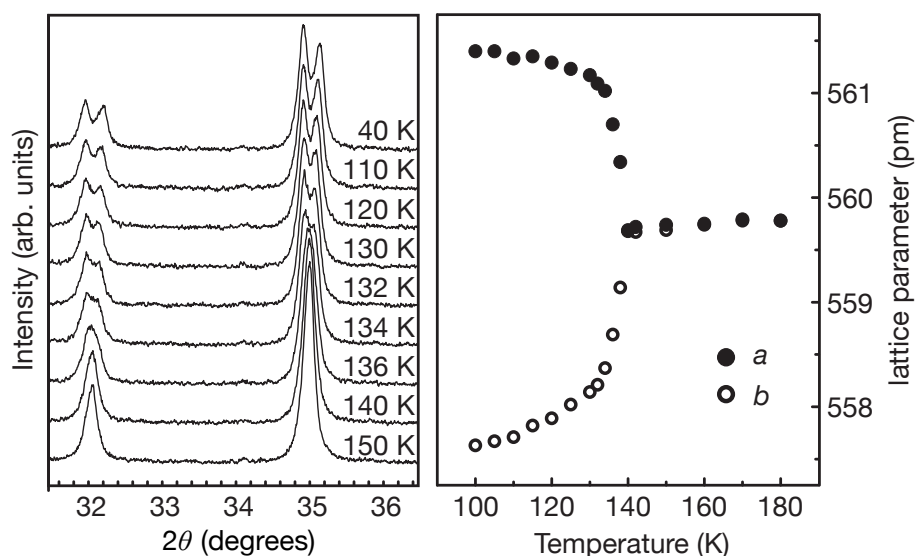
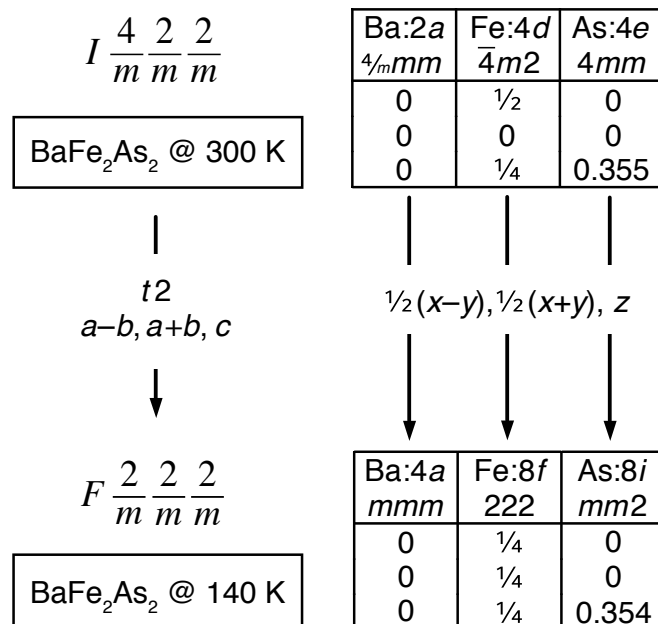


Figure 7.4: Splitting of the (110) and (112) reflections and variation of the lattice parameters with temperature. Values for the tetragonal phase above 140 K are multiplied by $\sqrt{2}$ for comparability.

The main effect of the phase transition appears in the Fe–Fe distances, where four equal bonds of 280.2 pm length split into two pairs of 280.8 and 278.7 pm length. This supports the idea that the Fe–Fe interactions are strongly involved in the SDW anomaly and play a certain role for the properties of BaFe₂As₂.

Temperature	297 K	20 K
Diffractometer	HUBER G670 (Cu-K α_1)	HUBER G670 (Cu-K α_1)
Rietveld package	GSAS	GSAS
Space group	<i>I4/mmm</i>	<i>Fmmm</i>
Lattice parameters	$a = 396.25(1)$ pm $c = 1301.68(3)$ pm	$a = 561.46(1)$ pm $b = 557.42(1)$ pm $c = 1294.53(3)$ pm
Cell volume	$V = 0.20438(1)$ nm ³	$V = 0.40514(2)$ nm ³
Z	2	4
Data points	8700	8675
Reflections	50	74
Atomic variables	4	4
Profile parameters	4	4

d range	0.979 – 6.508	0.981 – 6.473
R_P, R_{WP}, R_{F²}, χ²	0.0273, 0.0358, 0.0522, 1.431	0.0283, 0.0365, 0.0576, 1.392
Atomic parameters		
Ba	2a (0, 0, 0) <i>U</i> _{iso} = 95(5) pm ²	4a (0, 0, 0) <i>U</i> _{iso} = 69(5) pm ²
Fe	4d (½, 0, ¼) <i>U</i> _{iso} = 57(6) pm ²	8f (¼, ¼, ¼) <i>U</i> _{iso} = 64(4) pm ²
As	4e (0, 0, z) z = 0.3545(1) <i>U</i> _{iso} = 99(5) pm ²	8i (0, 0, z) z = 0.3538(1) <i>U</i> _{iso} = 65(5) pm ²
Bond lengths		
Ba–As	338.2(1) × 8	336.9(1) × 4 338.5(1) × 4
Fe–As	240.3(1) × 4	239.2(1) × 4
Fe–Fe	280.2(1) × 4	280.7(1) × 2 278.7(1) × 2
Bond angles		
As–Fe–As	111.1(1) × 2 108.7(1) × 4	111.6(1) × 2 108.7(1) × 2 108.1(1) × 2

Table 7.1: Crystallographic data of BaFe₂As₂ at 297 K and 20 K.Figure 7.5: Bärnighausen tree of the structural phase transition in BaFe₂As₂.

These results clearly prove a structural distortion in BaFe₂As₂. Apart from this structural analogy to LaFeAsO, also the electron count of the FeAs layers in BaFe₂As₂ and

LaFeAsO are identical because in both cases, one electron is transferred to FeAs according to (Ba_{0.5})⁺(FeAs)⁻ and (LaO)⁺(FeAs)⁻, respectively. Therefore, the nature of the structural transition is analogous to that in LaFeAsO, where a transition from the tetragonal space group *P4/nmm* to the orthorhombic space group *Cmme* occurs.^[114] Both transitions are connected with SDW instabilities within the iron layers.

7.1.2 Magnetic ordering

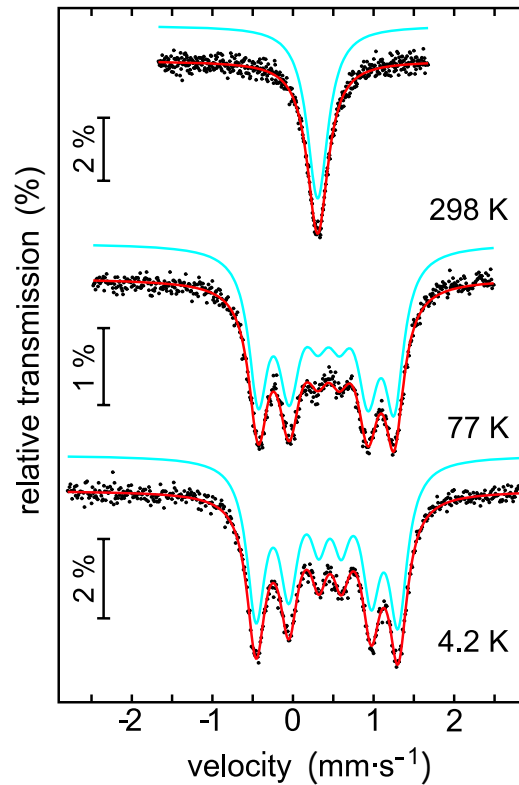
Undoped LaFeAsO does not only undergo a structural phase transition around 150 K^[114] but also shows anomalies in the specific heat, electrical resistance, and magnetic susceptibility at this temperature. Antiferromagnetic ordering of the magnetic moments was found below $T_N = 134$ K by neutron scattering.^[31] Electron doping with fluoride or oxygen deficiency, as well as hole doping with strontium, suppress both the phase transition and the magnetic ordering. The tetragonal phase becomes superconducting at $T_C = 25 - 41$ K in these compounds.^[14, 140]

⁵⁷Fe Mössbauer spectra of BaFe₂As₂ at 298, 77, and 4.2 K were recorded using the setup described in Chapter 2.8. They are shown in Figure 7.6 together with the transmission integral fits. The corresponding fitting parameters are listed in Table 7.2.

At room temperature, a single signal at an isomer shift of $\delta = 0.31$ mm·s⁻¹ was observed. Although the iron atoms have non-cubic site symmetry, no quadrupole splitting had to be considered for the fits. The observed isomer shift is slightly smaller than in SmFeAsO_{0.85}^[141] and LaFeAsO.^[102]

At 77 K, i.e. well below the transition temperature, a significant hyperfine field splitting was observed with a hyperfine field value of 5.23(1) T, which is even slightly larger than the hyperfine field observed in LaFeAsO (4.86 T).^[102b] A very small quadrupole splitting parameter of $-0.03(1)$ mm·s⁻¹ was included in the fits. This parameter accounts for the small tetragonal-to-orthorhombic structural distortion and a similar value has also been observed for the SDW system LaFeAsO below the transition temperature.^[102a]

The quadrupole splitting parameter then slightly increases to $-0.04(1)$ mm·s⁻¹ at 4.2 K (Table 7.2). The hyperfine field at the iron nuclei is 5.47(1) T and the corresponding magnetic moment was estimated to be $0.4 \mu_B$ per iron atom.

Figure 7.6: ⁵⁷Fe Mössbauer spectra of BaFe₂As₂.

Temperature (K)	δ (mm·s ⁻¹)	Γ (mm·s ⁻¹)	ΔE_Q (mm·s ⁻¹)	B_{hf} (T)
295	0.31(1)	0.32(1)		
77	0.43(1)	0.33(2)	-0.03(1)	5.23(1)
4.2	0.44(1)	0.25(1)	-0.04(1)	5.47(1)

Table 7.2: Fitting parameters for ⁵⁷Fe Mössbauer spectroscopy data of LaFePO. δ : isomer shift; Γ : experimental line width; ΔE_Q : quadrupole splitting parameter; B_{hf} : hyperfine field.

7.1.3 Resistivity, susceptibility and specific heat

In order to scrutinise the phase transition at about 150 K, the specific heat of BaFe₂As₂ was measured between 3 and 200 K according to the method described in Chapter 2.9. As can be clearly seen in Figure 7.7 (right), a pronounced anomaly of C_p at 140 K is visible. The characteristic lambda-like shape of the peak points to a second-order transition, as it is typical for magnetic ordering or a displacive structural change. From the inflection point of the anomaly, a transition temperature of

139.9(5) K was extracted. In the low-temperature region, the specific heat is of the form $C_p = \gamma \cdot T + \beta \cdot T^3$, where γ is the electronic and β is the lattice contribution. The Debye temperature Θ_D can be estimated from the equation $\beta = (12\pi^4 \cdot n \cdot k_B) / (5 \cdot \Theta_D^3)$, where k_B is the Boltzmann constant and n is the number of atoms per formula unit (see also Chapter 2.9). From a C_p/T vs. T^2 plot between 3.1 and 14 K (not depicted), $\gamma = 16(2) \text{ mJ} \cdot \text{K}^{-2} \cdot \text{mol}^{-1}$, $\beta = 2.0(5) \text{ mJ} \cdot \text{K}^{-4} \cdot \text{mol}^{-1}$ and $\Theta_D = 134(1) \text{ K}$ were determined.

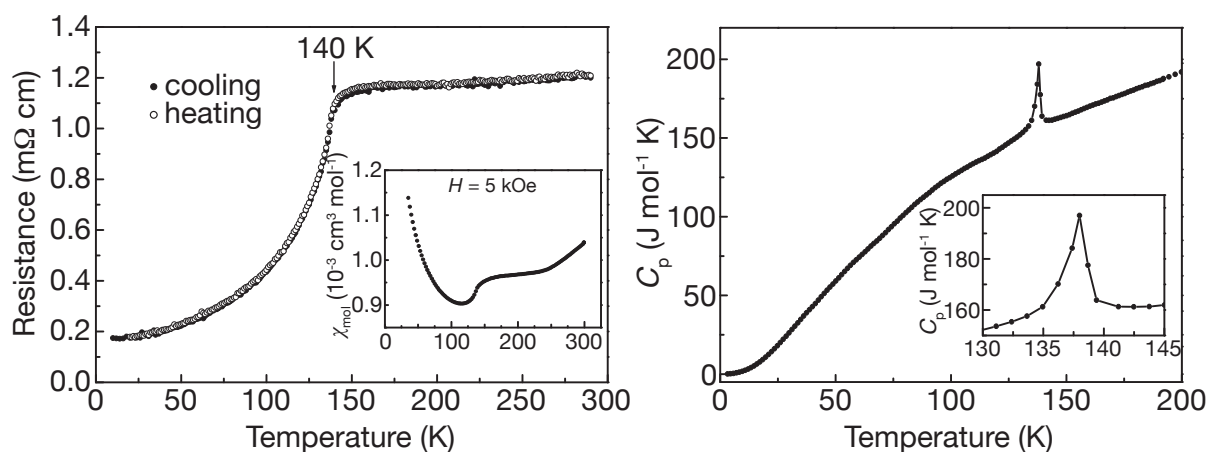


Figure 7.7: Left: DC electrical resistance ($I = 100 \mu\text{A}$). Left inset: Magnetic susceptibility of BaFe_2As_2 measured at 5 kOe. Right: Heat capacity (C_p) vs. temperature of BaFe_2As_2 . The right inset highlights the features between 130 and 145 K.

The temperature dependence of the DC electrical resistance is depicted in Figure 7.7 (left). BaFe_2As_2 is a poor metal with a relatively high resistance of about $1 \text{ m}\Omega \cdot \text{cm}$ at room temperature, which decreases only slightly on cooling. At 140 K, the resistance drops abruptly at first but then decreases monotonically to $0.2 \text{ m}\Omega \cdot \text{cm}$ at 10 K. This behaviour corresponds to that of undoped LaFeAsO , where the resistance is of the same magnitude at room K and drops in a similar fashion.^[118]

Also the general magnetic properties of BaFe_2As_2 and their response to the phase transition have been investigated. BaFe_2As_2 shows weak and only slightly temperature-dependent paramagnetism, which is several orders of magnitude too high for Pauli-paramagnetism. Below 140 K, χ drops at first but it increases again below 100 K. At temperatures above $\sim 250 \text{ K}$, the magnetic susceptibility increases linearly with temperature. A similar magnetic behaviour had already been described by

Pfisterer:^[138] The observed linear increase of susceptibility with temperature meanwhile is commonly attributed to itinerant electron antiferromagnetic spin fluctuations.^[120]

In conclusion, regarding the previously described structural and electronic properties of BaFe₂As₂ and its similarity to undoped LaFeAsO, BaFe₂As₂ is a very promising candidate for superconductivity for both structural and electronic reasons. BaFe₂As₂ exhibits a similar SDW anomaly at 140 K as LaFeAsO does at 150 K.^{xvi} Since a SDW instability is thought to be an important prerequisite for high- T_C superconductivity in the iron arsenides, these results strongly suggest that BaFe₂As₂ can serve as a parent compound for a new, oxygen-free class of iron arsenide superconductors with ThCr₂Si₂-type structure. All these results indicate that superconductivity in BaFe₂As₂ can either be induced by electron or hole doping, which would prove that superconductivity originates only from the iron arsenide layers, regardless of the separating sheets. Even more, superconductivity in doped BaFe₂As₂ would open new avenues to further high- T_C materials in the large family of ThCr₂Si₂-type compounds. Only shortly after these discoveries, superconductivity could indeed be induced in BaFe₂As₂ by hole doping with potassium (see next chapter).

7.2 Optimally doped Ba_{0.6}K_{0.4}Fe₂As₂

The fact that BaFe₂As₂ is an excellent candidate for inducing superconductivity has already been discussed in Chapter 7.1. The crystal structure of BaFe₂As₂ is shown in Figure 7.1 (right). This ternary arsenide contains FeAs layers identical to LaFeAsO, moreover with the same charge, and exhibits a SDW anomaly likewise. In this chapter, superconductivity in BaFe₂As₂ induced by hole doping is subject of discussion. It was achieved by partial substitution of the barium by potassium ions.

As stated above, undoped BaFe₂As₂ is a poor metal that undergoes simultaneous structural and magnetic phase transitions at 140 K, accompanied by strong anoma-

^{xvi} Yet, in contrast to LaFeAsO (Chapter 1.1.2) or SrFeAsF (Chapter 4.3), the structural and magnetic phase transitions occur at the same temperature.

lies in the specific heat, electrical resistance, and magnetic susceptibility. In the course of this phase transition, the space group symmetry changes from tetragonal ($I4/mmm$) to orthorhombic ($Fmmm$). Based on these findings, one can expect superconductivity in doped BaFe₂As₂. However, first attempts to realise electron doping by lanthanum substitution were unsuccessful – the required doping level could not be achieved. Then, hole doping by substituting the Ba²⁺ cations for K⁺, which has a similar ionic radius, was tried. In order to achieve doping levels of 0.15 – 0.2 electrons per FeAs unit, 30 % to 40 % of the barium ions had to be exchanged for potassium ions. This also seemed possible, because isostructural KFe₂As₂ had been known to exist.^[142] Ba_{1-x}K_xFe₂As₂ ($x = 0.3$ and 0.4) were successfully prepared by heating stoichiometric mixtures of the elements in alumina crucibles sealed in silica tubes under an atmosphere of purified argon.^[133, 142] Synthesis details can be found elsewhere.^[139, 143]

7.2.1 Crystal structure

Rietveld refinements of the powder data were performed with the GSAS package. While the pattern of BaFe₂As₂ could be completely fitted with a single phase, in the samples of KFe₂As₂ and Ba_{1-x}K_xFe₂As₂, FeAs (Westerveldite)^[144] was detected as impurity phase. It was included in the refinement and quantified to 6(1) at%. The substitution of 40 % barium for potassium could be clearly proved by the refinement of the site occupation parameters in the Rietveld fit of Ba_{0.6}K_{0.4}Fe₂As₂ (Figure 7.8). A summary of the crystallographic data is compiled in Table 7.3.

As mentioned above, a crucial aspect of the LaFeAsO superconductors is the suppression of the SDW anomaly by doping. Therefore, also the X-ray powder pattern of Ba_{0.6}K_{0.4}Fe₂As₂ at 20 K was measured. No broadening or splitting of the diffraction peaks as previously found in BaFe₂As₂ below 140 K could be detected. The inset of Figure 7.8 shows the temperature dependence of the (1 1 0) reflection of BaFe₂As₂ and Ba_{0.6}K_{0.4}Fe₂As₂ in comparison. The diffractogram of Ba_{0.6}K_{0.4}Fe₂As₂ measured at 20 K was successfully refined by using starting parameters from the undistorted tetragonal structure (space group $I4/mmm$). Table 7.3 shows almost identical crystallographic data of Ba_{0.6}K_{0.4}Fe₂As₂ at 297 and 20 K, respectively. Thus it is evident, that potassium doping has suppressed the structural transition in BaFe₂As₂.

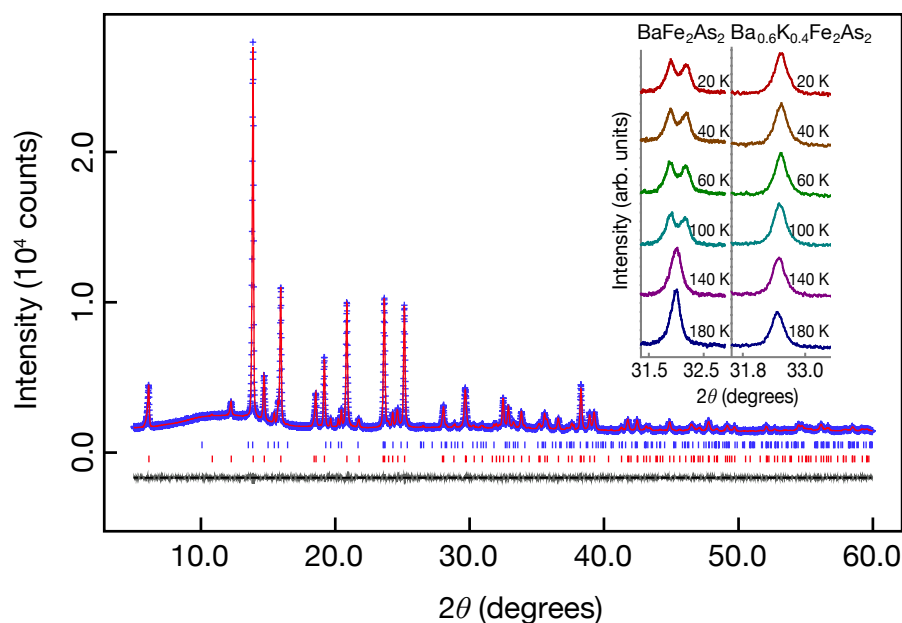


Figure 7.8: Rietveld fit of Ba_{0.6}K_{0.4}Fe₂As₂ at 297 K (space group *I4/mmm*). Inset: (110) reflections of BaFe₂As₂ and Ba_{0.6}K_{0.4}Fe₂As₂ on cooling.

Temperature	297 K	20 K
Diffractometer	STOE STADI P (Mo-K α_1)	HUBER G670 (Cu-K α_1)
Rietveld package	GSAS	GSAS
Space group	<i>I4/mmm</i>	<i>I4/mmm</i>
Lattice parameters	$a = 391.70(1)$ pm $c = 1329.68(1)$ pm	$a = 390.90(1)$ pm $c = 1321.22(4)$ pm
Cell volume	$V = 0.20401(1)$ nm ³	$V = 0.20189(1)$ nm ³
Z	2	2
Data points	5499	8790
Reflections	405	127
Atomic variables	5	5
Profile parameters	10	10
d range	0.639 – 6.648	0.971 – 6.606
R_p, R_w, R_F^2, χ^2	0.0202, 0.0258, 0.026, 1.347	0.0214, 0.0283, 0.093, 1.816

Atomic parameters			
K, Ba	2a (0, 0, 0) $U_{\text{iso}} = 130(8) \text{ pm}^2$	2a (0, 0, 0) $U_{\text{iso}} = 89(8) \text{ pm}^2$	
Fe	4d (1/2, 0, 1/4) $U_{\text{iso}} = 47(4) \text{ pm}^2$	4d (1/2, 0, 1/4) $U_{\text{iso}} = 84(7) \text{ pm}^2$	
As	4e (0, 0, z) $z = 0.3538(1) \quad U_{\text{iso}} = 70(3) \text{ pm}^2$	4e (0, 0, z) $z = 0.3538(1) \quad U_{\text{iso}} = 76(7) \text{ pm}^2$	
K:Ba ratio	42(1) : 58(1)	38(1) : 62(1)	
Bond lengths			
Ba-As	338.4(1) × 8	337.2(1) × 8	
Fe-As	239.6(1) × 4	238.8(1) × 4	
Fe-Fe	277.0(1) × 4	276.4(1) × 4	
Bond angles			
As-Fe-As	109.7(1) × 2 109.4(1) × 4	109.9(1) × 2 109.3(1) × 4	

Table 7.3: Crystallographic data of Ba_{0.6}K_{0.4}Fe₂As₂ at 297 K and 20 K.

7.2.2 Resistivity and magnetism

Also the electrical resistance of Ba_{1-x}K_xFe₂As₂ ($x = 0, 0.4$ and 1.0) has been measured according to the method described in Chapter 2.7.1. As depicted in Figure 7.9, BaFe₂As₂ has the highest resistance at room temperature and shows a drop at 140 K, which is linked to the SDW anomaly (see also Chapter 7.1). In contrast to this, the resistance of KFe₂As₂ is considerably smaller and decreases smoothly with temperature, as it is characteristic for a normal metal. The resistance of K-doped Ba_{0.6}K_{0.4}Fe₂As₂ is similar to that of KFe₂As₂ and does not show any sign of an anomaly at any temperature in agreement with the structural data. However, the resistance drops abruptly to zero at ~ 38 K, which clearly indicates superconductivity. Figure 7.10 (left) shows details of this transition. By using the 90 : 10 criterion, the midpoint of the resistive transition was determined as 38.1 K and the transition width as 1.5 K. The first deviation from the extrapolated resistance is at ~ 39 K, and zero resistance is achieved at 37.2 K. Consequently, superconductivity in Ba_{0.6}K_{0.4}Fe₂As₂ is completely analogous to that in LaFeAsO materials, but it could be achieved in an oxygen-free compound with ThCr₂Si₂-type structure. The T_C of 38 K

also is the highest critical temperature, which has been observed in any hole-doped iron arsenide superconductor so far [25 K in $(\text{La}_{1-x}\text{Sr}_x)\text{FeAsO}$]^[140b]

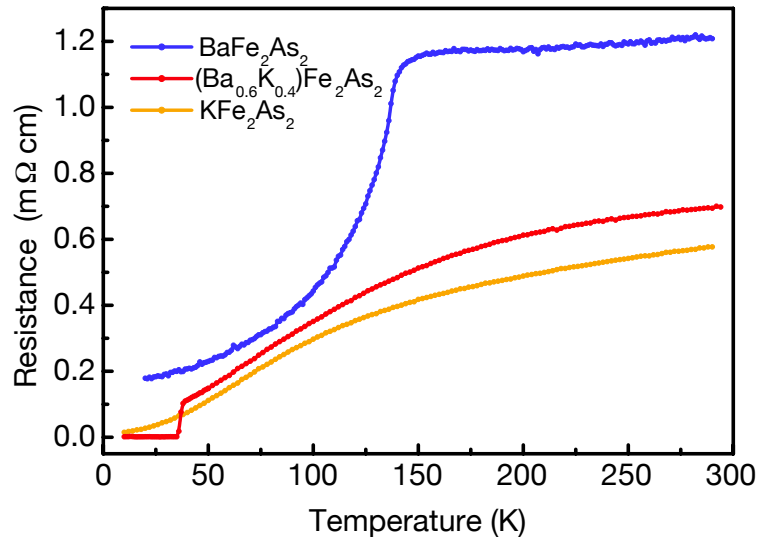


Figure 7.9: Resistivity of $\text{Ba}_{1-x}\text{K}_x\text{Fe}_2\text{As}_2$ ($x = 0, 0.4$ and 1.0).

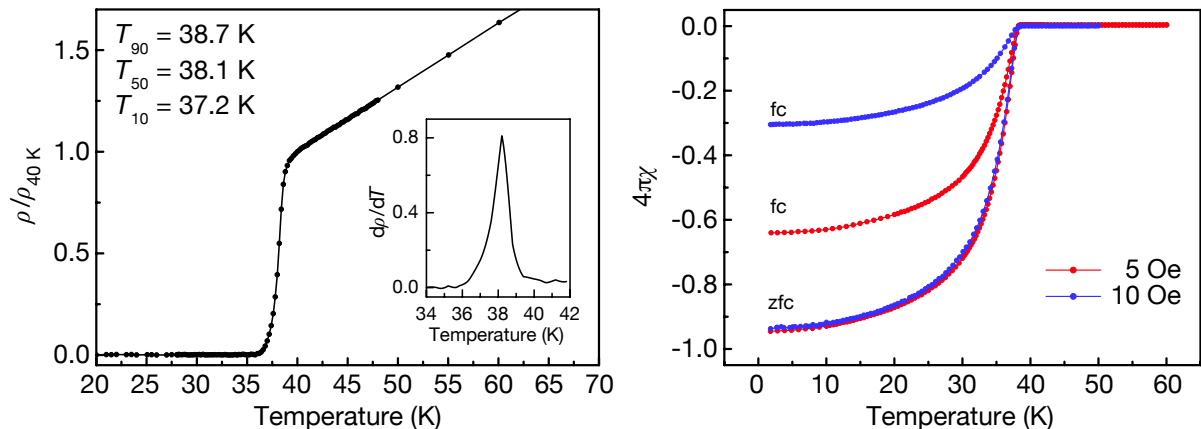


Figure 7.10: Left: Resistivity transition of $\text{Ba}_{0.6}\text{K}_{0.4}\text{Fe}_2\text{As}_2$. Left inset: First derivative of transition. Right: Shielding and Meissner measurements of $\text{Ba}_{0.6}\text{K}_{0.4}\text{Fe}_2\text{As}_2$.

In order to confirm superconductivity, the magnetic susceptibility of finely ground powder of $\text{Ba}_{0.6}\text{K}_{0.4}\text{Fe}_2\text{As}_2$ was measured according to the method described in Chapter 2.6.1. Zero-field-cooled (shielding) and field-cooled (Meissner) cycles measured at 10 and 5 Oe are shown in Figure 7.10 (right). The sample becomes diamagnetic at 38.3 K and shows 10% of the maximum shielding at 37.2 K. The zero-field-cooled branches of the susceptibilities measured at 10 and 5 Oe are almost identical and amount to -0.94 at 1.8 K, which is close to ideal diamagnetism

($4\pi\chi = -1$). The Meissner effect depends on the applied field and the measured susceptibility volume fractions at 1.8 K are -0.64 at 5 Oe and -0.3 at 10 Oe. These values of the shielding and Meissner fractions should be considered as estimates due to uncertainties regarding the density of the compacted powder and demagnetisation effects. However, the susceptibility data unambiguously prove bulk superconductivity of the $\text{Ba}_{0.6}\text{K}_{0.4}\text{Fe}_2\text{As}_2$ sample. Magnetisation isotherms of $\text{Ba}_{0.6}\text{K}_{0.4}\text{Fe}_2\text{As}_2$ at various temperatures were also recorded (Figure 7.11). They show that $\text{Ba}_{0.6}\text{K}_{0.4}\text{Fe}_2\text{As}_2$ is a type-II superconductor with a high H_{c1} ($T = 0$ K) of more than 1.3 kOe and a very high H_{c2} ($T = 0$ K) of far more than the SQUID magnetometer limit of 50 kOe. The temperature dependence of the lower critical fields is depicted in the inset of Figure 7.11.

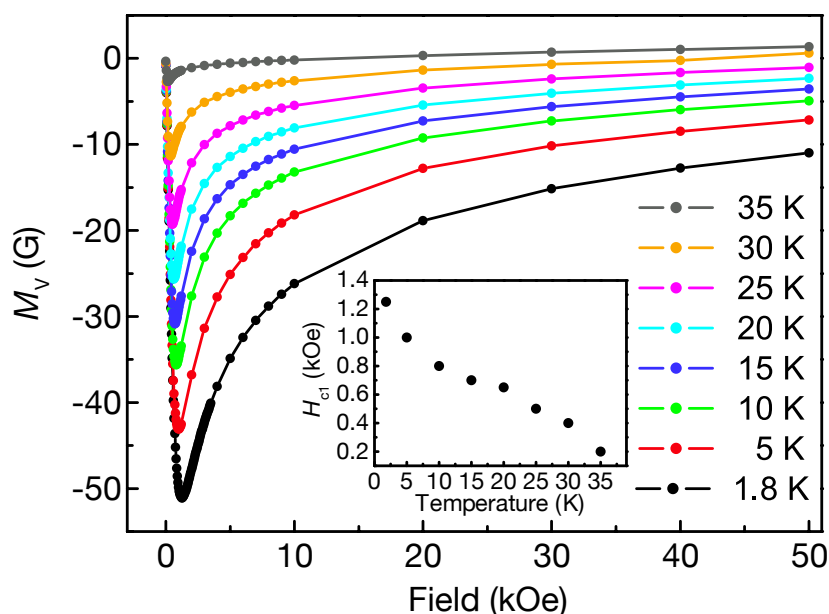


Figure 7.11: Magnetisation isotherms of $\text{Ba}_{0.6}\text{K}_{0.4}\text{Fe}_2\text{As}_2$. Inset: Temperature dependence of H_{c1} .

The estimated upper critical field H_{c2} ($T = 0$ K) of $\text{Ba}_{0.6}\text{K}_{0.4}\text{Fe}_2\text{As}_2$ is as high as 2.3 MOe (i.e. $B = 230$ T)^[145] according to the Werthamer-Helfand-Hohenberg (WHH) relation.^[146] However, care has to be taken with such estimates, as the extrapolation is far too long regarding the field limits of superconducting and even of ultra strong hybrid or pulsed magnets. More recent studies showed that the WHH formula overestimates the curvature of H_{c2} (T) for 122 superconductors and 600 – 750 kOe seem to be more realistic estimates of H_{c2} ($T = 0$ K).^[147] Anyhow, as of 2011, the magnitude

of H_{c2} is still a controversial topic.^[148] However, 122 superconductors surprisingly have isotropic superconducting properties despite their two-dimensional Fermi surfaces and in contrast to the 1111 iron arsenide superconductors, which renders them attractive materials for practical application.^[147b, 147c]

In summary, the first member of a new family of iron arsenide superconductors has been discovered. $\text{Ba}_{0.6}\text{K}_{0.4}\text{Fe}_2\text{As}_2$ with the ThCr_2Si_2 -type structure is a bulk superconductor with $T_C = 38$ K. The structural and electronic properties of the parent compound BaFe_2As_2 are closely related to the properties of LaFeAsO . Superconductivity could be induced by hole doping and a significantly higher T_C in comparison with hole-doped LaFeAsO was found. In contrast to previously stated opinions, these results suggest that hole doping is definitely a possible pathway to induce high- T_C superconductivity, at least in these oxygen-free compounds. Further optimisation may lead to even higher T_C s in ThCr_2Si_2 -type compounds, despite the fact that as of 2011, $\text{Ba}_{0.6}\text{K}_{0.4}\text{Fe}_2\text{As}_2$ remains the superconductor with the highest T_C in the whole, meanwhile huge class^[149] of 122 superconductors. Nevertheless, $\text{Ba}_{0.6}\text{K}_{0.4}\text{Fe}_2\text{As}_2$ already is an attractive material for both research and application. Its advantages of a simple structure, comparatively easy synthesis combined with the possibility to grow very large single crystals render it a highly valuable substance to examine the underlying physics. Therefore one can also expect a pathway towards better understanding of the superconducting mechanism in this and other iron pnictide superconductors. But also certain properties such as its high upper critical field, isotropic superconductivity, cheap starting materials and stability in air leave $\text{Ba}_{0.6}\text{K}_{0.4}\text{Fe}_2\text{As}_2$ one of the best choices for practical application among all iron pnictide superconductors so far. All this can be considered as a major breakthrough in superconductivity research since the discovery of the cuprates.

7.3 The solid solution series $\text{Ba}_{1-x}\text{K}_x\text{Fe}_2\text{As}_2$ ($x = 0 - 1$)

While the doping dependence of the structure and superconductivity has been intensively studied for LaFeAsO-type compounds, such information had not been available for $(\text{Ba}_{1-x}\text{K}_x)\text{Fe}_2\text{As}_2$. In electron-doped $\text{REFeAsO}_{1-\delta}$ ($\text{RE} = \text{La} - \text{Sm}$),^[150] the critical temperatures increase with higher doping levels and with decreasing lattice parameters. Conversely, the hole-doped system $(\text{La}_{1-x}\text{Sr}_x)\text{FeAsO}$ also shows increasing T_c s with higher doping levels and this is accompanied by increasing lattice parameters.^[151] However, all these results are limited by the fact that the exact oxygen or fluorine content in doped LaFeAsO compounds is unknown in most cases and furthermore, doping levels of more than $x \approx 0.2$ have not been achieved yet. Moreover, the changes in the lattice parameters are very small and their significance is often uncertain. In contrast to this, the potassium-doped BaFe_2As_2 system provides a good opportunity for doping studies.

In this chapter, the dependence of the crystal structures on the doping level and the phase diagram of the solid solution $(\text{Ba}_{1-x}\text{K}_x)\text{Fe}_2\text{As}_2$ are briefly discussed. A more detailed discussion is beyond the scope of this dissertation and can be found in the original literature^[152] and in [139].

The crystal structures of $(\text{Ba}_{1-x}\text{K}_x)\text{Fe}_2\text{As}_2$ were determined by Rietveld refinements of X-ray powder patterns at room temperature. Figure 7.12 shows the changes of the structure with potassium doping. The lattice parameters a and c change linearly with the potassium content over the whole range. The unit cell volume is constant within the experimental error, because the significant elongation of the c axis is almost compensated by the decrease of the a axis. Also the Fe–As and Ba(K)–As bond lengths remain unchanged. Both parameters vary by less than 0.4 % and are therefore not shown.

In addition to the lattice parameters, the Fe–Fe bond length and the As–Fe–As bond angle ε change significantly (by 5 – 7 %) on doping. Both decrease linearly with increasing potassium content, which means that the FeAs_4 tetrahedra become more elongated along the c axis, and the iron atoms move closer together. Interestingly, ε becomes the ideal tetrahedral angle of 109.47° at $x \approx 0.4$. Thus, the main effect of

doping on the crystal structure of $(\text{Ba}_{1-x}\text{K}_x)\text{Fe}_2\text{As}_2$ at room temperature are decreasing As–Fe–As bond angles and concurrent shortenings of the Fe–Fe distances.

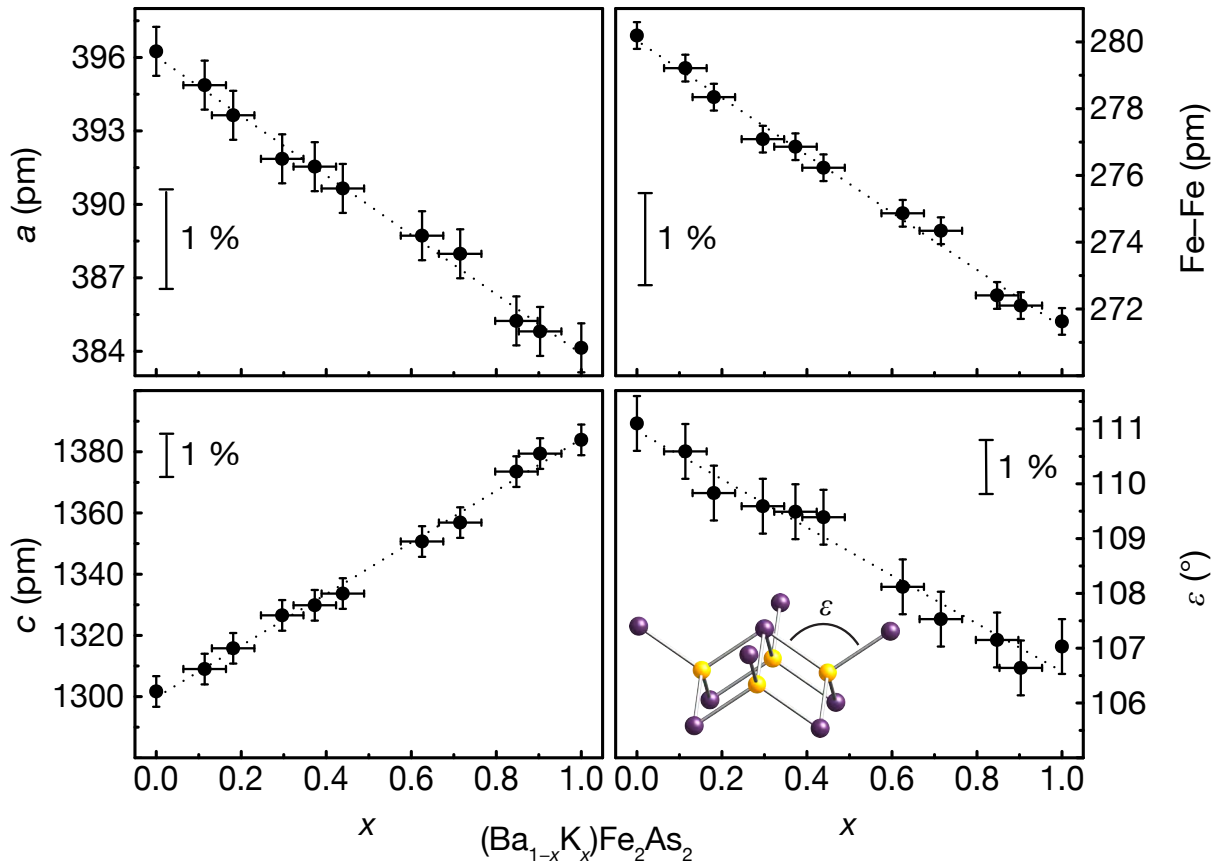


Figure 7.12: Course of the lattice parameters, Fe–Fe bond lengths and As–Fe–As angles (ε) with nominal doping level.

Finally, the superconducting transition temperatures T_C for $x = 0 - 1$ have been determined via resistivity measurements and structural transitions have been determined by temperature-programmed powder diffraction. Superconductivity was detected in all cases except for the undoped parent compound BaFe_2As_2 , but the transition temperatures vary strongly. BaFe_2As_2 is a poor metal with a specific resistivity around $1 \text{ m}\Omega\cdot\text{cm}$ at room temperature and it exhibits the previously discussed structural and magnetic phase transitions at 140 K (Chapter 7.1.3). At the smallest doping level of $x \approx 0.1$, the resistance anomaly is not completely suppressed, but shifted towards a lower temperature. There is an abrupt drop in the resistance at approximately 3 K, which is the onset of superconductivity. The superconducting transition temperatures increase significantly up to 25 K, 36 K and 38 K for $x = 0.2, 0.3$ and

0.4, respectively. Doping levels of $x > 0.5$ lead to a continuous decrease of T_C down to 3.8 K in KFe_2As_2 . The phase diagram in Figure 7.13 shows the superconducting critical temperatures (T_C), as well as the phase transition temperatures (T_o) in $(\text{Ba}_{1-x}\text{K}_x)\text{Fe}_2\text{As}_2$.

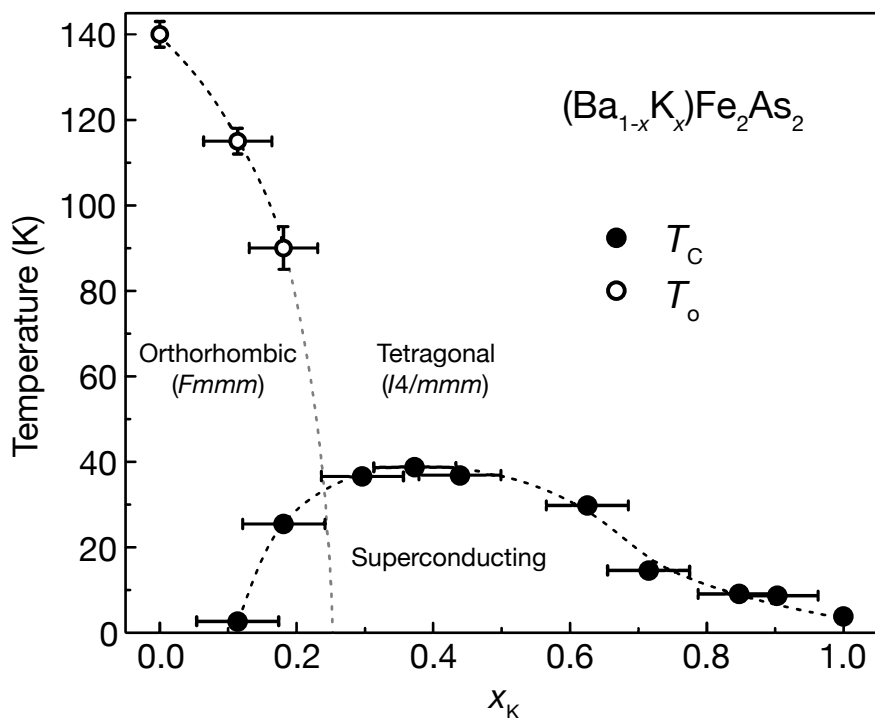


Figure 7.13: Phase diagram of $(\text{Ba}_{1-x}\text{K}_x)\text{Fe}_2\text{As}_2$ with critical and phase transition temperatures. Dashed lines are guides for the eye.

Superconductivity is found for all compositions except the parent compound BaFe_2As_2 and with $T_C > 30$ K in the range $x = 0.3 - 0.6$ with a maximum of 38 K close to $x = 0.4$. The orthorhombically distorted crystal structure exists up to $x = 0.2$, where T_C is approximately 25 K. According to these results, superconductivity coexists with the distorted orthorhombic structure and potentially with the antiferromagnetic state. A more detailed study of this underdoped region of the phase diagram was therefore carried out. The results can be found in the next chapter.

7.4 Underdoped $\text{Ba}_{1-x}\text{K}_x\text{Fe}_2\text{As}_2$ ($x = 0.1 - 0.3$)

In both the LaFeAsO (1111) and the BaFe_2As_2 (122) family, superconductivity evolves from poor metallic parent compounds with quasi two-dimensional tetrago-

nal crystal structures, which are subject to orthorhombic lattice distortions below certain transition temperatures (T_o). Static long-range antiferromagnetic ordering emerges with Néel temperatures (T_N) well below T_o in LaFeAsO ,^[31] but very close to T_o in BaFe_2As_2 (Chapter 7.1). The structural and magnetic transitions of the parent compounds are strongly affected by doping of the FeAs layers either with electrons or holes, and superconductivity appears at certain doping levels. For the underdoped phases in the transition zone, it had been reported that superconductivity and antiferromagnetic ordering are either separated or co-existing (see also Chapter 7.3). Also, the overlap of the orthorhombic distortion with the superconducting and antiferromagnetic areas in the phase diagrams had been disputed.

The first phase diagram of $\text{LaFeAsO}_{1-x}\text{F}_x$, constructed from μSR data, showed a sharp dividing line between the superconducting and the orthorhombic antiferromagnetic phases at $x = 0.045$.^[153] But neutron diffraction experiments showed that although the magnetic ordering vanishes around $x \approx 0.04$, the orthorhombic lattice still exists at least up to $x = 0.05$, where superconductivity has already emerged.^[154] This also is in line with other studies.^[155] Thus, in the case of the 1111-family, static antiferromagnetic ordering is completely suppressed before superconductivity emerges, but the orthorhombic lattice co-exists with superconductivity and the temperature difference between T_o and T_N increases with the doping level. This behaviour of the 1111 superconductors is strongly reminiscent of the monolayer high- T_C cuprates.^[156]

In the 122-family, co-existence of the orthorhombic structure with superconductivity was first published for $(\text{Ba}_{1-x}\text{K}_x)\text{Fe}_2\text{As}_2$ up to $x \approx 0.2$ ($T_C \approx 26$ K), which was found via X-ray powder diffraction and resistivity measurements (Chapter 7.3). Neutron diffraction experiments later also showed orthorhombic symmetry and long-range antiferromagnetic ordering co-existing up to $x = 0.3$ ($T_C < 15$ K).^[157]

However, the doping levels 'x' in Chapter 7.3 were determined from X-ray data by Rietveld refinements, whereas in [157], only the nominal compositions are given. Since diffraction methods provide the mean structural information on a rather long spatial scale, short-range phase inhomogeneities are averaged. Thus one may think that the observed co-existence of superconductivity with antiferromagnetic ordering

in $(\text{Ba}_{1-x}\text{K}_x)\text{Fe}_2\text{As}_2$ is due to phase separation in magnetic, non-superconducting and non-magnetic, superconducting mesoscopic domains. Local probes such as μSR and ^{57}Fe -Mössbauer spectroscopy however can provide more accurate information. In this chapter, the structural and magnetic transitions of polycrystalline, underdoped $(\text{Ba}_{1-x}\text{K}_x)\text{Fe}_2\text{As}_2$ ($x \leq 0.4$) are briefly discussed. The samples were characterised by magnetic susceptibility and specific heat measurements. The crystal structures and chemical compositions were determined by Rietveld refinements of X-ray powder patterns. Detailed temperature-dependent ^{57}Fe -Mössbauer spectra were recorded in order to detect the evolution of magnetic ordering on a local spatial scale. A more detailed discussion of the properties of underdoped $(\text{Ba}_{1-x}\text{K}_x)\text{Fe}_2\text{As}_2$ is beyond the scope of this dissertation and can be found elsewhere.^[158]

7.4.1 Crystal structures and phase transitions

Figure 7.14 shows the X-ray powder patterns of $(\text{Ba}_{1-x}\text{K}_x)\text{Fe}_2\text{As}_2$ ($x = 0.1, 0.2, 0.3$) at 300 K with Rietveld fits and difference curves.

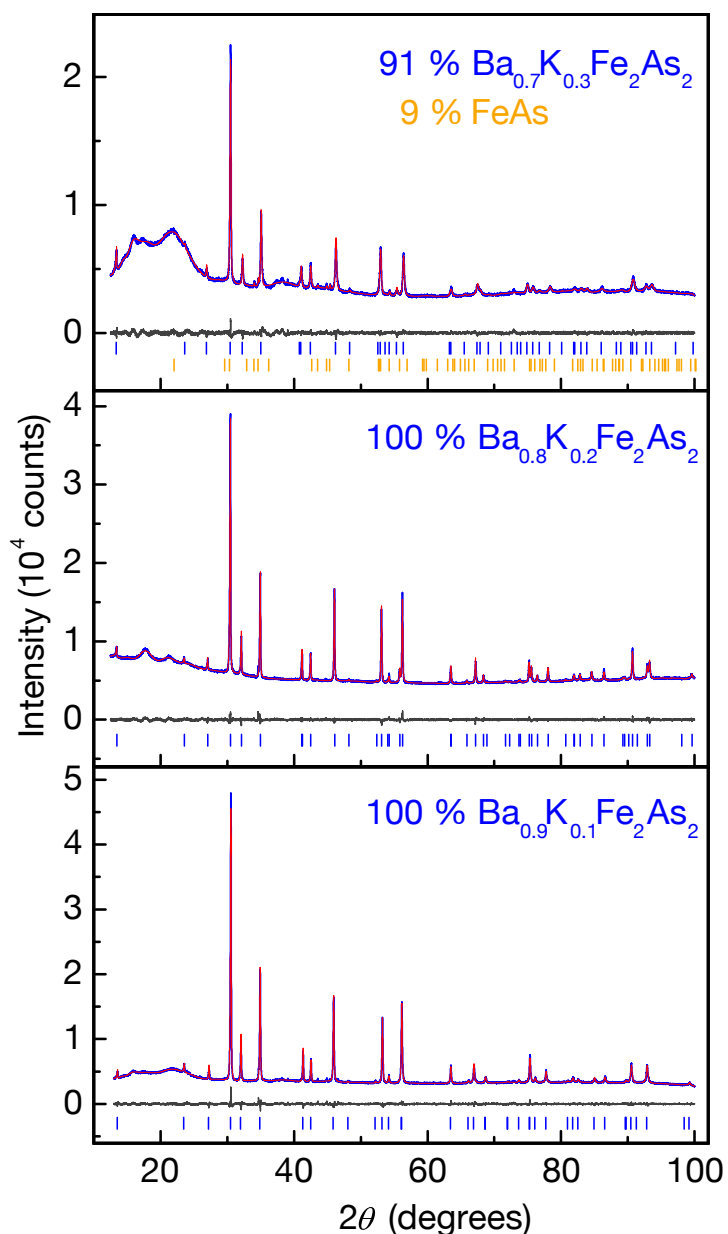


Figure 7.14: X-ray patterns and Rietveld fits of $(\text{Ba}_{1-x}\text{K}_x)\text{Fe}_2\text{As}_2$ ($x = 0.1, 0.2, 0.3$) at 300 K.

Crystallographic data and selected bond lengths and angles at 300 and 10 K, respectively, are compiled in Table 7.4. The temperature dependence of the a and b lattice parameters as determined by Rietveld refinements are shown in Figure 7.15.

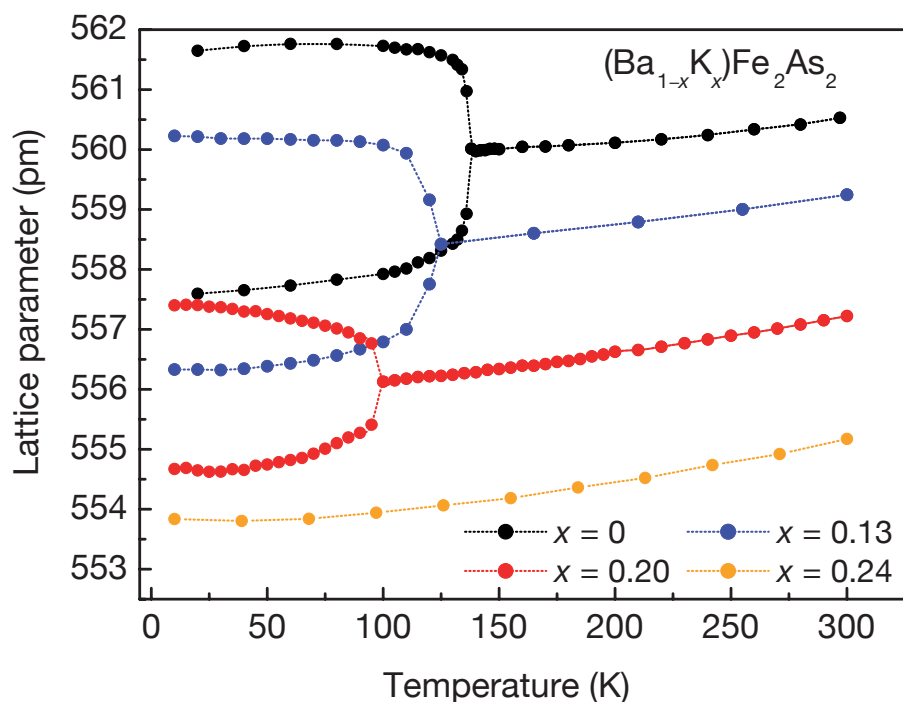


Figure 7.15: a and b lattice parameters of $(\text{Ba}_{1-x}\text{K}_x)\text{Fe}_2\text{As}_2$ ($x = 0, 0.1, 0.2, 0.3$).

In line with the results of Chapter 7.3, the parameter a of the tetragonal phase decreases with the doping level x , while c increases (not depicted). The tetragonal-to-orthorhombic phase transition is strongly affected by the potassium content. The transition temperature T_0 decreases to ~ 100 K at $x = 0.2$ and is no longer visible at $x = 0.3$. Also the magnitude of the distortion, i.e. the difference between a and b at 10 K, decreases from 0.73 % (at $x = 0$) down to 0.70 % (at $x = 0.1$) down to 0.49 % (at $x = 0.2$). Thus with increasing potassium doping levels, the structural transition of BaFe_2As_2 is shifted towards lower temperatures and also appears less pronounced. It is completely suppressed at $x = 0.3$ (Figure 7.15, amber curve).

	$x = 0.1$		$x = 0.2$		$x = 0.3$
Temperature	300 K	10 K	300 K	10 K	300 K
Diffractom.	G670	G670	G670	G670	G670
Software	TOPAS	TOPAS	TOPAS	TOPAS	TOPAS
Space group	$I4/mmm$	$Fmmm$	$I4/mmm$	$Fmmm$	$I4/mmm$
Lattice parameters (pm)	$a = 395.37(1)$ $c = 1310.60(1)$	$a = 560.07(1)$ $b = 556.20(1)$ $c = 1301.35(1)$	$a = 393.95(1)$ $c = 1318.90(3)$	$a = 557.34(1)$ $b = 554.64(1)$ $c = 1309.26(3)$	$a = 392.57(1)$ $c = 1327.02(3)$
V (nm³)	0.20487(1)	0.40538(1)	0.20469(1)	0.40472(1)	0.20451(1)
Z	2	4	2	4	2

Data points	17401	17401	17401	17401	17501
Reflections	46	70	46	70	46
Total var.	71	72	98	99	83
d range	1.012 – 6.553	1.006 – 6.507	1.009 – 6.595	1.005 – 6.546	1.007 – 6.635
R_p, R_{wp}	0.015, 0.0211,	0.015, 0.0210,	0.016, 0.0217,	0.017, 0.0229,	0.015, 0.0192,
R_{Bragg}, χ^2	0.0121, 1.319	0.0132, 1.308	0.0123, 1.190	0.0117, 1.222	0.0076, 1.212
Atomic prm.					
Ba	2a (0, 0, 0) <i>U</i> _{iso} = 119(4)	4a (0, 0, 0) <i>U</i> _{iso} = 45(4)	2a (0, 0, 0) <i>U</i> _{iso} = 173(7)	4a (0, 0, 0) <i>U</i> _{iso} = 117(8)	2a (0, 0, 0) <i>U</i> _{iso} = 181(6)
Fe	4d (½, 0, ¼) <i>U</i> _{iso} = 114(4)	8f (¼, ¼, ¼) <i>U</i> _{iso} = 43(4)	4d (½, 0, ¼) <i>U</i> _{iso} = 156(7)	8f (¼, ¼, ¼) <i>U</i> _{iso} = 102(8)	4d (½, 0, ¼) <i>U</i> _{iso} = 58(5)
As	4e (0, 0, z) z = 0.3547(1) <i>U</i> _{iso} = 147(4)	8i (0, 0, z) z = 0.3538(1) <i>U</i> _{iso} = 57(4)	4e (0, 0, z) z = 0.3545(1) <i>U</i> _{iso} = 129(7)	8i (0, 0, z) z = 0.3537(1) <i>U</i> _{iso} = 72(8)	4e (0, 0, z) z = 0.3545(1) <i>U</i> _{iso} = 79(5)
K : Ba ratio	14(1) : 86(1)	13(1) : 87(1)	20(1) : 80(1)	20(1) : 80(1)	24(1) : 76(1)
Bond lengths					
Ba–As	338.3(1) × 8	337.0(1) × 4 338.6(1) × 4	338.3(1) × 8	337.0(1) × 4 338.2(1) × 4	337.7(1) × 8
Fe–As	240.6(1) × 4	239.1(1) × 4	240.4(1) × 4	238.9(1) × 4	240.8(1) × 4
Fe–Fe	279.6(1) × 4	278.1(1) × 2 280.0(1) × 2	278.6(1) × 4	277.3(1) × 2 278.7(1) × 2	277.6(1) × 4
Bond angles					
As–Fe–As	110.5(1) × 2 109.0(1) × 4	111.2(1) × 2 108.9(1) × 2 108.3(1) × 2	110.1(1) × 2 109.2(1) × 4	110.7(1) × 2 109.0(1) × 2 108.6(1) × 2	109.2(1) × 2 109.6(1) × 4

Table 7.4: Crystallographic data of Ba_{1-x}K_xFe₂As₂ at 300 K and 10 K.

7.4.2 Superconductivity and antiferromagnetic ordering

The temperature dependence of the DC resistivity of (Ba_{1-x}K_x)Fe₂As₂ ($x = 0.1 - 0.3$) is shown in Figure 7.16. At the lowest doping concentration ($x = 0.1$), the typical SDW anomaly is still visible, but shifted towards lower temperatures and also less pronounced than in undoped BaFe₂As₂ (Chapter 7.1.3). A drop of the resistance below 3 K was observed, which can be associated with a superconducting transition, although zero resistance could not even be reached at 1.8 K. The curvature of the resistivity of (Ba_{0.8}K_{0.2})Fe₂As₂ is still reminiscent of a SDW anomaly, but extended over a larger temperature range between ~ 70 and 120 K. The superconducting transition

at ~ 24 K is rather broad (~ 4 K width), but zero resistance is clearly observed at 23 K. At the higher doping level of $x = 0.3$, the resistivity does not show any indications of the SDW anomaly any more and superconductivity emerges at $T_C = 33$ K.

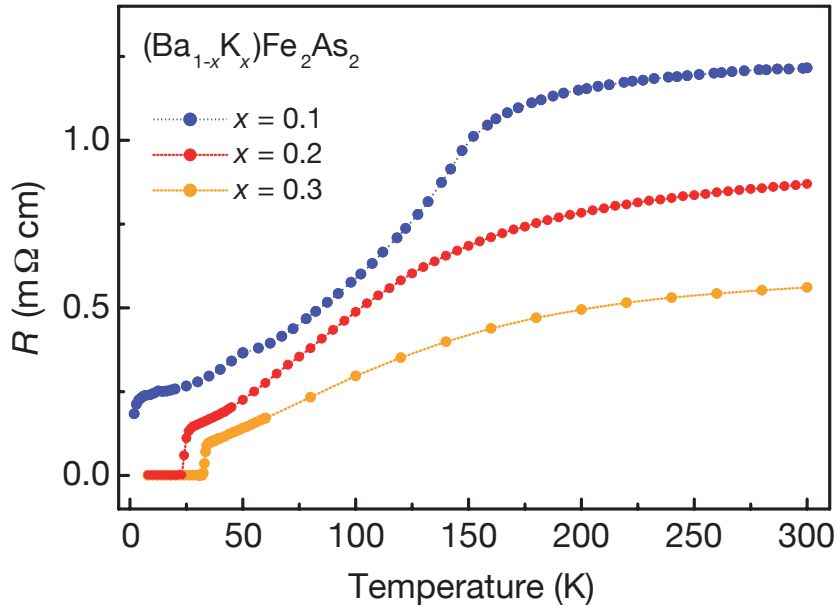


Figure 7.16: Temperature dependence of the DC resistivity of $(\text{Ba}_{1-x}\text{K}_x)\text{Fe}_2\text{As}_2$ ($x = 0.1, 0.2, 0.3$).

As Mössbauer spectroscopy is an excellent local probe for the determination of magnetic ordering, various ^{57}Fe -Mössbauer spectra of the underdoped $(\text{Ba}_{1-x}\text{K}_x)\text{Fe}_2\text{As}_2$ compounds were recorded. Furthermore, ^{57}Fe -Mössbauer spectroscopy can also be a useful analytical tool to detect impurity phases containing iron. In this chapter, only the ^{57}Fe -Mössbauer spectra at 4.2 K of $(\text{Ba}_{1-x}\text{K}_x)\text{Fe}_2\text{As}_2$ ($x = 0.1 - 0.4$) are shown and briefly discussed because of their importance concerning the magnetic ordering of the underdoped compounds (Figure 7.17). For a full discussion and additional temperature-dependent Mössbauer spectra, as well as additional AC susceptibility and specific heat measurements, refer to the original literature^[158] or to [139]. As can be seen in Figure 7.17, only at higher doping levels ($x \geq 0.3$), the antiferromagnetic ordering is completely suppressed. At doping levels of $x \leq 0.2$, the whole sample is antiferromagnetically ordered at 4.2 K, as no additional paramagnetic signal is visible. But the sample with $x = 0.2$ also is a bulk superconductor as determined by AC susceptibility measurements (not depicted) and in agreement with the resistivity measurements shown in Figure 7.16. These results

unambiguously prove co-existence of superconductivity and antiferromagnetic ordering.

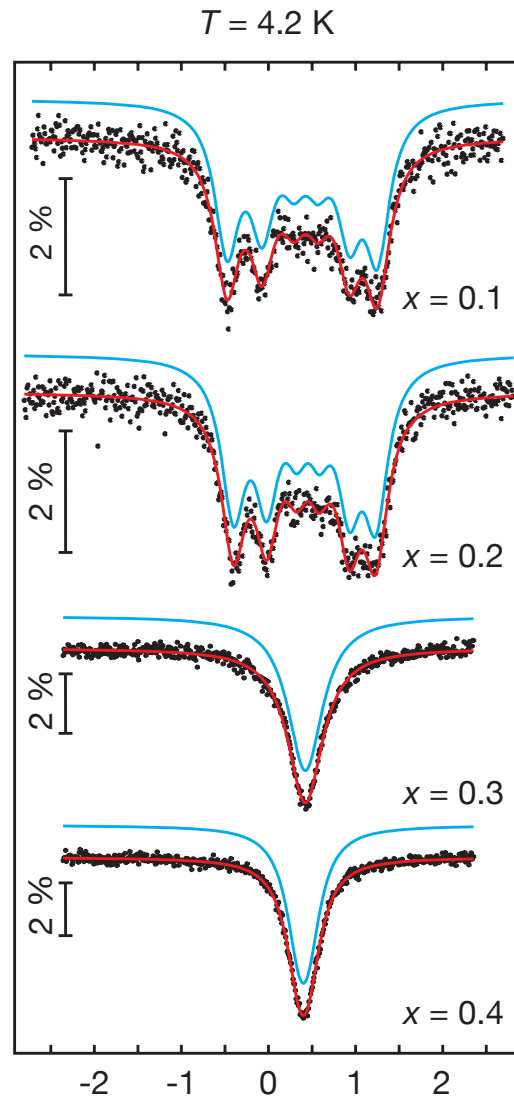


Figure 7.17: Mössbauer spectra of $(\text{Ba}_{1-x}\text{K}_x)\text{Fe}_2\text{As}_2$.

^{57}Fe -Mössbauer spectra of the underdoped compounds with $x = 0.1$ and $x = 0.2$ show temperature-dependent superposition of paramagnetic and antiferromagnetically ordered domains (not depicted), which may reflect chemical inhomogeneities of the Ba/K distributions resulting in different Néel temperatures of the domains. At lower temperatures however, more domains get magnetically ordered until the paramagnetic fractions are completely consumed. Thus there is no distinct phase separation, but rather a continuous distribution of the potassium concentration in the samples.

In summary, the doping dependences of the physical properties of $(\text{Ba}_{1-x}\text{K}_x)\text{Fe}_2\text{As}_2$ in the underdoped region were examined. The SDW anomaly connected with a structural phase transition is continuously suppressed by increasing doping concentration and no longer observed in $(\text{Ba}_{0.7}\text{K}_{0.3})\text{Fe}_2\text{As}_2$. Bulk superconductivity was present in all samples except in $(\text{Ba}_{0.9}\text{K}_{0.1})\text{Fe}_2\text{As}_2$, so the co-existence of superconductivity and antiferromagnetic ordering could be unambiguously proved.

These results contradict reports on mesoscopic phase separations in antiferromagnetically ordered and non-magnetic superconducting regions in single crystals of almost optimally doped $(\text{Ba}_{1-x}\text{K}_x)\text{Fe}_2\text{As}_2$ ^[159] and confirm the phase diagram depicted in Figure 7.13. In the polycrystalline materials studied here, the structural distortion and antiferromagnetic ordering are definitely absent already at $x = 0.3$. The origin of magnetically ordered fractions detected in almost optimally doped single crystals of $(\text{Ba}_{0.6}\text{K}_{0.4})\text{Fe}_2\text{As}_2$ with high T_C s may either be attributed to a strongly inhomogeneous potassium distribution caused by uncontrolled single crystal growth or by magnetic impurity phases such as FeAs with a Néel temperature of 77 K.^[144]

More recently, a high-resolution X-ray diffraction study on $\text{Ba}(\text{Fe}_{1-x}\text{Co}_x)_2\text{As}_2$ single crystals has been carried out.^[160] It clearly displays the co-existence of an orthorhombic crystal structure, antiferromagnetic order and bulk superconductivity at low temperatures in the underdoped regime of $\text{Ba}(\text{Fe}_{1-x}\text{Co}_x)_2\text{As}_2$. These experiments are therefore in line with the results in this chapter. In the diffraction study, also the order-parameter (i.e. the ‘orthorhombicity’) of each crystal has been measured. The bottom line of these experiments is that the order parameter increases at first on cooling below T_o (tetragonal-to-orthorhombic transition temperature) but if the temperature falls below the superconducting critical temperature, it *decreases* again. This behaviour suggests that there is a strong competition between itinerant magnetism and superconductivity. Under the assumption of the nematic ordering mechanism (see discussion in Chapter 4.3) one can therefore conclude, that superconductivity weakens the magnetic spin fluctuations, thereby suppressing the nematic order and in consequence also the orthorhombic distortion. Very recent examinations by *Wiesenmayer* have shown this behaviour also in bulk powders of underdoped $(\text{Ba}_{1-x}\text{K}_x)\text{Fe}_2\text{As}_2$.^[161]

8. $M\text{Fe}_2\text{As}_2$ ($M = \text{Sr}, \text{Eu}$)

Superconductivity in the iron arsenides is intimately connected with a SDW anomaly, which is accompanied by a structural and magnetic phase transition. The anomaly and transition can be suppressed by doping and the material becomes a superconductor. Meanwhile, it is generally accepted that spin-fluctuations play an important role in the superconducting mechanism of the iron pnictides (Chapter 1.1.2). Therefore, the nature of the phase transitions is important for a deeper understanding of the superconducting mechanism. However, precise structural data close to the phase transition had only been available for BaFe_2As_2 (Chapter 7.1.1) and LaFeAsO .^[33b, 114] SrFe_2As_2 had been studied by single crystal data of relatively low resolution,^[162] which did not allow an evaluation of the order parameter close to the transition temperature. Furthermore, the connection between the structural transition in SrFe_2As_2 and magnetic ordering as well as the structure of EuFe_2As_2 at low temperatures, had not been investigated. Therefore, the structural phase transitions of polycrystalline SrFe_2As_2 and EuFe_2As_2 were examined in detail by temperature-programmed X-ray powder diffraction. Also the association of the structural transition in SrFe_2As_2 with magnetic ordering was confirmed via ^{57}Fe -Mössbauer spectroscopy.

8.1 Synthesis

SrFe_2As_2 and EuFe_2As_2 were synthesised by heating mixtures of distilled Sr (Eu) metal, iron powder and sublimed arsenic at ratios of 1:2:2 in alumina crucibles according to Chapter 2.10.3. The mixtures were heated to 850 K at a rate of $50 \text{ K}\cdot\text{h}^{-1}$, kept at this temperature for 15 h and cooled down to room temperature. The reaction products were homogenised in an agate mortar, pressed into pellets and annealed at 900 K for 15 h. The obtained black crystalline powders of SrFe_2As_2 and EuFe_2As_2 are sensitive to air and moisture.

8.2 Crystal structure

SrFe_2As_2 exhibits a structural transition from the tetragonal space group $I4/mmm$ to the orthorhombic maximal subgroup $Fmmm$ according to the β - SrRhAs -type structure.^[163] The same transition had been previously observed in a BaFe_2As_2 powder sample (Chapter 7.1.1) and SrFe_2As_2 single crystals.^[162] Anomalies in the physical properties have been reported at 205 K for polycrystalline SrFe_2As_2 ^[164] and at 198 K for SrFe_2As_2 single crystals.^[162] In this chapter, the structural phase transition in SrFe_2As_2 at 203 K is confirmed by temperature-programmed X-ray powder diffraction. Figure 8.1 shows the experimental and fitted powder patterns of SrFe_2As_2 at room temperature. The inset clearly shows a distinct splitting of the (213) reflection, which was observed below 203 K. The structures were refined at room temperature and at 90 K, i.e. well below the transition temperature. The obtained crystallographic data are summarised in Table 8.1.

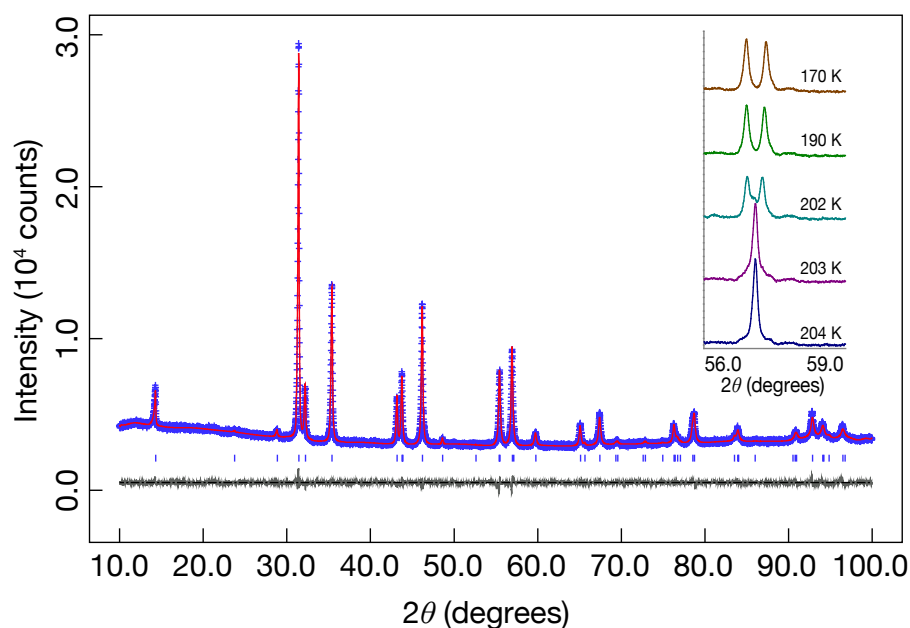


Figure 8.1: Rietveld fit of SrFe_2As_2 at 297 K (space group $I4/mmm$). Inset: (213) reflection.

Temperature	297 K	90 K
Diffractometer	HUBER G670 (Cu-K α_1)	HUBER G670 (Cu-K α_1)
Rietveld package	GSAS	GSAS
Space group	$I4/mmm$	$Fmmm$
Lattice parameters	$a = 392.43(1)$ pm $c = 1236.44(1)$ pm	$a = 557.83(3)$ pm $b = 551.75(3)$ pm $c = 1229.65(6)$ pm
Cell volume	$V = 0.19041(1)$ nm ³	$V = 0.37846(1)$ nm ³
Z	2	4
Data points	9000	5823
Reflections	46	145
Atomic parameters	4	5
Profile parameters	8	4
Background prm.	36	36
Other parameters	5	12
d range	0.981 – 6.182	0.963 – 6.148
$R_p, R_{wp}, R_F^2, \chi^2$	0.0232, 0.0306, 0.029, 1.601	0.0361, 0.0487, 0.104, 4.444
Atomic parameters		
Sr	$2a$ (0, 0, 0) $U_{\text{iso}} = 129(5)$ pm ²	$4a$ (0, 0, 0) $U_{\text{iso}} = 180(40)$ pm ²
Fe	$4d$ ($\frac{1}{2}$, 0, $\frac{1}{4}$) $U_{\text{iso}} = 72(4)$ pm ²	$8f$ ($\frac{1}{4}$, $\frac{1}{4}$, $\frac{1}{4}$) $U_{\text{iso}} = 60(20)$ pm ²
As	$4e$ (0, 0, z) $z = 0.3600(1)$ $U_{\text{iso}} = 86(4)$ pm ²	$8i$ (0, 0, z) $z = 0.3612(3)$ $U_{\text{iso}} = 60(20)$ pm ²
Bond lengths		
Sr–As	$327.0(1) \times 8$	$324.4(3) \times 4$ $327.0(3) \times 4$
Fe–As	$238.8(1) \times 4$	$239.1(3) \times 4$
Fe–Fe	$277.5(1) \times 4$	$278.9(1) \times 2$ $275.9(1) \times 2$
Bond angles		
As–Fe–As	$110.5(1) \times 2$ $108.9(1) \times 4$	$110.2(2) \times 2$ $109.5(1) \times 2$ $108.6(1) \times 2$

Table 8.1: Crystallographic data of SrFe_2As_2 at 297 K and 90 K.

An intensively discussed question is, whether the transition is of first or second-order. For second-order transitions, the space groups of the distorted and undistorted structures have to comply with a group–subgroup relationship according to *Her-*

mann's theorem.^[165] The space group $Fm\bar{3}m$ is a *translationengleiche* maximal subgroup of $I4/m\bar{3}m$ of index 2. Thus, from a group theoretical standpoint, one could expect a second-order transition with a continuous variation of the order parameter. Figure 8.2 shows the lattice parameters of SrFe_2As_2 as determined by Rietveld refinements. The lattice parameter a in the tetragonal structure has been multiplied by $\sqrt{2}$ for comparison.

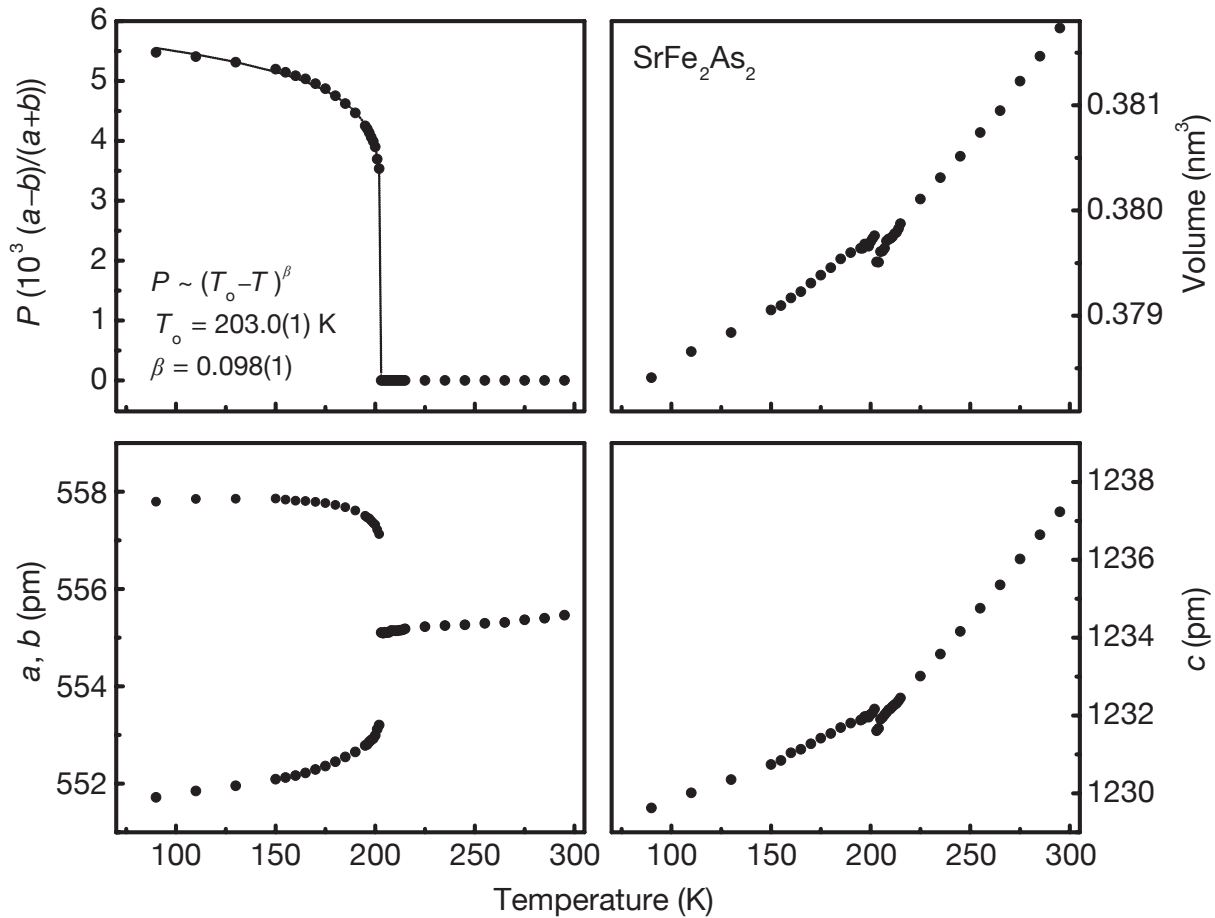


Figure 8.2: Variation of the lattice parameters and order parameter of SrFe_2As_2 with temperature. Error bars are within data points.

A rather abrupt splitting of the lattice parameters on cooling was detected below 203 K, which could indicate a first-order transition. The tetragonal axis $a_t = 555.11$ pm splits by $+2.0$ pm ($+0.365\%$) and -1.9 pm (-0.343%) within only 1 K, leading to $a_o = 557.13(3)$ pm and $b_o = 553.20(3)$ pm at 202 K. Below this temperature, a continuous increase of a_o and a decrease of b_o was observed. a_o saturates at 165 K towards a total change of $+0.67\%$, whereas b_o decreases further to a total change of -0.94% at 90 K. The different behaviour of the orthorhombic axes is

most likely a consequence of the magnetic ordering involved in the structural transition. This anisotropy can be understood if the spin moments at the iron atoms in SrFe_2As_2 are aligned parallel to one orthorhombic axis and perpendicular to the other, as observed in LaFeAsO ^[31] and BaFe_2As_2 ^[166]. The temperature dependence of the order parameter $P = (a-b)/(a+b)$ is presented in Figure 8.2. The data was fitted with the power law $P = q \cdot [(T_o - T)/T]^\beta$. The critical exponent $\beta = 0.098(1)$ and the critical temperature $T_o = 203.0(1)$ K were obtained. Simple power-law dependences defining critical exponents are generally valid close to the critical point, but the values of the critical exponents are often very different from the Landau prediction ($\beta = 1/2$). However, it is well known that the Landau theory fails to provide a general description of critical phenomena. In the present case, the two-dimensional character of the structure has to be taken into account and the exponent $\beta \approx 0.1$ is not too far from $1/8$, which is the prediction of the two-dimensional Ising model!^[167] So far, the structural transition of SrFe_2As_2 has a clear signature of second-order, but on the other hand some results point to a first-order mechanism. Typical signs for first-order transitions are the occurrence of a hysteresis and volume jump at T_o . Indeed, specific heat measurements^[164] show a hysteresis of ~ 0.2 K. This value is unexpectedly small, but consistent with the leap of the cell volume. A small leap at T_o is discernible from the volume plot in Figure 8.2, but $\Delta V/V$ is only 0.07 %. This is extremely small, especially if it is considered that the difference between the lattice parameters a and b is around 1 %. This very small hysteresis and volume jump does not unambiguously prove a first-order transition. This point of view is also supported by a comparison between the structural data of SrFe_2As_2 and those of other $M\text{Fe}_2\text{As}_2$ compounds like BaFe_2As_2 (Chapter 7.1.1).

Figure 8.3 shows the Rietveld fit of the EuFe_2As_2 sample. Crystallographic data for the ambient and low-temperature structures are compiled in Table 8.2. In Figure 8.4, the lattice and order parameters of EuFe_2As_2 , which were derived from Rietveld refinements, are presented. The exact progression of the c axis and thus volume in the proximity of T_o could not be determined. A behaviour similar to SrFe_2As_2 is observed, but T_o decreases to 190.0(1) K and the critical exponent increases to $\beta = 0.112(1)$. This trend continues in the case of BaFe_2As_2 with $T_o = 139$ K and

$\beta = 0.142$ (as determined from the data presented in Chapter 7.1.1). It seems that the critical exponent β scales with T_o and the transition indeed converges towards first-order (where β vanishes), but remains second-order even in SrFe_2As_2 . This is also what to expect from group theory. It is worth mentioning that the abruptness of a phase transition is by no means a cast-iron argument for a first-order mechanism. Often, the determination of the order of a phase transition is a question of data accuracy close to the critical point.

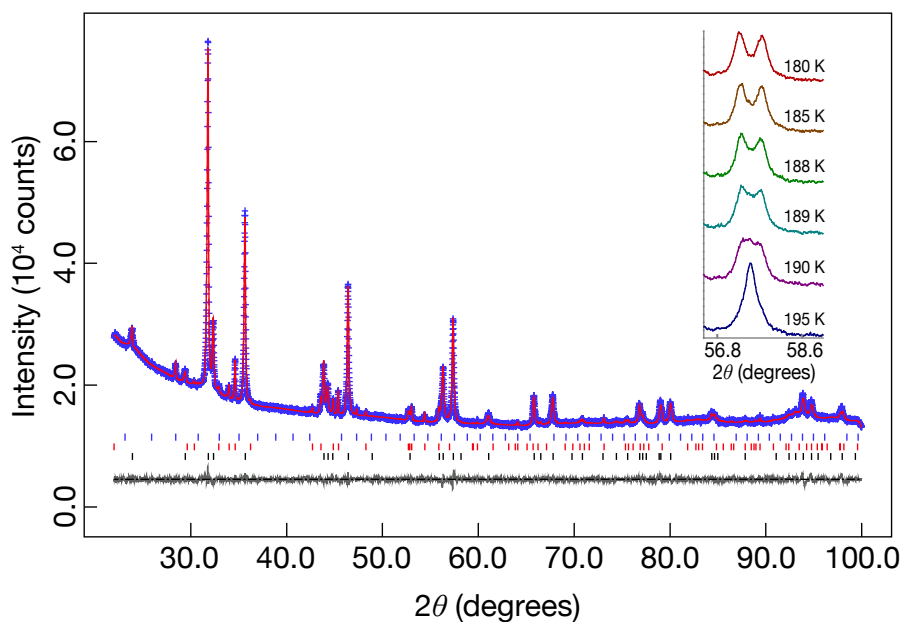


Figure 8.3: Rietveld fit of EuFe_2As_2 at 297 K (space group $I4/mmm$). FeAs (< 20 %) and Eu_2O_3 (< 1 %) were included as impurities. Inset: (213) reflection.

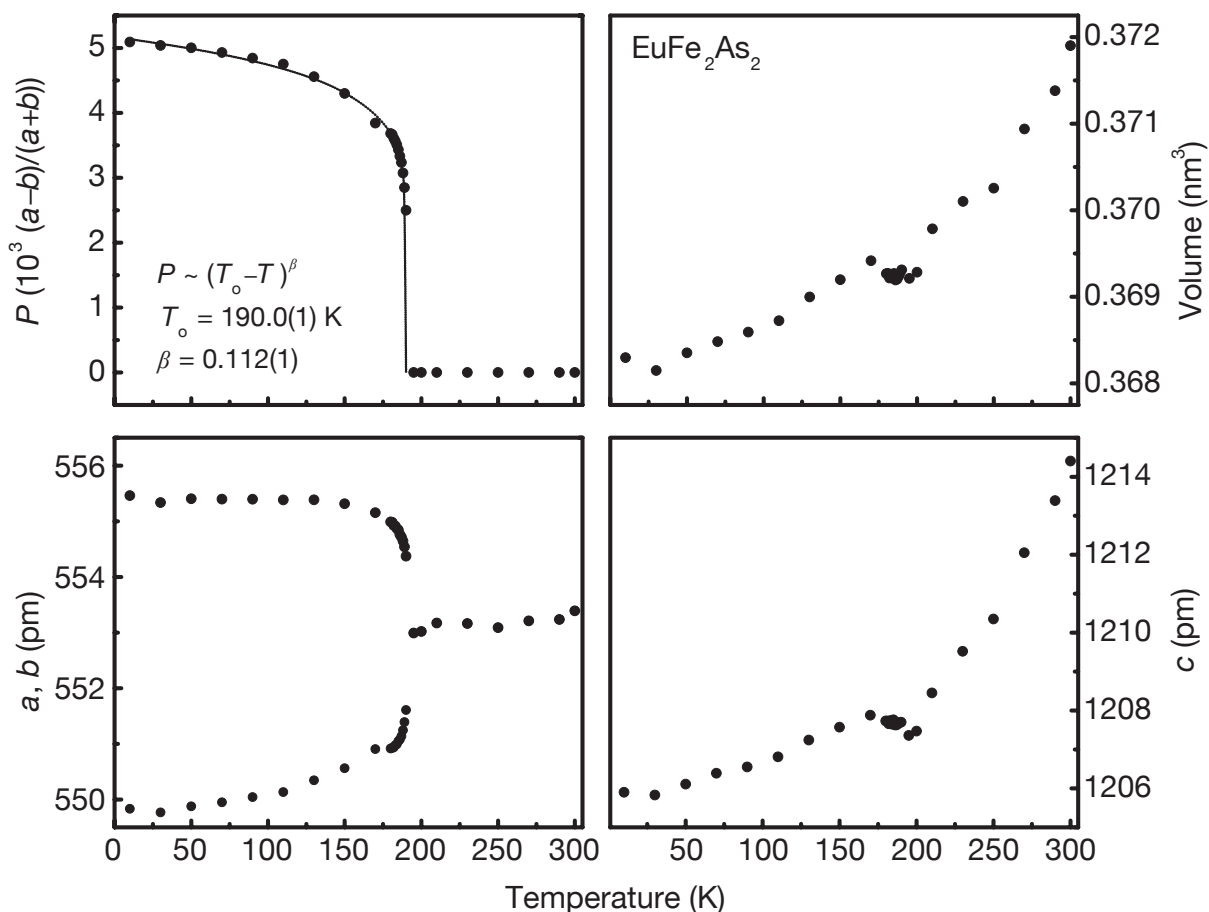


Figure 8.4: Variation of the lattice parameters and order parameter of EuFe_2As_2 with temperature. Error bars are within data points.

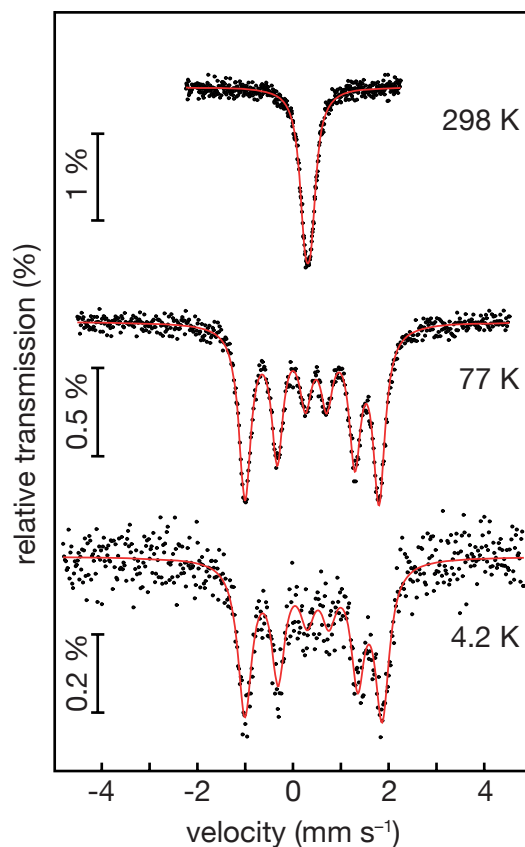
Temperature	297 K	10 K
Diffractometer	HUBER G670 (Cu- $K\alpha_1$)	HUBER G670 (Cu- $K\alpha_1$)
Rietveld package	GSAS	GSAS
Space group	$I4/mmm$	$Fmmm$
Lattice parameters	$a = 390.62(1)$ pm $c = 1212.47(2)$ pm	$a = 555.46(2)$ pm $b = 549.83(2)$ pm $c = 1205.90(4)$ pm
Cell volume	$V = 0.18501(1)$ nm ³	$V = 0.36830(1)$ nm ³
Z	2	4
Data points	7800	7650
Reflections	281	306
Atomic parameters	4	5
Profile parameters	8	10
Background pm.	36	36
Other parameters	20	24
d range	0.960 – 7.678	0.945 – 7.681

$R_p, R_{wp}, R_{F^2}, \chi^2$	0.0147, 0.0209, 0.047, 2.580	0.0131, 0.0237, 0.064, 2.371
Atomic parameters		
Sr	$2a$ (0, 0, 0) $U_{\text{iso}} = 123(5) \text{ pm}^2$	$4a$ (0, 0, 0) $U_{\text{iso}} = 73(6) \text{ pm}^2$
Fe	$4d$ ($1/2, 0, 1/4$) $U_{\text{iso}} = 91(6) \text{ pm}^2$	$8f$ ($1/4, 1/4, 1/4$) $U_{\text{iso}} = 47(6) \text{ pm}^2$
As	$4e$ (0, 0, z) $z = 0.3625(1)$ $U_{\text{iso}} = 96(5) \text{ pm}^2$	$8i$ (0, 0, z) $z = 0.3632(1)$ $U_{\text{iso}} = 87(6) \text{ pm}^2$
Bond lengths		
Sr–As	$322.6(1) \times 8$	$320.6(1) \times 4$ $323.0(1) \times 4$
Fe–As	$238.2(1) \times 4$	$238.3(1) \times 4$
Fe–Fe	$276.2(1) \times 4$	$277.7(1) \times 2$ $274.9(1) \times 2$
Bond angles		
As–Fe–As	$110.1(1) \times 2$ $109.1(1) \times 4$	$110.1(1) \times 2$ $109.6(1) \times 2$ $108.7(1) \times 2$

Table 8.2: Crystallographic data of EuFe_2As_2 at 297 K and 10 K.

8.3 Magnetic ordering

In order to clarify the connection between the structural phase transition in SrFe_2As_2 and magnetic ordering, ^{57}Fe -Mössbauer spectra of SrFe_2As_2 were recorded at 298, 77 and 4.2 K. They are depicted in Figure 8.5 together with transmission integral fits. In agreement with the ThCr_2Si_2 -type crystal structure, a single absorption line was observed at room temperature. At 77 K, which is well below the structural transition temperature, full magnetic hyperfine field splitting of the signal was detected. Excellent fits of the data were obtained with the parameters listed in Table 8.3.

Figure 8.5: ^{57}Fe Mössbauer spectra of BaFe_2As_2

The isomer shifts are similar to those found in BaFe_2As_2 ($\delta = 0.31 - 0.44 \text{ mm}\cdot\text{s}^{-1}$, see Chapter 7.1.2) Due to different ionic radii, a smaller c/a ratio of 3.15 was observed for SrFe_2As_2 in comparison to $c/a = 3.29$ in BaFe_2As_2 .^[133] The stronger compression of the $\text{FeAs}_{4/4}$ tetrahedra in the strontium compound is also reflected by the larger quadrupole splitting parameter. This is in good agreement with the ^{57}Fe -Mössbauer spectra for LaFePO (Chapter 3.2) and LaFeAsO ,^[102] which contain electronically very similar tetrahedral $\text{FeP}_{4/4}$ and $\text{FeAs}_{4/4}$ layers.

Temperature (K)	δ ($\text{mm}\cdot\text{s}^{-1}$)	Γ ($\text{mm}\cdot\text{s}^{-1}$)	ΔE_Q ($\text{mm}\cdot\text{s}^{-1}$)	B_{hf} (T)
298	0.31(1)	0.28(1)	-0.13(1)	-
77	0.44(1)	0.31(1)	-0.09(1)	8.70(1)
4.2	0.47(1)	0.37(6)	-0.09(1)	8.91(1)

Table 8.3: Fitting parameters for ^{57}Fe Mössbauer spectroscopy data of SrFe_2As_2 .

The hyperfine field detected at the iron nuclei in SrFe_2As_2 ($B_{\text{hf}} = 8.91 \text{ T}$) at 4.2 K is considerably higher than in BaFe_2As_2 (5.47 T, see Chapter 7.1.2). The magnetic behaviour of the iron arsenide layers strongly depends on the occupation of the Fe $3d_{x^2-y^2}$ orbitals, which itself depends on the position of the arsenic atoms.^[164] Thus, with smaller strontium and europium atoms, a stronger magnetism of the iron arsenide layers and consequently a higher ordering temperature can be observed, i.e. 140 K in BaFe_2As_2 , 205 K in SrFe_2As_2 ^[164] and 200 K in EuFe_2As_2 .^[168] The hyperfine fields show the same trend: 5.47 T in BaFe_2As_2 (Chapter 7.1.2), 8.91(1) T in SrFe_2As_2 and 8.5 T in EuFe_2As_2 .^[168] This is especially remarkable considering that the ordered magnetic moments of all three compounds lie in the range of 0.8 – 1.0 μ_{B} according to neutron diffraction experiments.^[169]

In summary, these results suggest a complex nature of the phase transitions in $M\text{Fe}_2\text{As}_2$ compounds due to competing order parameters with respect to their structural and magnetic components. It could be shown by Mössbauer spectroscopy that the transition of SrFe_2As_2 is accompanied by magnetic ordering, as it is also the case in BaFe_2As_2 and EuFe_2As_2 . Although the magnetic ordering is coupled to the lattice and both contributions are hard to distinguish due to their proximity, the focus of this chapter has been on the structural part. The determination of the lattice parameters close to T_0 are indicative of a second-order transition with continuously varying order parameters and power-law dependences for both SrFe_2As_2 and EuFe_2As_2 . This is typical for displacive structural transitions and consistent with the group-subgroup relationship between the $I4/mmm$ and $Fmmm$ space groups. A comparison of SrFe_2As_2 -, EuFe_2As_2 - and BaFe_2As_2 -data clearly reveals a relation between the transition temperatures and the critical exponents. Obviously, the transition becomes more and more continuous as T_0 decreases from SrFe_2As_2 towards BaFe_2As_2 . But of course the mechanism, which is responsible for the phase transition, is the same in all three cases. Hence, it can be concluded that all $M\text{Fe}_2\text{As}_2$ compounds with $M = \text{Ba}, \text{Sr}$ and Eu undergo second-order displacive structural phase transitions. As of 2011, the question if the transition is first or second-order in

the iron arsenides is still under dispute in the scientific community. For example, a neutron diffraction study on BaFe_2As_2 indeed suggests a first-order transition^[170] and so do many other reports on various other iron pnictides. However, a more recent heat capacity study on BaFe_2As_2 by *Rotundu* also shows the temperature-dependent development of the (228) reflection and order parameter of an annealed BaFe_2As_2 single crystal, which was determined with very high angular and temperature resolution.^[171] It clearly shows a rather continuous broadening of the (228) reflection between 145.6 K and 139.4 K, which can be interpreted as the beginning of a second-order transition. Below 139.4 K however, the two reflections (408) and (048) appear abruptly, which is clearly indicative of a first-order transition. This rather unusual behaviour possibly explains the differences that can be found throughout the literature.

9. $\text{Sr}_{1-x}\text{K}_x\text{Fe}_2\text{As}_2$ and $\text{Ca}_{1-x}\text{Na}_x\text{Fe}_2\text{As}_2$

Extensive efforts have been undertaken to understand the mechanism of superconductivity in the iron arsenide superconductors. Electronic structure calculations show that in the iron arsenides the electronic bands around the Fermi level are formed mainly by Fe and As states, while the bands of La–O or M ($M = \text{Na}, \text{Ca}, \text{K}, \text{Sr}$) atoms, respectively are far from the Fermi level (see also Chapter 1.1). It is therefore reasonable that superconductivity in these compounds depends on both structural and electronic properties of the FeAs layers. Inelastic neutron scattering measurements carried out on BaFe_2As_2 ^[172] have shown the presence of magnetic excitations (magnons)^{xvii}. Moreover, a resonant magnetic excitation in $\text{Ba}_{0.6}\text{K}_{0.4}\text{Fe}_2\text{As}_2$ that emerges exactly at T_c has been observed by inelastic neutron scattering.^[173] Therefore spin fluctuations are believed to play an important role for the mechanism of superconductivity. In particular, it has been calculated that phonons couple selectively to the spin system.^[174] Despite the fact that a simple electron–phonon coupling mechanism^[35] seems to be rather unlikely, it therefore is important to investigate the phonon spectrum experimentally. This can help to elucidate the role of phonons in the pairing mechanism in the superconducting phase. Electron–phonon coupling may be inferred from the changes of the phonon lifetimes and phonon energies. A very versatile way to measure such phonon energies is via inelastic neutron scattering experiments. Such experiments were carried out on 4.5 and 10 grams of $\text{Sr}_{1-x}\text{K}_x\text{Fe}_2\text{As}_2$ and $\text{Ca}_{1-x}\text{Na}_x\text{Fe}_2\text{As}_2$, respectively. Additionally, lattice-dynamical calculations on these compounds were performed, which are not subject of this thesis and can be found in the original literature.^[83] Special focus was put on electron–phonon coupling, which should be detectable in the form of changes upon doping and temperature in the spectra.

^{xvii} For a theoretical background, refer to Chapter 2.4.

9.1 Synthesis

The polycrystalline samples of $\text{Sr}_{0.6}\text{K}_{0.4}\text{Fe}_2\text{As}_2$ ($T_C = 32$ K, 4.5 g total) and $\text{Ca}_{0.6}\text{Na}_{0.4}\text{Fe}_2\text{As}_2$ ($T_C = 21$ K, 10 g total) were prepared by heating stoichiometric mixtures of the corresponding purified elements according to the synthesis method described in Chapter 2.10.3. All samples were prepared in batches of 3 – 4.5 g and heated and annealed several (3 – 4) times directly in sealed niobium tubes under an atmosphere of purified argon. After each annealing step, the mixtures were homogenised in an agate mortar and pressed into pellets of 6 mm diameter before the last annealing step. The samples were heated to 1073 – 1173 K ($\text{Sr}_{0.6}\text{K}_{0.4}\text{Fe}_2\text{As}_2$) and 973 – 1073 K ($\text{Ca}_{1-x}\text{Na}_x\text{Fe}_2\text{As}_2$) in the different annealing steps and kept at these temperatures for 30 to 48 h. In the first step, the mixtures were heated very slowly in the temperature range from 573 to 873 K and kept at this temperature for 12 h in order to prevent undesirable reactions. The phase purity of the polycrystalline samples was checked by X-ray powder diffraction after each annealing step. The compounds were always handled under an atmosphere of argon, as they are sensitive to air and moisture. Rietveld refinements were performed using the TOPAS Academic package (Chapter 2.2.4). For the $\text{Sr}_{1-x}\text{K}_x\text{Fe}_2\text{As}_2$ sample, a Fe impurity of 1.2 wt% was found and for $\text{Ca}_{1-x}\text{Na}_x\text{Fe}_2\text{As}_2$ unknown impurity phases were estimated to be less than 10 % (as derived by reflection integrals), which is acceptable for inelastic neutron scattering measurements. The superconducting volume fraction was checked via SQUID measurements of the shielding volume fraction.

9.2 Crystal structures

Both $\text{Sr}_{1-x}\text{K}_x\text{Fe}_2\text{As}_2$ and $\text{Ca}_{1-x}\text{Na}_x\text{Fe}_2\text{As}_2$ crystallise in the same structure as $\text{Ba}_{0.6}\text{K}_{0.4}\text{Fe}_2\text{As}_2$. However, for both samples, the observed reflections in the powder diffractograms are very broad (Figure 9.1), indicating inhomogeneous sample compositions. This is a common problem when synthesising large quantities of materials in one batch, as diffusion paths are very long. In the case of mixed alkaline / earth alkaline iron pnictides, this problem seems to be particularly present. Some reflections of the $\text{Sr}_{1-x}\text{K}_x\text{Fe}_2\text{As}_2$ sample are therefore very broad and asymmetric. Hence, a composition-dependent Rietveld study was carried out on the powder diffraction

pattern of this sample. For this composition-dependent study, a model with nine different, separately refined compositions was employed, where the lattice parameters, As z parameter and K : Sr ratio of the $2a$ site were allowed to refine freely, while the temperature factors as well as preferred orientation were constrained together for all compositions. The obtained Rietveld fit is depicted in Figure 9.1 (top). The resulting composition distribution, lattice parameter a , pnictogen z parameter as well as K : Sr ratio as functions of the c lattice parameter are depicted in Figure 9.2. The c lattice parameter was chosen as x -coordinate because this lattice parameter is the measure with the smallest relative standard deviation. For the $\text{Ca}_{1-x}\text{Na}_x\text{Fe}_2\text{As}_2$ sample, the anisotropic broadening of the reflections could be sufficiently described with the model of *Le Bail* and *Jouanneaux* (see also Chapter 2.2.6). Even though this model is meant to describe mainly the consequences of anisotropic strain, crystallite defects or stacking faults, it also proved successful in describing the present effects of inhomogeneous sample composition. In this case, only averaged parameters (i.e. lattice parameters, atomic positions and occupancies) could be derived. In the original literature, the refined values of $\text{Ca}_{1-x}\text{Na}_x\text{Fe}_2\text{As}_2$ without width anisotropy were published.

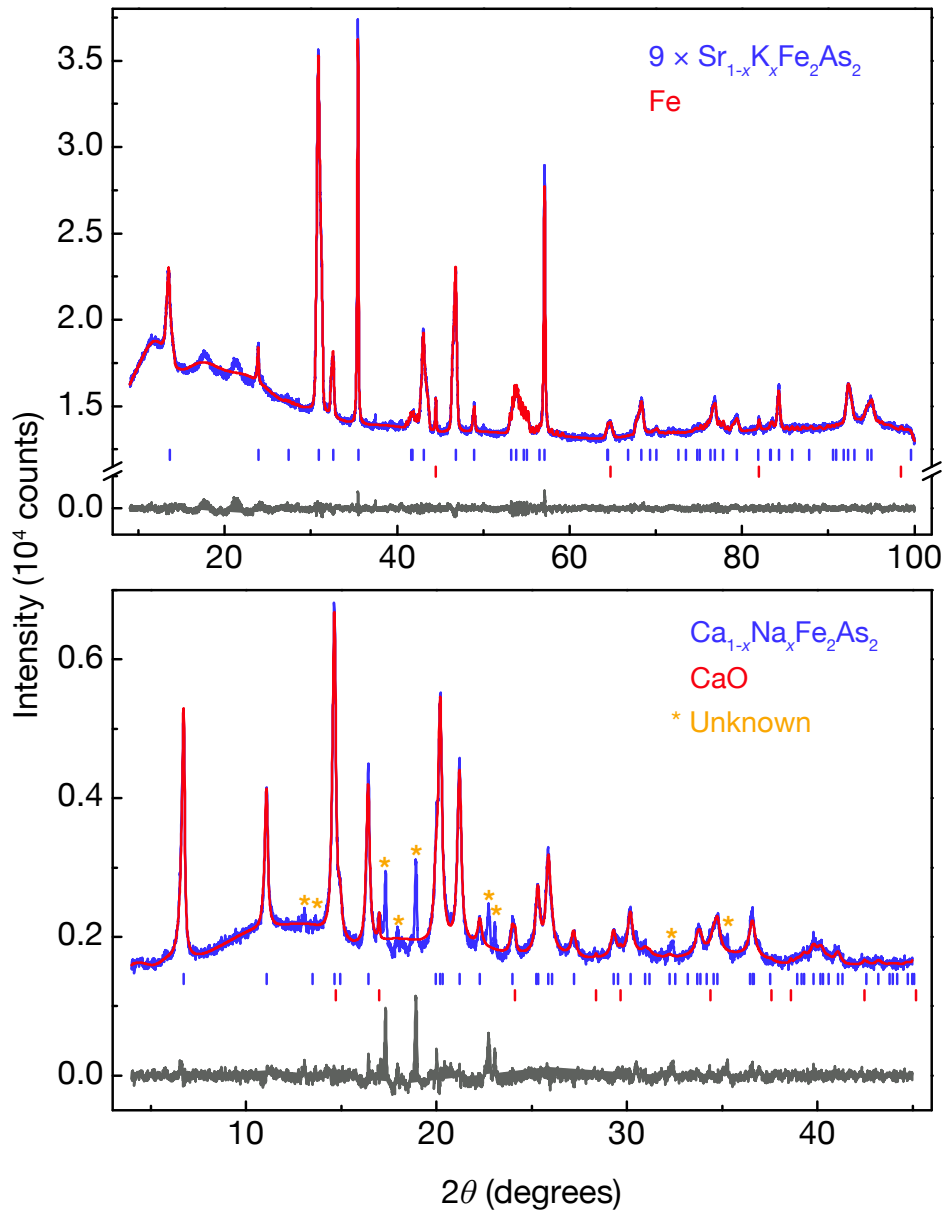


Figure 9.1: Powder pattern and Rietveld fits of $\text{Sr}_{1-x}\text{K}_x\text{Fe}_2\text{As}_2$ (top) and $\text{Ca}_{1-x}\text{Na}_x\text{Fe}_2\text{As}_2$ (bottom).

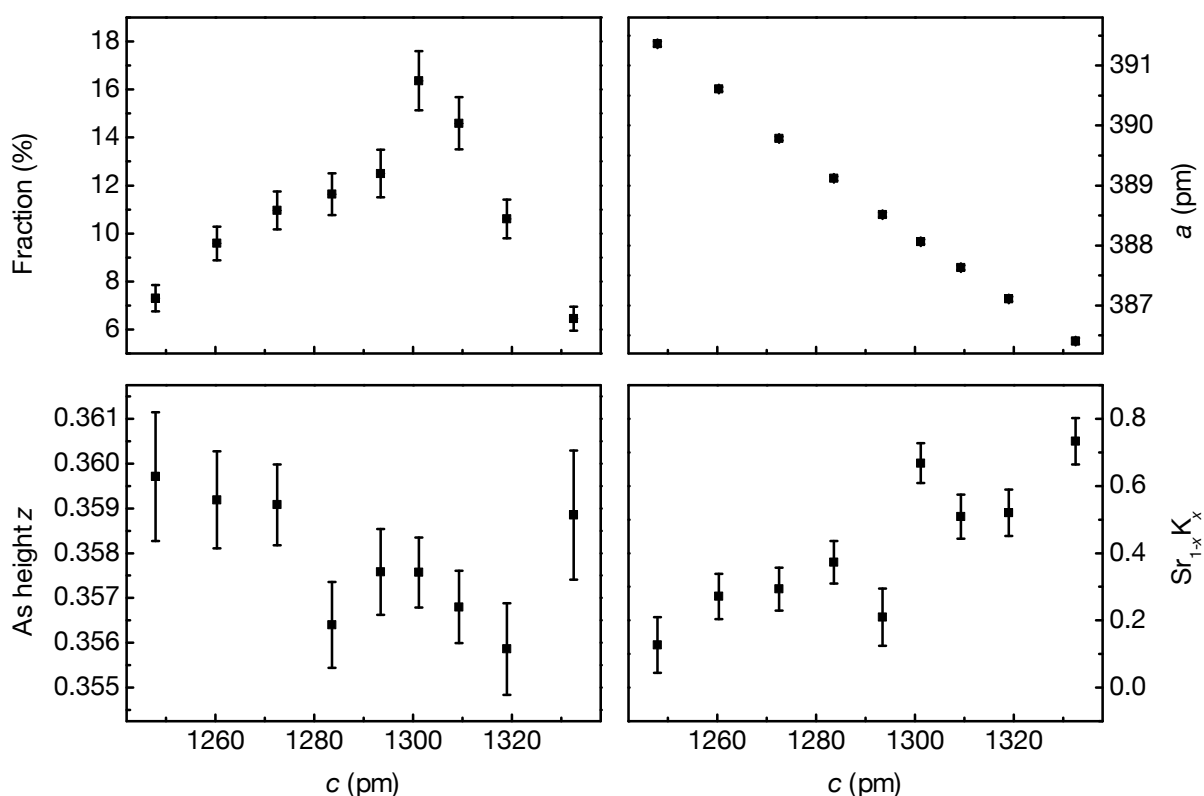


Figure 9.2: Composition distribution, lattice parameters and pnictogen height of $\text{Sr}_{1-x}\text{K}_x\text{Fe}_2\text{As}_2$ (error bars: 3σ).

Crystallographic details of the averaged crystal structures of both $\text{Sr}_{1-x}\text{K}_x\text{Fe}_2\text{As}_2$ and $\text{Ca}_{1-x}\text{Na}_x\text{Fe}_2\text{As}_2$ are listed in Table 9.1. For the $\text{Sr}_{1-x}\text{K}_x\text{Fe}_2\text{As}_2$ sample, the obtained values lack standard deviations because of non-trivial error propagation.

Compound	$\text{Sr}_{1-x}\text{K}_x\text{Fe}_2\text{As}_2$	$\text{Ca}_{1-x}\text{Na}_x\text{Fe}_2\text{As}_2$
Temperature	297 K	297 K
Diffractometer	HUBER G670 (Cu- $\text{K}\alpha_1$)	STOE STADI P (Mo- $\text{K}\alpha_1$)
Rietveld package	TOPAS	TOPAS
Averaging method	Composition-dependent Rietveld refinement; weighted statistical mean derived via Origin. ^[90]	<i>Le Bail-Jouanneaux</i> approach (width anisotropy only)
Space group	$I4/mmm$	$I4/mmm$
Lattice parameters	$a = 388.6$ pm $c = 1293.3$ pm	$a = 385.3(1)$ pm $c = 1206.2(3)$ pm
Cell volume	$V = 0.1953$ nm ³	$V = 0.17907(5)$ nm ³
Z	2	2

Data points	18201	4100
Reflections	45	53
Atomic variables	21 (all compositions)	5
Profile parameters	5	16
Background prm.	36	36
Other parameters	36	14
<i>d</i> range	1.008 – 6.506	0.918 – 6.031
<i>R</i>_P, <i>R</i>_{WP}, <i>R</i>_{Bragg}, χ^2	0.00753, 0.0100, n/a, 1.228	0.0275, 0.0442, 0.003, 2.006
Atomic parameters		
(K, Sr) / (Na, Ca)	2a (0, 0, 0) <i>U</i> _{iso} = 196 pm ²	2a (0, 0, 0) <i>U</i> _{iso} = 63(74) pm ²
Fe	4d (½, 0, ¼) <i>U</i> _{iso} = 142 pm ²	4d (½, 0, ¼) <i>U</i> _{iso} = 242(25) pm ²
As	4e (0, 0, <i>z</i>) <i>z</i> = 0.3577 <i>U</i> _{iso} = 114 pm ²	4e (0, 0, <i>z</i>) <i>z</i> = 0.3671(3) <i>U</i> _{iso} = 154(28) pm ²
A : EA ratio	42 : 58	57(9) : 43(9)
Bond lengths		
(A, EA)–As	330.7 × 8	316.1(2) × 8
Fe–As	239.1 × 4	238.8(3) × 4
Fe–Fe	274.8 × 4	272.4(1) × 4
Bond angles		
As–Fe–As	108.7 × 2 109.8 × 4	107.4(2) × 2 110.5(1) × 4

Table 9.1: Averaged crystal structures of Sr_{1-x}K_xFe₂As₂ and Ca_{1-x}Na_xFe₂As₂ at 297 K.

9.3 Superconductivity

The superconducting character of the samples was checked via susceptibility measurements under zero-field-cooled (shielding) and field-cooled (Meissner) cycles of finely ground powder samples using the SQUID magnetometer described in Chapter 2.6.1 at 15 Oe. The samples showed superconducting transitions at 32 K and 21 K in Sr_{1-x}K_xFe₂As₂ and Ca_{1-x}Na_xFe₂As₂, respectively and reached bulk superconductivity at system base temperature (Figure 9.3). In accordance with the crystallographic findings in the last chapter, the superconducting transition of Sr_{1-x}K_xFe₂As₂

appears broadened, as the superconducting transition temperature strongly depends on the K : Sr ratio of the sample.

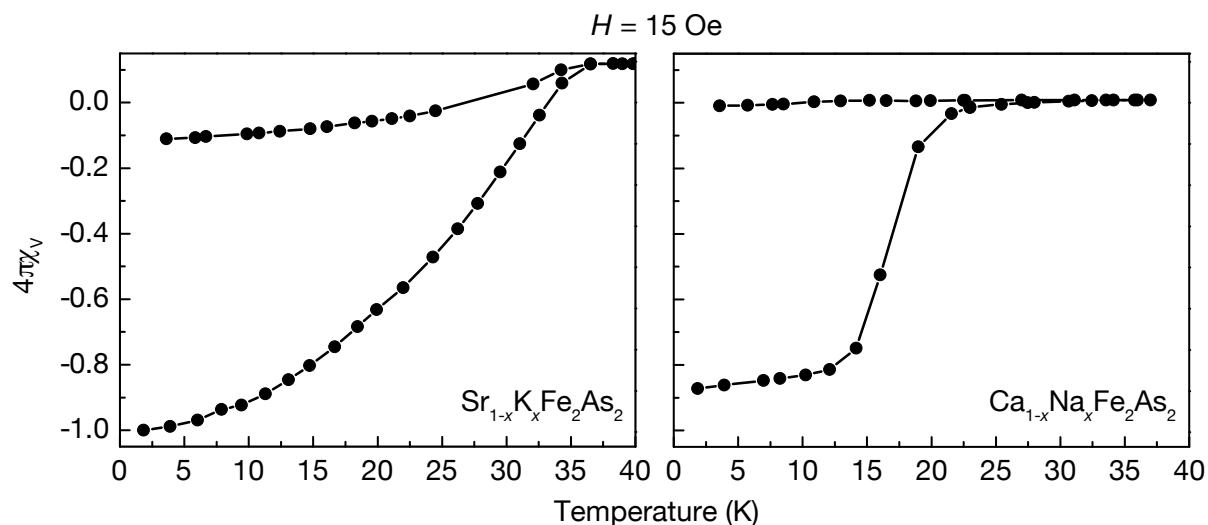


Figure 9.3: Zero-field-cooled (shielding) and field-cooled (Meissner) measurements of $\text{Sr}_{1-x}\text{K}_x\text{Fe}_2\text{As}_2$ and $\text{Ca}_{1-x}\text{Na}_x\text{Fe}_2\text{As}_2$.

9.4 Inelastic neutron scattering

Inelastic neutron scattering experiments were performed using the IN4C and IN6 time-of-flight spectrometers at the Institut Laue Langevin (ILL), France in the setup described in Chapter 2.4.2. For general considerations about inelastic neutron scattering measurements, refer to Chapter 2.4.1.

The experimental $S(Q, E)$ measured for $\text{Sr}_{1-x}\text{K}_x\text{Fe}_2\text{As}_2$ and $\text{Ca}_{1-x}\text{Na}_x\text{Fe}_2\text{As}_2$ using the IN4C spectrometer are shown in Figure 9.4. In contrast to reports on similar measurements^[173] carried out on powder samples of $\text{Ba}_{0.6}\text{K}_{0.4}\text{Fe}_2\text{As}_2$ using the MERLIN spectrometer at ISIS,^[175] these measurements do not show any signs of resonant spin excitations. However, the (Q, E) range attainable using the IN4C spectrometer is reduced compared to that of MERLIN at low- Q values. This, in addition to a lower signal-to-noise ratio on the IN4C spectrometer, could have prevented detecting this weak feature. While it would be tempting to conclude from this data that such an excitation is absent, further investigations might be necessary in order to be certain. However, to date, no further inelastic neutron scattering measurements of any of

these compounds have been performed on a spectrometer with better low- Q resolution, so this question still remains open.

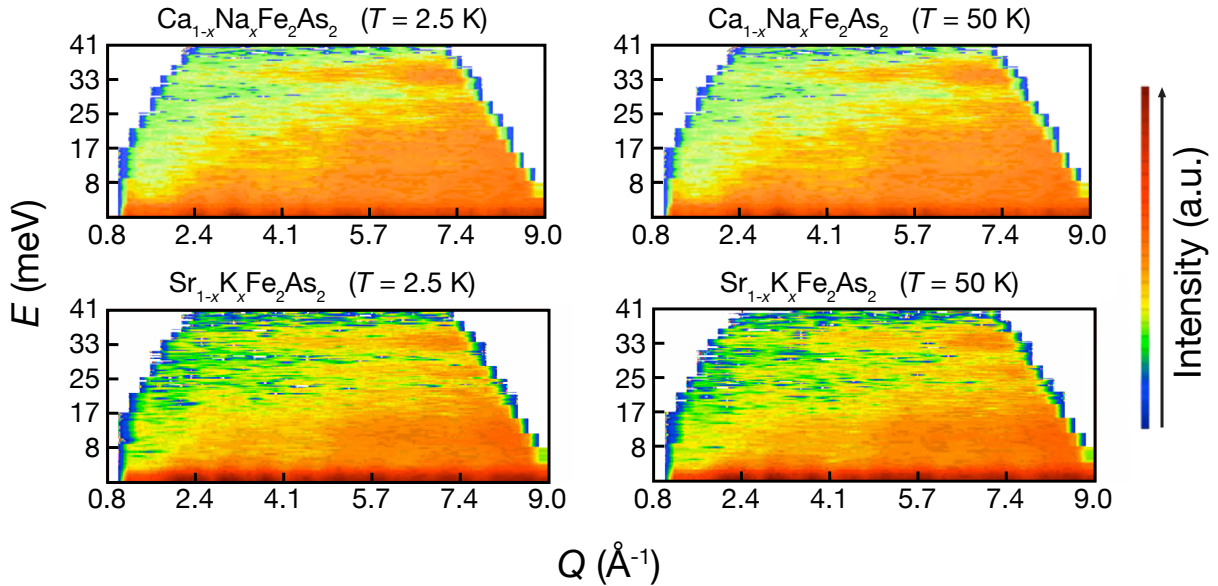


Figure 9.4: Experimental $S(Q, E)$ plots for $\text{Sr}_{1-x}\text{K}_x\text{Fe}_2\text{As}_2$ (bottom) and $\text{Ca}_{1-x}\text{Na}_x\text{Fe}_2\text{As}_2$ (top) at 2.5 K and 50 K (IN4C spectrometer). At 2.5 K, no additional features at low- Q ($< 2 \text{ \AA}^{-1}$) indicating spin excitations, are visible.

The generalised phonon density of states obtained from $S(Q, E)$ for both compounds at 2.5 K and 50 K together with a calculated model are shown in Figure 9.5. One can clearly see a strong similarity between the generalised density of states measured above and below the superconducting transition temperature for both $\text{Sr}_{1-x}\text{K}_x\text{Fe}_2\text{As}_2$ and $\text{Ca}_{1-x}\text{Na}_x\text{Fe}_2\text{As}_2$. This suggests that the formation of Cooper pairs only has a very minor influence on the overall vibration spectrum. The calculation details of the phonon DOS are beyond the scope of this dissertation and can be found in the original literature.^[83]

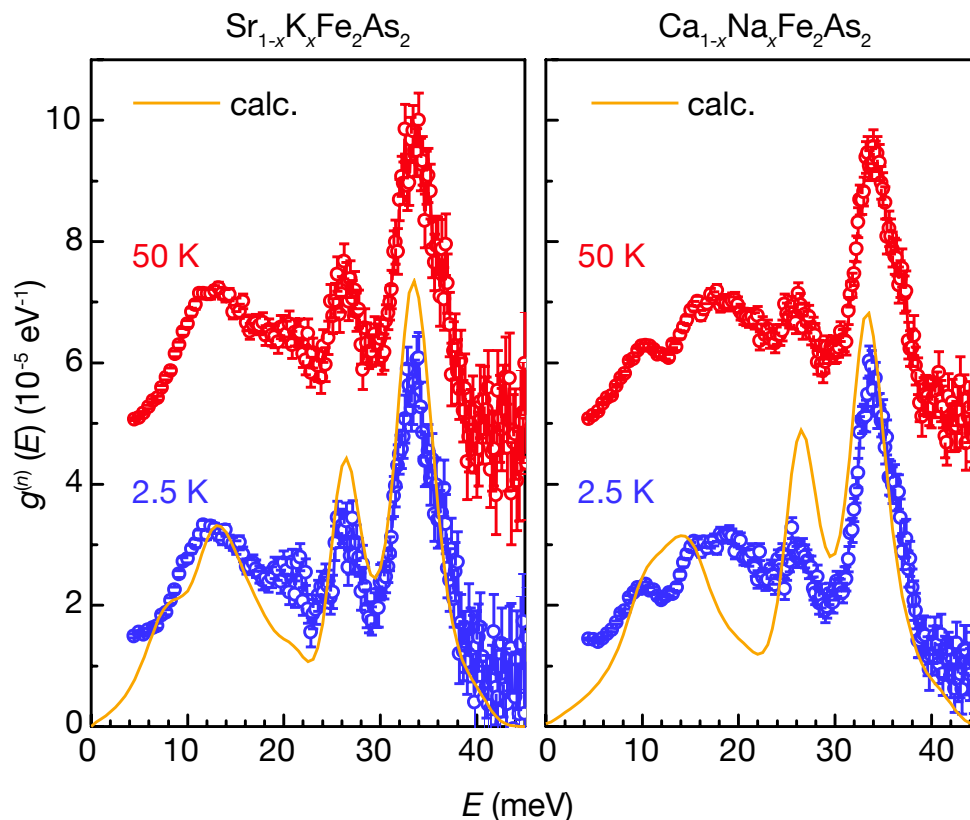


Figure 9.5: Experimental and calculated phonon spectra of $\text{Sr}_{1-x}\text{K}_x\text{Fe}_2\text{As}_2$ (left) and $\text{Ca}_{1-x}\text{Na}_x\text{Fe}_2\text{As}_2$ (right) at 2.5 K and 50 K as derived from the IN4C data. The phonon spectra at 50 K have an offset of $4 \cdot 10^{-5} \text{ eV}^{-1}$.

The phonon densities of states measurements at low temperatures were completed with measurements of higher resolution in the low-energy (i.e. low-frequency) range (0 – 20 meV) using the IN6 spectrometer. These are depicted in Figure 9.6, details of the measurement setup can be found in Chapter 2.4.2. Due to the cryostat setup of the beam line, the measurements were limited to higher temperatures. The phonon densities of states of BaFe_2As_2 , $\text{Ca}_{1-x}\text{Na}_x\text{Fe}_2\text{As}_2$ and $\text{Sr}_{1-x}\text{K}_x\text{Fe}_2\text{As}_2$ measured at 300 K (Figure 9.6, bottom) show pronounced differences in the low-energy half of the spectral range. However, it is not evident to attribute these changes to simple mass renormalisation effects of the phonon modes involving the different atomic weights of Ba, Sr and Ca respectively.

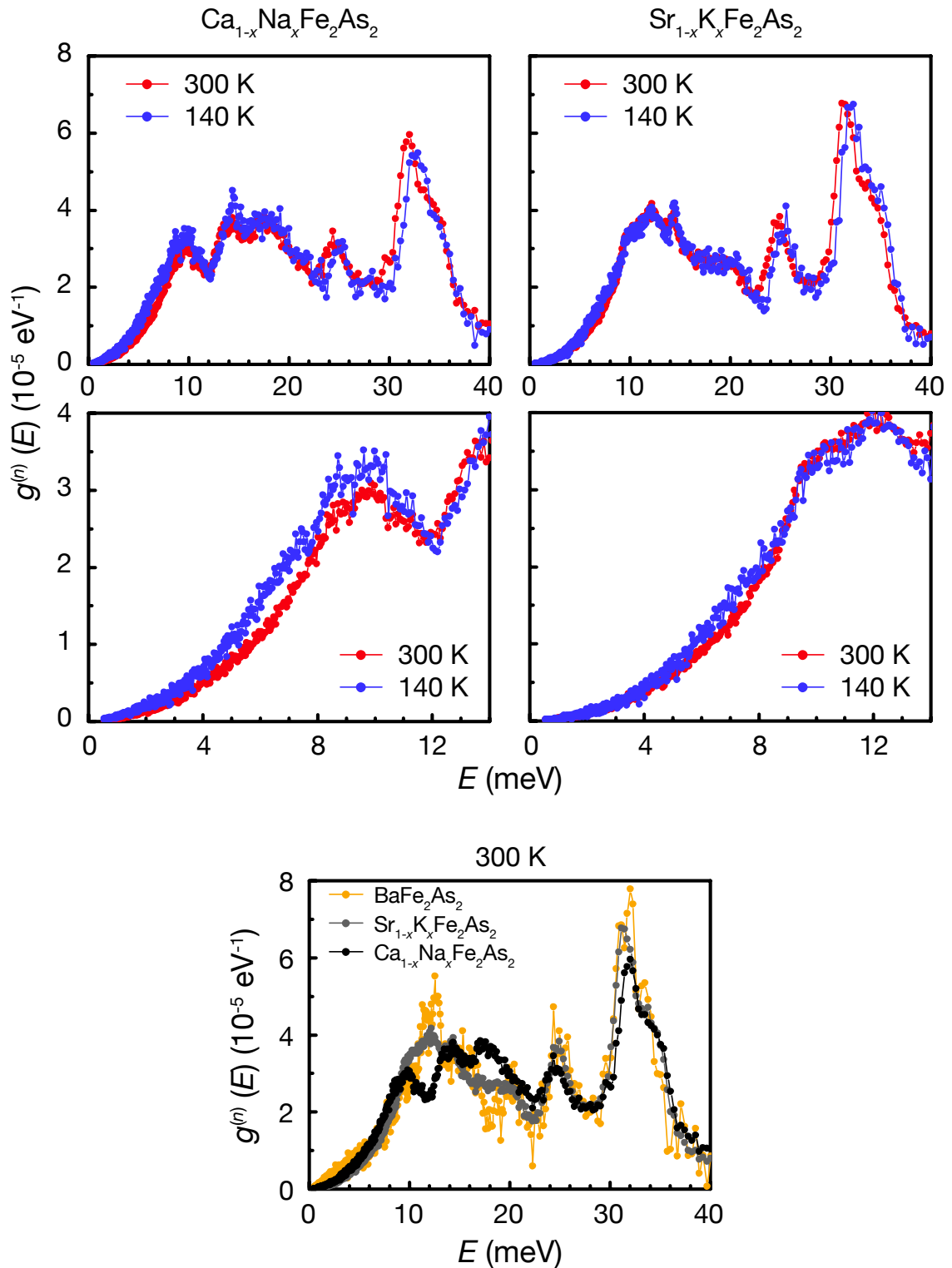


Figure 9.6: Top: Experimental phonon spectra of $\text{Ca}_{1-x}\text{Na}_x\text{Fe}_2\text{As}_2$ (left) and $\text{Sr}_{1-x}\text{K}_x\text{Fe}_2\text{As}_2$ (right) at 140 K and 300 K (IN6 data). Middle: Magnification of the low-energy range. Bottom: Comparison between $\text{Sr}_{1-x}\text{K}_x\text{Fe}_2\text{As}_2$, $\text{Ca}_{1-x}\text{Na}_x\text{Fe}_2\text{As}_2$ and BaFe_2As_2 at 300 K.

Qualitatively, the phonon spectra show that the peak at about 21 meV in the BaFe_2As_2 and $\text{Sr}_{1-x}\text{K}_x\text{Fe}_2\text{As}_2$ compounds is shifted to a lower energy of about 17.5 meV in $\text{Ca}_{1-x}\text{Na}_x\text{Fe}_2\text{As}_2$. If the unit-cell dimensions of $\text{Ca}_{1-x}\text{Na}_x\text{Fe}_2\text{As}_2$, BaFe_2As_2 , and $\text{Sr}_{1-x}\text{K}_x\text{Fe}_2\text{As}_2$ are compared, it is evident that while all three compounds feature nearly the same lattice parameters a , the c lattice parameter of $\text{Ca}_{1-x}\text{Na}_x\text{Fe}_2\text{As}_2$ is about 10 % shorter in comparison with the other compounds. This implies that the $M\text{--As}$ ($M = \text{Ca} / \text{Na}$) and Fe--As bond lengths are slightly reduced in $\text{Ca}_{1-x}\text{Na}_x\text{Fe}_2\text{As}_2$ with regard to the other compounds (see also crystallographic details in Table 9.1). This contraction of the unit cell and in the bond lengths should normally result in shifting the phonon modes, if at all, to higher energies. The fact that the contrary is observed indicates that the bonding scheme is different for $\text{Ca}_{1-x}\text{Na}_x\text{Fe}_2\text{As}_2$. The $\text{Ca}^{2+} / \text{Na}^+$ layers thus seem not just to be mere charge reservoirs. The unit cell contraction is accompanied by a substantial change in the free structural parameter of As (from $z = 0.3577$ to $z = 0.3671$). It is known from DFT calculations that this parameter has a crucial influence on the binding and in particular on the phonon frequencies^[174] in BaFe_2As_2 . It may be speculated that it equally has substantial responsibility for the changes observed here. A further clarification of these facts requires reliable *ab initio* calculations for the doped compounds, a task, which still has not been satisfactorily completed.

Apart from the doping dependence, also the temperature dependence of the phonon spectra may give valuable insight into the dynamics of these superconductors. Usually, phonon modes are found to shift towards higher energies with decreasing temperature, as the unit cell is contracted and chemical bonds become stronger. This is actually what is observed for the high-frequency band at 34 meV on cooling from 300 K down to 140 K. It can be seen that at 140 K, the bands around 25 and 34 meV are narrower and shifted to higher energies in comparison with the data at 300 K. Contrary to the high-frequency bands, the low-energy phonon modes up to about 10 meV soften in both $\text{Ca}_{1-x}\text{Na}_x\text{Fe}_2\text{As}_2$ and $\text{Sr}_{1-x}\text{K}_x\text{Fe}_2\text{As}_2$ as the temperature is decreased from 300 to 140 K (Figure 9.6, middle). In $\text{Ca}_{1-x}\text{Na}_x\text{Fe}_2\text{As}_2$, the softening amounts to about 1 meV while for $\text{Sr}_{1-x}\text{K}_x\text{Fe}_2\text{As}_2$, the softening is about 0.5 meV. A similar softening of low-frequency phonon modes has e.g. been observed in the unconventional superconductor $\text{LuNi}_2\text{B}_2\text{C}$.^[176] In general, however, there is no simple

relation between temperature-induced softening and electron–phonon coupling. In the present case, the behaviour of the system under pressure may give an indication, corresponding measurements have been performed in a later study.^[84]

Superconductivity emerges in the parent compounds $E\text{Fe}_2\text{As}_2$, when the structural phase transition and magnetic ordering are suppressed. Many experiments suggest that both the magnetic and thus structural phase transitions in the undoped parent compounds, as well as the emergence of superconductivity are electronic in origin (refer to Chapters 4.3 and 7.4.2). This strong correlation of structural and electronic properties would be compatible with a softening of low-energy phonon modes observed in $\text{Ca}_{1-x}\text{Na}_x\text{Fe}_2\text{As}_2$ and $\text{Sr}_{1-x}\text{K}_x\text{Fe}_2\text{As}_2$ due to electron–phonon coupling. The larger magnitude of softening in $\text{Ca}_{1-x}\text{Na}_x\text{Fe}_2\text{As}_2$ may indicate that electron–phonon coupling in this compound is stronger than in $\text{Sr}_{1-x}\text{K}_x\text{Fe}_2\text{As}_2$. Since the phonon softening is observed only in the normal state of both doped samples, it is unlikely to be directly associated with superconductivity, and this is despite the isotope effect observed in the pnictide superconductors.^[177] As the tetragonal-to-orthorhombic phase transition is suppressed in the superconducting compounds, the structural phase transition does not appear to be relevant to the observed phonon softening.

In summary, inelastic neutron scattering measurements of both $\text{Ca}_{1-x}\text{Na}_x\text{Fe}_2\text{As}_2$ and $\text{Sr}_{1-x}\text{K}_x\text{Fe}_2\text{As}_2$ at the IN4C spectrometer did not reveal any signs of resonant spin excitations. This is in contrast to the findings in other superconducting iron arsenides. However, the attainable angular and energy resolution of this spectrometer at low scattering angles is limited, so the absence of magnons is not conclusive.

Furthermore, experimental phonon studies of the superconductors $\text{Ca}_{1-x}\text{Na}_x\text{Fe}_2\text{As}_2$ and $\text{Sr}_{1-x}\text{K}_x\text{Fe}_2\text{As}_2$ have been carried out. It could be shown that doping affects mainly the lower and intermediate vibration frequencies. In particular, the region around 20 meV shows a very strong renormalisation; mass effects and lattice contraction alone cannot explain these changes. Therefore, the type of $E\text{A}^{2+} / \text{A}^+$ ions seems to influence the bonding in the FeAs layers. These buffer layers thus cannot be considered as mere charge reservoirs. The high-frequency band reacts moder-

ately to doping. In both compounds, the low-energy phonon modes soften with temperature. This softening, which is stronger in $\text{Ca}_{1-x}\text{Na}_x\text{Fe}_2\text{As}_2$, might be due to electron–phonon coupling. No anomalous effects are observed in the phonon spectra when passing the superconducting transition temperature. All this indicates that while electron–phonon coupling is present, it cannot be solely responsible for the formation of Cooper pairs. This is in line with early DFT calculations on $\text{LaFeAsO}_{1-x}\text{F}_x$ by *Boeri*, who has found only very weak electron–phonon coupling.^[35]

10. $\text{FeSe}_{1-x}\text{Te}_x$

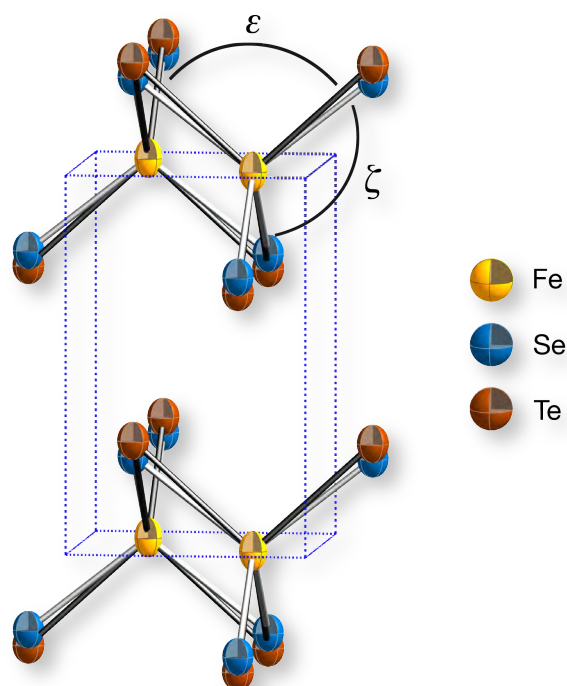


Figure 10.1: Crystal structure of $\text{FeSe}_{0.44}\text{Te}_{0.56}$ with Se / Te split positions.

β -FeSe with the tetragonal anti-PbO-type structure^[178] can be considered as the most fundamental iron-based superconductor as it consists only of tetrahedral layers containing iron and selenium without any separating atoms or building blocks. It therefore seems to be the ideal system to study the underlying physics, which turned out to have many analogies to that of the iron arsenide superconductors.^[14, 143, 179] However, soon after the discovery of superconductivity in FeSe with $T_C = 8 \text{ K}$,^[180] some studies revealed differences between iron selenides and pnictides. Examples are an extreme sensitivity of superconductivity to stoichiometry,^[181] a huge increase of T_C under pressure,^[182] or the absence of long-range magnetic ordering and an orthorhombic or even monoclinic symmetry of the superconducting phase.^[183] In contrast to the selenide, the binary iron telluride with anti-PbO-type structure^[184] is not superconducting, even under pressure.^[185] This may be due to the fact that stoichiometric FeTe does not exist, but only $\text{Fe}_{1+\delta}\text{Te}$ with $\delta \approx 0.05 - 0.15$. These excess iron atoms between the layers may be detrimental to superconductivity.^[186] Despite of

this, superconductivity exists in the solid solution FeSe_{1-x}Te_x with a maximum T_C of about 14 K close to FeSe_{0.5}Te_{0.5}.^[187]

The FeSe_{1-x}Te_x system has been intensively studied with respect to the interplay between structural or magnetic degrees of freedom and superconductivity. It is accepted that magnetic fluctuations play an important role, and calculations revealed a strong sensitivity of the magnetic moment on the so-called ‘chalcogen height’, i.e. the distance of the Se/Te atoms from the plane of iron atoms.^[188] According to this, the magnetic exchange parameter J alters by a factor of 2 – 5 when this chalcogen height varies by only 10 pm. Such subtle dependences of the magnetic and superconducting properties are also known from the iron pnictides,^[189] which re-emphasises the importance of accurate and correct structural data. However, against the background of several published crystal structures of FeSe_{1-x}Te_x,^[190] it is surprising that even simple crystal chemical aspects have been completely disregarded. Selenium and tellurium have quite different ionic radii: $r_{\text{Se}^{2-}} = 198$ pm and $r_{\text{Te}^{2-}} = 221$ pm.^[191] Therefore, one cannot expect that both ions occupy the 2c Wyckoff position with the same z-coordinate in the layered PbO-type structure, and it is questionable why the structure is described with Se and Te sharing the same coordinates in many publications. Only in a publication by *Lehman*,^[192] different z-coordinates of Se and Te in FeSe_{0.5}Te_{0.5} were proposed. These had been determined laboriously and with low precision from an analysis of the pair density function (PDF) obtained from neutron powder diffraction data.

In this chapter, a single-crystal X-ray diffraction study of FeSe_{0.44}Te_{0.56} is presented, which easily reveals the distinct z-coordinates of Se and Te with a one order of magnitude better accuracy compared to the PDF method. A quite large degree of structural disorder therefore exists, which has been neglected in previous studies. Yet, it emphasises the robustness of superconductivity against randomness.

10.1 Experimental

Synthesis details can be found in the original literature.^[193] The phase purity of FeSe_{0.4}Te_{0.6} was checked via powder diffraction (Mo-K α_1 radiation). A Rietveld refinement using the TOPAS package revealed only traces of impurity phases (Figure 10.2). The refined lattice parameters are $a = 380.61(2)$ pm and $c = 608.71(3)$ pm. Superconductivity was confirmed by measuring the AC susceptibility (see Figure 10.3). A relatively broad transition with an onset of T_C at 14 K was found. Such broad transitions in FeSe_{1-x}Te_x superconductors have also been observed by others,^[190, 194] and may be due to a certain sample composition inhomogeneity. This also correlates with the observed anisotropic reflection widths and shapes in the powder diffractogram.

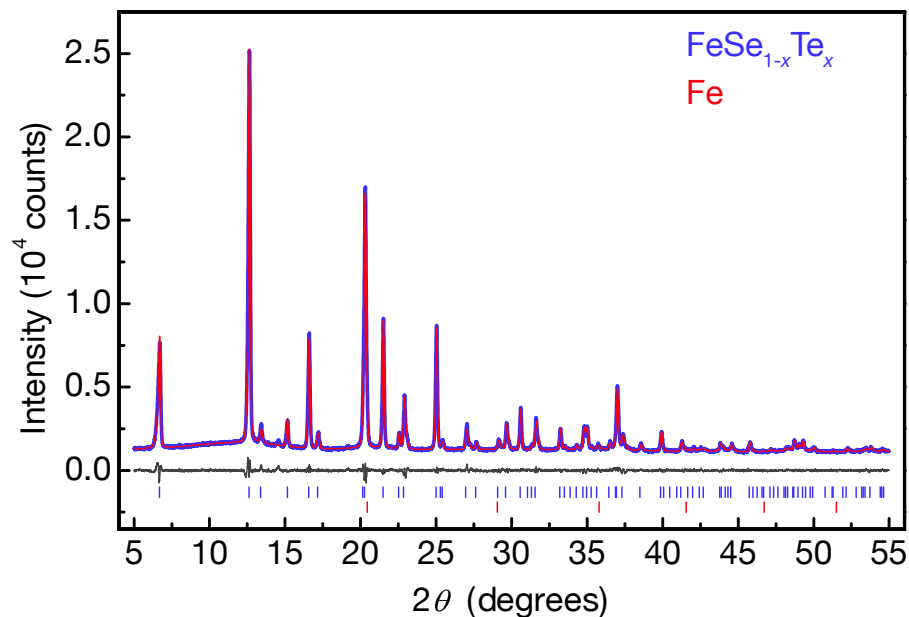


Figure 10.2: Rietveld fit of FeSe_{1-x}Te_x at 297 K (space group $P4/nmm$).

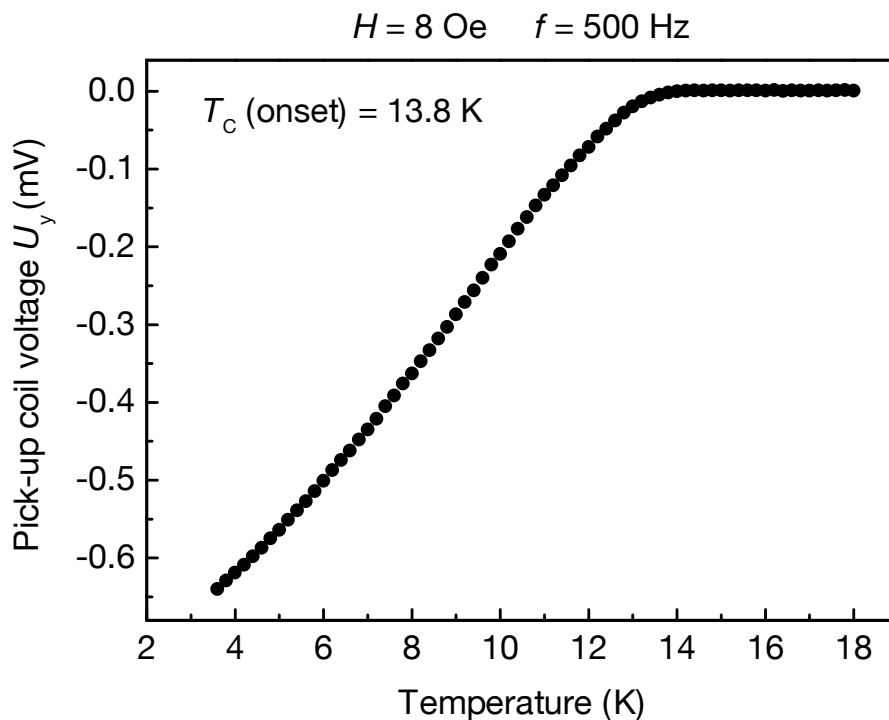


Figure 10.3: Differential pick-up coil voltage of FeSe_{1-x}Te_x (proportional to χ').

A small plate-like single crystal of about $15 \times 20 \times 30 \text{ }\mu\text{m}^3$ was selected from the polycrystalline sample and checked by Laue photographs using white radiation from a Mo anode. Diffraction data up to $2\theta = 90^\circ$ (50 pm resolution) were collected at 173 K on an OXFORD Xcalibur 4-circle diffractometer equipped with a CCD detector. Graphite-monochromised Mo-K α radiation from a conventional sealed X-ray tube was used. The measured intensities were carefully corrected for absorption effects. The atomic positions from [190] were used as starting parameters ($z_{\text{Se/Te}} = 0.27388$) and refined with the least-squares method using the JANA2006 program package.^[195] The positional and thermal parameters of Se and Te were refined independently, while their occupation parameters were constrained to unity.

10.2 Single crystal refinement

The initial refinement of the data using only one z-coordinate already resulted in small residuals of $R1 = 0.029$ and $wR2 = 0.051$. However, the inspection of the anisotropic displacement parameters showed a three times larger displacement parameter U_{33} compared to U_{11} . It is known that such elongations can be artefacts from insufficient absorption corrections, especially due to anisotropic crystal dimen-

sions. For this reason, several refinements were performed using different absorption models. This revealed only a small dependence, which cannot explain a factor of three in the anisotropy. In the next step, the Se and Te *z*-coordinates were refined independently. The refinement immediately converged to different values for Se ($z \approx 0.246$) and Te ($z \approx 0.286$), while the residuals dropped to $R1 = 0.023$ and $wR2 = 0.05$. Moreover, the anisotropy of the still combined (Se, Te) thermal ellipsoid was reduced from a factor of ~ 3 to a factor of ~ 1.3 . The necessary independent refinement of the anisotropic displacements is difficult, because the *z*-coordinates and the U_{33} parameters are strongly correlated. However, due to the high-resolution data ($2\theta_{\max} \approx 90^\circ$), the correlations remained acceptable and did not destabilise the refinement. The refinement finally converged to residuals $R1 = 0.022$, $wR2 = 0.041$ and $\text{GooF} = 0.98$. A careful check of the ΔF Fourier map did not reveal any residual electron densities from additional Fe atoms between the layers. Regarding the Fe atom within the layer, all refinements showed an elongation of the thermal ellipsoid along *z* with an anisotropy of a factor of ~ 2 . This probably is the response of the iron atoms to their different (Se, Te) coordination environments, leading to a small puckering of the Fe plane.

10.3 Crystal structure

The crystal structure of FeSe_{0.44}Te_{0.56} is depicted in Figure 10.1. A summary of the crystallographic data is compiled in Table 10.1.

Temperature	297 K
Diffractometer	OXFORD Xcalibur
Radiation	Mo K α
Structure refinement	Jana2006
Space group	<i>P4/nmm</i> (<i>o2</i>)
Lattice parameters	$a = 379.96(2)$ pm $c = 598.95(6)$ pm
Cell volume	$V = 0.08647(1)$ nm ³
Z	2
Calculated density	6.23 g·cm ⁻³
Absorption coefficient	26.6 mm ⁻¹

Absorption correction	multi-scan
Transmission (min, max)	0.39, 1.00
2θ range	10.7 – 90.23
Reflections (total)	913
Reflections (independ.)	246
Reflections with $I > 3 \sigma(I)$	173
$R_{\text{int}}, R_{\sigma}$	0.037, 0.038
$R1, wR2 [(I > 3 \sigma(I))]$	0.022, 0.041
$R1, wR2$ [all data]	0.042, 0.043
Largest resid. peak, hole	0.98 eÅ ³ , -1.59 eÅ ³
CSD No.	421334
Atomic parameters	
Fe	2a (3/4, 1/4, 0) occ. 1 $U_{11} = 64(2) \text{ pm}^2$ $U_{33} = 132(4) \text{ pm}^2$
Se	2c (1/4, 1/4, z) z = 0.2468(7) occ. 0.44(1) $U_{11} = 80(6) \text{ pm}^2$ $U_{33} = 116(7) \text{ pm}^2$
Te	2c (1/4, 1/4, z) z = 0.2868(3) occ. 0.56(1) $U_{11} = 84(5) \text{ pm}^2$ $U_{33} = 118(7) \text{ pm}^2$
Bond lengths	
Fe–Se	240.7(3) × 4
Fe–Te	256.1(1) × 4
Bond angles	
Se–Fe–Se	104.1(1) × 2 (ϵ) 112.15(6) × 4 (ζ)
Te–Fe–Te	95.75(4) × 2 (ϵ) 116.74(2) × 4 (ζ)
Se–Fe–Te	99.99(9) × 4 114.32(5) × 8

Table 10.1: Crystallographic data of FeSe_{0.44}Te_{0.56}.

This redetermination of the crystal structure clearly reveals the distinct positions of Se and Te. This is also expected from crystal chemical reasons and agrees with the assumption made in [192]. The resulting chalcogen heights are $h_{\text{Se}} = 147.8 \text{ pm}$ and $h_{\text{Te}} = 171.8 \text{ pm}$. In terms of bond lengths, the Fe–Se bond length is by 15.4 pm shorter than the Fe–Te bond. In comparison to the binary compounds, the Fe–Se bond is slightly longer (by 1.6 %) than in FeSe^[178a] and the Fe–Te bond is slightly shorter (by 1.8 %) than in Fe_{1+ δ} Te.^[184] This is also plausible from a chemical point of view, in contrast to an averaged Fe–(Se, Te) bond length, if only one z-parameter is

used. Also the (Se, Te)–Fe–(Se, Te) bond angles depend significantly on the z-coordinates. Iron occupies a position with $\bar{4}m2$ site symmetry, therefore the angle which is bisected by the c-axis (ε) and the angle which is bisected by the *ab*-plane (ζ) are related by $\cos(\zeta) = -\frac{1}{2} \cdot [1 - \cos(\varepsilon)]$. In the present case, three independent angles ε have to be considered: Te–Fe–Te, Se–Fe–Se and Te–Fe–Se. For completeness, also the dependent angles ζ are listed in Table 10.1.

In the case of the iron pnictide superconductors, it has been argued that the geometry of the FePn₄ (Pn = P, As) tetrahedra plays an important role. T_C is seemingly maximised when the bond angles are close to the ideal tetrahedral angle of 109.47°^[196]. The latter has not been observed in the FeCh (Ch = Se, Te) systems, but the large increase of T_C under pressure suggests that such structural details really play an important role in the superconducting mechanism. Furthermore, it is undoubted that the coordination of the iron atoms affects the Fermi surface topology, which is a very similar situation as in the FePn superconductors.^[197] Also, the magnetic moments depend strongly on the height of the pnictogen^[198] and chalcogen^[188] atoms; thus the difference Te–Se = 24 pm as a consequence of the split positions is indeed a strong effect. With respect to the studies on structural effects in the FeSe_{1-x}Te_x system,^[188, 190, 199] one can point out that the changes in the geometry introduced by the split position of Se and Te are at least one magnitude larger than any effect induced by temperature or pressure.

A further implication of these results concerns the discussion on the robustness of superconductivity in iron-based materials with regard to the s_±-wave scenario.^[32a] Generally, superconductivity is expected to be rather sensitive to impurities or other kinds of randomness.^[200] In this context, it is remarkable that the superconducting temperature increases from 8 K in FeSe to 14 K in FeSe_{1-x}Te_x ($x \approx 0.5$). This is in stark contrast to the strong geometrical disorder, which is caused by Te-doping. Detailed calculations taking this aspect into account are necessary to fully understand the consequences of this disorder on the superconducting properties of FeSe_{1-x}Te_x.

In conclusion, the crystal structure of FeSe_{0.44}Te_{0.56} has been redetermined by refinements of high-resolution single-crystal X-ray data and as a result, distinctively different *z*-coordinates for Se and Te were found. This leads to a lower local symmetry of the iron atoms as the Fe–*Ch* bond lengths are split by 15.4 pm. This is an implication of the different chalcogen heights (147.8 pm and 171.8 pm, respectively). Such large effects have not yet been considered in any calculation of electronic and magnetic properties, which are known to be highly sensitive to bond lengths and angles. Since the superconducting transition temperature in FeSe_{1-x}Te_x increases up to $x \approx 0.5$ despite the significant Se / Te disorder, these results point out the robustness of superconductivity in iron-based materials against structural randomness.

11. $\text{Sr}_3\text{Sc}_2\text{O}_5\text{Fe}_2\text{As}_2$

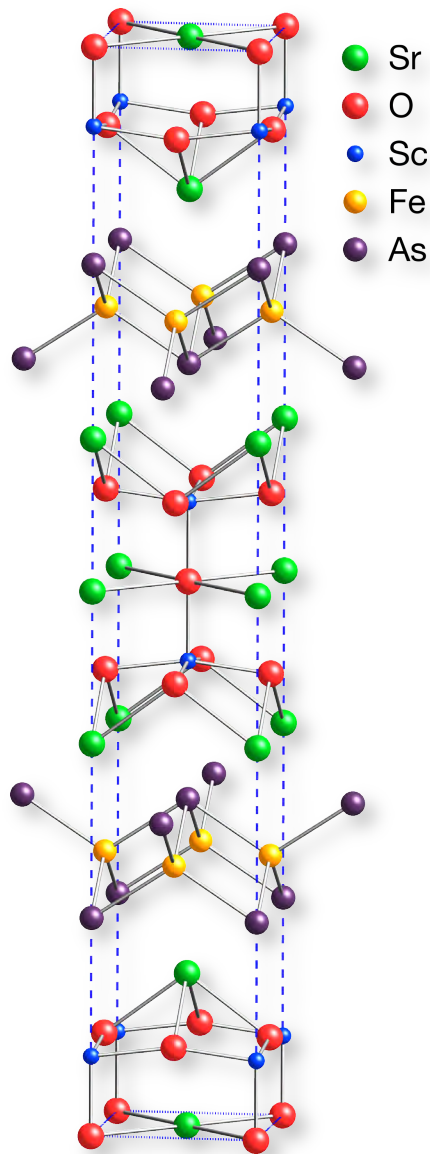


Figure 11.1: Crystal structure of $\text{Sr}_3\text{Sc}_2\text{O}_5\text{Fe}_2\text{As}_2$.

Despite substantial progress that has been made within a short period of time since the discovery of the iron arsenide superconductors in 2008, the exact formula that creates higher T_c s in these compounds is far from being clear. So, especially the quest for new members in the large family of iron-based superconductors with possibly even higher critical temperatures (T_c) attracts the attention of many researchers. Several empirical relations between the structure of the iron pnictide superconductors and their critical temperatures have been proposed. Some groups

saw an interconnection between the symmetry of the iron pnictide tetrahedra and T_C (the less distorted the tetrahedra, the higher the T_C). Others suggested a correlation between the dimensionality of the crystal structures and the maximum attainable critical temperatures: The largest T_C s of up to 56 K appear in ZrCuSiAs-type compounds like $\text{SmFeAsO}_{1-x}\text{F}_x$ ^[15] and $\text{Ca}_{1-x}\text{Nd}_x\text{FeAsF}$ ^[201] where the iron arsenide tetrahedral layers are well separated by (OSm) layers (or $\text{FCa}_{1-x}\text{Nd}_x$ layers, respectively). In ThCr_2Si_2 -type materials like $\text{Ba}_{1-x}\text{K}_x\text{Fe}_2\text{As}_2$, where the FeAs layers are only separated by barium atoms, the highest observed T_C is 38 K (Chapter 7.2.2) and in LiFeAs with an even smaller layer separation, T_C decreases to 18 K.^[202] Finally, in the so-called '11' iron chalcogenide compounds such as $\text{FeSe}_{1-x}\text{Te}_x$ (Chapter 10), the maximum achievable T_C is even further reduced. An overview of the different structure types and maximum T_C s is depicted in Figure 11.2.

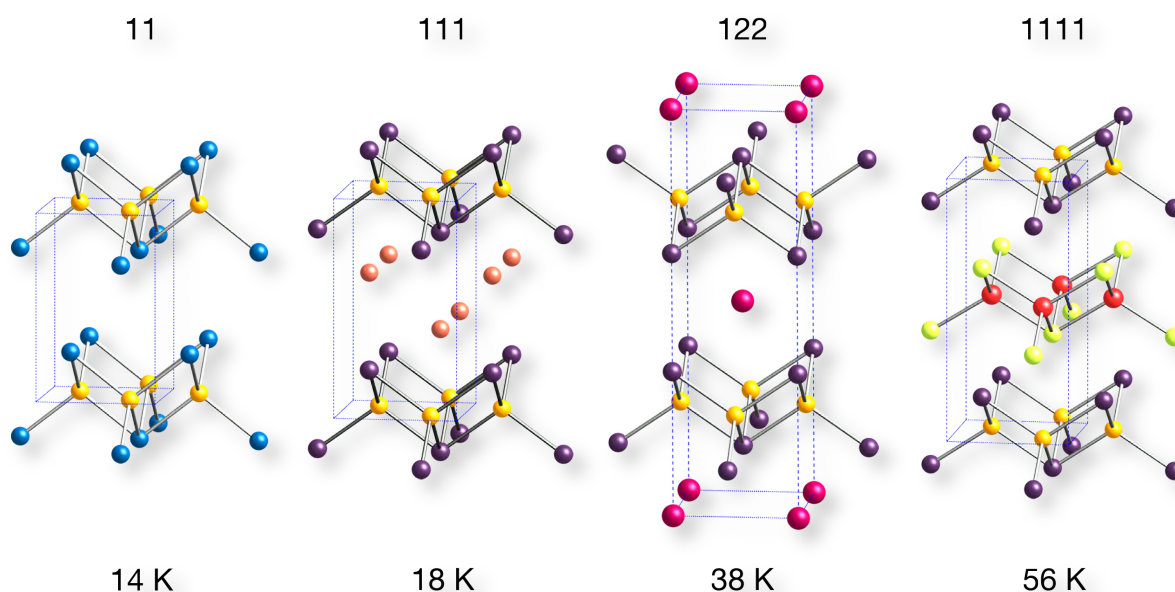


Figure 11.2: Different iron-based superconductor families and maximum T_C s.

However, such proposed relations between T_C and for example the separation of the FeAs layers (i.e. the two-dimensional character) are not justified by any theoretical argument. They may have their origin in some rather far-fetched relationships to the cuprate superconductors. Nevertheless, as long as no other directions towards higher T_C s are available, the search for new iron pnictides with low-dimensional structures is a promising task. By the beginning of 2009, new compounds derived

from structures with isoelectronic copper sulfide (CuS) layers^[203] were reported,^[204] among them the superconductors $\text{Sr}_2\text{ScO}_3\text{FeP}$ ($T_C = 17$ K)^[205] and $\text{Sr}_2\text{VO}_3\text{FeAs}$ ($T_C = 37$ K, refer to [206] and Chapter 14). However, these compounds become superconducting without doping, and they also lack the supposed preconditions for superconductivity in other iron arsenides, because they neither show structural distortions nor antiferromagnetic ordering. Thus, in these compounds the origin of superconductivity remains unclear just as its absence in the previously reported compound $\text{Sr}_3\text{Sc}_2\text{O}_5\text{Fe}_2\text{As}_2$.^[204a] In order to complete the structural and magnetic data of this compound, the low-temperature crystal structure and the results of a ^{57}Fe -Mössbauer spectroscopy study of $\text{Sr}_3\text{Sc}_2\text{O}_5\text{Fe}_2\text{As}_2$ are therefore presented in this chapter. Furthermore, crystallographic relationships that may be useful in the search of new, layered iron-based superconductors are given.

11.1 Synthesis

$\text{Sr}_3\text{Sc}_2\text{O}_5\text{Fe}_2\text{As}_2$ was synthesised by heating a stoichiometric mixture of strontium, scandium, iron (II) oxide and arsenic oxide in an alumina crucible sealed in a silica ampoule according to the synthesis method described in Chapter 2.10.3. The mixture was heated to 1323 K at a rate of $200 \text{ K}\cdot\text{h}^{-1}$, kept at this temperature for 60 h and cooled down to room temperature. The product was homogenised in an agate mortar, pressed into a pellet and sintered at 1323 K for 60 h.

11.2 Crystal structure

Powder patterns were recorded (HUBER G670) and refined (TOPAS) with a single $\text{Sr}_3\text{Sc}_2\text{O}_5\text{Fe}_2\text{As}_2$ phase according to the description in Chapter 2.2. The refined crystal structure of $\text{Sr}_3\text{Sc}_2\text{O}_5\text{Fe}_2\text{As}_2$ (Figure 11.3) at room temperature is in good agreement with ^[204a].

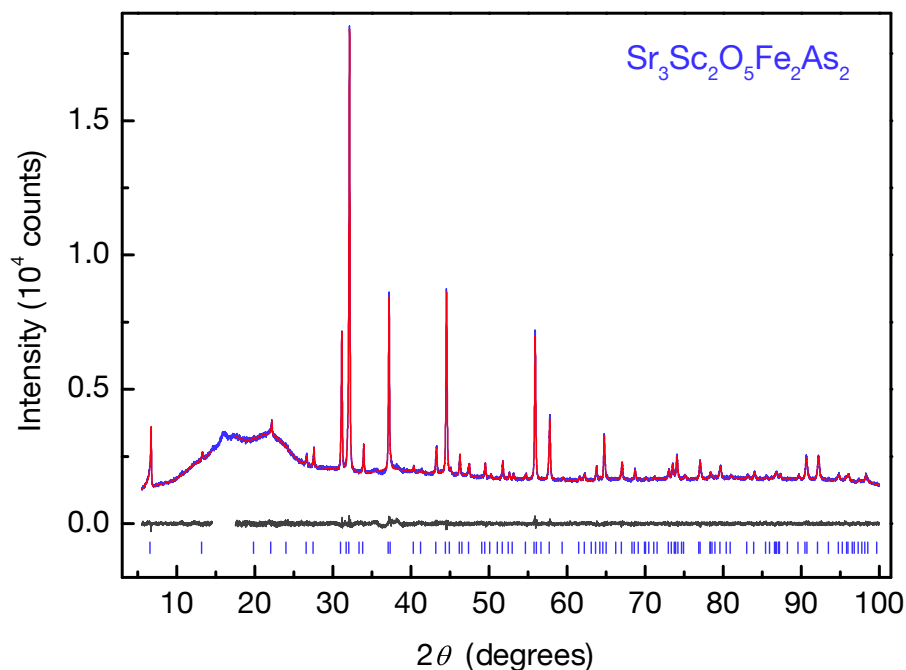


Figure 11.3: Rietveld fit of $\text{Sr}_3\text{Sc}_2\text{O}_5\text{Fe}_2\text{As}_2$ at 297 K (space group $I4/mmm$).

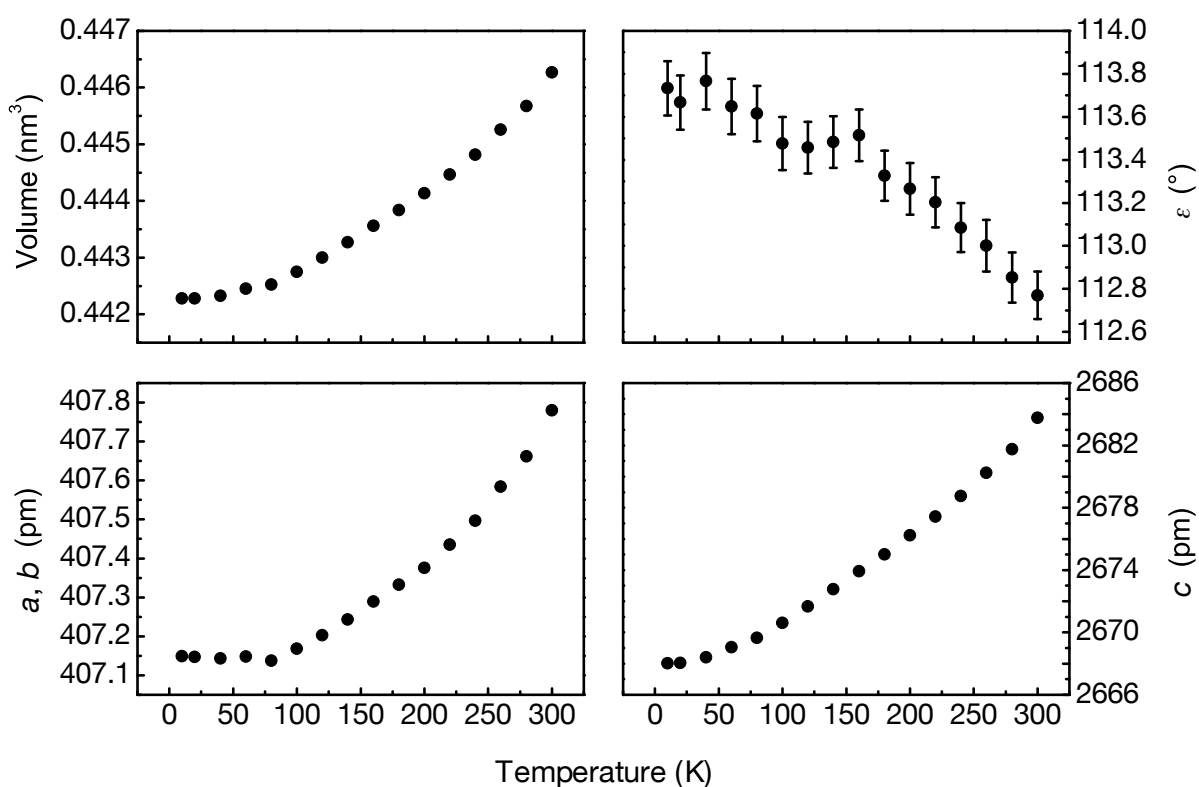
No evidence of any structural instability at low temperatures was detected. The crystallographic data of $\text{Sr}_3\text{Sc}_2\text{O}_5\text{Fe}_2\text{As}_2$ at 300 and 10 K are compiled in Table 11.1. The course of the lattice parameters and As–Fe–As angles on cooling does not reveal any anomaly, as shown in Figure 11.4. While the lattice parameter a decreases by only 0.61 pm, the c lattice parameter decreases by 16.7 pm on cooling down to 10 K. Thus, the thermal contraction of the unit cell is anisotropic according to $(\Delta c/c) : (\Delta a/a) \approx 4.2$. The more pronounced shrinkage of the c axis leads to a slight increase of the vertical As–Fe–As angle (ε) by about 1° , i.e. the FeAs layers become flatter. The Fe–Fe nearest neighbour distance in $\text{Sr}_3\text{Sc}_2\text{O}_5\text{Fe}_2\text{As}_2$ is about 1 % longer than in LaFeAsO ,^[168] and the As–Fe–As angles are almost identical in both structures. Interestingly, the course of the As–Fe–As angle ε exhibits a slight kink at around 150 K (i.e. the temperature, where many other iron arsenide parent compounds exhibit a tetragonal-to-orthorhombic distortion). Whether this is an artefact due to the resolution limit of the powder diffraction experiment or a real effect yet remains arcane.

Temperature	300 K	10 K
Diffractometer	HUBER G670 (Cu-K α_1)	HUBER G670 (Cu-K α_1)
Rietveld package	TOPAS	TOPAS
Space group	<i>I4/mmm</i>	<i>I4/mmm</i>
Lattice parameters	$a = 407.81(1)$ pm $c = 2683.86(5)$ pm	$a = 407.20(1)$ pm $c = 2667.19(5)$ pm
Cell volume	$V = 0.44635(2)$ nm ³	$V = 0.44225(1)$ nm ³
Z	2	2
Data points	18298	17575
Reflections	99	99
Constraints	1	1
Atomic variables	10	10
Profile variables	6	6
Anisotropy var.	24	24
Background var.	60	60
Other variables	5	5
Excluded 2θ ranges^{a)}	14.5° – 17.5°	11.3° – 13.0°; 14.0° – 18.9°
d range	1.008 – 13.419	1.006 – 13.336
R_P, R_{WP}, R_{Bragg}, χ^2	0.014, 0.018, 0.005, 0.832	0.014, 0.019, 0.006, 0.810
Atomic parameters		
Sr1	2b (0, 0, ½) $U_{\text{iso}} = 152(5)$ pm ²	2b (0, 0, ½) $U_{\text{iso}} = 46(5)$ pm ²
Sr2	4e (0, 0, z) $z = 0.3604(1)$ $U_{\text{iso}} = 63(4)$ pm ²	4e (0, 0, z) $z = 0.3601(1)$ $U_{\text{iso}} = 26(4)$ pm ²
Sc1	4e (0, 0, z) $z = 0.0727(1)$ $U_{\text{iso}} = 116(7)$ pm ²	4e (0, 0, z) $z = 0.0730(1)$ $U_{\text{iso}} = 58(7)$ pm ²
Fe1	4d (0, ½, ¼) $U_{\text{iso}} = 115(5)$ pm ²	4d (0, ½, ¼) $U_{\text{iso}} = 33(5)$ pm ²
As1	4e (0, 0, z) $z = 0.1996(1)$ $U_{\text{iso}} = 151(5)$ pm ²	4e (0, 0, z) $z = 0.2002(1)$ $U_{\text{iso}} = 83(5)$ pm ²
O1	8g (0, ½, z) $z = 0.0828(1)$ $U_{\text{iso}} = 97(10)$ pm ²	8g (0, ½, z) $z = 0.0826(1)$ $U_{\text{iso}} = 79(10)$ pm ²
O2	2a (0, 0, 0) $U_{\text{iso}} = 97(10)$ pm ²	2a (0, 0, 0) $U_{\text{iso}} = 79(10)$ pm ²

Bond lengths (pm)				
Sr–O	$254.6(2) \times 4$	$288.4(1) \times 4$	$254.7(2) \times 4$	$287.9(1) \times 4$
	$301.6(3) \times 8$		$299.9(3) \times 8$	
Sc–O	$195.1(2) \times 1$	$205.7(1) \times 4$	$194.8(2) \times 1$	$205.2(1) \times 4$
Fe–Fe	$288.4(1) \times 4$		$287.9(1) \times 4$	
Fe–As	$244.8(1) \times 4$		$243.1(1) \times 4$	
Bond angles (°)				
As–Fe–As	$107.8(1) \times 4$	$112.8(1) \times 2$ (ϵ)	$107.4(1) \times 4$	$113.8(1) \times 2$ (ϵ)
O–Sc–O	$89.0(1) \times 4$	$97.6(1) \times 4$	$89.1(1) \times 4$	$97.1(1) \times 4$
	$164.9(2) \times 2$		$165.8(2) \times 2$	

Table 11.1: Crystallographic data of $\text{Sr}_3\text{Sc}_2\text{O}_5\text{Fe}_2\text{As}_2$ at 300 and 10 K.

a) Exclusion due to artefacts from the HUBER G670 low-temperature option.

Figure 11.4: Variation of the lattice parameters and As–Fe–As angle (ϵ) of $\text{Sr}_3\text{Sc}_2\text{O}_5\text{Fe}_2\text{As}_2$ with temperature. Lattice parameter errors are within data points.

11.3 Structural relationships

The structure of Sr₃Sc₂O₅Fe₂As₂, space group *I4/mmm*, Wyckoff sequence *ge³dba*, is closely related to other structures with different composition. The different site occupancy variants and the corresponding free *z* parameters for the 8*g* (0, 1/2, *z*) and 4*e* (0, 0, *z*) sites are listed in Table 11.2. The first representative of this structure type was the mineral chalcotallite (K,Tl)₂Cu₇SbS₄.^[207] Later, the ternary germanides SmNi₃Ge₃^[208] and U₃Co₄Ge₇^[209] and the quaternary and quinary compounds listed in Table 11.2 have been reported.

The large structural diversity of this structure type enables the formation of FeAs, CuS, CoGe, NiGe, and PtP tetrahedral layers, which can be separated by either intermetallic or oxidic layers, leading to different bonding patterns. The tetrahedral layers consist of the atoms at Wyckoff positions 4*e* (4th column in Table 11.2) and 4*d* (6th column in Table 11.2). It is noteworthy that for some representatives, the transition metal atoms switch between the 4*e* and 4*d* sites, but this does not follow the course of electronegativities.

Although the atoms occupy the same Wyckoff positions, nature allows for variations in the different compounds, i.e. the lattice parameters and the free *z* parameters of the 8*g* and 4*e* sites. This allows a high flexibility for this structural arrangement. A careful inspection of the *z* parameters listed in Table 11.2 readily reveals differences between the eight compounds. Based on this comparison, the eight compounds can be divided into two groups. The first group consists of Sr₃Sc₂O₅Fe₂As₂, Sr₃Fe₂O₅Cu₂S₂, Sr₃Sc₂O₅Cu₂S₂, and (K/Tl)₂Cu₇SbS₄, and the second group of U₃Co₄Ge₇, SmNi₃Ge₃, Eu₂Pt₇AlP_{2.95}, and Eu₂Pt_{7.3}Mg_{0.7}P₃. Since these structural differences significantly affect the chemical bonding, these two groups of compounds are isopointal^{[210], xviii, [211]} rather than strictly isotypic.

^{xviii} According to IUCr, two structures are isopointal if

(i) they have the same space-group type or belong to a pair of enantiomorphic space-group types

(ii) the atomic positions, occupied either fully or partially at random, are the same in both structures, i.e. the complete sequence of the occupied Wyckoff positions (including the number of times each Wyckoff position is occupied) is the same for both structures when the structural data have been standardised.

Compound	8g (z)	4e (z)	4e (z)	4e (z)	4d	2b	2a	Ref.
Sr ₃ Sc ₂ O ₅ Fe ₂ As ₂	O1 (0.0828)	Sr2 (0.6396)	As1 (0.1996)	Sc1 (0.0727)	Fe1	Sr1	O2	-
Sr ₃ Fe ₂ O ₅ Cu ₂ S ₂	O1 (0.0798)	Sr2 (0.6418)	S (0.1956)	Fe (0.0718)	Cu	Sr1	O2	[212]
Sr ₃ Sc ₂ O ₅ Cu ₂ S ₂	O1 (0.087)	Sr2 (0.6431)	S (0.195)	Sc (0.073)	Cu	Sr1	O2	[213]
(K/Tl) ₂ Cu ₇ SbS ₄	Cu1 (0.0570)	Tl+K (0.6483)	S2 (0.214)	S1 (0.093)	Cu2	Sb	Cu3	[207]
U ₃ Co ₄ Ge ₇	Ge2 (0.08041)	U2 (0.67001)	Ge3 (0.2025)	Co1 (0.1174)	Co2	Ge1	U1	[209]
SmNi ₃ Ge ₃	Ni1 (0.0553)	Sm (0.6535)	Ni2 (0.1999)	Ge1 (0.1063)	Ge2	Ge4	Ge3	[208]
Eu ₂ Pt ₇ AlP _{2.95}	Pt3 (0.0705)	Eu (0.6652)	Pt1 (0.2074)	P2 (0.1195)	P1	Al	Pt2	[214]
Eu ₂ Pt _{7.3} Mg _{0.7} P ₃	Pt3 (0.0734)	Eu (0.6665)	Pt1 (0.2080)	P2 (0.1214)	P1	Mg _{0.7} Pt _{0.3}	Pt2	[214]

Table 11.2: Site occupancies for tetragonal structures with the Pearson symbol *tl28* (no. 139), space group *I4/mmm*, and the Wyckoff sequence *ge³dba*. The *z* parameters of the 8*g* and 4*e* sites (if refined) are listed in parentheses. These *z* parameters correspond to settings (0, 1/2, *z*) for the 8*g* and (0, 0, *z*) for the 4*e* sites.

11.4 Magnetism and Mössbauer spectroscopy

Figure 11.5 shows the magnetic susceptibility of Sr₃Sc₂O₅Fe₂As₂ at 100 Oe. It can be seen that Sr₃Sc₂O₅Fe₂As₂ is a substance, which does not show any signs of magnetic ordering or phase transition in the whole temperature range between 1.8 and 300 K. However, as in other non-superconducting iron arsenide parent compounds, the susceptibility is several orders of magnitude higher than expected for a Pauli-paramagnetic metal. Above ~ 100 K, the susceptibility linearly increases with temperature. This feature was also observed in other iron pnictide parent compounds (refer to Chapters 4.4 and 7.1.3 for example).

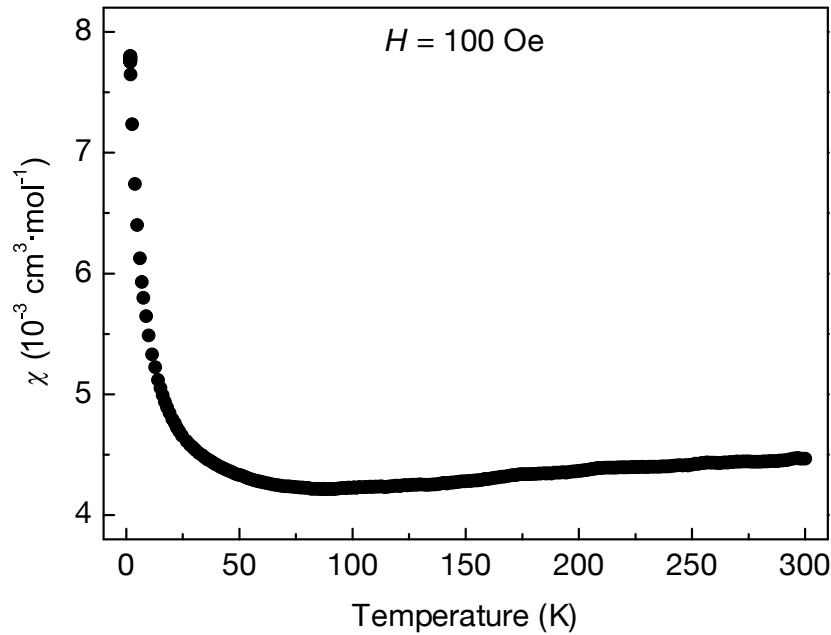
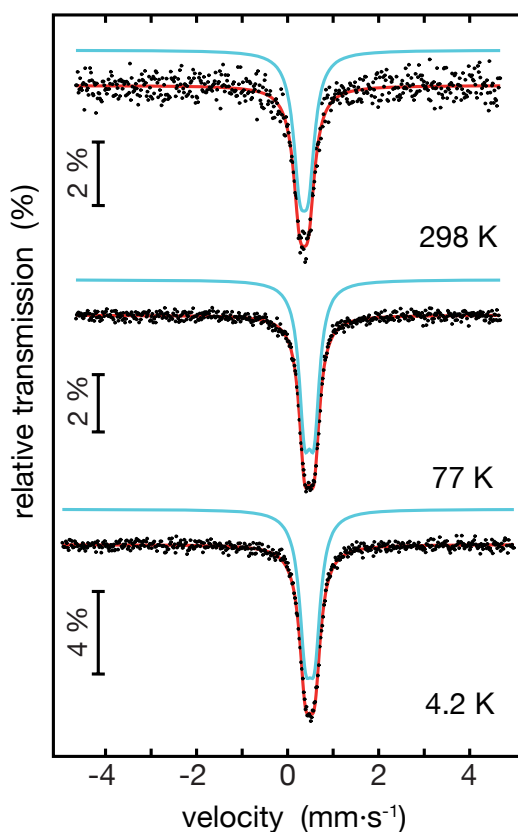


Figure 11.5: Magnetic susceptibility of Sr₃Sc₂O₅Fe₂As₂ at 100 Oe.

⁵⁷Fe Mössbauer spectra of Sr₃Sc₂O₅Fe₂As₂ at various temperatures are presented in Figure 11.6 together with transmission integral fits. The corresponding fitting parameters are listed in Table 11.3. In accordance with the presence of a single Fe site, a single signal was observed at an isomer shift of $\delta = 0.36(1) \text{ mm} \cdot \text{s}^{-1}$ and an experimental line width $\Gamma = 0.34(1) \text{ mm} \cdot \text{s}^{-1}$ subject to quadrupole splitting of $\Delta E_Q = 0.19(1) \text{ mm} \cdot \text{s}^{-1}$ at room temperature. The non-cubic site symmetry ($\bar{4}m2$) of the iron atoms is reflected in the quadrupole splitting value. For 77 and 4.2 K, single signals were observed at isomer shifts $\delta = 0.47(1) \text{ mm} \cdot \text{s}^{-1}$ and $\delta = 0.49(1) \text{ mm} \cdot \text{s}^{-1}$, respectively. The increase of the isomer shift with decreasing temperature can be considered as a second-order Doppler shift (SODS).^{xix, [215]} These parameters compare well with ⁵⁷Fe-Mössbauer data of LaFeAsO,^[102] LaFePO (Chapter 3.2), SrFe₂As₂ (Chapter 8.3) and BaFe₂As₂ (Chapter 7.1.2). Down to 4.2 K, the ⁵⁷Fe Mössbauer spectra of Sr₃Sc₂O₅Fe₂As₂ give no hint for magnetic ordering, which is consistent with the magnetic data.

^{xix} The Second-Order Doppler Shift is a temperature-dependent effect on the centre shift of a Mössbauer spectrum. Above 0 K, atoms in a lattice oscillate about their mean position. Although the frequency of this oscillation is such high that the mean displacement during the lifetime of a Mössbauer event is zero, the second term in the Doppler shift depends on v^2 , leading to the mean square displacement being non-zero.

Figure 11.6: ^{57}Fe Mössbauer spectra of $\text{Sr}_3\text{Sc}_2\text{O}_5\text{Fe}_2\text{As}_2$.

Temperature (K)	δ ($\text{mm}\cdot\text{s}^{-1}$)	Γ ($\text{mm}\cdot\text{s}^{-1}$)	ΔE_Q ($\text{mm}\cdot\text{s}^{-1}$)
298	0.36(1)	0.34(1)	0.19(1)
77	0.47(1)	0.30(1)	0.21(1)
4.2	0.49(1)	0.32(1)	0.20(1)

Table 11.3: Fitting parameters for ^{57}Fe Mössbauer spectroscopy data of $\text{Sr}_3\text{Sc}_2\text{O}_5\text{Fe}_2\text{As}_2$.

11.5 DFT calculations

A volume optimisation of $\text{Sr}_3\text{Sc}_2\text{O}_5\text{Fe}_2\text{As}_2$ has been performed via DFT calculations (WIEN2k) according to the method described in Chapter 2.1 (GGA, non-magnetic calculations). The results of this volume optimisation are depicted in Figure 11.7. In Table 11.4, the optimised calculated model is compared to the experimentally obtained crystal structure. The calculated lattice parameters and cell volume deviate

only 0.3 % or less from the experimentally obtained values and also the relaxed atomic parameters compare very well to the real structure (the differences between all calculated and observed atomic heights are less than 0.6 % of the *c* axis). This is in contrast to the findings in other iron arsenides like SrFeAsF, where the deviations between calculated and experimental structures are one order of magnitude larger (see also Chapter 4.5). The good agreement in the case of Sr₃Sc₂O₅Fe₂As₂ may be attributed to both the more rigid perovskite-like separation layers as well as the absence of structural and magnetic phase transitions.

	Experimental	Calculated (DFT)
Lattice parameters	<i>a</i> = 407.81(1) pm <i>c</i> = 2683.86(5) pm	<i>a</i> = 407.6 pm <i>c</i> = 2678.9 pm
Cell volume	<i>V</i> = 0.44635(2) nm ³	<i>V</i> = 0.44501 nm ³
Atomic parameters		
Sr1	2 <i>b</i> (0, 0, ½)	2 <i>b</i> (0, 0, ½)
Sr2	4 <i>e</i> (0, 0, <i>z</i>) <i>z</i> = 0.3604(1)	4 <i>e</i> (0, 0, <i>z</i>) <i>z</i> = 0.3577
Sc1	4 <i>e</i> (0, 0, <i>z</i>) <i>z</i> = 0.0727(1)	4 <i>e</i> (0, 0, <i>z</i>) <i>z</i> = 0.0744
Fe1	4 <i>d</i> (0, ½, ¼)	4 <i>d</i> (0, ½, ¼)
As1	4 <i>e</i> (0, 0, <i>z</i>) <i>z</i> = 0.1996(1)	4 <i>e</i> (0, 0, <i>z</i>) <i>z</i> = 0.2054
O1	8 <i>g</i> (0, ½, <i>z</i>) <i>z</i> = 0.0828(1)	8 <i>g</i> (0, ½, <i>z</i>) <i>z</i> = 0.0852
O2	2 <i>a</i> (0, 0, 0)	2 <i>a</i> (0, 0, 0)

Table 11.4: Comparison between calculated and experimental crystal structures of Sr₃Sc₂O₅Fe₂As₂.

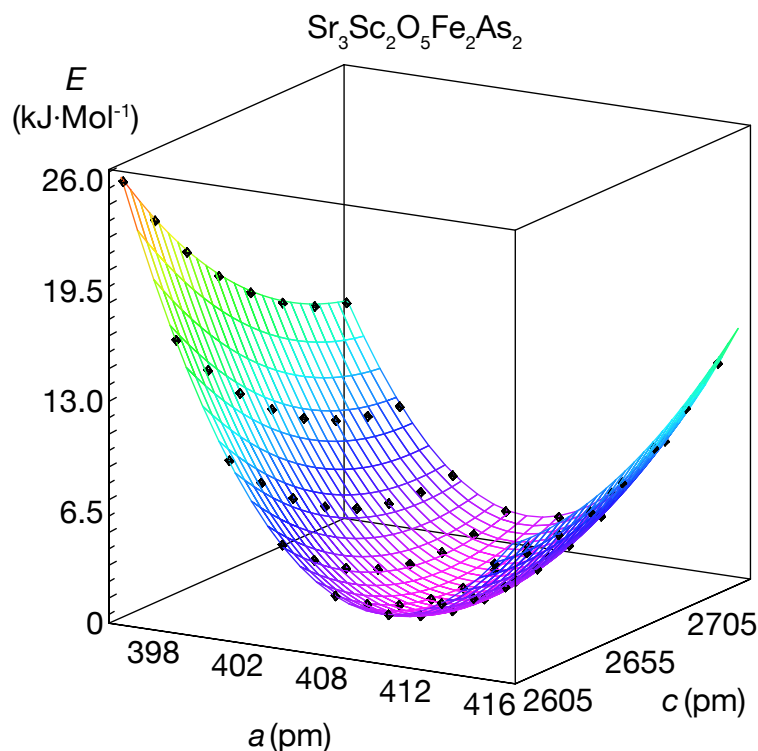


Figure 11.7: Energy dependence of the a and c lattice parameters in $\text{Sr}_3\text{Sc}_2\text{O}_5\text{Fe}_2\text{As}_2$. Black diamonds: DFT calculations.

In summary, the quinary 32522-type compound $\text{Sr}_3\text{Sc}_2\text{O}_5\text{Fe}_2\text{As}_2$ could be successfully synthesised via an alternative synthesis route. It was characterised by temperature-programmed powder diffraction, susceptibility measurements as well as Mössbauer spectroscopy. Despite $\text{Sr}_3\text{Sc}_2\text{O}_5\text{Fe}_2\text{As}_2$ resembling other iron arsenide parent compounds like LaFeAsO with respect to their crystal structures at room temperature, the physical properties of $\text{Sr}_3\text{Sc}_2\text{O}_5\text{Fe}_2\text{As}_2$ are different. $\text{Sr}_3\text{Sc}_2\text{O}_5\text{Fe}_2\text{As}_2$ neither exhibits a structural nor a superconducting nor any other magnetic phase transition. The reason for this behaviour, however, is still unclear. Mixing of the different transition metals as a cause for the absence of superconductivity, which can be expected to happen in other quinary systems (see Chapters 13.8 and 14.3), seems to be hardly possible here, as the atomic radii of Sr and Sc are quite different.

DFT calculations were carried out in order to perform a structure optimisation, which was then related to the experimental crystal structure. It could be shown that the calculated model is very close to the experimental findings. Additionally, a short

crystallographic overview on $\text{Sr}_3\text{Sc}_2\text{O}_5\text{Fe}_2\text{As}_2$ and its relation to seven other closely related compounds was given, which manifests the large potential of this and other stacking variants of compounds with tetrahedral layers. For the future, one can therefore expect a rich variety of further compounds having a rather complex crystal structure and also new discoveries of iron-based superconductors and parent compounds.

12. Ba₂ScO₃FeAs

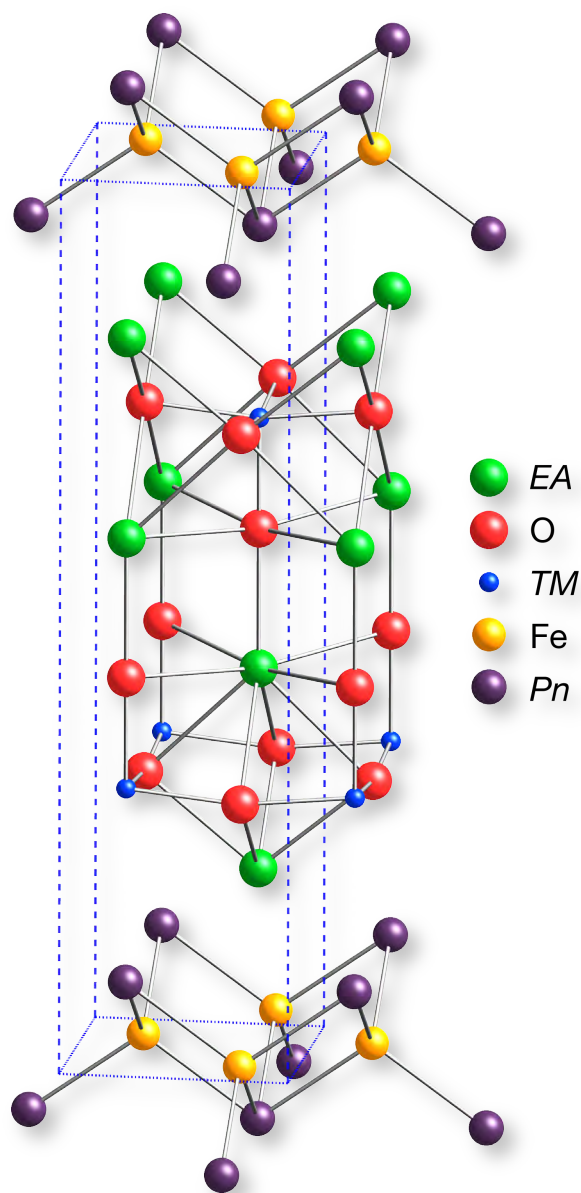


Figure 12.1: Crystal structure of Ba₂ScO₃FeAs (*EA* = Ba, *TM* = Sc, *Pn* = As).

As it has been discussed in the previous chapter, Sr₃Sc₂O₅Fe₂As₂ has been the first reported compound with a lower dimensionality than in the 1111 compounds. In this chapter, the new iron arsenide oxide Ba₂ScO₃FeAs, the first member of the new 21311 family is presented. It is an iron arsenide with Sr₂GaO₃CuS-type structure and just like Sr₃Sc₂O₅Fe₂As₂, Ba₂ScO₃FeAs is a compound with iron arsenide tetrahedral layers separated by perovskite-like metal oxide interlayers. Yet, the interlayer dis-

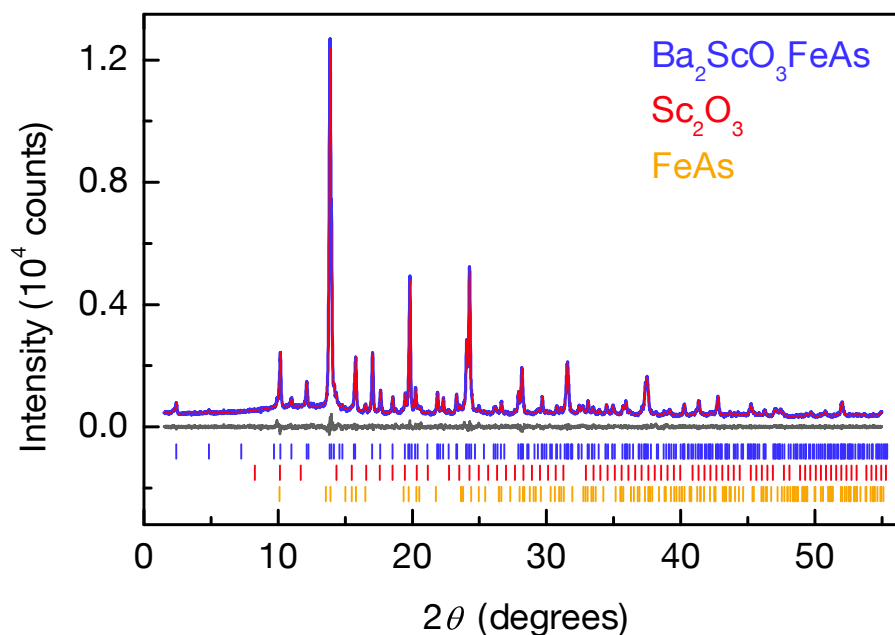
tance between two iron arsenide slabs is even larger (Figure 12.1). The crystal structure of Ba₂ScO₃FeAs was determined via X-ray powder diffraction and the physical properties were characterised by magnetic susceptibility and electrical resistivity measurements, as well as ⁵⁷Fe Mössbauer spectroscopy. Furthermore, the electronic structure of Ba₂ScO₃FeAs is compared with the parent compounds of the superconducting iron arsenides.

12.1 Synthesis

Ba₂ScO₃FeAs was synthesised by heating stoichiometric mixtures of barium, scandium, iron (III) oxide and arsenic oxide in alumina crucibles sealed in silica ampoules under an atmosphere of purified argon according to the method described in Chapter 2.10.3. The mixtures were heated to 1323 K at a rate of 80 K·h⁻¹, kept at this temperature for 60 h and cooled down to room temperature. The products were homogenised in an agate mortar, pressed into pellets and sintered at 1323 K for 60 h, reground, pressed into pellets and sintered again at 1323 K for 50 h.

12.2 Crystal structure

The crystal structure of Ba₂ScO₃FeAs is isotypic to the oxide sulfide Sr₂GaO₃CuS,^[203b] which crystallises in the space group *P4/nmm*. Figure 12.2 shows X-ray powder patterns, which could be fitted with a tetragonal Ba₂ScO₃FeAs phase, as well as Sc₂O₃ and FeAs as minor impurity phases. The crystal structure of Ba₂ScO₃FeAs is shown in Figure 12.1. Crystallographic data, selected bond lengths and the parameters of the Rietveld fits are compiled in Table 12.1. Further details of the structure determination may be obtained from Fachinformationszentrum Karlsruhe, 76344 Eggenstein-Leopoldshafen, Germany on quoting the Registry No. CSD-420654.

Figure 12.2: Rietveld fit of Ba₂ScO₃FeAs at 297 K (space group *P4/nmm*).

Temperature	297 K
Diffractometer	STOE STADI P (Mo-K α_1)
Rietveld package	TOPAS
Space group	<i>P4/nmm</i> (<i>o2</i>)
Lattice parameters	$a = 412.66(5)$ pm $c = 1680.0(2)$ pm
Cell volume	$V = 0.28609(7)$ nm ³
Z	2
Data points	5350
Reflections	259 (main phase)
Constraints	1
Atomic variables	12
Profile variables	5
Anisotropy var.	24
Background var.	48
Imp. phase var.	20
Other variables	12
<i>d</i> range	0.763 – 16.800
$R_p, R_{wp}, R_{Bragg}, \chi^2$	0.036, 0.047, 0.008, 1.186
CSD No.	420654

Atomic parameters			
Ba1	2c ($\frac{3}{4}, \frac{3}{4}, z$)	$z = 0.1860(1)$	$U_{\text{iso}} = 163(6) \text{ pm}^2$
Ba2	2c ($\frac{3}{4}, \frac{3}{4}, z$)	$z = 0.4145(1)$	$U_{\text{iso}} = 129(6) \text{ pm}^2$
Sc1	2c ($\frac{1}{4}, \frac{1}{4}, z$)	$z = 0.3092(4)$	$U_{\text{iso}} = 61(14) \text{ pm}^2$
Fe1	2a ($\frac{3}{4}, \frac{1}{4}, 0$)		$U_{\text{iso}} = 190(11) \text{ pm}^2$
As1	2c ($\frac{1}{4}, \frac{1}{4}, z$)	$z = 0.0777(2)$	$U_{\text{iso}} = 103(11) \text{ pm}^2$
O1	4f ($\frac{1}{4}, \frac{3}{4}, z$)	$z = 0.2898(7)$	$U_{\text{iso}} = 262(32) \text{ pm}^2$
O2	2c ($\frac{1}{4}, \frac{1}{4}, z$)	$z = 0.427(1)$	$U_{\text{iso}} = 262(32) \text{ pm}^2$
Bond lengths (pm)			
Ba–O	266(2) × 1	270.2(8) × 4	292.6(2) × 4 294.0(9) × 4
Sc–O	198(2) × 1	208.9(2) × 4	
Fe–Fe	291.8(1) × 4		
Fe–As	244.1(2) × 4		
Bond angles (°)			
As–Fe–As	106.6(1) × 4	115.4(1) × 2 (ε)	
O–Sc–O	88.6(1) × 4	99.0(4) × 4	162.1(7) × 2

Table 12.1: Crystallographic data of Ba₂ScO₃FeAs at 297 K.

The FeAs layers perpendicular to the *c* axis are separated by barium atoms from scandium oxide and barium oxide layers according to a stacking order (ScO₂)(BaO)(BaO)(ScO₂). The interlayer distance of the iron arsenide layers equals the *c* lattice parameter for this structure type, thus Ba₂ScO₃FeAs (*c* = 1680 pm) exhibits a very high iron arsenide interlayer distance. Additionally recorded temperature-dependent powder patterns (Huber G670) did not reveal any structural phase transition down to 10 K (Figure 12.3). At 10 K, the corresponding lattice parameter *a* is decreased by 0.92 pm and the *c* lattice parameter by 6.0 pm. In contrast to Sr₃Sc₂O₅Fe₂As₂ (Chapter 11.2) the As–Fe–As angles are constant in Ba₂ScO₃FeAs at all temperatures within the errors of the refinement.

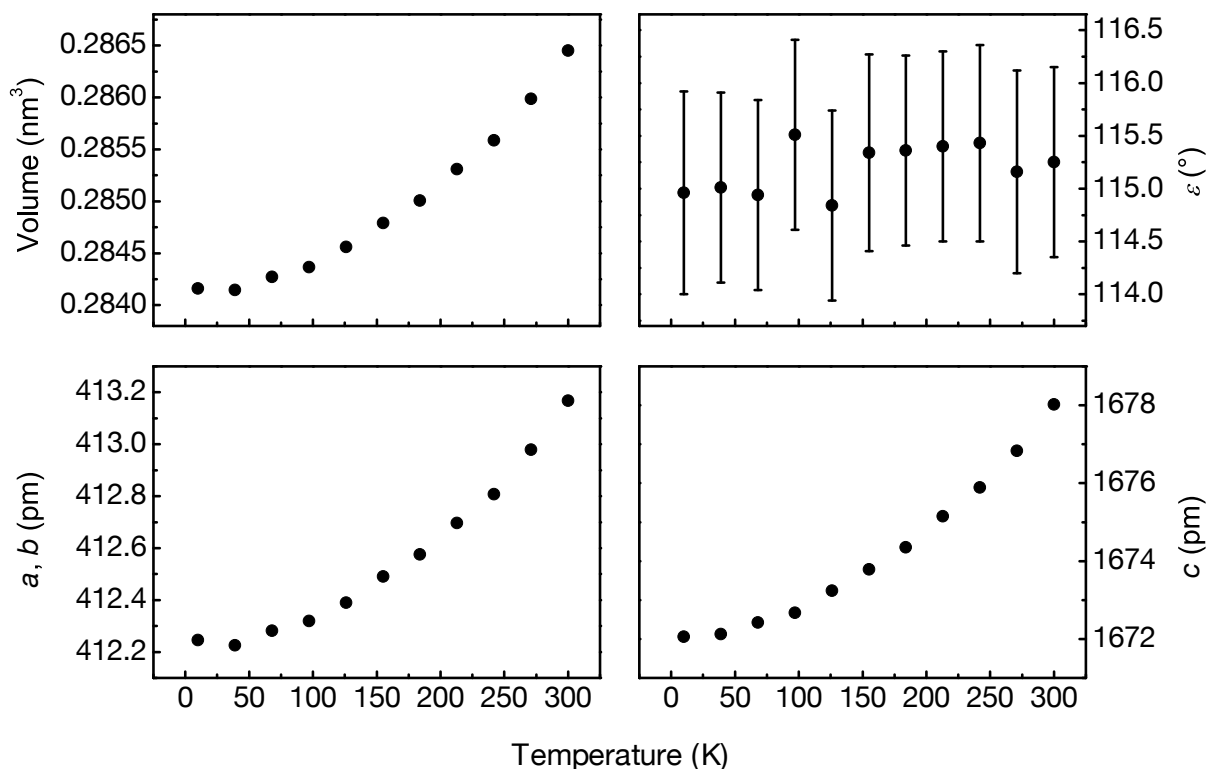


Figure 12.3: Variation of the lattice parameters and refined As–Fe–As angle (ε) with temperature (Huber G670). Lattice parameter errors are within data points.

12.3 Magnetism, resistivity and Mössbauer spectroscopy

Figure 12.4 shows the magnetic susceptibility of Ba₂ScO₃FeAs between 1.8 and 300 K. The observed paramagnetism is several orders of magnitude too high for Pauli-paramagnetism. No sign of any anomaly in the course of the magnetic susceptibility at any applied external magnetic field was visible. The increase of the susceptibility at low temperatures as well as the form of the hysteresis loop at 1.8 K is possibly due to the presence of a ferromagnetic impurity. The resistivity of Ba₂ScO₃FeAs is depicted in Figure 12.5. It is a poor metal in the whole measured temperature range and does not show any anomaly. Both magnetism and resistivity therefore indicate that there is no occurrence of a spin-density wave anomaly in Ba₂ScO₃FeAs.

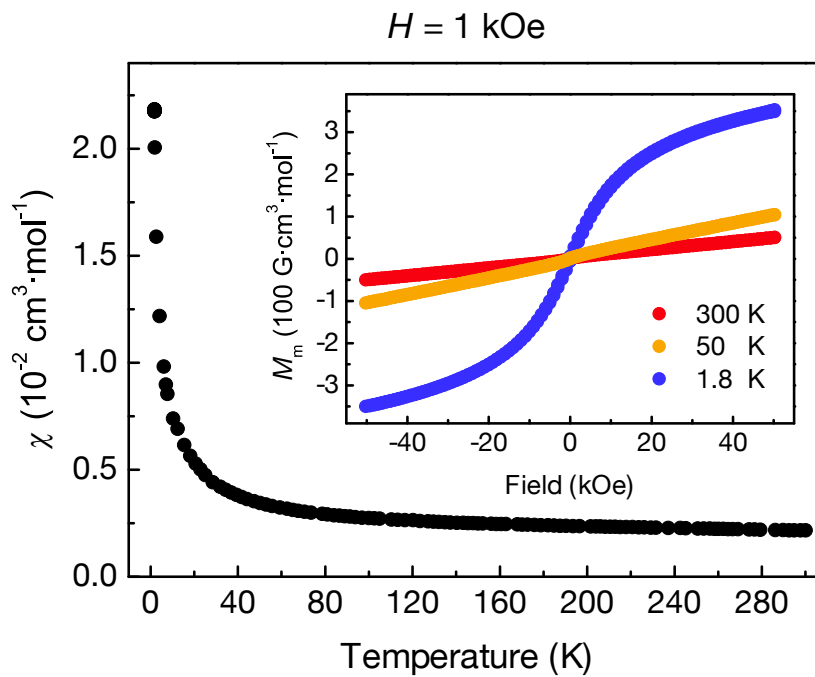


Figure 12.4: Magnetic susceptibility of Sr₃Sc₂O₅Fe₂As₂ at 100 Oe. Inset: Hysteresis loops.

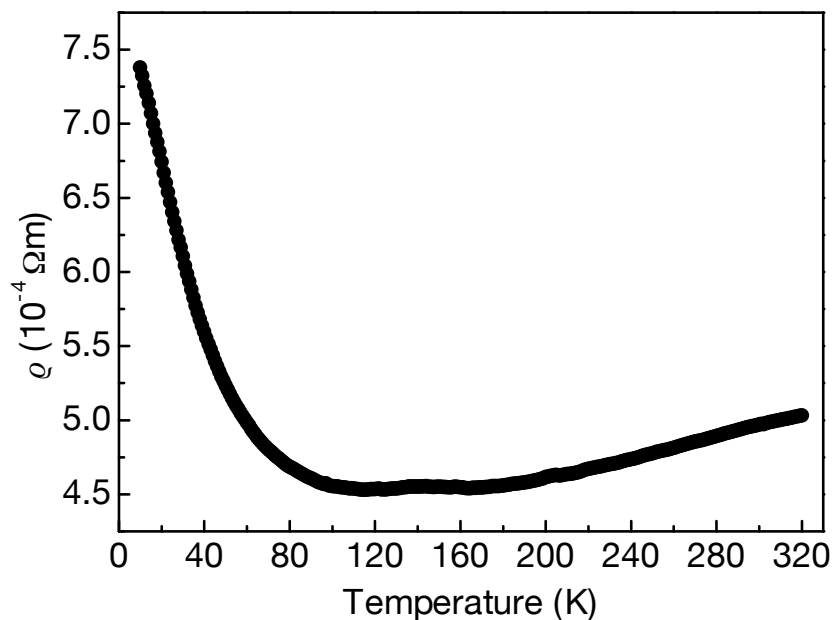


Figure 12.5: Resistivity of Ba₂ScO₃FeAs.

Figure 12.6 shows the ⁵⁷Fe Mössbauer spectra of the Ba₂ScO₃FeAs sample at various temperatures together with transmission integral fits. The fitting parameters are listed in Table 12.2. In agreement with the single Fe site in the crystal structure, the

spectra at 298, 77, and 4.2 K show single signals, which are subject to weak quadrupole splitting. The 77 K isomer shifts of Ba₂ScO₃FeAs (Table 12.2), Sr₃Sc₂O₅Fe₂As₂ (Chapter 11.4), and Sr₂CrO₃FeAs (Chapter 13.4) are almost identical. One can thus assume a similar electronic situation within the tetrahedral FeAs layers in all three compounds. They are also comparable to LaFePO (Chapter 3.2) and SrFe₂As₂ (Chapter 8.3). The increase of the isomer shift with decreasing temperature (0.35 → 0.50 mm·s⁻¹) results from a second-order Doppler shift. The spectra give no hint for magnetic ordering of the iron moments down to 4.2 K.

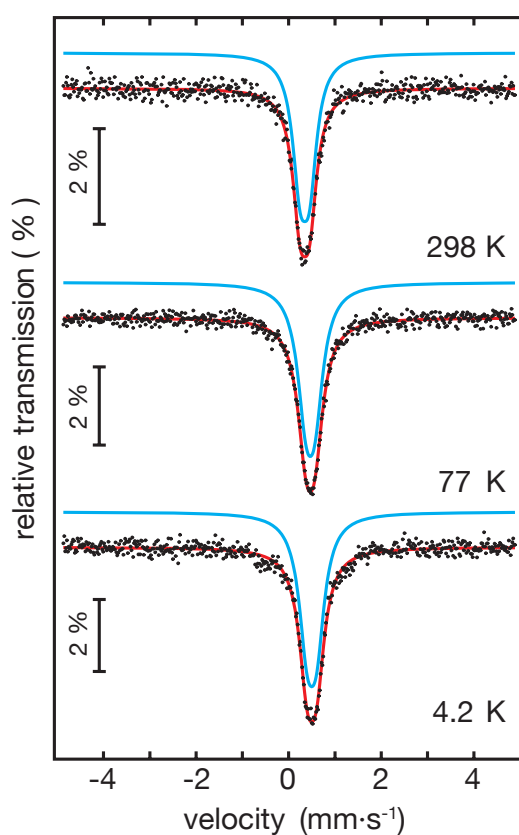


Figure 12.6: ⁵⁷Fe Mössbauer spectra of Ba₂ScO₃FeAs.

Temperature (K)	δ (mm·s ⁻¹)	Γ (mm·s ⁻¹)	ΔE_Q (mm·s ⁻¹)
298	0.35(1)	0.39(1)	0.21(1)
77	0.47(1)	0.45(1)	0.20(1)
4.2	0.50(1)	0.43(2)	0.20(1)

Table 12.2: Fitting parameters for ⁵⁷Fe Mössbauer spectroscopy data of Ba₂ScO₃FeAs.

12.4 Electronic structure

The electronic structures of the iron arsenide superconductors have frequently been described^[216] and some (maybe hidden) electronic order with respect to superconductivity is still under discussion.^[217] Also Sr₃Sc₂O₅Fe₂As₂ and the superconducting phosphide Sr₂ScO₃FeP have been studied.^[218] In all cases, the calculations predict a Fermi surface consisting of hole-like pockets at the centre of the Brillouin zone (Γ) and similar electron-like pockets at the corners (M), which become largely congruent by a nesting vector (π, π) . This Fermi surface nesting is an unstable situation and typically favours charge-density or spin-density ordering, often connected with structural distortions. For details, also refer to Chapter 1.1.2. Therefore, the band structure of Ba₂ScO₃FeAs was calculated in order to examine if the rather large metal oxide building blocks between the FeAs layers induce any perceptible perturbation of the bands close to the Fermi level and thus Fermi surface.

DFT calculations were performed according to Chapter 2.1 with the WIEN2k program package. 4374 k -points ($27 \times 27 \times 6$ mesh) were used in the irreducible wedges of the Brillouin zones. The basis sets consisted of 4192 plane-waves up to a cut-off $r_{\text{mt}} \cdot k_{\text{max}} = 8.0$. The atomic sphere radii r_{mt} were 2.50 (Ba), 1.97 (Sc), 2.43 (Fe), 2.16 (As) and 1.75 au (O).

The band structure of Ba₂ScO₃FeAs (Figure 12.7, left) shows the typical features known from the iron arsenide superconductors.^[216a] Iron 3d band contributions (emphasised in Figure 12.7, left) clearly dominate the vicinity of the Fermi level, where no significant contributions of the oxide layers are found. Also the Fermi surface (Figure 12.7, right) reveals the typical cylinders around Γ and M and provides the unstable nesting situation mentioned above. Thus, from the view of the electronic structure, one would expect structural and magnetic anomalies in Ba₂ScO₃FeAs. The origin of the absence of a structural or magnetic instability and superconductivity in this and the related compounds is unclear and still under investigation.

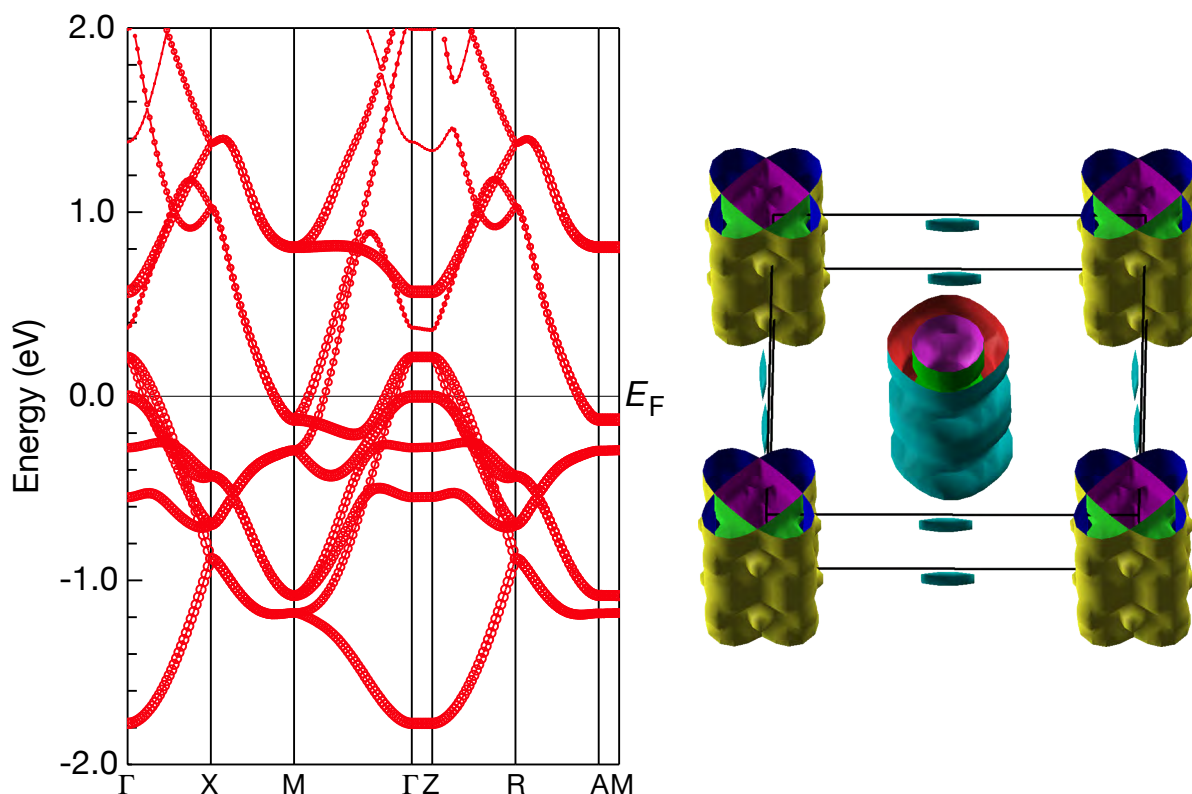


Figure 12.7: Left: Section of the band structure of Ba₂ScO₃FeAs with the iron 3d contributions emphasised (GGA, WIEN2k). Right: The Fermi surface showing the typical cylinders around the centre (Γ , hole-like) and the corners (M, electron-like).

In conclusion, the new iron arsenide oxide Ba₂ScO₃FeAs crystallises in the tetragonal Sr₂GaO₃CuS-type structure and exhibits a large distance between the FeAs layers due to separation by large perovskite-like metal oxide blocks. Only the recently discovered iron arsenides of the type Ca_{*n*+1}(Sc,Ti)_{*n*}O_{*y*}Fe₂As₂^[219] exhibit even higher iron arsenide interlayer distances. Ba₂ScO₃FeAs is a poor metal and does not show any structural or magnetic anomaly, even though the electronic structure predicts a nested Fermi surface. ⁵⁷Fe-Mössbauer spectra are in agreement with the absence of magnetic ordering at the iron site. Interestingly, the closely related compound Sr₂ScO₃FeAs possibly shows antiferromagnetic order of the iron atoms as it has been proposed recently due to Mössbauer and μ SR spectroscopy experiments.^[220] Reasons for this situation, however, remain unclear and have to be investigated in

further detail.^{xx} Even though the absence of magnetic ordering in the formally undoped compound Ba₂ScO₃FeAs is puzzling, it should also be interesting to examine compounds where Sc is exchanged for other transition metals. As such d-metals can be magnetic due to unpaired electrons and as they also have different numbers of valence electrons, they may influence the local electronic structure of the iron arsenide layers. As a consequence, exchanging Sc for other transition metals could even induce superconductivity. This proved true for example for the compound Sr₂VO₃FeAs (Chapter 14). However, also Sr₂CrO₃FeAs, which is discussed in the next chapter, has very interesting and surprising properties.

^{xx} The relevant Mössbauer spectra in the literature are of relatively poor quality and also the observed ordered magnetic moment of $\sim 0.1 \mu_B$ per iron atom is spuriously small. However, the magnetically ordered volume fractions were determined to be 100 % in both the Mössbauer and μ SR experiments.

13. Sr₂CrO₃FeAs

In this chapter, the new iron arsenide oxide Sr₂CrO₃FeAs is discussed. It shares the key feature of tetragonal iron arsenide layers with other iron arsenide superconductors and is isotypic to the previously discussed Ba₂ScO₃FeAs (Chapter 12). The crystal structure of Sr₂CrO₃FeAs was determined via X-ray and neutron diffraction and the physical properties were characterised by magnetic susceptibility, electrical resistivity and ⁵⁷Fe Mössbauer spectroscopy measurements.

13.1 Synthesis (I)

A small sample (600 mg) of Sr₂CrO₃FeAs was synthesised according to the method described in Chapter 2.10.3 by heating a stoichiometric mixture of strontium, chromium, iron (III) oxide and arsenic oxide in alumina crucibles sealed in silica ampoules under an atmosphere of purified argon. The mixture was heated to 1323 K at a rate of 80 K·h⁻¹, kept at this temperature for 60 h and cooled down to room temperature. The products were homogenised in an agate mortar, pressed into pellets and sintered at 1323 K for 60 h, reground, pressed into pellets and sintered again at 1323 K for 50 h.

13.2 Crystal structure

The crystal structure of Sr₂CrO₃FeAs is isotypic to the oxide sulfide Sr₂GaO₃CuS^[203b] in the space group *P4/nmm*. Figure 13.1 shows a X-ray powder pattern, which could be completely fitted with one single phase using starting parameters from [203b]. Crystallographic data, selected bond lengths and the parameters of the Rietveld fits are compiled in Table 13.1. Further details of the structure determinations may be obtained from Fachinformationszentrum Karlsruhe, 76344 Eggenstein-Leopoldshafen, Germany on quoting the Registry No. CSD-420653.

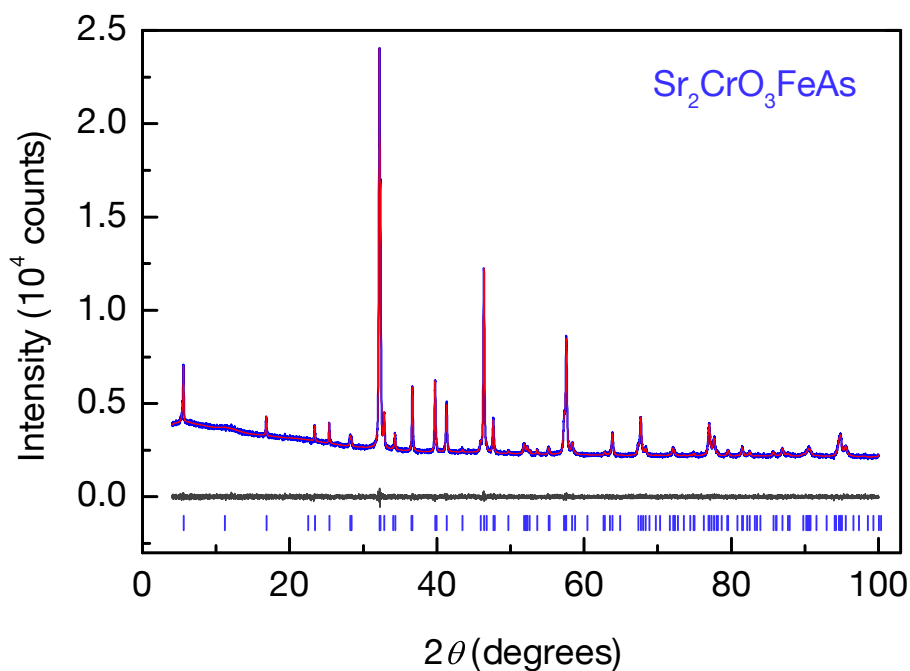


Figure 13.1: Rietveld fit of the 600 mg sample Sr₂CrO₃FeAs at 297 K (space group *P4/nmm*).

Temperature	297 K
Diffractometer	STOE STADI P (Cu-K α_1)
Rietveld package	TOPAS
Space group	<i>P4/nmm</i> (<i>o2</i>)
Lattice parameters	$a = 391.12(1)$ pm $c = 1579.05(3)$ pm
Cell volume	$V = 0.24156(1)$ nm ³
Z	2
Data points	9600
Reflections	108
Constraints	0
Atomic variables	13
Profile variables	5
Anisotropy var.	12
Background var.	48
Imp. phase var.	0
Other variables	8
<i>d</i> range	1.003 – 15.790
R_p, R_{wp}, R_{Bragg}, χ^2	0.014, 0.018, 0.002, 0.969
CSD No.	420653

Atomic parameters			
Sr1	2c (3/4, 3/4, z)	z = 0.1957(2)	$U_{\text{iso}} = 83(5) \text{ pm}^2$
Sr2	2c (3/4, 3/4, z)	z = 0.4150(1)	$U_{\text{iso}} = 98(7) \text{ pm}^2$
Cr1	2c (1/4, 1/4, z)	z = 0.3108(2)	$U_{\text{iso}} = 88(9) \text{ pm}^2$
Fe1	2a (3/4, 1/4, 0)		$U_{\text{iso}} = 77(8) \text{ pm}^2$
As1	2c (1/4, 1/4, z)	z = 0.0899(2)	$U_{\text{iso}} = 79(8) \text{ pm}^2$
O1	4f (1/4, 3/4, z)	z = 0.2931(4)	$U_{\text{iso}} = 78(22) \text{ pm}^2$
O2	2c (1/4, 1/4, z)	z = 0.4313(6)	$U_{\text{iso}} = 88(30) \text{ pm}^2$
Bond lengths (pm)			
Sr–O	242.7(9) × 1	248.8(4) × 4	274.4(5) × 4 277.8(1) × 4
Cr–O	190(1) × 1	197.5(1) × 4	
Fe–Fe	276.6(1) × 4		
Fe–As	241.7(2) × 4		
Bond angles (°)			
As–Fe–As	110.2(1) × 4	108.0(1) × 2 (ε)	
O–Cr–O	88.9(1) × 4	98.1(2) × 4	163.7(4) × 2

Table 13.1: Crystallographic data of the 600 mg sample Sr₂CrO₃FeAs at 297 K.

In comparison with Ba₂ScO₃FeAs (Chapter 12.2), the Fe–As bonds are shorter and the FeAs_{4/4} tetrahedra are less distorted in Sr₂CrO₃FeAs ($\varepsilon = 108.0^\circ$ in Sr₂CrO₃FeAs vs. $\varepsilon = 115.4^\circ$ in Ba₂ScO₃FeAs). Also the Fe–Fe distance is significantly shorter in the strontium compound (276.6 pm) than in the barium compound (291.8 pm). This may be attributed to the lesser-required space of the strontium ions and it shows that the geometry of the FeAs layer is generally flexible and can be adapted to different oxide blocks. As for Ba₂ScO₃FeAs, the powder patterns recorded at lower temperatures did not reveal any structural phase transitions in Sr₂CrO₃FeAs down to 10 K (Figure 13.2). At 10 K, the corresponding lattice parameter *a* is decreased by 0.73 pm and the *c* lattice parameter by 8.4 pm in Sr₂CrO₃FeAs. Unlike in Sr₃Sc₂O₅Fe₂As₂, the more pronounced shrinkage of the *c* axis in comparison to the *a* axis on cooling does not lead to an increase of the vertical As–Fe–As angle (ε) but rather a slight decrease of about 0.5°.

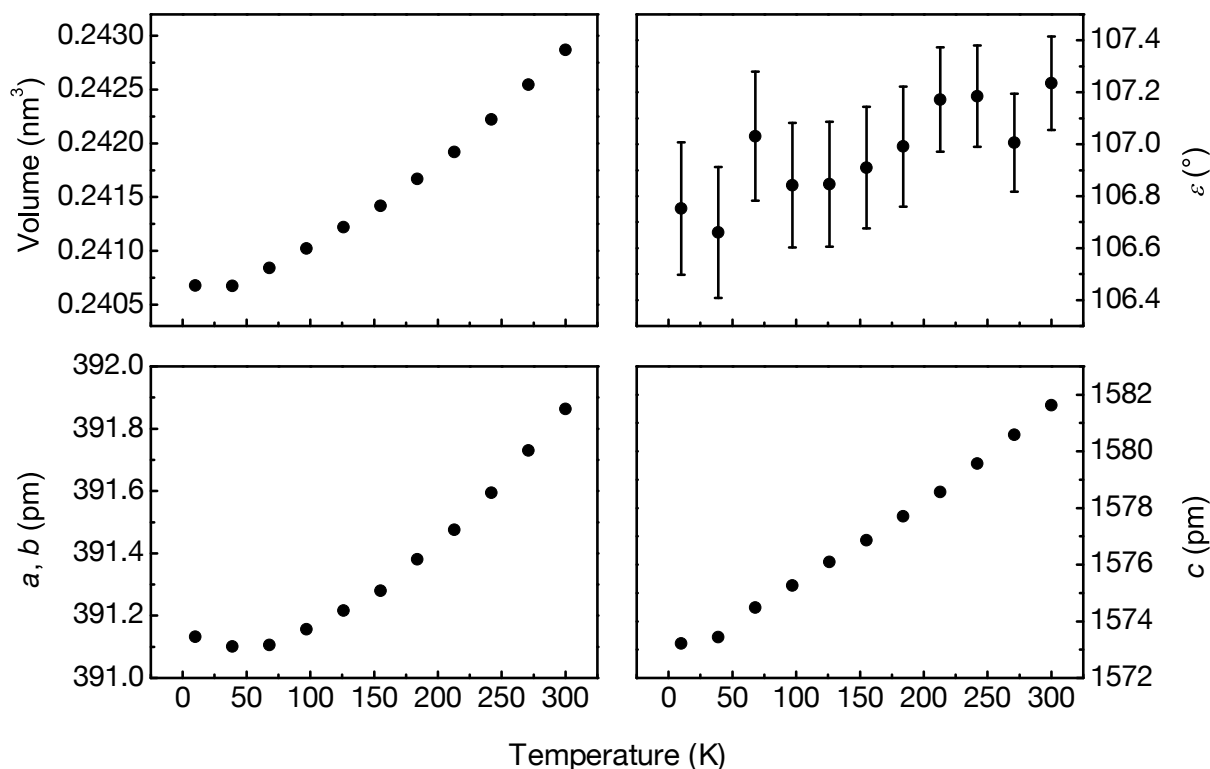


Figure 13.2: Variation of the lattice parameters and refined As–Fe–As angle (ε) with temperature (Huber G670). Lattice parameter errors are within data points.

13.3 Magnetic susceptibility and resistivity

Figure 13.3 (left) shows the magnetic susceptibility of Sr₂CrO₃FeAs between 1.8 and 360 K. The compound obeys the Curie-Weiss law above ~ 160 K. An effective magnetic moment of $3.83(3) \mu_B$ was found, which is in good agreement with the theoretical spin-only value of $3.87 \mu_B$ for Cr³⁺ ($S = 3/2$). The paramagnetic temperature is $-141(3)$ K. Antiferromagnetic ordering is discernible and the highest susceptibility was reached at $T_N \approx 31$ K. Hysteresis loops reveal only traces of ferromagnetic impurities at 1.8 K (Figure 13.3, right). As will be discussed in Chapter 13.9, the origin of the anomaly around 120 K is due to short-ranged antiferromagnetic ordering of the compound at this temperature. Sr₂CrO₃FeAs does not show any sign of a spin-density wave anomaly in the course of the magnetic susceptibility at any applied external magnetic field. The resistivity of Sr₂CrO₃FeAs is depicted in Figure 13.4. It shows that Sr₂CrO₃FeAs is a poor metal over the whole measured temperature range and does not show any feature indicative of a SDW anomaly.

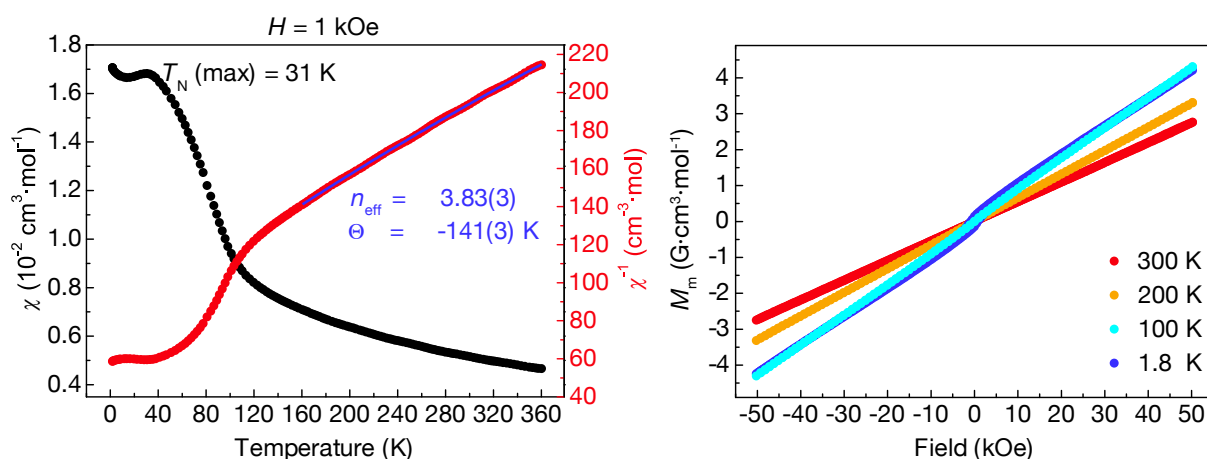


Figure 13.3: Left: Susceptibility (black) and inverse susceptibility (red) with Curie-Weiss fit (blue) of Sr₂CrO₃FeAs at 1 kOe. Right: Hysteresis loops.

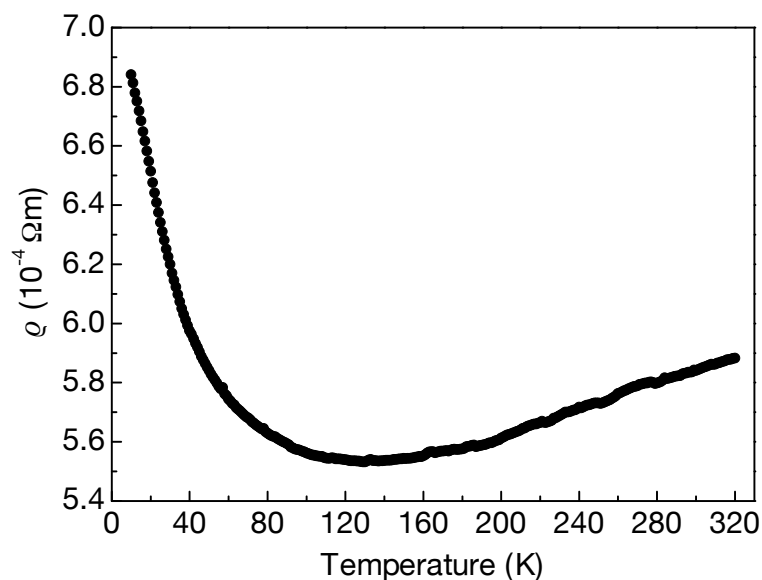


Figure 13.4: Resistivity of Sr₂CrO₃FeAs.

13.4 Mössbauer spectroscopy

The ⁵⁷Fe Mössbauer spectra collected for Sr₂CrO₃FeAs at various temperatures are shown in Figure 13.5 together with transmission integral fits. The corresponding fitting parameters are summarised in Table 13.2. As expected from the crystal structure (one iron site), the spectra at 298, 77, and 40 K are well reproduced with single signals, which are subject to weak quadrupole splitting due to the non-cubic site symmetry ($\bar{4}m2$) of the iron atoms. Within the standard deviations, the observed

isomer shift, the experimental line width, and the quadrupole splitting of $\text{Sr}_2\text{CrO}_3\text{FeAs}$ are almost identical with those obtained for $\text{Sr}_3\text{Sc}_2\text{O}_5\text{Fe}_2\text{As}_2$ (Chapter 11.4), indicating a similar electronic situation for the iron atoms in both arsenide oxides. The increase of the isomer shift with decreasing temperature ($0.29 \rightarrow 0.45 \text{ mm}\cdot\text{s}^{-1}$) is due to a second-order Doppler shift (SODS) well known for iron compounds.

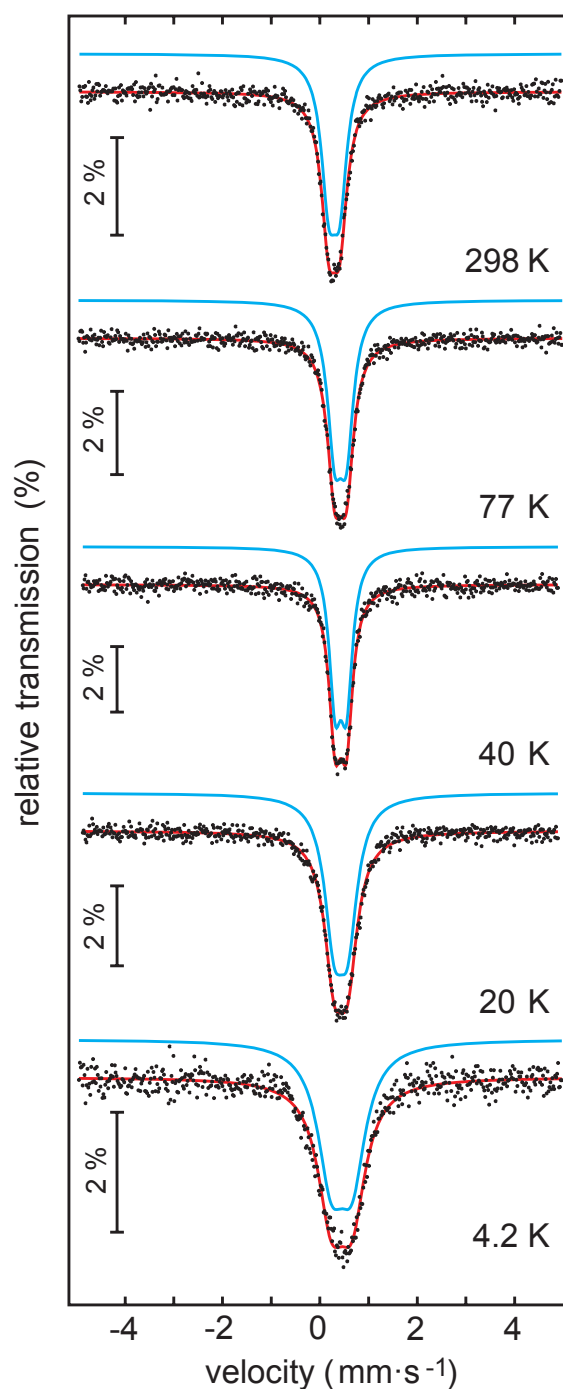


Figure 13.5: ^{57}Fe Mössbauer spectra of $\text{Sr}_2\text{CrO}_3\text{FeAs}$.

Temperature (K)	δ (mm·s ⁻¹)	Γ (mm·s ⁻¹)	ΔE_Q (mm·s ⁻¹)
298	0.29(1)	0.37(1)	0.22(1)
77	0.42(1)	0.36(1)	0.24(1)
40	0.43(1)	0.31(1)	0.23(1)
20	0.43(1)	0.48(1)	0.28(1)
4.2	0.45(1)	0.67(2)	0.43(1)

Table 13.2: Fitting parameters for ⁵⁷Fe Mössbauer spectroscopy data of Sr₂CrO₃FeAs.

In contrast to Sr₃Sc₂O₅Fe₂As₂ and Ba₂ScO₃FeAs (Chapter 11.4 and 12.3), where no magnetic ordering is observed down to 4.2 K, the chromium atoms in Sr₂CrO₃FeAs reveal antiferromagnetic ordering. This is also reflected in the ⁵⁷Fe Mössbauer spectra at 20 and 4.2 K, i.e. well below the Néel temperature. In the magnetically ordered regime, significant broadening of the Mössbauer signal was observed and the fits revealed increased line width and quadrupole splitting parameters. Since the transferred field (B_{hf}) is small, independent refinement of all parameters, δ , Γ , ΔE_Q , and B_{hf} showed strong correlations. In order to get an estimate for the transferred field, the 4.2 K spectrum was fitted with various fixed values for the hyperfine field. A reasonable fit was obtained for a fixed hyperfine field of 0.5 T and the refined values $\delta = 0.45(1)$ mm·s⁻¹, $\Gamma = 0.84(2)$ mm·s⁻¹, and $\Delta E_Q = 0.24(1)$ mm·s⁻¹. From these fitting tests a transferred hyperfine field of 0.5 ± 0.2 T at 4.2 K was estimated.

13.5 Absence of superconductivity

All these examinations clearly prove that Sr₂CrO₃FeAs is neither superconducting nor anomalous regarding the iron magnetism. This is quite surprising in the context of the closely related compound Sr₂VO₃FeAs being a superconductor. Sr₂VO₃FeAs even exhibits a relatively high T_C of up to 37 K (Chapter 14 and [206]). However, synthesis of single-phase samples of the 21311-compounds is generally difficult and published X-ray powder patterns of various compounds of this structural family revealed significant amounts of impurity phases. This is especially true in the case of the abovementioned superconductor Sr₂VO₃FeAs but also in the isotypic superconductor Sr₂(Mg,Ti)O₃FeAs;^[221] where the anticipated product is hardly even the main

phase of the sample. Such multi-phase samples casted serious doubts about the true chemical composition also of Sr₂CrO₃FeAs. These suspicions became even stronger when efforts to synthesise the new compound Sr₂O₂MnFe₂As₂ failed but resulted in the formation of Sr₂Mn₃O₂As₂, which was partially doped with iron at the Mn sites. These findings have suggested that at least partial mixing of different transition metals seems possible, which led to the synthesis of a larger sample of Sr₂CrO₃FeAs for a combined neutron and X-ray diffraction study and also for experiments with polarised neutrons. This allowed a precise redetermination of the crystal structure revealing its true chemical composition and also opened up the possibility to determine the antiferromagnetic spin structure of Sr₂CrO₃FeAs.

13.6 Synthesis (II)

4 g Sr₂CrO₃FeAs for neutron scattering experiments were synthesised by heating stoichiometric mixtures of the same starting materials as described in Chapter 13.1 in four separate batches of 1 g. Each mixture was heated to 1173 K at a rate of 80 K·h⁻¹, kept at this temperature for 60 h and cooled down to room temperature. The products were homogenised in an agate mortar, pressed into pellets and sintered at 1323 K for 60 h. The batches were then united, reground, pressed into pellets of 14 mm in diameter and sintered together at 1323 K for 50 h.

13.7 Neutron diffraction, refinement details

Powder diffraction patterns at various temperatures were recorded at the high-flux powder diffractometer D20 at Institut Laue-Langevin according to Chapter 2.2.2. Rietveld refinements of the D20 nuclear scattering patterns were performed with the TOPAS package according to Chapter 2.2.4. Preferred orientation of the crystallites was described with the March Dollase function. The Fe:Cr ratio on both the iron and the chromium site were allowed to refine freely. Additionally, powder diffraction patterns were recorded using polarised neutrons at the polarised spectrometer DNS at FRM II (Garching, Germany) at different temperatures according to Chapter 2.2.2. Both the nuclear and magnetic DNS powder patterns were interpolated, scaled and converted to a format with a constant step width and refined with the GSAS pack-

age (see also Chapters 2.2.2 and 2.2.4). The standard Gaussian profile function with asymmetry corrections (CW profile function 1) was used as reflection profiles. To obtain accurate changes of the ordered magnetic moments at different temperatures, only the Gaussian parameters U and W were refined using the 3.5 K pattern and held constant at all other temperatures. The scaling factor obtained from the nuclear scattering contribution was corrected for the number of formula units per unit cell and taken as reference for the magnetic scattering contribution. A shifted Chebychev series of 9th order was used as background function and the parameters were allowed to refine freely for each temperature. Structural parameters for all refinements were taken from an additional refinement (combined nuclear and magnetic scattering) performed with GSAS using the low-temperature diffraction data taken at D20.

13.8 Redetermined crystal structure

Figure 13.6 shows the neutron powder pattern of Sr₂CrO₃FeAs measured at the D20 diffractometer at 300 K. It could be fitted successfully with a tetragonal Sr₂GaO₃CuS-type Sr₂CrO₃FeAs main phase and FeAs, as well as SrO as minor impurity phases. Yet another small impurity phase could not be identified and its largest peak was therefore excluded from the refinement. The crystal structure of Sr₂CrO₃FeAs (origin choice 1) is shown in Figure 13.9 (left). No structural phase transition was observed down to 6.5 K. The crystallographic data at 300 K (Table 13.3) are in good agreement with the X-ray data in Chapter 13.2. However, the refinement of the neutron data unambiguously shows a mixed occupancy of iron and chromium at the iron site 2a (93±1 % Fe : 7±1 % Cr), while no mixed occupancy at the chromium site or any oxygen deficiency were detected within one standard deviation. Full occupancy of the iron site was found in an X-ray refinement of the sample (Chapter 21.3.1, Appendix). These findings strongly suggest at least partial interchangeability of the 3d-metals Fe and Cr in the FeAs layers. This Cr-doping of the Fe-site could also explain why Sr₂CrO₃FeAs does neither display a spin-density wave anomaly nor superconductivity. This situation is very similar to that in Cr-doped BaFe₂As₂, where small amounts of chromium at the iron site in BaFe_{2-x}Cr_xAs₂

strongly affect the SDW anomaly and this apparently is detrimental to superconductivity.^[222]

Mixing of iron with other d-metals in the FeAs layers may also occur in other 21331 or 32522-systems, and one cannot rule out that the alleged stoichiometric 37 K superconductor Sr₂VO₃FeAs is in fact a doped compound likewise (refer to Chapter 14). The crystallographic data (neutrons) do not show any oxygen deficiencies; unlike it has been reported for Sr₂VO_{3- δ} FeAs.^[223] However, no detailed structural data of these compounds have been published.

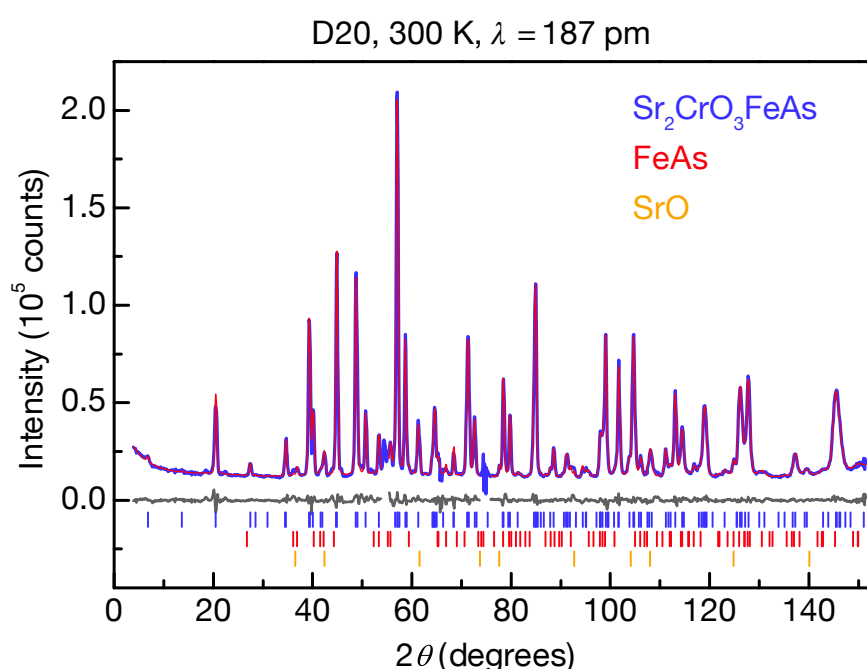


Figure 13.6: Rietveld fit of the 4 g sample Sr₂CrO₃FeAs at 300 K (D20).

Temperature	300 K
Diffractometer	D20, ILL ($\lambda = 187$ pm)
Rietveld package	TOPAS
Space group	<i>P4/nmm</i> (<i>o1</i>)
Lattice parameters	$a = 391.71(7)$ pm $c = 1578.0(2)$ pm
Cell volume	$V = 0.2421(1)$ nm ³
Z	2
Data points	1446
Excluded regions	$54.0 - 55.1^\circ 2\theta$; $73.9 - 75.7^\circ 2\theta$
Reflections	118 (main phase); 1 impurity reflection excluded

Constraints	0		
Atomic variables	15		
Profile variables	6		
Anisotropy var.	24		
Background var.	12		
Imp. phase var.	21		
Other variables	6		
<i>d</i> range	0.966 – 15.780		
<i>R</i>_P, <i>R</i>_{WP}, <i>R</i>_{Bragg}, χ^2	0.030, 0.045, 0.011, 0.812		
Atomic parameters			
Sr1	2c (0, 1/2, z)	z = 0.8059(3)	<i>U</i> _{iso} = 131(9) pm ²
Sr2	2c (0, 1/2, z)	z = 0.5856(3)	<i>U</i> _{iso} = 145(12) pm ²
Cr:Fe 0.99(1):0.01(1)	2c (0, 1/2, z)	z = 0.3104(4)	<i>U</i> _{iso} = 69(19) pm ²
Fe:Cr 0.93(1):0.07(1)	2a (0, 0, 0)		<i>U</i> _{iso} = 85(9) pm ²
As1	2c (0, 1/2, z)	z = 0.0883(2)	<i>U</i> _{iso} = 192(13) pm ²
O1	4f (0, 0, z)	z = 0.2943(2)	<i>U</i> _{iso} = 93(7) pm ²
O2	2c (0, 1/2, z)	z = 0.4308(3)	<i>U</i> _{iso} = 172(12) pm ²
Bond lengths (pm)			
Sr–O	244.3(6) × 1	251.7(3) × 4	272.6(4) × 4 278.2(1) × 4
Cr–O	190.0(8) × 1	197.5(1) × 4	
Fe–Fe	277.0(1) × 4		
Fe–As	240.4(3) × 4		
Bond angles (°)			
As–Fe–As	109.6(1) × 4	109.1(2) × 2 (ε)	
O–Cr–O	89.0(1) × 4	97.4(2) × 4	165.2(4) × 2

Table 13.3: Crystallographic data of the 4 g sample Sr₂CrO₃FeAs at 300 K (D20).

13.9 Neutron diffraction, antiferromagnetic ordering

The susceptibility measurements on Sr₂CrO₃FeAs in Chapter 13.3 revealed Curie-Weiss behaviour above 160 K with an effective magnetic moment $\mu_{\text{eff,exp}} = 3.83(3) \mu_{\text{B}}$. As this is typical for Cr³⁺-ions in the $^4F_{3/2}$ state ($\mu_{\text{eff,calc}} = 3.87 \mu_{\text{B}}$), one can expect that the observed magnetism is due to the chromium atoms only, whereas the iron sites do not carry any magnetic moments. Furthermore, a drop of the $\chi(T)$ plot below 31 K together with a large negative Weiss constant $\Theta = -141(3)$ K indicated antiferromag-

netic ordering. Neutron patterns measured at the D20 diffractometer showed additional peaks appearing below 35 K (Figure 13.7). These magnetic reflections could be indexed with the primitive tetragonal cell $|\mathbf{a}'| = |\mathbf{a} - \mathbf{b}| = \sqrt{2} \cdot |\mathbf{a}|$, $|\mathbf{c}'| = |\mathbf{c}|$ according to a magnetic propagation vector $\mathbf{q} = (\frac{1}{2}, \frac{1}{2}, 0)$ based on the original tetragonal unit cell.

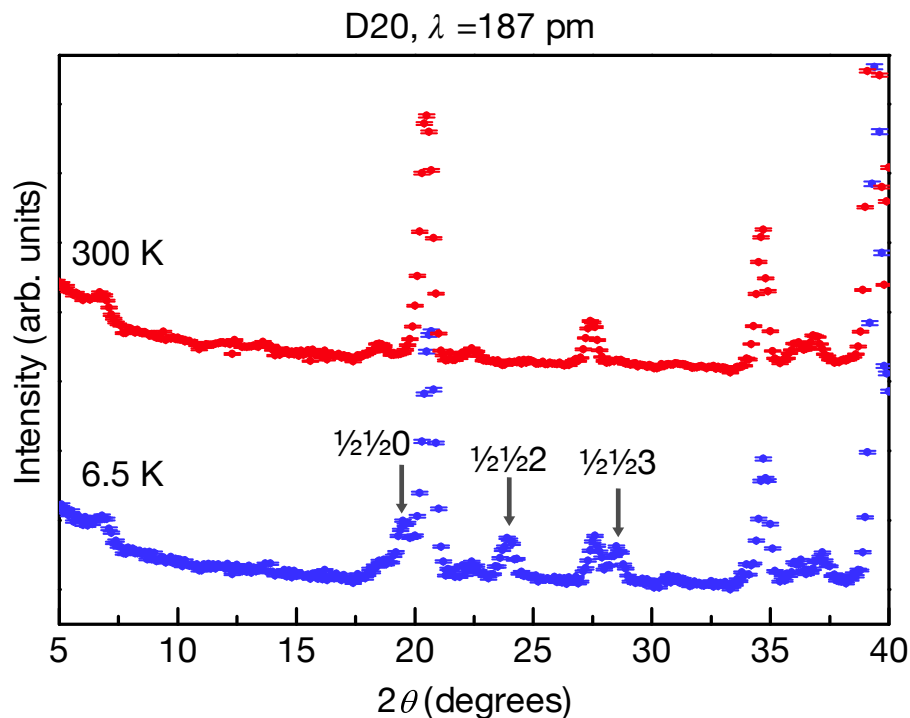


Figure 13.7: Neutron powder diffractograms of Sr₂CrO₃FeAs at 300 K and 6.5 K (D20).

In order to separate nuclear and magnetic scattering, experiments with polarised neutrons were performed at the DNS diffractometer. Sharp magnetic reflections are discernible below T_N , indicating long-range antiferromagnetic ordering of the Cr-sublattice (Figure 13.8). Moreover, magnetic diffuse scattering due to short-range spin correlations can clearly be observed above T_N . At temperatures above 120 K, Sr₂CrO₃FeAs displays Curie-Weiss-like paramagnetic scattering only. Short-range antiferromagnetic spin correlations begin to emerge below ~ 100 K. The observed asymmetric diffuse scattering profile strongly suggests that the short-range spin correlations are two-dimensional in nature.

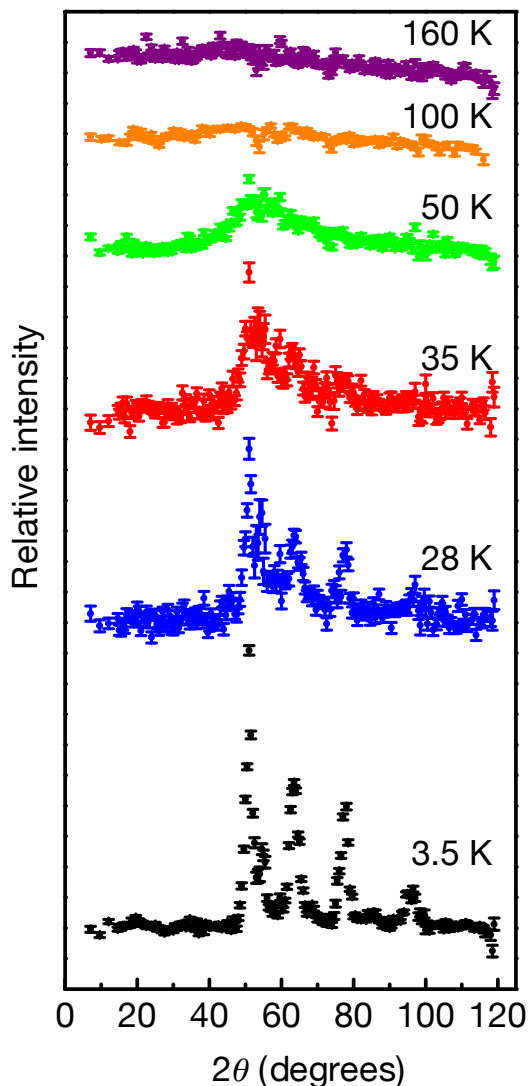


Figure 13.8: Magnetic scattering contribution (DNS).

From the observed \mathbf{q} -vector ($\frac{1}{2}, \frac{1}{2}, 0$), a chequerboard-like spin arrangement of C-type was assumed, which is reversed between two adjacent chromium layers along \mathbf{c} . Since these layers are at the z -coordinates ± 0.31 , no G-type pattern is possible.^{xxi} A first expected spin alignment along \mathbf{c} did not reproduce the observed data, therefore models with orientations within the (\mathbf{ab}) -plane were developed. The by far best fit was found with an alignment along $[\mathbf{a} - \mathbf{b}]$ and reversed along \mathbf{a} and \mathbf{b} based on the original tetragonal cell. This arrangement required the orthorhombic magnetic space group $C_p mma'$ (Litvin No. 67.15.591)^[224] (Chapter 21.5, Appendix), where Cr³⁺

^{xxi} The different magnetic ordering types for simple cubic lattices are depicted in Figure 21.3 in the Appendix (Chapter 21.4).

occupies the $4g$ $(0, \frac{1}{4}, z)$ Wyckoff position and the magnetic moments of Cr³⁺ align along the orthorhombic a' -axis, building up a checkerboard arrangement in each Cr layer at both heights z and \bar{z} (Figure 13.9).

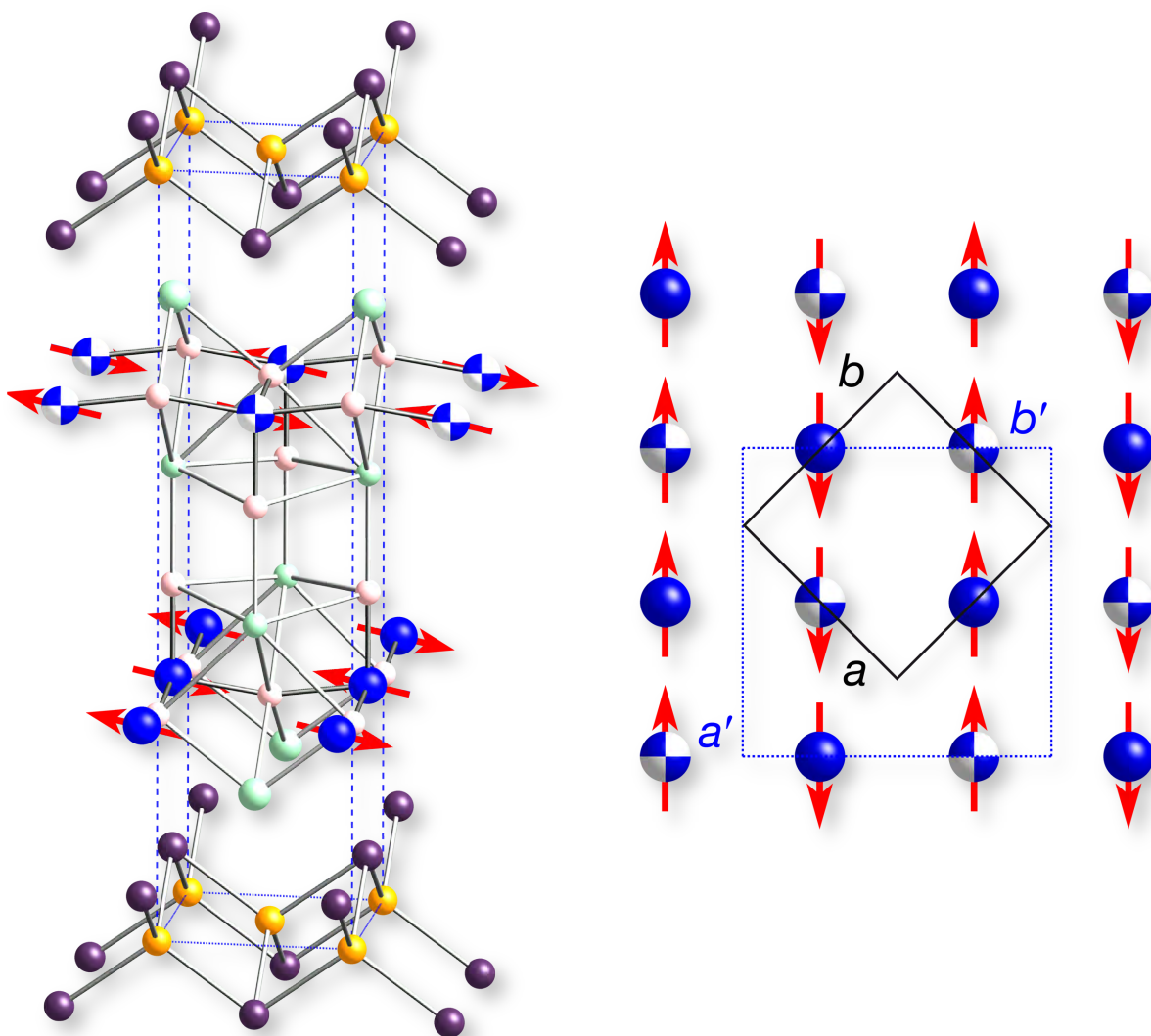


Figure 13.9: Left: Crystal structure of Sr₂CrO₃FeAs (*o1*) and magnetic ordering of the Cr atoms. Cr atoms at height z are depicted as solid, Cr atoms at height \bar{z} as chequered spheres. Right: The tetragonal crystallographic unit cell is depicted as black, the orthorhombic magnetic cell as dashed blue square. The transformation from the tetragonal to the orthorhombic cell is $\mathbf{a}' = \mathbf{a} - \mathbf{b}$, $\mathbf{b}' = \mathbf{a} + \mathbf{b}$, $\mathbf{c}' = \mathbf{c}$ with an origin shift of $(-\frac{1}{4}, \frac{1}{4}, 0)$.

By testing different magnetic space groups and different spin orientations, any other model for the magnetic ordering in a direct magnetic subgroup derived from the crystallographic space group *Cmme* could be unambiguously ruled out. Sections of the nuclear and magnetic powder patterns recorded at 3.5 K and corresponding

Rietveld refinements are depicted in Figure 13.10 (left). The ordered magnetic moment of a Cr³⁺-ion was refined to be 2.75(5) μ_B at 3.5 K, which is close to the expected 3 μ_B . The evolution of the magnetic ordering becomes evident from the order parameter and its temperature dependence as depicted in Figure 13.10 (right). It follows the power law $a \cdot [(T_N - T) / T_N]^\beta$ with $a = 2.84(3)$, $T_N = 36.0(5)$ K and $\beta = 0.22(2)$. The exponent β is between the idealised 2D and 3D Ising values ($1/8$ and $5/16$, respectively), which agrees with the fact that the magnetic arrangement of each Cr-layer at height z is coupled with the corresponding \bar{z} -layer and the magnetism therefore can be explained neither strictly two- nor three-dimensionally.

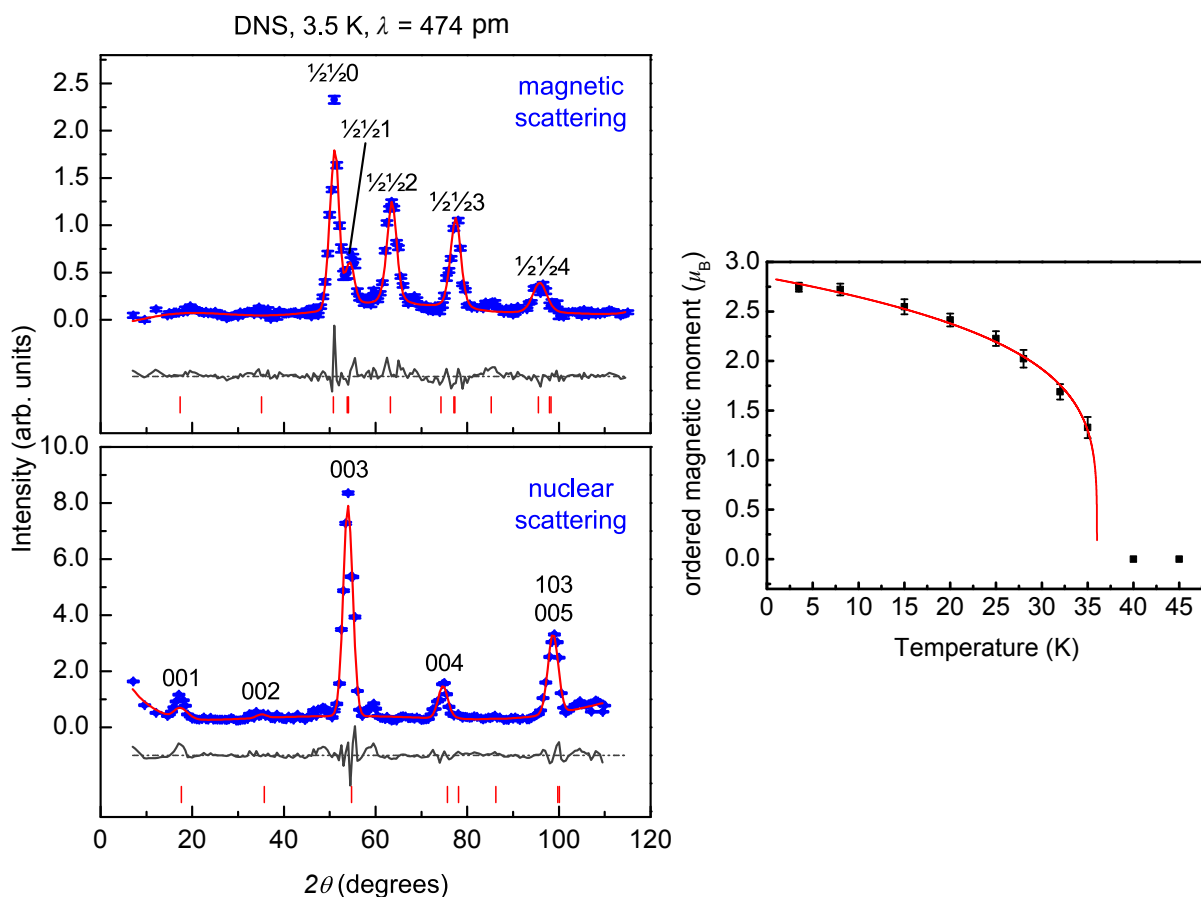


Figure 13.10: Left: Magnetic and nuclear reflections of Sr₂CrO₃FeAs (blue) and Rietveld fit (red) at 3.5 K measured at the polarised spectrometer DNS. The magnetic space group is C_{Pmma}' and the crystallographic space group $P4/nmm$. The miller indices of the magnetic reflections were transformed to the tetragonal cell for comparability. Red markers: Reflection conditions of both space groups. Right: Variation of the refined ordered magnetic moment of the Cr-sublattice with temperature. The temperature dependence follows the simple power law $a \cdot [(T_N - T) / T_N]^\beta$ (red curve).

In summary, the iron arsenide oxide Sr₂CrO₃FeAs crystallises in the tetragonal Sr₂GaO₃CuS-type structure (space group *P4/nmm*) and exhibits a large distance between the FeAs layers due to separation by large perovskite-like metal oxide blocks. The compound shows paramagnetism above 160 K in agreement with Cr³⁺ ($S = \frac{3}{2}$). Short-range spin correlations from the Cr³⁺-ions begin to appear below ~ 100 K and long-range antiferromagnetic ordering below $T_N = 36.0(5)$ K as determined via polarised neutrons. The magnetic structure is of the C-type with the Cr-spins oriented parallel to $[\mathbf{a} - \mathbf{b}]$ and with all nearest-neighbour Cr³⁺ moments antiferromagnetically aligned, thus forming a chequerboard arrangement. Sr₂CrO₃FeAs is a poor metal over the whole temperature range and does not show any structural or magnetic anomalies (apart from the antiferromagnetic ordering of the Cr³⁺ ions). ⁵⁷Fe Mössbauer spectra are in agreement with the absence of magnetic ordering at the iron site, but a small hyperfine field is transferred to the iron nuclei from the adjacent magnetically ordered CrO₂ layers.

The crystallographic structure of Sr₂CrO₃FeAs was redetermined via neutron diffraction experiments on the D20 diffractometer. A mixed occupancy of chromium and iron in the FeAs layers was found, which points out the ability of substitution between similar 3d-metals in these compounds. This kind of Cr-doping may also be the reason for the absence of both a SDW anomaly and superconductivity. But even more, such non-stoichiometries may also occur in similar compounds such as the superconductor Sr₂VO₃FeAs. Mixed occupancy may also be responsible for the different physical behaviour of these compounds when compared with the 1111- and 122-iron arsenides. Deviations from the ideal stoichiometry have especially to be taken into account when discussing their electronic structures, which are crucial for enabling superconductivity.

14. Sr₂VO₃FeAs

In the by now grown class of iron-based superconductors, enormous progress has already been made in order to throw light on the underlying physics. It has become increasingly accepted that the weak magnetism inside the iron layers plays a decisive role in triggering superconductivity (see [225] and Chapter 1.1.2), even though the exact relation to the pairing mechanism is still unclear. This weak magnetism appears as a spin-density wave in all iron-based materials with simple PbFCI^[31, 226] and ThCr₂Si₂-related structures (Chapter 7.1) and is intimately connected with nesting of cylinder-shaped Fermi surfaces by a wave vector $\mathbf{q} = (\pi, \pi)$ ^[32a]. However, no SDW of that or similar kind has been observed in the more complex arsenides EA₂TMO₃FeAs (EA = Sr, Ba; TM = Sc, Cr, V) (Chapters 12 and 13) where the isoelectronic (FeAs)⁻ layers are separated by larger perovskite-like (EA₂TMO₃)⁺ blocks. Among them, only the V-compound Sr₂VO₃FeAs is superconducting with transition temperatures of up to 37 K^[206] and it has been controversially argued whether in this case the V atoms significantly contribute to the Fermi surface^[227] or not.^[228] If this is not the case, the topology of the Fermi surface turns out to have the same essential features as in the other FeAs superconductors, otherwise one has to assume a different superconducting mechanism in the case of Sr₂VO₃FeAs. The latter however seems to be improbable with respect to the T_C , which is strikingly similar to that of other iron arsenide superconductors.

If one assumes that the superconducting mechanism in Sr₂VO₃FeAs is the same as in the other iron arsenides, the absence of a SDW anomaly may suggest that the FeAs layer is intrinsically doped. Vanadium can easily adopt oxidation states between V¹⁺ and V⁴⁺ and would thus be able to supply electrons to or accept electrons from the FeAs layers. Indeed, a recent X-ray absorption study indicates the presence of V³⁺ and V⁴⁺ in Sr₂VO₃FeAs.^[229] But even if this is the case, it will remain confusing that also Sr₂ScO₃FeAs (where the scandium valence has to be exactly +3) does neither exhibit a SDW anomaly nor any other magnetic effect.^[204b]

A general problem, however, is that thorough investigations of Sr₂VO₃FeAs are hampered by the often poor quality of the samples, which always contain significant amounts of the ternary vanadium oxides Sr₂VO₄ and / or Sr₃V₂O_{7- δ} .^[206, 229-230] However,

the authors do not specify quantitative phase fractions for the most part. This might be dangerous in the present case because these impurities contain V⁴⁺ and therefore exhibit at least weak paramagnetism.

Another fact that has hardly been noticed so far, concerns the true stoichiometry and homogeneity of the EA₂TMO₃FeAs compounds. The ionic radii of Fe²⁺, V^{2+/3+}, and Cr³⁺ are similar and in the face of synthesis temperatures of more than 1000 °C, their mixing is highly plausible. The chromium compound Sr₂CrO₃FeAs indeed is not stoichiometric but intrinsically Cr-doped in the iron layer (see also Chapter 13.8) and this mixing probably poisons superconductivity. Such mixing of iron and vanadium may equally concern Sr₂VO₃FeAs and if this is the case, only small amounts of V in the Fe layer may already affect its electronic and magnetic properties.

In order to clarify this, the synthesis of Sr₂VO₃FeAs has been optimised in order to minimise the amounts of impurity phases, which allowed for combined X-ray and neutron powder scattering investigations. In this chapter, the exact stoichiometry, magnetism, and superconductivity of differently prepared Sr₂VO₃FeAs samples are presented. One can show that the superconducting phase is almost ideally stoichiometric, whereas V doping, which can easily be achieved within the Fe layer, suppresses superconductivity. Furthermore, susceptibility data and hints to magnetic ordering of the V-sublattice from neutron-scattering data are given and discussed.

14.1 Synthesis

Sr₂VO₃FeAs was synthesised by heating mixtures of strontium, vanadium, iron (III) oxide and arsenic oxide in a molar ratio of 20:11:5:5 (corresponding to 10 % excess vanadium). Two separate batches of 1 g were prepared in alumina crucibles sealed in silica ampoules according to the synthesis method described in Chapter 2.10.3. Each mixture was heated to 1323 K at a rate of 60 K·h⁻¹, kept at this temperature for 60 h and cooled down to room temperature. The products were homogenised in an agate mortar, pressed into pellets, and sintered at 1323 K for 60 h. The latter step was performed twice. The batches were then united, reground, pressed into pellets of 6 mm in diameter, and sintered together at 1323 K for 68 h. The obtained black crystalline product Sr₂VO₃FeAs is stable in air. Sr₂VO₃(Fe_{0.93}V_{0.07})As was synthesised by heating mixtures of strontium, vanadium, iron (III) oxide, arsenic ox-

ide and vanadium (V) oxide in a ratio of 100:54:20:25:3 (corresponding to 20 % surplus vanadium and 20 % iron deficiency), in two separate batches accordingly.

14.2 Resistivity and susceptibility

Resistivity measurements of the undoped sample show a rather broad superconducting transition at 33 K (Figure 14.1). Superconductivity has been verified by zero-field-cooled / field-cooled measurements using the SQUID magnetometer described in Chapter 2.6.1. However, the estimated superconducting volume fraction is only ~ 20 %. No superconductivity has been detected in the V-doped sample.

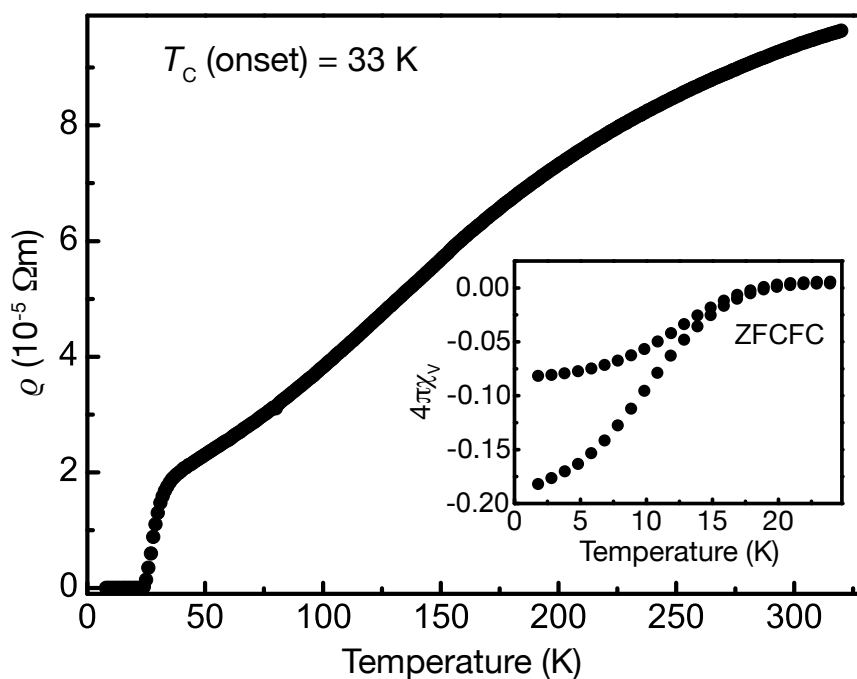


Figure 14.1: Resistivity of $\text{Sr}_2\text{VO}_3\text{FeAs}$. Inset: Zero-field-cooled / field-cooled measurements (20 Oe)

The susceptibilities of V-doped and undoped $\text{Sr}_2\text{VO}_3\text{FeAs}$ measured at 1 kOe and hysteresis loops at different temperatures are depicted in Figure 14.2. Both samples exhibit Curie-Weiss-like paramagnetic behaviour between 160 and 390 K. Anomalies appear at ~ 150, ~ 70, and ~ 50 K in the stoichiometric sample and likewise also in the V-doped sample. Almost the same behaviour has been reported in [229], where the authors suggested possible magnetic transitions of the Sr_2VO_3 -layers. In

this paper also the absence of a structural phase transition has been reported in agreement with the neutron-scattering data of the next chapter (see below).

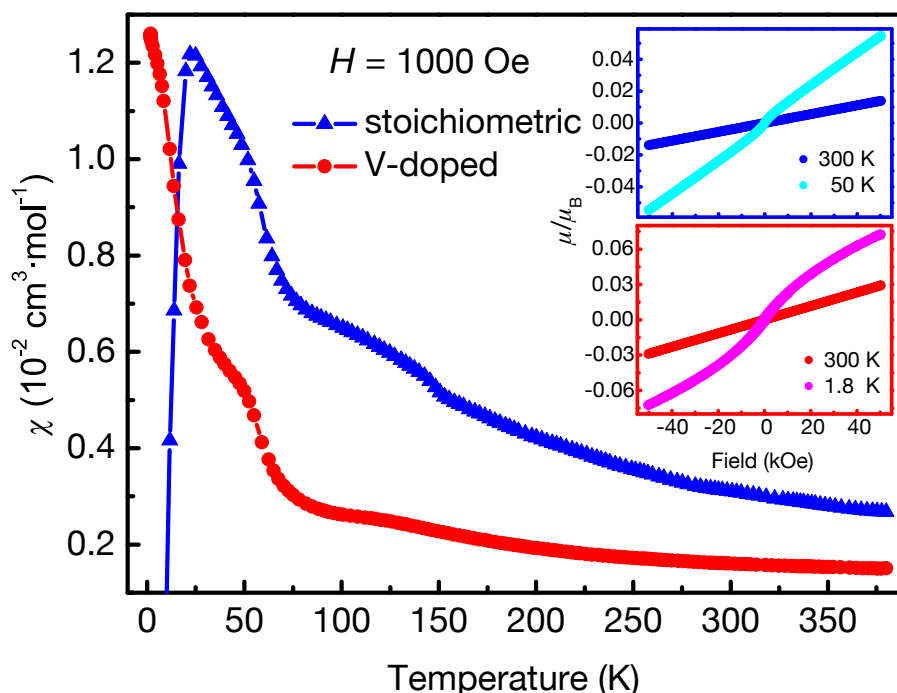


Figure 14.2: Molar susceptibility of Sr₂VO₃FeAs (blue triangles) and Sr₂VO₃(Fe_{0.93}V_{0.07})As (red circles) at 1 kOe. Insets: Hysteresis loops of Sr₂VO₃FeAs (top) and Sr₂VO₃(Fe_{0.93}V_{0.07})As (bottom).

14.3 Crystal structure

X-ray powder-diffraction patterns at room temperature were recorded using the STOE Stadi P diffractometer (Cu-K α_1 radiation, Chapter 2.2.1). Neutron powder-diffraction patterns at 300 K and 4 K were recorded at the high-resolution powder diffractometer SPODI at FRM II (Garching, Germany) with incident wavelengths of 155 pm and 146 pm, respectively (Chapter 2.2.2). Rietveld refinements were performed with the TOPAS package according to the general method described in Chapter 2.2.4. Preferred orientation of the crystallites was described using March Dollase or spherical harmonics functions. The Fe:V ratio at both the iron and the vanadium site were determined by refining the occupancies of the neutron and / or X-ray powder data. Any oxygen deficiency was ruled out by refining the occupancy of all oxygen sites.

The crystallographic data of Sr₂VO₃FeAs and Sr₂VO₃(Fe_{0.93}V_{0.07})As are compiled in Table 14.1, the powder patterns and Rietveld fits are depicted in Figure 14.3. The

amounts of impurity phases were determined by quantitative Rietveld analyses. The undoped sample consists of $\text{Sr}_2\text{VO}_3\text{FeAs}$ (89.0 wt%), $\text{Sr}_3\text{V}_2\text{O}_{7-\delta}$ (7.8 wt%), FeAs (2.9 wt%), and traces of SrO (0.3 wt%), the doped sample consists of $\text{Sr}_2\text{VO}_3(\text{Fe}_{0.93}\text{V}_{0.07})\text{As}$ (87.3 wt%) and $\text{Sr}_3\text{V}_2\text{O}_{7-\delta}$ (12.7 wt%) as determined by neutron diffraction. However, the doped sample also shows small amounts of a further, unidentified impurity phase, which could not be included in the refinement. The lattice parameters change only slightly on V doping (a is shortened by 1.2 pm, c is unchanged) but the refinement of the Fe site (neutron data) displays a mixed occupancy of Fe and V in a ratio of $93\pm 1\%$ Fe : $7\pm 1\%$ V in the doped sample. Since the X-ray data give full occupancy of the $2a$ Wyckoff position (see Table 14.1), any vacancies at the Fe site can be ruled out and the Fe / V mixing is therefore unambiguous. In contrast to this, the superconducting, undoped sample is almost exactly stoichiometric regarding the V, Fe, and O occupancies.

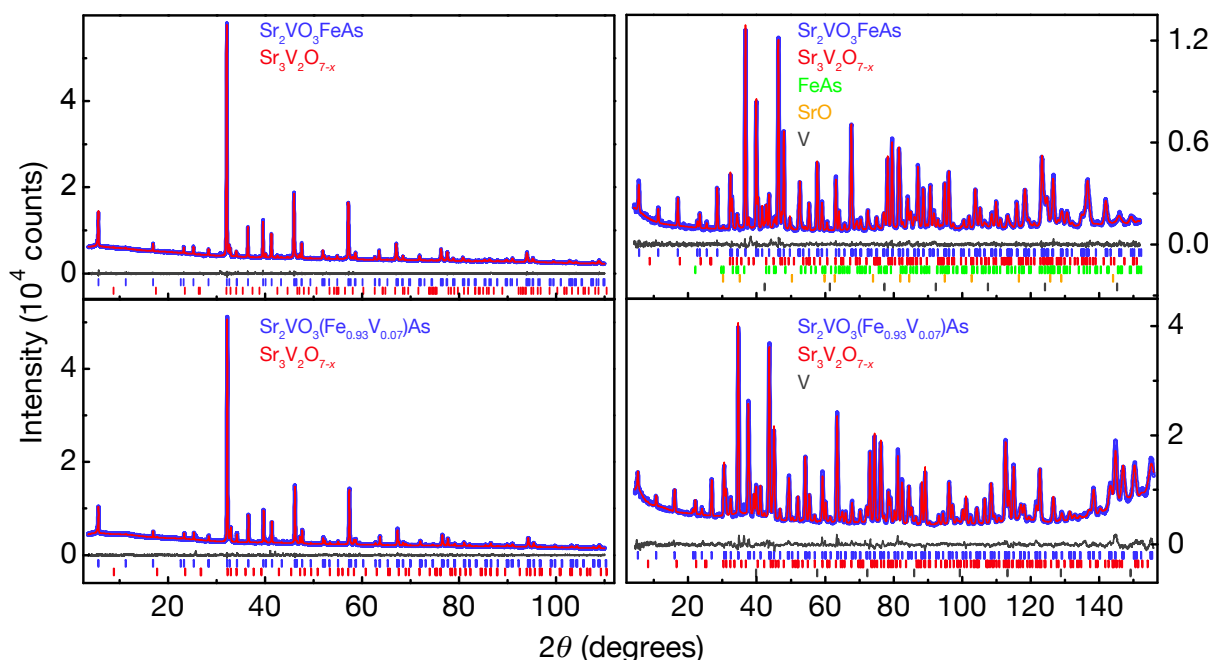


Figure 14.3: X-ray (left) and neutron (right) powder patterns of $\text{Sr}_2\text{VO}_3\text{FeAs}$ and $\text{Sr}_2\text{VO}_3(\text{Fe}_{0.93}\text{V}_{0.07})\text{As}$ with Rietveld refinements.

	Sr ₂ VO ₃ FeAs		Sr ₂ VO ₃ (Fe _{0.93} V _{0.07})As	
Diffractometer	STOE (X-ray)	SPODI (neutron)	STOE (X-ray)	SPODI (neutron)
Wavelength	154 pm	155 pm	154 pm	146 pm
Software	TOPAS	TOPAS	TOPAS	TOPAS
Temperature	297 K	300 K	297 K	300 K
Space group	<i>P4/nmm</i> (o1)	<i>P4/nmm</i> (o1)	<i>P4/nmm</i> (o1)	<i>P4/nmm</i> (o1)
Lattice parameters^{a)} (pm)	<i>a</i> = 394.58(1) <i>c</i> = 1573.1(1)	<i>a</i> = 393.5(1) <i>c</i> = 1570(1)	<i>a</i> = 393.38(1) <i>c</i> = 1573.1(1)	<i>a</i> = 393.1(1) <i>c</i> = 1573(1)
<i>V</i>^{a)} (nm³)	0.2449(1)	0.243(1)	0.2434(1)	0.243(1)
<i>Z</i>	2	2	2	2
Data points	10650	2955	10650	3029
Reflections^{b)}	130	196	130	238
Total variables	101	95	94	113
<i>d</i> range	0.941 – 15.735	0.797 – 15.700	0.939 – 15.717	0.749 – 15.719
<i>R_p</i>, <i>R_{wp}</i>, <i>R_{Bragg}</i>	0.0147, 0.0196, 0.0050	0.0317, 0.0412, 0.0101	0.0187, 0.0264, 0.0044	0.0321, 0.0405, 0.0231
Atomic parameter				
Sr1 [2 <i>c</i> (0, ½, <i>z</i>)]	<i>z</i> = 0.8100(1) <i>U</i> _{iso} = 131(5)	<i>z</i> = 0.8096(1) <i>U</i> _{iso} = 39(5)	<i>z</i> = 0.8096(2) <i>U</i> _{iso} = 171(6)	<i>z</i> = 0.8092(2) <i>U</i> _{iso} = 49(7)
Sr2 [2 <i>c</i> (0, ½, <i>z</i>)]	<i>z</i> = 0.5859(1) <i>U</i> _{iso} = 220(7)	<i>z</i> = 0.5858(2) <i>U</i> _{iso} = 96(6)	<i>z</i> = 0.5862(2) <i>U</i> _{iso} = 239(9)	<i>z</i> = 0.5852(2) <i>U</i> _{iso} = 82(7)
V / Fe [2 <i>c</i> (0, ½, <i>z</i>)]	<i>z</i> = 0.3080(3) <i>U</i> _{iso} = 167(9)	<i>z</i> = 0.306(2) <i>U</i> _{iso} = 38 ^{c)} 1.00(1) : 0.00(1) ^{d)}	<i>z</i> = 0.3086(3) <i>U</i> _{iso} = 179(11)	<i>z</i> = 0.309(3) <i>U</i> _{iso} = 25 ^{c)} 1.00(1) : 0.00(1) ^{d)}
Fe / V [2 <i>a</i> (0, 0, 0)]	<i>U</i> _{iso} = 134(10) occ. = 0.99(1) ^{e)}	<i>U</i> _{iso} = 43(5) 0.99(1) : 0.01(1) ^{d)}	<i>U</i> _{iso} = 131(13) occ. = 1.00(1) ^{e)}	<i>U</i> _{iso} = 40(6) 0.93(1) : 0.07(1) ^{d)}
As [2 <i>c</i> (0, ½, <i>z</i>)]	<i>z</i> = 0.0891(2) <i>U</i> _{iso} = 113(7)	<i>z</i> = 0.0896(2) <i>U</i> _{iso} = 34(6)	<i>z</i> = 0.0900(2) <i>U</i> _{iso} = 178(10)	<i>z</i> = 0.0901(2) <i>U</i> _{iso} = 52(7)
O1 [4 <i>f</i> (0, 0, <i>z</i>)]	<i>z</i> = 0.2921(4) <i>U</i> _{iso} = 93(19) ^{f)} occ. = 1.00(1) ^{e)}	<i>z</i> = 0.2933(1) <i>U</i> _{iso} = 56(5) occ. = 1.00(1) ^{e)}	<i>z</i> = 0.2958(5) <i>U</i> _{iso} = 305(31)	<i>z</i> = 0.2951(1) <i>U</i> _{iso} = 65(7) occ. = 1.00(1) ^{e)}
O2 [2 <i>c</i> (0, ½, <i>z</i>)]	<i>z</i> = 0.4310(4) <i>U</i> _{iso} = 93(19) ^{f)} occ. = 1.00(1) ^{e)}	<i>z</i> = 0.4297(1) <i>U</i> _{iso} = 94(8) occ. = 1.00(1) ^{e)}	<i>z</i> = 0.4313(7) <i>U</i> _{iso} = 419(54)	<i>z</i> = 0.4308(2) <i>U</i> _{iso} = 131(10) occ. = 1.00(1) ^{e)}

Table 14.1: Crystallographic data of Sr₂VO₃FeAs and Sr₂VO₃(Fe_{0.93}V_{0.07})As.

- a) Separate refinements without anisotropy parameters.
b) Main phase.
c) Restrained as minimum value.
d) Constrained to a total occupancy of 1.
e) Restrained to a total occupancy ≤ 1.
f) *U*_{iso} of O1 and O2 were constrained.

14.4 Magnetic ordering

The neutron powder pattern of undoped, superconducting Sr₂VO₃FeAs at 4 K shows weak additional peaks at the Q values 0.525, 1.49, and possibly 0.28 Å⁻¹ (marked with arrows in Figure 14.4). These reflections can be indexed as satellites of the (00ℓ) reflections according to $Q_{(001)+\Delta Q}$, $Q_{(004)-\Delta Q}$, and $Q_{(001)-\Delta Q}$ with $\Delta Q \approx 0.123$ Å⁻¹, respectively. This suggests incommensurate, possibly helical magnetic ordering along the c axis with a propagation vector $\mathbf{q} \approx (0, 0, 0.306)$ in reciprocal lattice units. Since low-temperature ⁵⁷Fe-Mössbauer data do not show any signal splitting,^[229] ordering of the V-sublattice is expected. This supports the idea of highly correlated vanadium in Sr₂VO₃FeAs, where vanadium d-states are removed from the Fermi level by the magnetic exchange splitting. Recent angle-resolved photoemission experiments^[231] are in agreement with this model likewise. Even though these data strongly suggest the existence of magnetic ordering, they should be considered as preliminary. Further experiments in the low- Q region with polarisation analysis are required for a precise determination of the magnetic structure and of the temperature dependence of the magnetic order parameter.

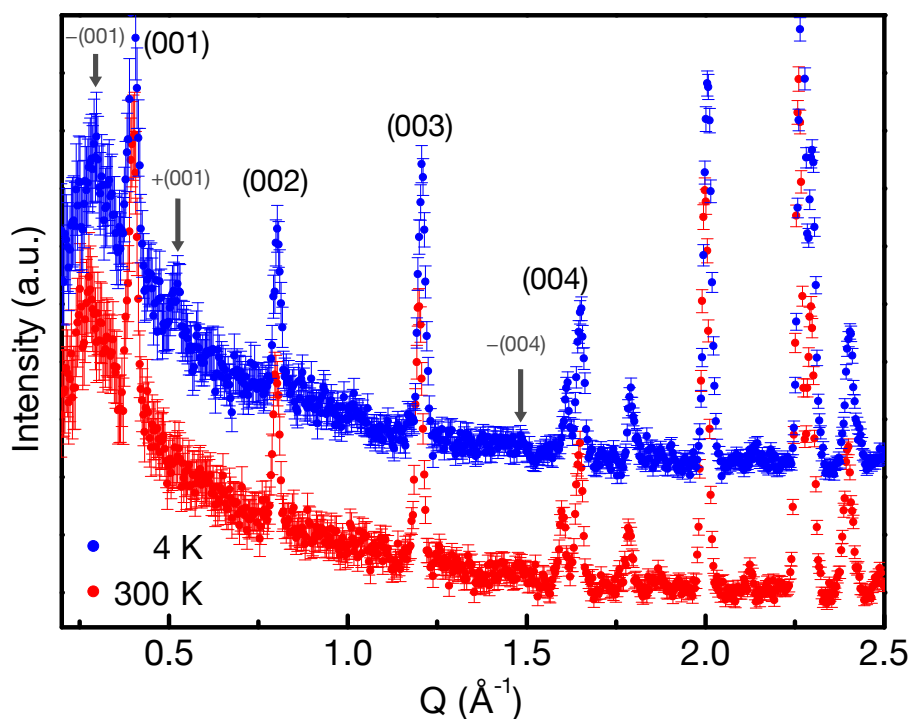


Figure 14.4: Neutron powder patterns of Sr₂VO₃FeAs at 4 K (top) and 300 K (bottom). Magnetic reflections are marked with arrows.

In summary, it could be shown that Sr₂VO₃FeAs is sensitive to Fe / V mixing in the FeAs layer, which is detrimental to superconductivity. A V-doping level of only 7 %, unambiguously detected by neutron diffraction, suppresses superconductivity completely, while the superconducting phase is nearly stoichiometric. It therefore seems reasonable to suppose that even smaller Fe / V inhomogeneities are intrinsic in this material and may be responsible for the scattered critical temperatures and superconducting phase fractions reported throughout the literature. Small but significant additional reflections emerge in the neutron powder pattern of superconducting Sr₂VO₃FeAs at 4 K. A preliminary analysis indicates incommensurate, possibly helical magnetic ordering of the V moments with a propagation vector $\mathbf{q} \approx (0, 0, 0.306)$. This is in agreement with strongly correlated vanadium, which does not significantly contribute to the Fermi surface. Thus, Sr₂VO₃FeAs is in line with the other iron pnictide superconductors and represents no new paradigm, although the absence of iron magnetism and possible self-doping effects remain open questions.

15. Summary and outlook

A multitude of new superconducting and non-superconducting iron pnictides and related compounds of various structure types has successfully been synthesised in batch sizes between 600 mg and 10 g. Many of these compounds have been thoroughly examined for small crystallographic effects or structural phase transitions via single crystal diffraction, temperature-programmed X-ray powder diffraction and neutron powder diffraction. Further physical properties were characterised via temperature-dependent measurements of the resistivity, magnetism, specific heat and Mössbauer spectroscopy. In several cases neutron scattering (elastic and inelastic) was employed in order to characterise specific magnetic properties like the spin structure, to characterise phononic properties or to check for the presence of magnetic excitations. Additionally, DFT calculations were performed in order to illuminate and interpret certain physical properties like magnetism, superconductivity, structure or optical semiconducting gaps.

15.1 Summary

La(Co_xFe_{1-x})PO

The solid solution La(Co_xFe_{1-x})PO could successfully be synthesised in a tin flux in a single annealing step for each composition. The highest possible T_C is 7 K, which is already achieved in undoped LaFePO. At higher cobalt doping levels, the superconducting critical temperature gradually decreases and for $x = 0.05$, a complete loss of superconductivity occurs. This is in contrast to the system La(Co_xFe_{1-x})AsO, in which a maximum T_C of 14 K is attained for $x = 0.11$.

Although LaFePO and LaFeAsO have remarkably similar electronic structures that indicate an electron-mediated superconducting mechanism, LaFePO lacks any structural and magnetic phase transition. This absence of magnetic ordering down to 4 K could be confirmed via Mössbauer spectroscopy, which has the advantage that it is a local probe. While La(Co_xFe_{1-x})PO is a paramagnetic metal for $x = 0 - 0.6$ in the temperature range between 7 and 300 K, ferromagnetic ordering is visible for $x = 0.7 - 1$ below Curie temperatures of 40 - 50 K. As found by powder diffraction,

the c lattice parameter gradually decreases on cobalt doping, while a in $\text{La}(\text{Co}_x\text{Fe}_{1-x})\text{PO}$ ($x = 0 - 1$) decreases at first (up to a doping level of $x = 0.4$) but then increases again. In $\text{La}(\text{Co}_x\text{Fe}_{1-x})\text{PO}$, the iron phosphide and lanthanum oxide layers are compressed along the c axis ($\varepsilon = 119^\circ - 122^\circ$), which is far from the ideal tetrahedral geometry ($\varepsilon = 109.47^\circ$). It is possible that these structural discrepancies have a strong influence on the exact superconducting mechanism and hence T_c .

SrFeAsF

The new quaternary iron arsenide fluoride SrFeAsF has been successfully synthesised by a solid-state reaction. It resembles the known parent compound LaFeAsO in some remarkable aspects: SrFeAsF is a poor metal at room temperature and undergoes a probably second-order structural phase transition at ~ 180 K, which is followed by a magnetic phase transition at ~ 130 K as observed by ^{57}Fe Mössbauer spectroscopy. Consequently, SrFeAsF exhibits a similar SDW anomaly as LaFeAsO , only at slightly higher temperatures. Since this SDW instability is assumed to be an important prerequisite for high- T_c superconductivity in iron arsenides, SrFeAsF can serve as a parent compound for a new, oxygen-free class of iron arsenide superconductors with ZrCuSiAs -type structure. Later, superconductivity with critical temperatures of up to 56 K has been successfully induced in La -^[124] Sm -^[125] and Nd -doped^[126] SrFeAsF by other groups. A drawback yet is the lack of a synthesis strategy for single-phase samples of these doped compounds so far. Further optimisation of the synthesis of these doped compounds is therefore crucial for a possible application of these alkaline earth fluoride iron arsenide superconductors. However, the large separation between the structural and magnetic phase transition temperatures in undoped SrFeAsF render this compound an excellent model system to study the underlying physics of the phase transitions.

EuMnPF

The new compound EuMnPF could be synthesised from a NaCl / KCl salt flux. In contrast to LaFePO , EuMnPF is not superconducting above 1.8 K and unlike the iron pnictides with their weak magnetism at the iron centres, the Mn^{2+} atoms of EuMnPF exhibit a strong, localised magnetism. EuMnPF is a paramagnetic metal in the whole

temperature range with the magnetism arising from the Eu^{2+} atoms. The spins of the Mn-atoms are probably antiferromagnetically ordered below a T_N of more than 380 K in spite of Mn–Mn bond lengths, which are roughly the same as the Fe–Fe bond lengths in LaFePO. To date, $\text{EuFeAsF}^{[123]}$ with a SDW anomaly below 153 K is known as the only ZrCuSiAs-type compound with similar $(\text{FEu})^+$ tetrahedral layers. The hypothetical compounds EuFePF and EuMnAsF , however, are not known to exist.

REZnPO

In contrast to the superconductors LaFePO and LaNiPO, LaZnPO and other *REZnPO* compounds are non-metals, which show optical band-gaps of different magnitude. Some *REZnPO* compounds exhibit dimorphism. DFT band structure calculations of these compounds show a similarity between the valence bands of the tetragonal (α) and rhombohedral (β) polymorph, as they possess mainly P-3p character. The conduction bands have mainly Zn-4s character, however a significant contribution of *RE*-5d occurs in rhombohedral *REZnPO*, which is responsible for a smaller optical band gap in this polymorph. Variations of the energy gaps of tetragonal *REZnPO* can be explained by hybridisation of Zn-4s + *RE*-5d + *RE*-4f orbitals for the conduction band. DFT volume optimisations of α - and β -PrZnPO show β -PrZnPO to be more stable by $10.7 \text{ kJ}\cdot\text{mol}^{-1}$.

$\text{Ba}_{1-x}\text{K}_x\text{Fe}_2\text{As}_2$

Although BaFe_2As_2 is a long-known compound, it had not been thoroughly characterised at the time it had first been synthesised. It was therefore recharacterised in detail via temperature-programmed X-ray powder diffraction, Mössbauer spectroscopy as well as resistivity, susceptibility and specific heat measurements. Regarding the results from these measurements in combination with the striking structural and electronic similarity to undoped LaFeAsO, BaFe_2As_2 has been found to be a highly promising candidate to induce superconductivity. BaFe_2As_2 exhibits a tetragonal-to-orthorhombic phase transition and a SDW anomaly at about 140 K and this SDW instability is assumed to be an important prerequisite for high- T_C superconductivity. It therefore had seemed likely that superconductivity could be induced by electron or by hole doping.

After trying several dopants, superconductivity could in fact be induced in BaFe_2As_2 by hole doping with potassium and thus $\text{Ba}_{0.6}\text{K}_{0.4}\text{Fe}_2\text{As}_2$, the first member of a new family of iron arsenide superconductors has been discovered. Like BaFe_2As_2 , $\text{Ba}_{0.6}\text{K}_{0.4}\text{Fe}_2\text{As}_2$ crystallises in the ThCr_2Si_2 -type structure, but unlike BaFe_2As_2 , it is a bulk superconductor below 38 K. In comparison with hole-doped LaFeAsO with a T_C of only 25 K, this is a significant increase. The new superconductor was characterised via measurements of the resistivity, magnetism and temperature-programmed X-ray powder diffraction. Both the structural phase transition and the SDW anomaly, which are both present in BaFe_2As_2 , were found to be completely suppressed in $\text{Ba}_{0.6}\text{K}_{0.4}\text{Fe}_2\text{As}_2$. A complete phase diagram of $\text{Ba}_{1-x}\text{K}_x\text{Fe}_2\text{As}_2$ was therefore created, which showed superconductivity and the SDW coexisting in the underdoped region between $x = 0.1$ and $x = 0.2$. Hence, this region was characterised in more detail by measurements of the resistivity as well as in-depth crystallographic and Mössbauer studies. It has become evident that both the SDW anomaly and the structural phase transition are continuously suppressed with an increasing doping concentration ($x = 0 - 0.3$) and no longer observed in $(\text{Ba}_{0.7}\text{K}_{0.3})\text{Fe}_2\text{As}_2$. Bulk superconductivity was detected in all samples with $x > 0.1$, so the co-existence of superconductivity and antiferromagnetic ordering could be unambiguously proved.

SrFe₂As₂ and EuFe₂As₂

The compounds SrFe_2As_2 and EuFe_2As_2 have been synthesised and their crystallographic and magnetic phase transitions have been examined in detail by temperature-programmed powder diffraction and Mössbauer spectroscopy. In summary, a complex nature of the phase transitions was found due to competing order parameters with respect to their structural and magnetic components. It could be shown that the crystallographic transition of SrFe_2As_2 is accompanied by magnetic ordering, as it is also the case in BaFe_2As_2 and EuFe_2As_2 . The determination of the lattice parameters close to the crystallographic phase transition temperature indicates a second-order transition in both SrFe_2As_2 and EuFe_2As_2 . This is typical for displacive structural transitions and consistent with the group-subgroup relationship between the corresponding space groups $I4/mmm$ and $Fmmm$. The transition becomes more and more continuous as the transition temperature decreases from SrFe_2As_2 to-

wards BaFe_2As_2 . Under the assumption that the transition mechanism is the same in all three compounds one can conclude that all of them undergo second-order displacive structural transitions. As of 2011, the question if the phase transition in the iron arsenides is first or second-order, however is still under dispute in the scientific community. For details, refer to Chapter 8.2.

$\text{Sr}_{1-x}\text{K}_x\text{Fe}_2\text{As}_2$ and $\text{Ca}_{1-x}\text{Na}_x\text{Fe}_2\text{As}_2$

Large batches of $\text{Sr}_{1-x}\text{K}_x\text{Fe}_2\text{As}_2$ and $\text{Ca}_{1-x}\text{Na}_x\text{Fe}_2\text{As}_2$ could successfully be synthesised via solid-state reactions and the samples were thereafter examined via inelastic neutron scattering measurements. Both $\text{Ca}_{1-x}\text{Na}_x\text{Fe}_2\text{As}_2$ and $\text{Sr}_{1-x}\text{K}_x\text{Fe}_2\text{As}_2$ did not reveal any signs of resonant spin excitations, which is in contrast to the findings in other superconducting iron arsenides. However, because of limitations in the employed spectrometer one cannot conclusively prove that such magnons are definitely absent.

Additionally, experimental phonon studies of these superconductors have been carried out. It could be shown that doping affects mainly the lower and intermediate vibration frequencies and there are indications that the exact type of EA^{2+} / A^+ ions additionally influences the bonding within the FeAs layers.

In both $\text{Sr}_{1-x}\text{K}_x\text{Fe}_2\text{As}_2$ and $\text{Ca}_{1-x}\text{Na}_x\text{Fe}_2\text{As}_2$, the low-energy phonon modes soften with temperature. Electron–phonon coupling might cause this softening. But as no anomalous effects are observed in the phonon spectra, when passing the superconducting transition temperature, this coupling cannot be solely responsible for the formation of Cooper pairs.

$\text{FeSe}_{1-x}\text{Te}_x$

The crystal structure of $\text{FeSe}_{0.44}\text{Te}_{0.56}$ has been redetermined by refinements of high-resolution single-crystal X-ray data and as a result, distinctively different z-coordinates for Se and Te were found. This leads to a lower local symmetry of the iron atoms by a Fe–Ch bond lengths splitting of more than 15 pm. Such large effects have not yet been considered in any calculation of the electronic and magnetic properties of these compounds and as such calculations are known to be very sen-

sitive towards even more subtle changes, this finding is a crucial prerequisite for more accurate calculations.

Since the superconducting transition temperature in $\text{FeSe}_{1-x}\text{Te}_x$ increases up to doping levels of $x \approx 0.5$ despite the disorder, which is induced at the same time, these findings underline the robustness of superconductivity against structural randomness in all iron-based superconductors.

$\text{Sr}_3\text{Sc}_2\text{O}_5\text{Fe}_2\text{As}_2$

The quinary 32522-type compound $\text{Sr}_3\text{Sc}_2\text{O}_5\text{Fe}_2\text{As}_2$ has been successfully synthesised via an alternative synthesis route. It was characterised by temperature-programmed powder diffraction, susceptibility measurements as well as Mössbauer spectroscopy. DFT calculations were carried out to perform a structure optimisation, which was related to the crystal structure. The iron arsenide tetrahedral layers in $\text{Sr}_3\text{Sc}_2\text{O}_5\text{Fe}_2\text{As}_2$ exhibit a very similar local symmetry as in other iron arsenides, but in spite of this, neither a structural nor a superconducting nor any other magnetic phase transition could be observed. The reason for this behaviour, however, is still unclear.

Additionally, $\text{Sr}_3\text{Sc}_2\text{O}_5\text{Fe}_2\text{As}_2$ was compared to seven other related compounds, which manifests the large potential of these and other stacking variants of tetrahedral layers. One can therefore expect a rich crystal chemistry for further complex iron pnictides.

$\text{Ba}_2\text{ScO}_3\text{FeAs}$

The new quinary iron arsenide oxide $\text{Ba}_2\text{ScO}_3\text{FeAs}$ has been successfully synthesised via a solid-state reaction. It crystallises in the tetragonal $\text{Sr}_2\text{GaO}_3\text{CuS}$ -type (21311 or 42622) structure and exhibits a large distance between the iron arsenide layers due to separation by bulky metal oxide blocks. $\text{Ba}_2\text{ScO}_3\text{FeAs}$ is a poor, paramagnetic metal and does not show any structural or magnetic anomaly, even though the electronic structure predicts a nested Fermi surface. Also ^{57}Fe -Mössbauer spectra are in agreement with the absence of magnetic ordering at the iron site. This absence of magnetic ordering in the formally undoped compound $\text{Ba}_2\text{ScO}_3\text{FeAs}$ is puzzling and the origin of this behaviour is still unclear. General loss

of superconductivity in such two-dimensional compounds with very large FeAs interlayer distances cannot be the cause for this, because meanwhile other iron arsenide superconductors with even higher interlayer distances and high T_c s are known to exist.

Sr₂CrO₃FeAs

The new quinary iron arsenide oxide Sr₂CrO₃FeAs has been successfully synthesised via a solid-state reaction in a small and a large batch. It is isotypic to Ba₂ScO₃FeAs and therefore and exhibits a big distance between the iron arsenide layers due to separation by large perovskite-like metal oxide blocks. The compound shows Curie-Weiss paramagnetism above 160 K due to Cr³⁺ ($S = 3/2$). Short-range spin correlations from the Cr³⁺-ions begin to appear below ~ 100 K and long-range antiferromagnetic ordering below $T_N = 36.0(5)$ K as determined via polarised neutrons. The magnetic structure is of the C-type with the Cr-spins oriented parallel to $[\mathbf{a} - \mathbf{b}]$ with all nearest-neighbour Cr³⁺ moments antiferromagnetically aligned, thus forming a chequerboard arrangement. Sr₂CrO₃FeAs is a poor metal over the whole temperature range and does not show any structural or magnetic anomalies apart from the antiferromagnetic ordering of the Cr³⁺ ions. ⁵⁷Fe Mössbauer spectra confirm the absence of magnetic ordering at the iron site.

The crystallographic structure of Sr₂CrO₃FeAs was redetermined via neutron powder diffraction and a mixed occupancy of chromium and iron at the iron site within the FeAs layers was found. This does not only show the possibility of substitution between similar 3d-metals in these types of compounds, but the Cr-doping may also be the reason for the absence of both a SDW anomaly and superconductivity. Mixed occupancy may also be one key factor explaining the different physical behaviour of various other quinary iron pnictides when compared with the 1111- and 122 iron arsenides. Moreover, deviations from the ideal stoichiometry have especially to be taken into account when discussing the electronic structures of such compounds.

Sr₂VO₃FeAs

After a careful synthesis optimisation, large batches of different samples with the nominal composition Sr₂VO₃FeAs could be synthesised in comparatively high quali-

ty. It could be shown via a combined neutron and X-ray powder diffraction study, that $\text{Sr}_2\text{VO}_3\text{FeAs}$ is sensitive to Fe / V mixing in the FeAs layer. This mixing probably is detrimental to superconductivity. A V-doping level of only 7 % suppresses superconductivity completely, while the superconducting phase is nearly stoichiometric. Low-temperature neutron powder diffraction revealed small but significant additional reflections, which emerge in the neutron powder pattern of superconducting $\text{Sr}_2\text{VO}_3\text{FeAs}$. A preliminary analysis of these reflections indicates incommensurate, possibly helical magnetic ordering of the V-moments with a propagation vector of $\mathbf{q} \approx (0, 0, 0.306)$. This is in agreement with strongly correlated vanadium, which does not significantly contribute to the Fermi surfaces. Thus, $\text{Sr}_2\text{VO}_3\text{FeAs}$ is in line with the other iron pnictide superconductors and does not represent a new paradigm, although the absence of iron magnetism and possible self-doping effects remain open questions.

15.2 Outlook

Before the discovery of high-temperature superconductivity in the iron pnictides, many people had believed that superconductivity research had come to an impasse. Enormous progress has been made since then and there is no doubt that a new era in superconductivity research has begun. This is not only reflected in the extraordinarily high number of publications within not even three years, also first attempts to produce materials suitable for practical application have been very promising. For example, superconducting wires and tapes, partly with high critical currents, could already be successfully manufactured from the 1111-^[232] 11-^[233] and 122-type^[234] compounds. Especially promising is also the growth of epitaxial thin films of certain iron-based superconductors.^[235] In a very recent study, a much greater robustness of $\text{Ba}(\text{Fe}_{2-x}\text{Co}_x)\text{As}_2$ to misaligned adjacent grains compared to the cuprate superconductors was found. This consolidates the use of iron arsenides of this structure type for practical application due to comparatively easy processability.^[236]

A lot of progress has also been made regarding the physical background of the superconducting mechanism in the iron-based superconductors. For example, the electronic structure of several compounds has been experimentally resolved e.g. via

Chapter 15: Summary and outlook

ARPES measurements and the predicted band structures and Fermi-surface nesting conditions could be confirmed.^[237] The magnetism in the non-superconducting iron pnictide parent compounds has also been elucidated and there are first explanations for the unexpectedly low ordered magnetic moment.^[238] Also the s_{\pm} symmetry of the superconducting order parameter was correctly determined and it is accepted that it plays an important role in how superconductivity works in the iron pnictides.^[239] For further details about the superconducting mechanism, refer also to Chapter 1.1.2. Probably one of the most remarkable findings is that the phase diagrams of all iron pnictide superconductors are strikingly similar to those of other unconventional superconductors (i.e. cuprates, organic and heavy-fermion superconductors). Although there are still uncertainties, in all cases the weak magnetism must be suppressed before bulk superconductivity appears. This points to the key role of magnetic spin fluctuations as a ‘glue’ for superconductivity and even gives rise to the hope to finally derive a generalised theory of unconventional superconductivity.^[239] However, many questions still remain open. An often-noted point is that a universal formula to create superconductors with high critical temperatures is still unknown, but much simpler and more basic attributes of the iron-based superconductors are not yet fully understood. For example, the sensitivity of the superconductivity to the geometry of the iron pnictide layers,^[240] the effect of phonons in the superconducting mechanism,^[177, 241] the role of quantum critical points^{[242], xxii, [243]} and especially the true nature of the magneto-structural phase transitions and their implications to superconductivity are still disputed controversially. Also a very recent publication on the possible evolution of the superconducting order parameter in the underdoped region of $\text{Ba}_{1-x}\text{K}_x\text{Fe}_2\text{As}_2$ from d-wave to s_{\pm} -wave raises new questions.^[244]

Some pressing questions with respect to the results of this dissertation also remain unanswered. One issue concerns the class of 56 K superconductors of the EAFeAsF -type. There, the reason for the poor sample quality is still undetermined so far. This is disappointing, especially as these compounds are theoretically very promising for application due to their high critical temperatures, stability in air and cheap starting materials. While the synthesis of the undoped parent compounds is

^{xxii} Quantum critical points are special phase transitions at 0 K in solids, which arise from zero temperature quantum fluctuations associated with Heisenberg’s uncertainty principle.

mastered easily, to this day it has not been possible to obtain single-phase samples of the corresponding superconductors by doping with rare earth metals.

Another important question concerns the puzzling properties of the 37 K superconductor $\text{Sr}_2\text{VO}_3\text{FeAs}$. While the presence of antiferromagnetic ordering in the vanadium sublattice could be substantiated for the first time within this dissertation, the exact spin structure of this compound has not been clarified yet. Currently, there are ongoing efforts by *Hummel* to synthesise large quantities of $\text{Sr}_2\text{VO}_3\text{FeAs}$ in order to perform investigations with polarised neutrons. Furthermore, the existence of self-doping in this iron arsenide should be conclusively clarified.

Last but not least, there are still no conclusive reasons for the absence of both superconductivity and any structural or magnetic phase transition in the non-magnetic compounds $\text{Sr}_3\text{Sc}_2\text{O}_5\text{Fe}_2\text{As}_2$, $\text{Sr}_2\text{ScO}_3\text{FeAs}$ and $\text{Ba}_2\text{ScO}_3\text{FeAs}$. This also raises the question to what extent the magnetic ordering and / or lattice instabilities, which have been observed in other pnictides, are truly necessary conditions for superconductivity.

From the chemical point of view, this is very unfortunate, because these more complex compounds possibly provide the necessary degrees of freedom for new materials with critical temperatures of more than 56 K. Every possible effort should therefore be made, for example, to grow at least small single crystals suitable for examinations via synchrotron X-ray diffraction. Also the search for new materials, for example for iron pnictides with more than one FeAs interlayer distance, should continue. The importance of this undertaking is underlined by recent findings of high-temperature superconductivity in iron arsenides like $\text{Ca}_{n+1}(\text{Sc,Ti})_n\text{O}_y\text{Fe}_2\text{As}_2$ with extremely thick oxide layers between the iron arsenide layers.^[219] This does not only show the outstanding variety, which is possible in the class of iron arsenide superconductors, it also demonstrates that the quest for new iron-based materials can continue for years or even decades. In this context, it does not seem unlikely that the final breakthrough of the iron pnictides lies in complex compounds with critical temperatures way beyond those of today's record holders.

16. AC susceptometer

A fully automated differential dual-coil AC susceptometer, which operates between 3.4 and 320 K with a closed-cycle refrigerator, was developed for measurements of the AC susceptibility in solid samples. A guide with general considerations to constructing an AC susceptometer can be found elsewhere.^[245] It was taken as a design guide for several features of the AC susceptometer introduced in this chapter. The setup of this susceptometer is depicted in Figure 16.1.



Figure 16.1: AC Susceptometer (left) with controllers (right).

16.1 Overview

The technical specifications of the AC susceptometer are as follows:

Cryostat, cold head and compressor:

- SHI-950 two-stage closed-cycle refrigerator system with ^4He exchange gas (JANIS RESEARCH CORPORATION)
- RDK-408D2 cold head (SUMITOMO HEAVY INDUSTRIES LTD.)
- Water-cooled F-50 compressor unit (SUMITOMO HEAVY INDUSTRIES LTD.) operating at 400 V (three-phase current), 50 Hz

Temperature control:

- Model 332 temperature controller (LAKE SHORE CRYOTRONICS, INC.) operating in dual-channel mode with a manually calibrated sextuple-zone P / I / D control for both control loops. Primary control loop: He exchange gas. Secondary control loop: sample holder. For general temperature controller tuning instructions, refer e.g. to [246].

Sample transport:

- DC transport unit with vertical and axial stepper motors (QUANTUM DESIGN). Refer to Chapter 16.4 for the specification of the sample transport controller.

Coil design:

- Primary coil with 973 loops and compensated dual-coil pick-up system. Refer to Chapter 16.2 for details.

Oscillator/Lock-in amplifier:

- 7260 DSP oscillator / lock-in amplifier (EG&G / SIGNAL RECOVERY). Internal resistance of oscillator: 50Ω . Recommended primary coil series resistor: 50Ω (the oscillator signal is then undistorted up to $\sim 3.5 V_{\text{rms}}$ primary voltage). Resistance of cables: 0.6Ω . For operation with the highest precision, the following lock-in amplifier settings are recommended:

- Operating mode: signal recovery
- Input connector shells: float 1 k Ω pull-up
- Input device: bipolar (10 k Ω input impedance)
- Coupling: AC
- Reference: internal
- Filter slope: 24 dB/octave

16.2 Coil design

The coil bobbin was cut out of a TECASINT 2011 polyimide rod (ENSINGER GMBH, Nufringen) on a lathe. First, the pick-up (secondary) coils were wound in opposite directions using a 100 μm enamelled copper wire (1453 turns per coil). The primary coil was wound directly on top of the pick-up coils with a 180 μm enamelled copper wire (973 turns, 4 layers). Figure 16.2 shows the upper pick-up coil during winding on a special coil-winding lathe (top) and the complete coil (bottom).



Figure 16.2: Winding of the upper pick-up coil on a lathe (top).
Complete coil with a test sample (bottom).

The primary coil resistance was measured at different temperatures (Table 16.1) in order to calculate the total impedance and thus magnetic field for all temperatures (the interpolated temperatures were derived from a polynomial series fit of 7th order).

Temp. (K)	3.4	20	40	60	80	100	120	140	160
Resist. (Ω)	0.1	0.1	0.5	1.6	3.5	5.1	7.4	9.3	11.5
Temp. (K)	180	200	220	240	260	280	300	320	
Resist. (Ω)	14.5	16.3	18.2	20.0	22.8	24.9	26.8	29.3	

Table 16.1: Measured primary coil resistance for different temperatures

The self-inductance L of the coil is calculated as:

$$L = \frac{\mu_0 \cdot N^2 \cdot A}{l}$$

μ_0 : permeability of free space ($4\pi \cdot 10^{-7} \text{ T}^2 \cdot \text{m}^3 \cdot \text{J}^{-1}$)
 N : number of turns (973)
 A : area of one loop ($\pi \cdot r^2 = 1.327 \cdot 10^{-4} \text{ m}^2$)
 l : length of coil (0.0495 m)

The total impedance of the coil is dependent on frequency and temperature and calculated as:

$$Z = \sqrt{R^2 + (2 \cdot \pi \cdot f \cdot L)^2}$$

R : total resistance (coil + resistor + int. resist.)
 f : frequency

The effective current through the coil is:

$$I_{\text{eff}} = \frac{U_{\text{eff}}}{Z}$$

The magnetic flux density (in G) can therefore be calculated as:

$$B = \frac{\mu_0 \cdot N \cdot I_{\text{eff}}}{l} \cdot 10^4$$

B is dependent on U_{eff} , f and T .

The temperature and voltage dependence of B at $T = 300$ K and the temperature and frequency dependence of B at $f = 1.333$ kHz are depicted in Figure 16.3. An automated Maple^[49] worksheet with the calculations is available for download.^[247] It can easily be adapted to calculate different primary coil characteristics. In the software AC Susceptometer control, the primary coil characteristics are automatically calculated on processing the raw data files (see Chapter 16.5).

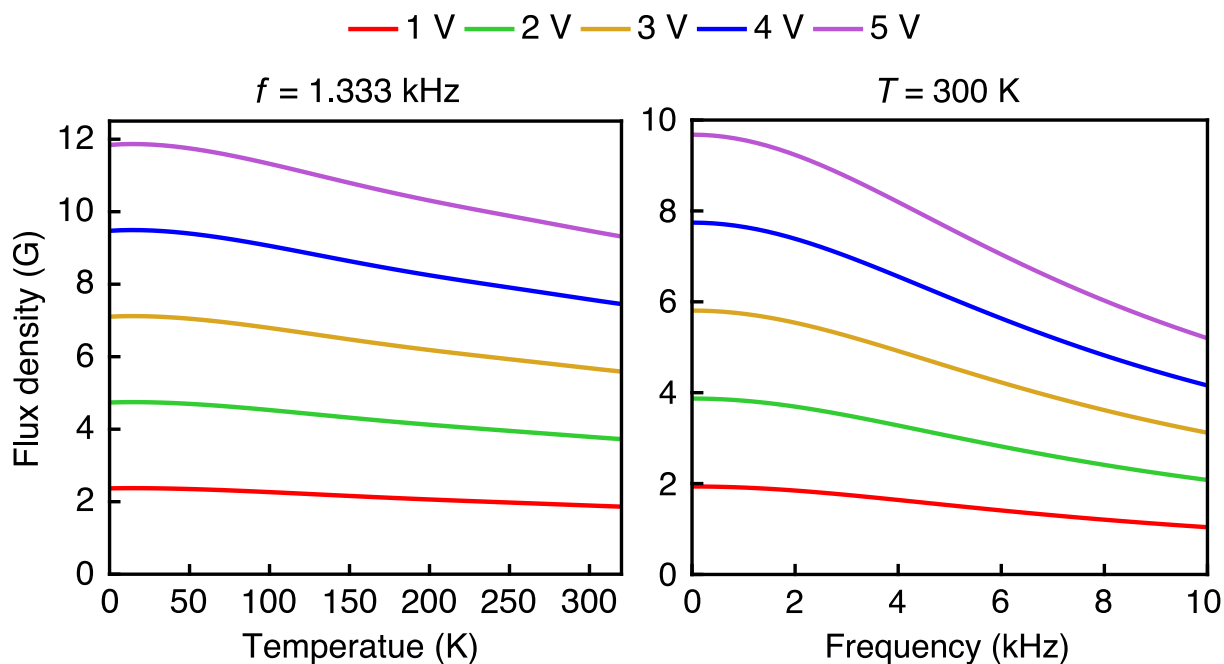


Figure 16.3: Calculated characteristics of the currently used primary coil. Temperature / voltage dependence (left) and frequency / voltage dependence (right).

As the input impedance of the lock-in amplifier is very high in comparison with the pick-up coil impedance, the resistance change of the secondary coils with temperature is negligible. The imbalance of the secondary coils and the inhomogeneity of the magnetic field created by the primary coil lead to an error signal, which was compensated as far as possible by carefully adjusting the loops of the primary coil's upper layer. The primary coil was fastened solely via insulating tape and a cable tie so that later re-adjustment of the primary coil remains possible. The residual error signal ($< 140 \mu\text{V}$ at 1 V primary voltage, 1.333 kHz and room temperature in the final susceptometer setup) is then compensated *in situ* via differential coil measurements using the sample transport described in Chapter 16.4.

16.3 Coil holder, wiring

The coil was attached to the bottom end of the sample rod feed-through of the SHI-950 cryostat via a non-magnetic brass ring and four brass screws. The electrical connection of the coil is a pluggable design with symmetrical (twisted-pair) 200 μm enamelled copper wires connecting the coil plug to the SHI-950 'B' electrical feed-through. The corresponding 'B' plug is then connected to both the oscillator (after passing a breakout box with a variable primary coil series resistor) and the lock-in amplifier. For both connections, coaxial cables with an impedance of 50 Ω have to be used.

16.4 Sample transport

A Quantum Design DC sample transport was available for sample centring and differential coil measurements. An aluminium platform with suitable vacuum flange was designed and constructed in cooperation with *Hackl* (Walther Meißner Institut, Garching) to mechanically connect the sample transport to the JANIS cryostat. The sample transport and the platform are depicted in Figure 16.4.



Figure 16.4: Aluminium platform with QUANTUM DESIGN DC sample mount.

As the DC sample transport contains two stepper motors (for vertical motion and for axial rotation), a RS232 controllable dual-channel stepper controller was designed and built. It is based on the RN stepper controller by ROBOTIKHARDWARE.DE and was modified according to the sample transport circuitry. The circuit and wiring diagrams of both the stepper controller and the sample transport can be found in the appendix (Chapter 21.6). The stepper controller is designed to operate in bridged mode, i.e. with a shared voltage supply for the controller unit and both stepper motors. A voltage of $12 V_{DC}$ is recommended, voltages of up to $15 V_{DC}$ are possible. The recommended currents, speed and acceleration to reliably and safely drive the stepper motors of the sample transport can be found in Table 16.2, the stepper motor controller is depicted in Figure 16.5. As sample holder, a 1500×2 mm carbon fibre-reinforced rod was cast into a 300×3 mm brass rod with Stycast resin, which itself was put through a blue QUANTUM DESIGN DC SQUID feed-through plug on one side. On the other side, a gas permeable straw holder was attached to the carbon fibre rod. A drinking straw (5 mm outer diameter) with a size 5 gelatine capsule (IPHAS

PHARMA-VERPACKUNG GMBH) as sample container can be attached to the straw holder (Figure 16.6).

Setting	Vertical stepper	Axial stepper
Start up current (mA)	100	25
Movement current (mA)	100	25
Hold current (mA)	50	15
Speed	249	252
Acceleration	251	253

Table 16.2: Recommended stepper motor settings

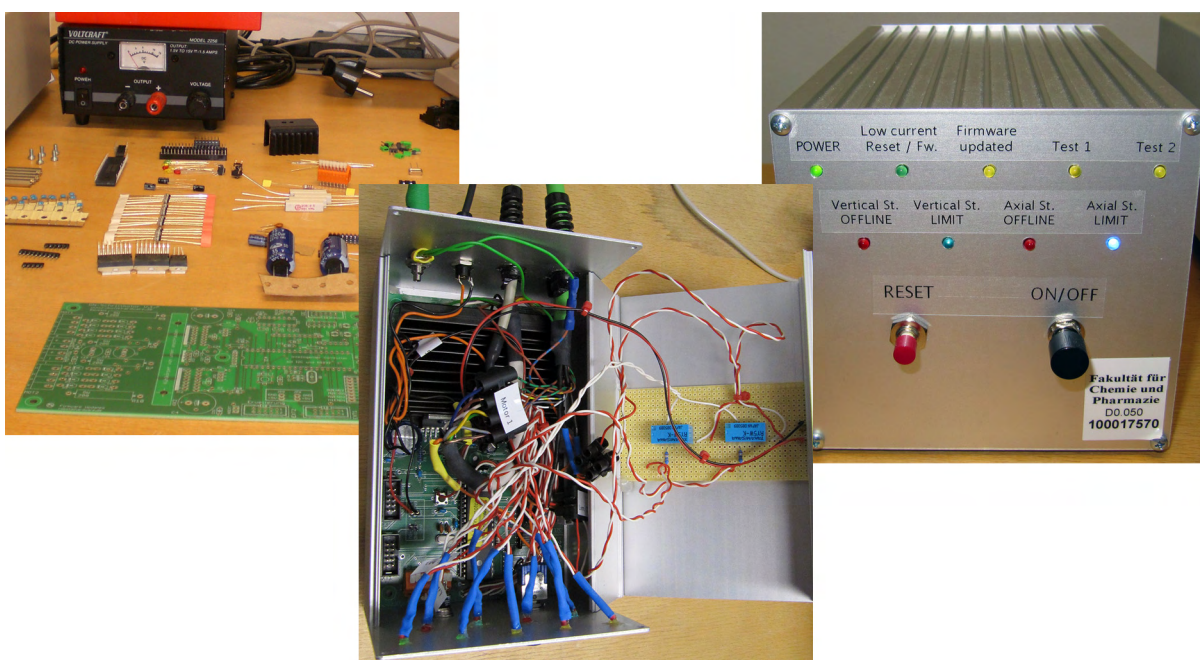


Figure 16.5: Stepper motor controller. Left: PCB and devices. Middle: Open chassis. Right: Finished stepper motor controller in operation.



Figure 16.6: AC Susceptometer sample rod / holder (shortened) with straw and sample.

16.5 AC susceptometer control software

The AC susceptometer control software was developed in LabVIEW.^[248] A full discussion of the software is beyond the scope of this thesis as the source code currently consists of 82 virtual instruments (.vi files) with a total size of almost 2 Mbytes. The source code however is available for download.^[249] In this chapter, a brief explanation of the most important features of the GUI is provided.

16.5.1 User interface

The main user interface of AC susceptometer control is depicted in Figure 16.7. It was designed in such way that most features necessary for measurements are accessible via the main window, ruling out unnecessary dialogs and menu items. At any stage, a context-sensitive help is available directly in the software ('HELP' button) and also a quick start guide is provided ('Quick start').

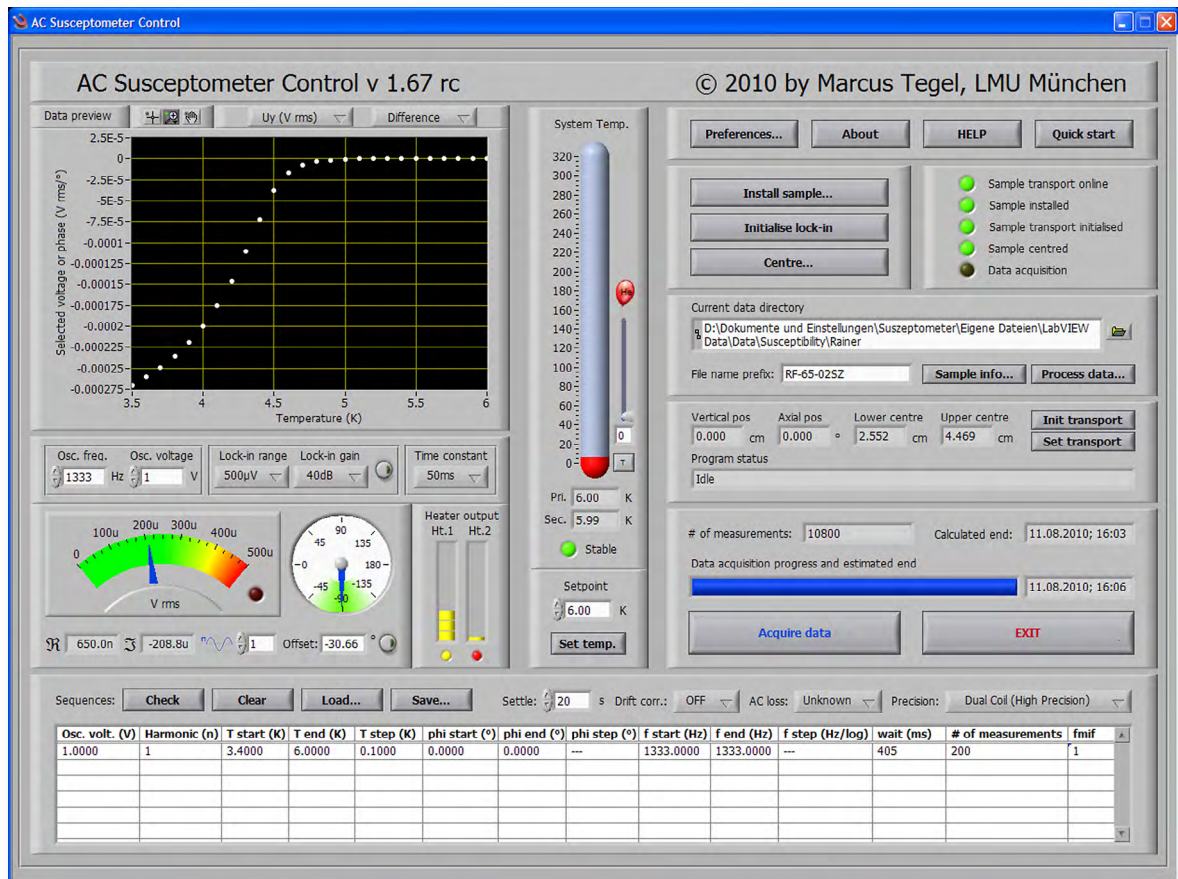


Figure 16.7: GUI of AC susceptometer control v. 1.67 rc

Chapter 16: AC susceptometer

The user interface is grouped into 12 different control regions containing several control elements. These elements are listed and briefly explained in this chapter.

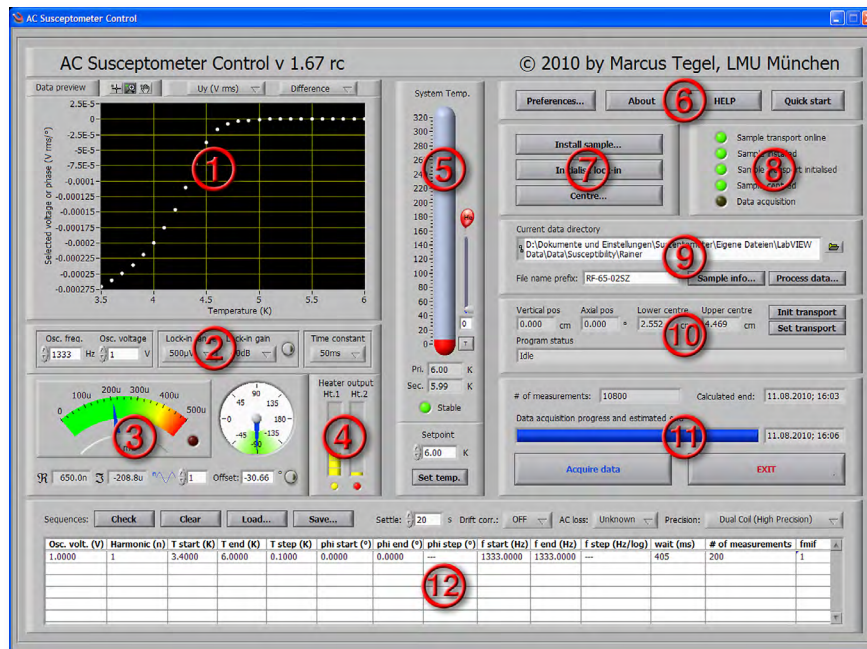


Figure 16.8: Control regions of AC Susceptometer Control

1. Data preview panel

- Unit selector:

U_x Display the real part of the pick-up voltage, which is proportional to the imaginary magnetic response of the sample M'' .

U_y Display the imaginary part of the pick-up voltage, which is proportional to the real magnetic response of the sample M' .

U Display the magnitude of the pick-up voltage.

Ph Display the phase of the pick-up voltage.

- Coil selector:

Difference Display the difference between upper and lower pick-up coil (this setting is recommended for dual coil measurements).

Lower coil	Display the lower coil values only (e.g. for single coil measurements).
Upper coil	Display the upper coil values only (e.g. for troubleshooting purposes).
• Data preview:	Displays susceptibility data during or after measurements. Depending on the selected unit and coil(s), the raw voltage or phase from the lock-in amplifier readout of the corresponding pick-up coil(s) is displayed.

2. Oscillator and lock-in settings

- Osc. freq.: Displays the current oscillator frequency. This value can be modified to set a new frequency.
- Osc. voltage: Displays the current oscillator voltage. This value can be changed to set a new voltage. The oscillator voltage is roughly proportional to the primary magnetic field. For the exact relation of the primary voltage to the magnetic field, refer to Chapter 16.2.
- Lock-in range: Displays the current measuring range of the lock-in amplifier. This value can be modified to set a new lock-in range.
- Lock-in gain: Displays the current lock-in amplifier gain (sensitivity). This value can be modified to set a new gain.
- Auto button: Perform auto-ranging of the lock-in amplifier (auto-ranges both lock-in range and gain).
- Time constant: Displays the current integration time of the lock-in amplifier. This value can be modified to set a new integration time.

3. Lock-in readout and lock-in phase/harmonics control

- Pick-up readout: Displays an analogue readout of the pick-up coils. The range of the meter corresponds to the lock-in amplifier
-

- range. The red LED indicates a lock-in amplifier overload.
- Pick-up phase: Displays the phase of the pick-up coil signal.
 - \Re and \Im : Displays the real and imaginary part of the pick-up coil voltage. The imaginary part of the pick-up coil is proportional to the real magnetic response of the sample M' .
 - Harmonics select.: Display the n^{th} harmonic of the readout signal ('1' = fundamental).
 - Offset: Displays the current phase offset of the lock-in amplifier. This value changes upon 'nulling' the phase.
 - Auto button: Nulls the phase of the lock-in amplifier. The sample must be outside both primary and pick-up coils for correct nulling (i.e. a sample position of 0 cm or more than 8 cm in the current susceptometer setup)

4. Heater indicators

- Bar graphs: These are indicators of the current heater output power for the primary (^4He exchange gas) and secondary (sample holder) heaters.
- LEDs: The LEDs beneath the bar graphs are indicators for the current heater power ranges (which depend on the zone settings but also indicate heater malfunction):

grey = Heater offline or out of order.

blue = Heater range 'low' (primary heater only).

yellow = Heater range 'medium' (primary heater only).

red = Heater range 'high'.

5. Temperature control

- Thermometer: Displays an analogue readout of the system temperature (red bar). If there is any difference between the primary

-
- and secondary temperature sensors, the magnitude of this difference is indicated as a blue bar.
- He slider: Forces measurements to halt at the selected temperature for additional helium injections. This can be useful if a lower system base temperature is required.
 - T button: Displays the temperature course of both temperature sensors since last time 'Set temp.' has been pressed (up to 1800 seconds). This function is very useful to perform a re-calibration of the temperature controller's *P / I / D* settings or for troubleshooting purposes.
 - Pri.: Displays the current temperature of the primary (⁴He exchange gas) sensor.
 - Sec.: Displays the current temperature of the secondary (sample holder) sensor.
 - Stable: This LED is an indicator if the current temperature is stable:
 grey = Temperature is unstable.
 green = Temperature is stable.
 yellow (blinking) = Temperature is stable (settling for thermal equilibration). The temperature stable criteria can be modified in the 'Preferences...' section.
 - Setpoint: Displays the current temperature set point. This value can be modified to change the set point (**'Set temp.' has to be pressed in order for the changes to take effect**).
 - Set temp.: Alters the temperature to the value specified under 'Set-point'.

6. Help and settings

- Preferences...: Opens a dialog window with various program, hardware, tolerance and calibration settings. These settings usually do not have to be modified between different measure-
-

ments. However, e.g. if the coil is replaced or modified, the coil settings can be altered here.

- About: Displays information about the susceptometer software.
- HELP: Opens the context-sensitive help.
- Quick start: Displays a quick start guide.

7. Initialisation

- Install sample...: Switches off the sample transport so that a new sample can be installed. After installing the new sample and clicking 'OK', a dialog of the sample's properties appears. Then, the sample transport is re-initialised.
- Initialise lock-in: Moves the sample roughly into the lower pick-up coil and auto-ranges the lock-in amplifier (range / gain). Then, the sample is moved to position '0 cm' and the lock-in amplifier's phase is nulled. These steps have to be performed prior to a centring scan either manually or via the 'Initialise lock-in' function.
- Centre...: Opens a dialog for sample centring. This has to be performed each time after a new sample is installed.

8. Initialisation status

- Sample tr. online: Indicates if the stepper controller is online (green LED).
- Sample installed: Indicates if a sample is currently installed (green LED). 'Install sample...' has to be pressed at least once if a new sample is installed.
- Sample tr. initial.: Indicates if the sample transport has been initialised (green LED). Usually, a sample transport initialisation is performed automatically on installing a new sample.
- Sample centred: Indicates if a centring scan has been performed (green LED). Please note that non-magnetic or weakly magnetic samples cannot be centred.

-
- Data acquisition: Indicates if a data acquisition is currently in progress (blinking yellow LED)

9. Sample information and data processing

- Curr. data dir.: Displays the path of the data files for the next data acquisition.
- File name prefix: This is the file prefix of all new data files for the next data acquisition.
- Sample info...: Opens a dialog with the current sample information. Any sample information can be altered *prior* to a measurement. If any changes of the sample information are required *after* a measurement, the sample information can be changed in the headers of the corresponding 'raw' files with a text editor.
- Process data...: Opens the data processing dialog in order to automatically convert 'raw' data files (containing the raw pick-up voltages) to '.mag' files with magnetic units. The conversion process utilises the sample information in the header of the 'raw' data files.

10. Sample movement and program status

- Vertical pos.: Displays the current vertical position of the sample.
 - Axial pos.: Displays the current axial position of the sample.
 - Lower centre: Displays the position of the lower pick-up coil as determined via the sample-centring scan.
 - Upper centre: Displays the position of the upper pick-up coil as determined via the sample-centring scan.
 - Init transport: (Re)-initialises the sample-transport (e.g. if the sample transport has been switched off or if the home position got lost).
 - Set transport: Opens a dialog to manually move the sample to any position.
-

11. Data acquisition panel

- # of measurements: Displays the calculated total number of lock-in amplifier readouts for the entire sequences table.
- Calculated end: Displays the calculated end time based on the current measurement sequences table. The calculation is performed on the basis of pre-calibrated, hard-coded reference times for various cooling / heating ramps and the required lock-in data acquisition times.
- Estimated end: Displays the extrapolated end time of a currently running data acquisition.
- Data acquisition pr.: The progress indicator of the currently running acquisition.

12. Sequences table / global temperature / coil control

- Check: Checks the current sequences table for errors and calculates an end time (see also Section 11 'Calculated end')
- Clear/Load/Save: Clears the sequence table / loads sequences / saves sequences.
- Settle: This is the temperature settle time (to wait for thermal equilibration) after a temperature change in a measurement sequence.
- Drift corr.: Enables an empirical coil drift correction (drift is the change of the pick-up coils' phase offset on temperature changes). As this still is an experimental feature, measurements should currently be performed (and calibrated) *without* coil drift correction.
- AC loss: Enables an empirical AC loss correction (if samples are known to have zero AC loss at the beginning of each sequence). Although this is useful for coil setups with a shortened primary coil such as the currently used coil,

-
- this still is an experimental feature. Measurements should currently be performed *without* AC loss correction (set to unknown).
- Precision: This is the selector for single coil or dual coil (differential) measurements. As any error signal is subtracted, dual coil measurements are highly recommended in all cases.
 - Osc. voltage: Specifies the voltage of the oscillator of a measurement sequence. The oscillator voltage is roughly proportional to the primary magnetic field. For the exact relation of the primary voltage to the magnetic field, refer to Chapter 16.2.
 - Harmonic: Specifies the n^{th} harmonic of the readout signal to be recorded in a measurement sequence ('1' = fundamental, i.e. normal magnetism).
 - T start: Specifies the start temperature in a measurement sequence.
 - T end: Specifies the end temperature in a measurement sequence.
 - T step: Specifies the temperature step size in a measurement sequence.
 - ϕ start: Specifies the start angle (for sample rotation) in a measurement sequence.
 - ϕ end: Specifies the end angle (for sample rotation) in a measurement sequence.
 - ϕ step: Specifies the angle step size (for sample rotation) in a measurement sequence.
 - f start: Specifies the start frequency in a measurement sequence.
 - f end: Specifies the end frequency in a measurement sequence.
 - f step: Specifies the frequency step size in a measurement sequence in the following way:
-

- a) Numerical values specify a linear frequency step size.
 - b) If 'log' is appended to the step size n , frequency steps are calculated in $\frac{1}{n}$ ths of the corresponding \log_{10} . For example, a start frequency of 1000 Hz, an end frequency of 10 Hz and 'f step' of 2 log will result in measurement of the frequencies 1000, 500, 100, 50 and 10 Hz.
- wait: This is the time delay of the lock-in amplifier between two consecutive measurements. This delay needs to be at least 2.1, 4.1, 6.1, or 8.1 times the lock-in time constant for 6, 12, 18, 24 dB/octave lock-in filter slope ('Preferences...'), respectively and will be coerced to the appropriate minimum if set lower.
 - # of measurements: Specifies the number of measurements in a measurement sequence.
 - fmif: Specifies a frequency-dependent multiplication factor. In case of frequency-dependent measurements, 'fmif' indicates how often the measurements will be repeated at the lowest given frequency (which can either be 'f start' or 'f end'). Example: A setting of 'f start' to 1 Hz, 'f end' to 10000 Hz, '# of measurements' to 10 and 'fmif' to 5 will result in 10 measurements at 10000 Hz and 50 measurements at 1 Hz. This function works both for logarithmic and linear frequency steps.

16.5.2 Centring dialog

As every sample has to be accurately centred in both pick-up coils in order to measure the magnetic response, the sample centring process opens a separate window (Figure 16.9). The following control elements are available there:

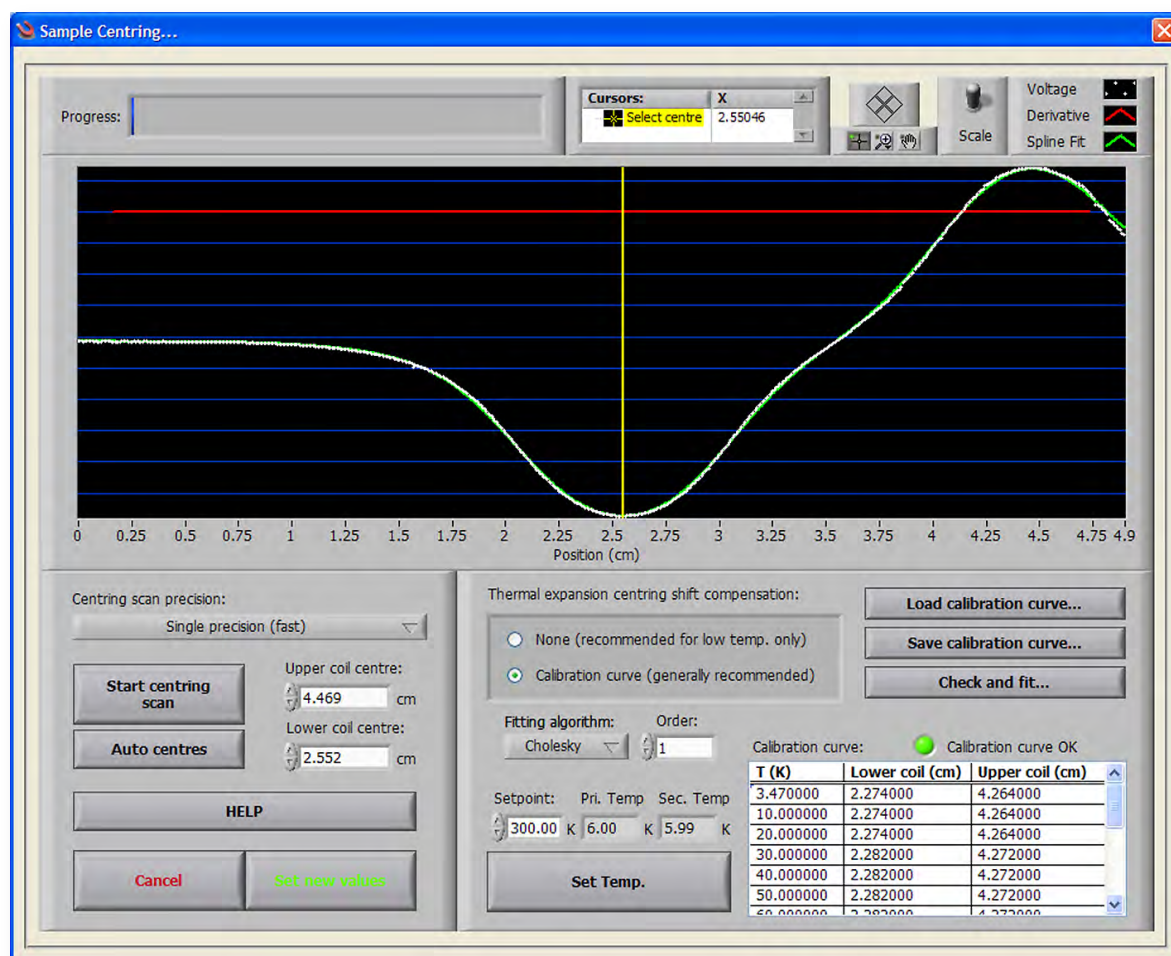


Figure 16.9: Centring dialog of AC Susceptometer Control. A diamagnetic (superconducting) centring signal is visible.

- **Progress:** This is the centring progress indicator.
- **Cursors:** The cursors window displays the position of the movable, yellow cursor for manual centring purposes.
- **Scale:** Switches between pick-up coil voltage and voltage derivative view (y -axis).
- **Curve:** Displays the pick-up coil raw voltage (white points), derivative of the raw voltage (red curve) and raw voltage spline fit (green curve) versus sample position. The y -axis is free of units as only relative changes are relevant.
- **Centring scan prec.:** Specifies the number of measurements for each position. For weakly magnetic samples, the centring scan

precision can be increased at the expense of an extended centring time.

- Start centring scan: Performs a new centring scan.
 - Auto centres: Automatically determines the coil centre positions after a centring scan. This feature is very reliable and therefore highly recommended.
 - Upper/lower coil c.: The pick-up coil centre positions, which were determined either automatically ('Auto centres') or manually ('Cursors'), are entered here. In case of 'Auto centres' this is performed automatically.
 - Help: Displays a context-sensitive help.
 - Cancel: Closes the centring dialog without saving changes.
 - Set new values: Closes the centring dialog and accepts both the new coil centres and the thermal expansion calibration curve.
 - Thermal exp. c.s.c.: Selector for the compensation method for thermal expansion of the sample holder and coil ('Calibration curve' is recommended).
 - Fitting algorithm: Selector for the fitting method of the calibration curve ('Cholesky' is recommended).
 - Order: Polynomial order for the calibration curve fitting function ('1' = linear fit is recommended).
 - Setpoint: Can be used to specify a new temperature set point (e.g. if a new thermal expansion calibration curve is recorded). **'Set Temp.' has to be pressed in order for the changes to take effect.**
 - Pri./Sec. Temp.: Displays the current temperature of the primary / secondary sensor.
 - Set Temp.: Change set point to value specified above.
 - Load calibr. curve: Loads a calibration curve.
 - Save calibr. curve: Saves a calibration curve.
 - Check and fit: Checks the values in the calibration table and performs least squares fitting with the method specified above.
-

- Calibr. curve table: The positions of both pick-up coil centres can be entered here for different temperatures as calibration curve.

16.5.3 Other dialogs

Additionally, a couple of other dialogs are available, such as the sample information dialog (after a new sample is installed or when ‘Sample info...’ is pressed). The latter dialog is self-explaining. Furthermore, the ‘Process data...’ dialog is important, as all recorded ‘.raw’ data files are converted into ‘.mag’ files containing magnetic units in this step. In the ‘File name prefix’ field, the data processing can be restrained to files starting with this prefix. Both dialogs are depicted in Figure 16.10.

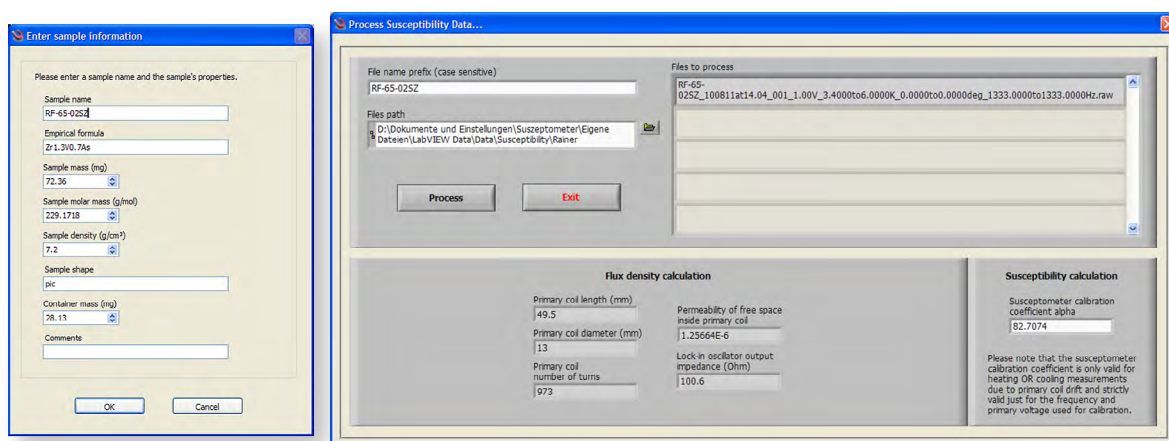


Figure 16.10: Sample information and process data dialogs.

Various program preferences (i.e. calibration, coil and hardware settings, tolerances, email address for notifications, etc.) are available on pressing ‘Preferences...’ in the AC Susceptometer main window, an example for such a preference pane is depicted in Figure 16.11.

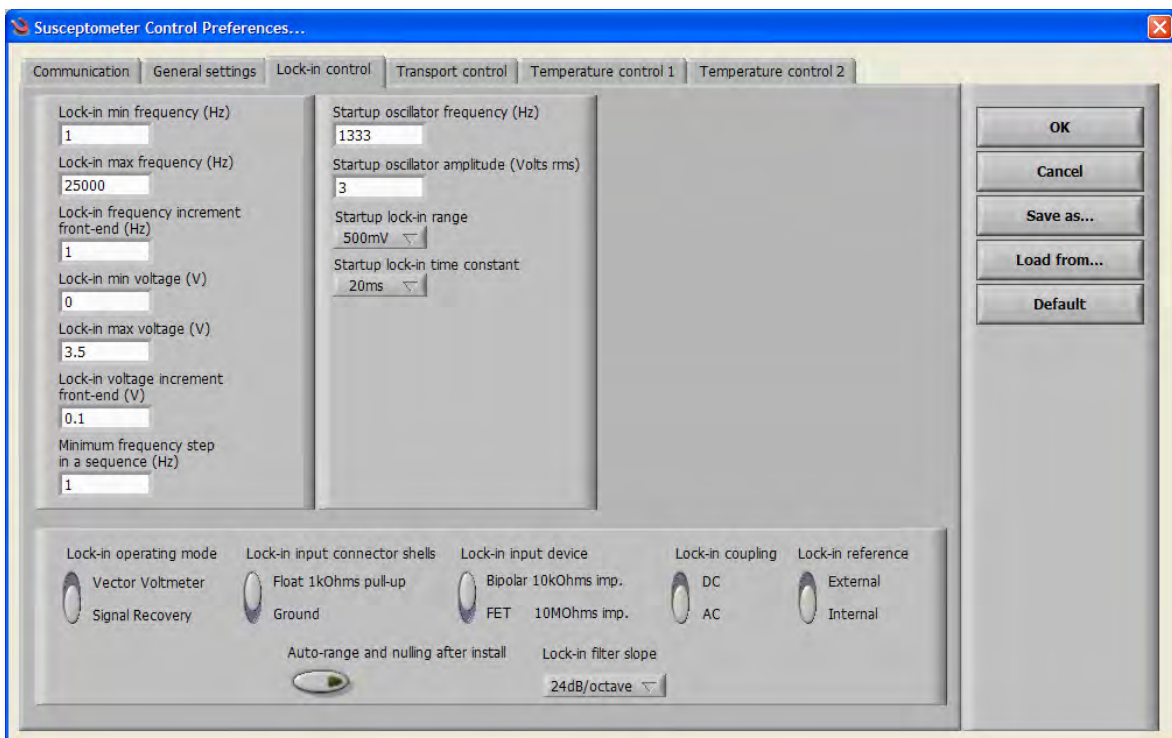


Figure 16.11: Example preference pane (Lock-in settings).

17. Four-terminal conductometer

17.1 Overview



Figure 17.1: Overall conductometer setup during a measurement. Left: Cryostat setup with sample rod inserted. Middle: Temperature controller and computer. Right: Source and nanovolt meters.

An automatic four-terminal conductometer was developed for measurements of the specific resistivity in solid samples. It uses the same cryostat and sample mounting system as the AC susceptometer described in Chapter 16 and can be used without removing the coil, sample transport and measuring equipment of the AC susceptometer. Measurements of the electrical resistivity can be performed on pellets of polycrystalline samples (4 mm in diameter, thickness 0.2 to 2.1 mm) using the sample holder design described in Chapter 17.2. Generally, the current-reversal four-terminal sensing method is used. A KEITHLEY Source Meter 2400 is employed as current source in order to generate square waves with amplitudes of 2 μA to 5 mA and

frequencies of either 2 or 0.4 Hz (1 or 5 PLC, respectively). The differential voltage drop between signal-high and signal-low is recorded with a KEITHLEY 2182 nanovoltmeter. The overall setup is depicted in Figure 17.1.

17.2 Sample holder design

A special sample holder was designed so that the cryostat from the AC susceptometer can also be used for resistivity measurements without removing the susceptometer coil or sample transport. As the susceptometer coil's inner diameter is only ~ 6 mm, the resistivity sample holder had to be miniaturised accordingly. Moreover, the sample holder had to be re-usable and easily detachable from the sample rod. The sample rod also was designed to fit to the existing measuring equipment (source meter and nanovoltmeter). Ten sample holders were manufactured from circuit boards (PCBs), which had been milled by *Lopez-Diaz* at the Fraunhofer IAF, Freiburg. FR4 with a thickness of 1.5 mm and a copper layer thickness of $30 \mu\text{m}$ was employed as circuit board material. The milling layout of a PCB's copper layer is depicted in Figure 17.2.

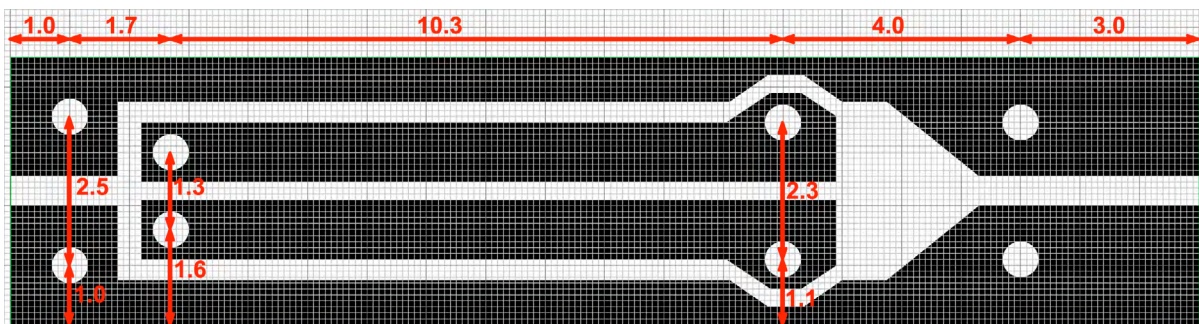


Figure 17.2: Layout of the PCB copper layer (black) of the sample holder.
Grid spacing: 0.1 mm.

OMNETICS MCP-05-SS plugs (Part no. A22000-001) were soldered to the PCB with GOODFELLOW hard-temper 0.5 mm beryllium copper ($\text{Cu}_{98}\text{Be}_2$) wire (Part no. CU075320).

Four beryllium copper pins were soldered to the PCB as sample terminals and the bottom of the PCB was casted into Stycast resin as corrosion protection for the hard-terminal variant. A complete sample holder with hard-temper terminals is de-

picted in Figure 17.3. Instead of hard-temper beryllium copper terminals, soft and more flexible (e.g. 0.2 mm) copper wires can be soldered into the terminal bore holes in order to measure small samples of any shape. Furthermore, shrink tubing can serve as temporary corrosion protection and to fix the sample on the PCB (Figure 17.5). This also enables resistivity measurements of highly air sensitive compounds, as all preparation steps can then be performed in a glove box under an atmosphere of argon (Figure 17.4).



Figure 17.3: Complete sample holder with hard terminals.

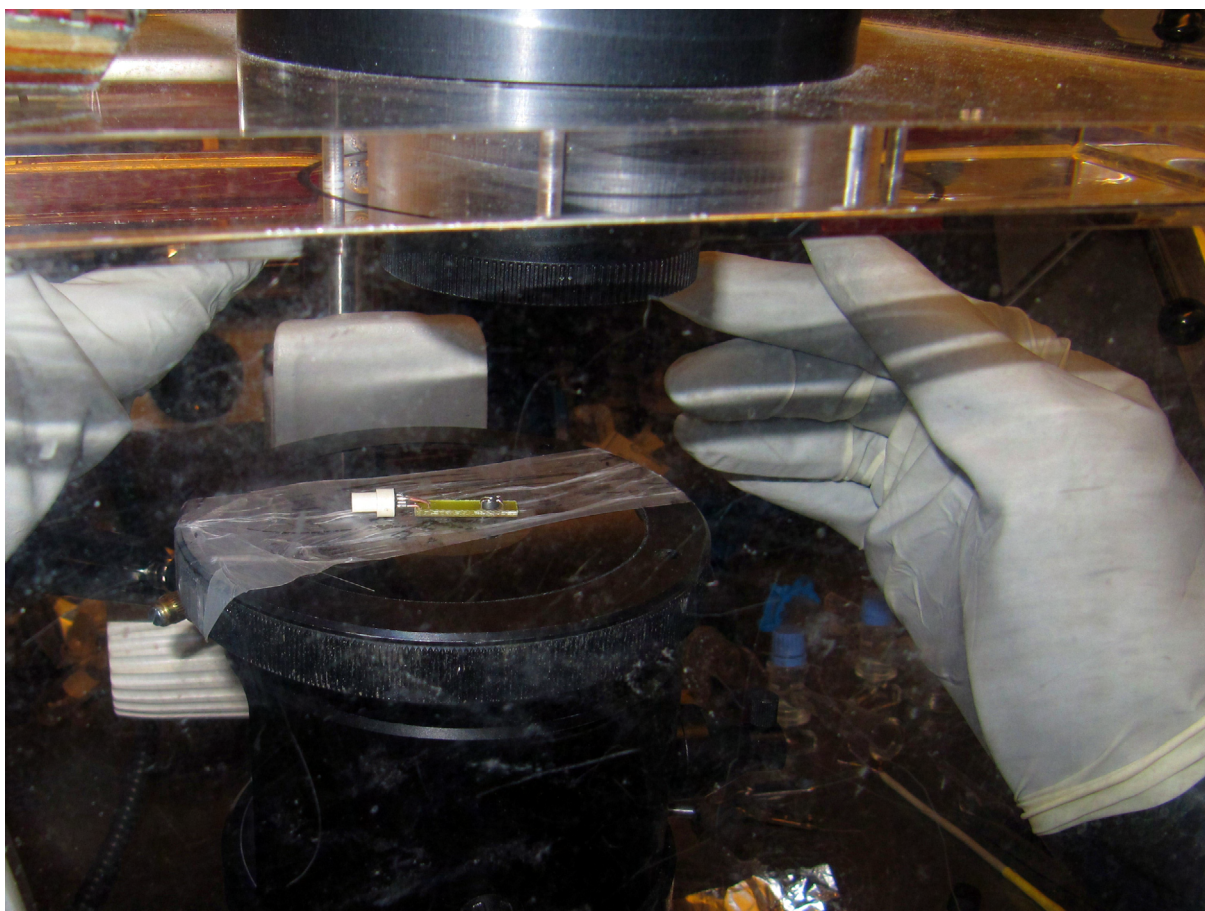


Figure 17.4: Conductivity sample preparation under inert conditions (glove box).

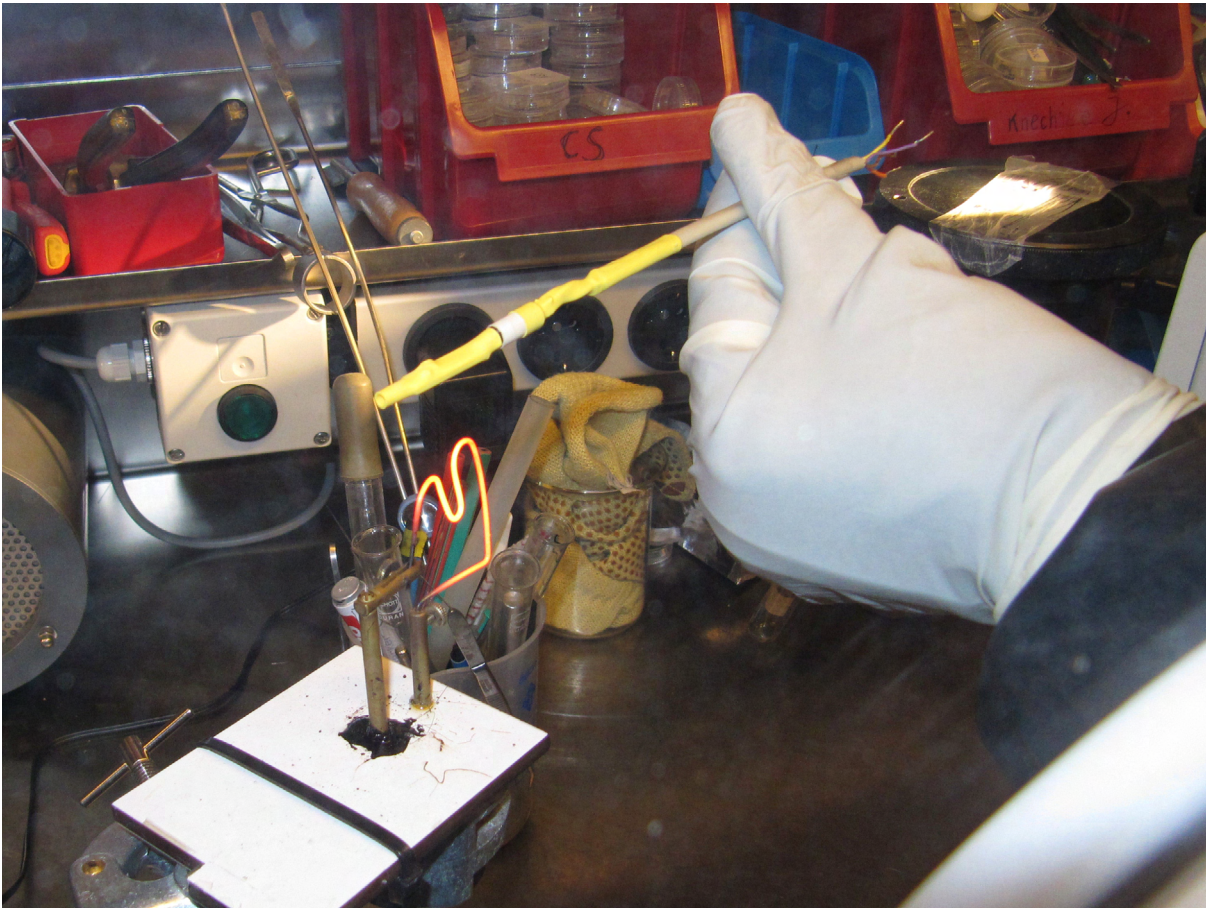


Figure 17.5: Fixation and protection of the sample via shrink tubing (glove box).

17.3 Sample rod, wiring

The sample rod was made from a 1500 × 3 mm stainless steel rod. LAKE SHORE Quad-TwistT-Cryogenic wire (36 AWG) was cast into the rod using Stycast resin and an OMNETICS MCS-05-SS socket (Part no. A22001-001) was soldered and cast to one end of the rod. The other end was put through a blue QUANTUM DESIGN DC SQUID feed-through plug and a FISCHER K 102 A053-130 + plug with E3 102.5/3.5 | 102.212 collet was attached to this end. The sample rod design is depicted in Figure 17.6.



Figure 17.6: Resistivity sample rod with sample holder and sample.

The sample rod is connected to a breakout box with a symmetrical (twisted-pair) data cable. The wiring diagram of the sample holder, sample rod, data cable and connectors is depicted in Figure 17.7. Twisted wire pairs are marked with a curly brace.

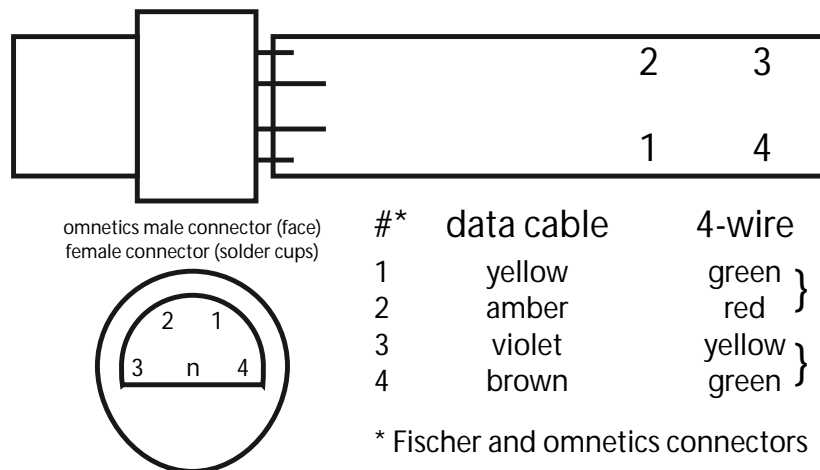


Figure 17.7: Resistivity sample holder (wiring diagram).

17.4 Conductivity control software

The Conductivity Control interface shares the key elements (control regions) with the AC susceptometer control software (Chapter 16.5). The source code is available for download.^[250] No sample transport or any form of software calibration is required for resistivity measurements (calibration of the source and nanovolt meters are performed in hardware). Therefore, the only additional windows are the sample information and the data processing dialogs. The conductivity control main window is shown in Figure 17.8.

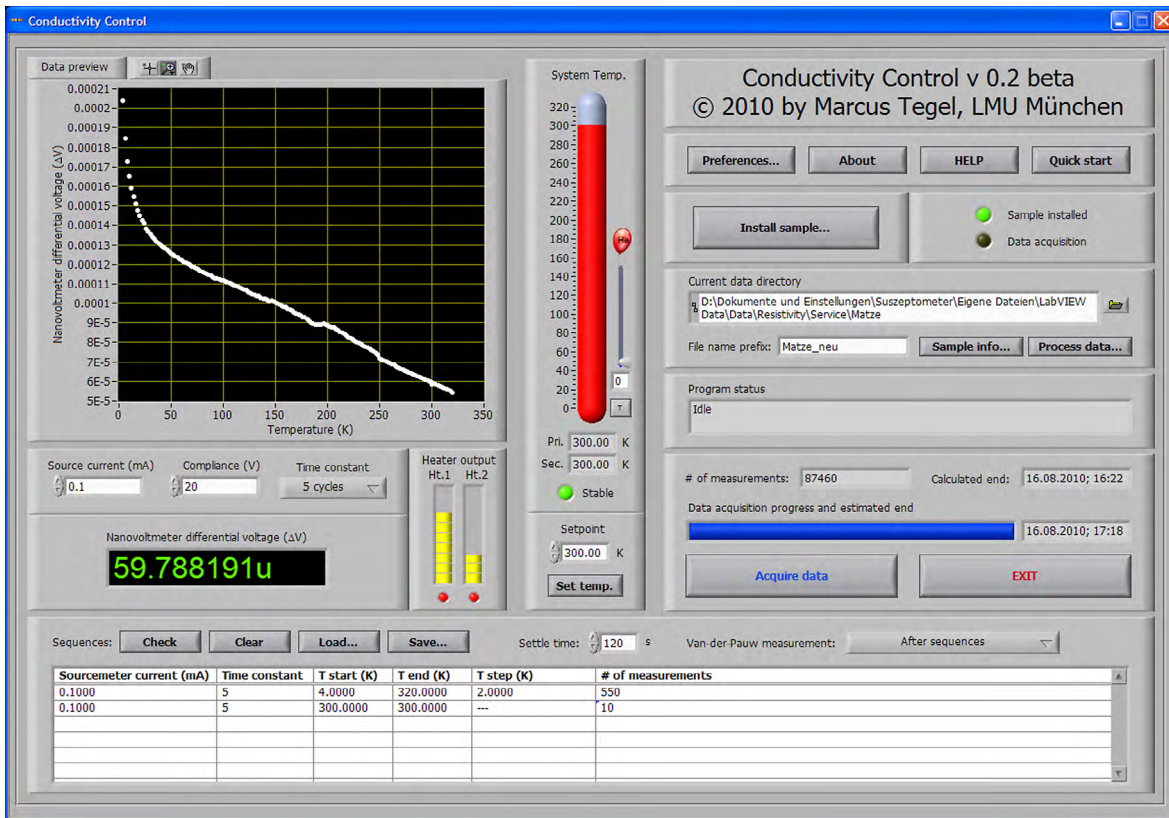


Figure 17.8: Graphical user interface of Conductivity Control v. 0.2 (beta).

Only the control elements which differ from the AC susceptometer control software are discussed here. For all other elements as well as the general program layout, refer to Chapter 16.5.

- **Source current:** Specifies the amplitude (current) of the generated square wave.
- **Compliance:** Specifies the maximum source voltage through the sample (this must be chosen as small that the maximum voltage drop across the sample does not overload the nanovoltmeter input (12 V in the current setup). The sample holder and connectors allow a maximum compliance of ~ 40 V.
- **Time constant:** Specifies the number of power line cycles to integrate. Only 1 or 5 power line cycles are available, 5 cycles are recommended.

- Nanovoltmeter ΔV : Displays the differential voltage across the sample.
- V.-d.-Pauw meas.: Specifies the time when the van-der-Pauw measurement is to be performed (before or after measurement of the sequences).
- Process data...: Performs van-der-Pauw approximation and calculates specific resistivity from recorded raw data ('.rwr') files.

18. HConvert

For convenient batch conversion, range addition, angular thinning, angular binning and beam stop clipping of HUBER G670 Imaging Plate data .gdf files, the JAVA program HConvert has been created. Both a pre-compiled .class file and the source code are available for download:^[51, 251] HConvert's output files include .gsa (half resolution offset subtracted GSAS files), .xy (full resolution ASCII XY files), .xyd (thinned ASCII XY files) and .xyb (binned ASCII XY files). All four output files are generated automatically for each time HConvert is invoked. Old output files are overwritten without further notice.

For the .gsa (GSAS) files, the background offset of the imaging plate is analysed and subtracted in order to correct GSAS' evaluation of counting statistics and thus residual values. For the same purpose, GSAS files may additionally be scaled. This might be necessary for very long measurements, i.e. measurements with millions of counts. The R_{exp} residuals appear artificially low (and χ^2 is too high) in these cases. However, care has to be taken when manipulating the scaling factor.

The .xy files can be loaded directly e.g. in TOPAS Academic and the .xyd or .xyb files can be imported e.g. in STOE WinXPOW, as this program does not allow more than 10000 data points. In thinned (.xyd) files, only every n^{th} data point is taken (which can be useful, when the total number of counts is important). For other purposes, binned (.xyb) files can be taken, which greatly improves the available signal / noise ratio.

HConvert is invoked with the following command on any Mac / Windows / Linux command line (Java needs to be in the search path and HConvert.class either in the Java class search path or in the current directory):

```
java HConvert FILE_PREFIX [LeftBoundary] [ThinningBinning]
                             [ExcludeLeft] [ExcludeRight]
                             [Multiply_GSAS_By]
```

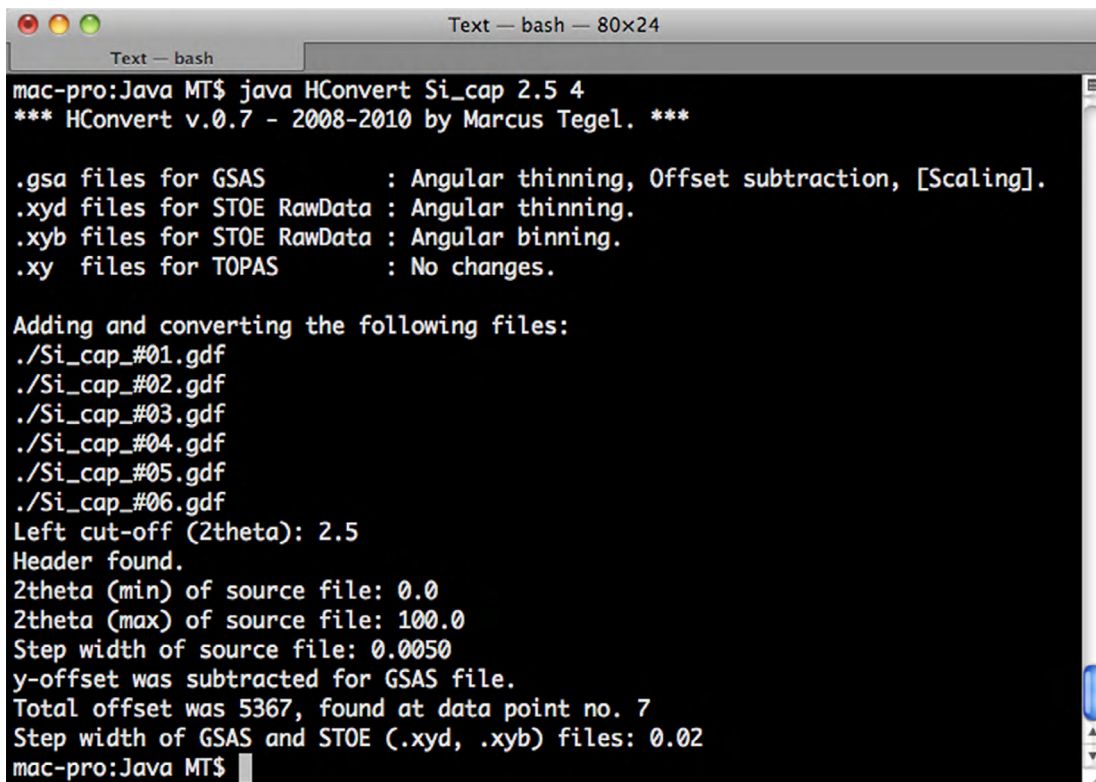
Commands in brackets are optional and replaced by default values if left blank [LeftBoundary = $5.5^\circ 2\theta$ beam stop clipping; thinning / binning of every second data point; no exclusion range; GSAS multiplication factor = 1].

Help is available via:

```
java HConvert
```

If more than one file starting with the same FilePrefix exist, the intensities of these files are added automatically, which can be used to combine multiple measurements. The range between LeftBoundary and RightBoundary will be interpolated linearly and must additionally be excluded from the counting statistics in Rietveld refinements.

An example of how to use HConvert (addition of 6 .gdf files beginning with 'Si_cap', left cut-off $2.5^\circ 2\theta$, binning of 4 data points) is depicted in Figure 18.1.



```
mac-pro:Java MT$ java HConvert Si_cap 2.5 4
*** HConvert v.0.7 - 2008-2010 by Marcus Tegel. ***

.gsa files for GSAS      : Angular thinning, Offset subtraction, [Scaling].
.xyd files for STOE RawData : Angular thinning.
.xyb files for STOE RawData : Angular binning.
.xy files for TOPAS      : No changes.

Adding and converting the following files:
./Si_cap_#01.gdf
./Si_cap_#02.gdf
./Si_cap_#03.gdf
./Si_cap_#04.gdf
./Si_cap_#05.gdf
./Si_cap_#06.gdf
Left cut-off (2theta): 2.5
Header found.
2theta (min) of source file: 0.0
2theta (max) of source file: 100.0
Step width of source file: 0.0050
y-offset was subtracted for GSAS file.
Total offset was 5367, found at data point no. 7
Step width of GSAS and STOE (.xyd, .xyb) files: 0.02
mac-pro:Java MT$
```

Figure 18.1: HConvert usage example.

19. SQUID Processor

A MultiVu (SQUID) data batch processor software has been created. It allows the automatic calculation of various magnetic quantities from recorded QUANTUM DESIGN MultiVu .dat files. Multiple .dat files (of the same substance) can be processed at once and the sample properties are automatically extracted from the data files' headers as far as possible. Executable files (Mac / Windows) are available for download^[91] and require the LabVIEW run time libraries in order to be executed.^[248] The graphical user interface of the software is depicted in Figure 19.1. Functions to correct the measured magnetic moment for both diamagnetism arising from the sample container (e.g. a gelatine capsule) and for diamagnetic increments were also implemented into the software. As an exception, the software expects the use of SI units for diamagnetic increments (in units of $10^{-11} \text{ m}^3 \cdot \text{mol}^{-1}$), such as in Table A.6 in [252]. The following magnetic quantities are calculated and written into ASCII .mgs files (values in scientific notation with decimal point and semicolon as separator): The corrected magnetic moment of the whole sample (M_s), volume magnetisation (M), gram magnetisation (M_g), molar magnetisation (M_m), volume susceptibility (χ), gram susceptibility (χ_g), molar susceptibility (χ_m), inverse molar susceptibility (χ_m^{-1}), the magnetic volume fraction ($4\pi\chi$) and the permanent atomic magnetic moment per magnetic centre (μ / μ_B). If the magnetic moment per formula unit rather than the magnetic moment per magnetic centre is required, 'Number of magnetic centres' has to be set to one. Any output files are stored in a subdirectory of the chosen file path called 'Converted'. Any existing files will be overwritten without further notice.

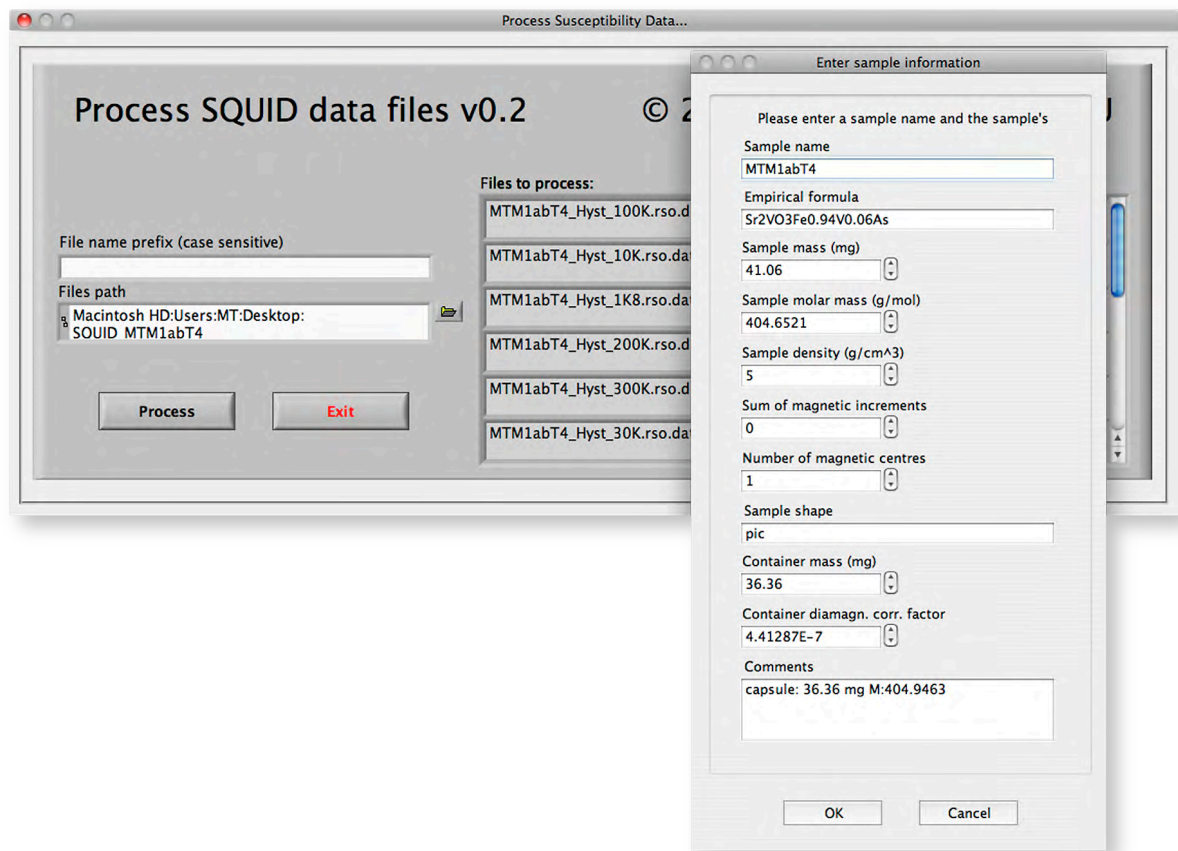


Figure 19.1: Graphical user interface of the SQUID processor program.

20. Molar weight calculator

A simple, yet powerful molar weight calculator has been written in LabVIEW as both standalone software and a LabVIEW module (virtual instrument) for implementation into other LabVIEW projects. This module has also been implemented into the AC susceptometer control and SQUID processor software. The standalone software is available for download (Mac / Windows)^[253] The calculator accepts round and square brackets of any depth, crystal solvents (in the form of e.g. *5H₂O), many organic groups and ligands and also decimal fractions. Separation of elements and / or organic groups is performed automatically. The graphical user interface of the standalone molar weight calculator is depicted in Figure 20.1.

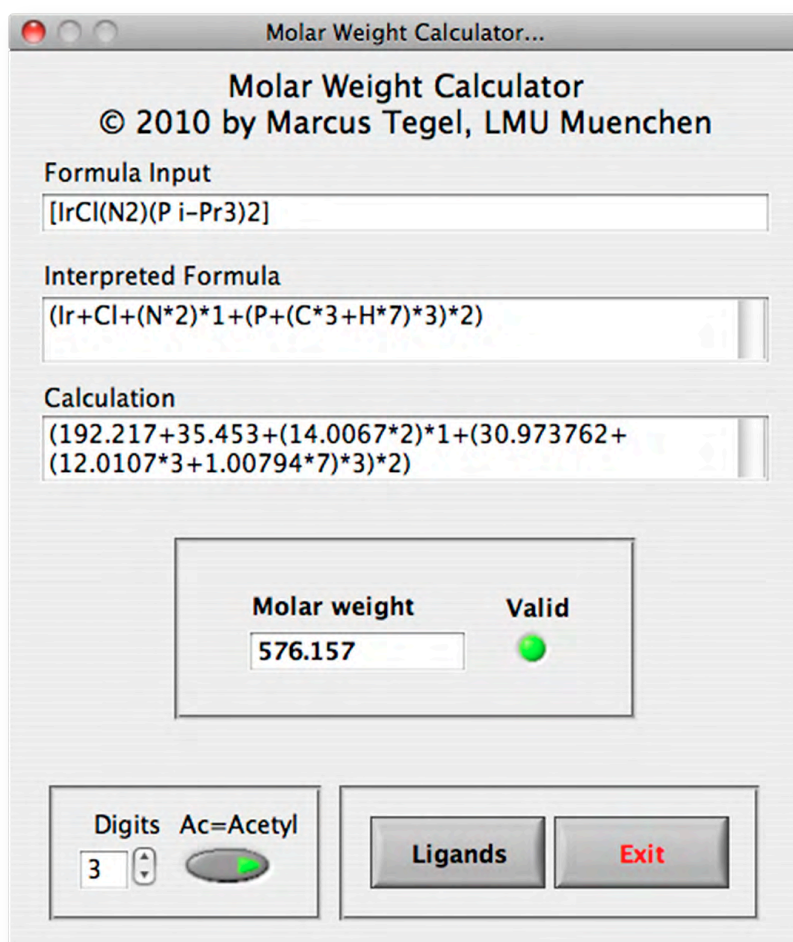


Figure 20.1: Molar weight calculator.

21. Appendix

21.1 Superconducting order parameters

In Figure 21.1, schematic representations of different superconducting order parameters are depicted.^[254] In all three cases, the Fermi surfaces are approximated by circles. The height of the ‘rubber sheets’ is proportional to the magnitude of the order parameters.

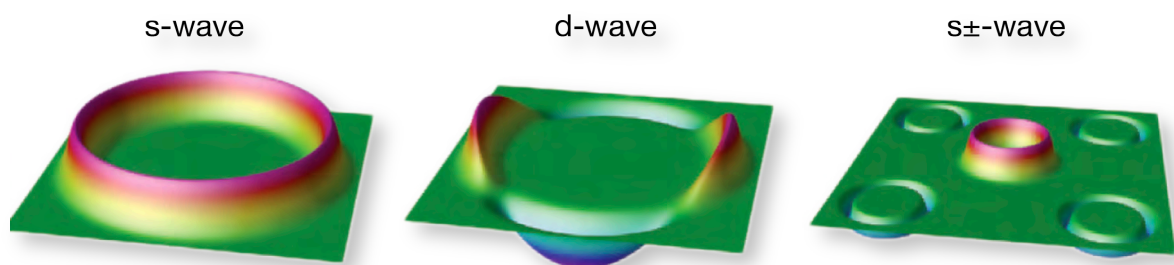


Figure 21.1: Schematic representations of different superconducting order parameters.

21.2 WIEN2k compiler and linker options for Mac OS X

For WIEN2k 9.x, icc 11, fcc 11 and mkl 10, and XCode Tools 3.0, the following WIEN2k compiler and linker settings were used:

```

Compiler options:  -lmkl_intel_lp64 -lmkl_intel_thread
                  -lmkl_core -lguide -lpthread-FR -mp1 -w
                  -prec_div -pc80
                  -pad -ip -DINTEL_VML -O3
Linker Flags:     $(FOPT) -L/Library/Frameworks/
                  Intel_MKL.framework/Libraries/em64t
                  -lpthread
Preprocessor flags: '-DParallel'
R_LIB (LAPACK+BLAS): -lmkl_intel_lp64 -lmkl_intel_thread
                  -lmkl_core -lguide -lpthread

```

21.3 Additional Rietveld refinements

21.3.1 Sr₂CrO₃FeAs (Sample II, X-ray)

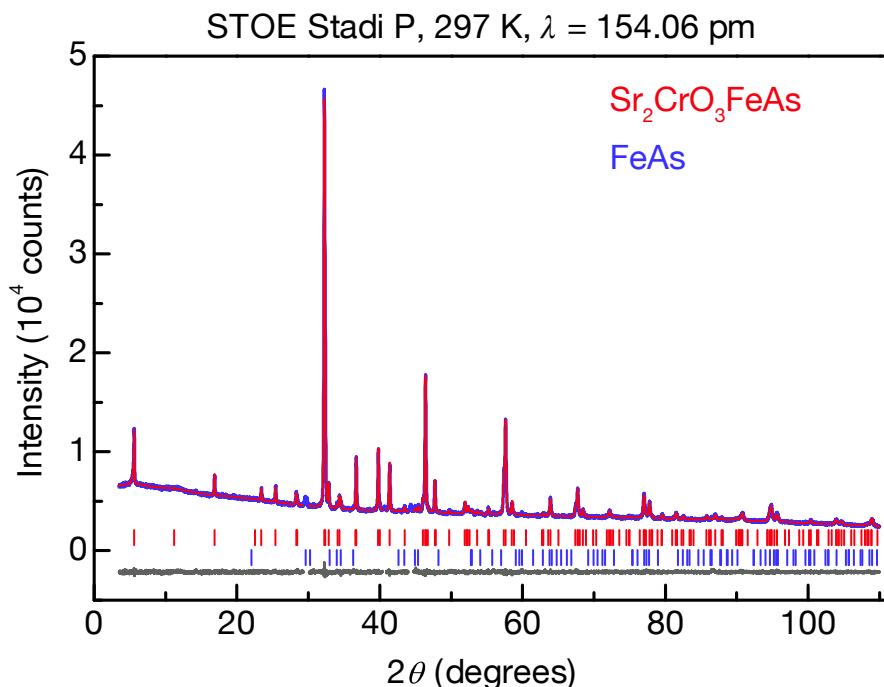


Figure 21.2: Rietveld fit of the 4 g sample Sr₂CrO₃FeAs at 297 K (space group *P4/nmm*).

Temperature	297 K
Diffractometer	STOE STADI P (Cu-K α_1)
Rietveld package	TOPAS
Space group	<i>P4/nmm</i> (<i>o2</i>)
Lattice parameters	$a = 391.24(1)$ pm $c = 1576.23(2)$ pm
Cell volume	$V = 0.24127(1)$ nm ³
Z	2
Data points	10441
Reflections	127 (main phase)
Excluded ranges	29.3 – 30.1; 40.4 – 40.9; 44.0 – 44.7
Constraints	1
Atomic variables	13
Profile variables	5
Anisotropy var.	0
Background var.	36
Imp. phase var.	6
Other variables	5

d range	0.942 – 15.762		
R_P, R_{WP}, R_{Bragg}, χ^2	0.013, 0.017, 0.006, 1.089		
Atomic parameters			
Sr1	2c ($\frac{3}{4}$, $\frac{3}{4}$, z)	z = 0.1940(1)	$U_{iso} = 123(4) \text{ pm}^2$
Sr2	2c ($\frac{3}{4}$, $\frac{3}{4}$, z)	z = 0.4150(1)	$U_{iso} = 180(6) \text{ pm}^2$
Cr1	2c ($\frac{1}{4}$, $\frac{1}{4}$, z)	z = 0.3104(2)	$U_{iso} = 157(8) \text{ pm}^2$
Fe1 [occ 1.00(1)]	2a ($\frac{3}{4}$, $\frac{1}{4}$, 0)		$U_{iso} = 177(9) \text{ pm}^2$
As1	2c ($\frac{1}{4}$, $\frac{1}{4}$, z)	z = 0.0887(1)	$U_{iso} = 110(7) \text{ pm}^2$
O1	4f ($\frac{1}{4}$, $\frac{3}{4}$, z)	z = 0.2950(3)	$U_{iso} = 159(14) \text{ pm}^2$
O2	2c ($\frac{1}{4}$, $\frac{1}{4}$, z)	z = 0.4279(5)	$U_{iso} = 159(14) \text{ pm}^2$
Bond lengths (pm)			
Sr–O	247.5(7) × 1	252.2(4) × 4	272.2(4) × 4 277.4(1) × 4
Cr–O	185.3(8) × 1	197.1(1) × 4	
Fe–Fe	276.7(1) × 4		
Fe–As	240.5(1) × 4		
Bond angles (°)			
As–Fe–As	109.8(1) × 4	108.9(1) × 2 (ε)	
O–Cr–O	89.1(1) × 4	97.1(2) × 4	165.9(3) × 2

Table 21.1: Crystallographic data of the 4 g sample $\text{Sr}_2\text{CrO}_3\text{FeAs}$ at 297 K.

21.4 Magnetic ordering types

The possible commensurate magnetic ordering types in a simple cubic lattice are depicted in Figure 21.3 together with the corresponding magnetic propagation vectors.^[87] Black and white balls denote oppositely oriented spins. Within each ordering type, different spin orientations are favourable (not depicted).

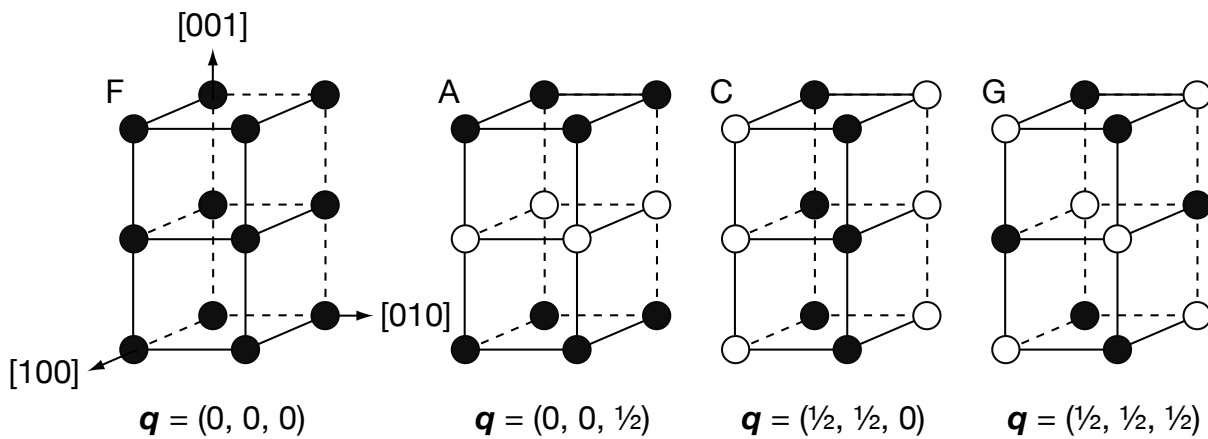
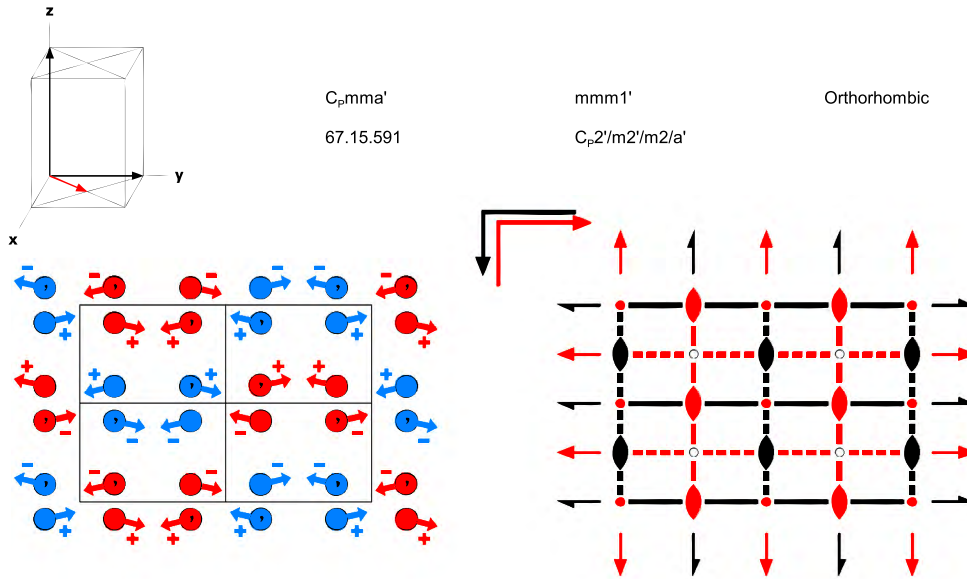


Figure 21.3: Different ordering modes for simple cubic lattices and propagation vectors.

21.5 C_{Pmma}' colour group^[224]



C_{Pmma}'
67.15.591

$mmm1'$
 $C_{P2}'/m2'/m2/a'$

Orthorhombic

Origin at center ($2'/m$) at $2'/m2'/aa'$

Asymmetric unit $0 \leq x \leq 1/2; 0 \leq y \leq 1/4; 0 \leq z \leq 1/2$

Symmetry Operations

- For (0,0,0) + set
- | | | | |
|---|--|--|--|
| (1) 1
(1 0,0,0) | (2) 2 $1/4,0,z$
(2 _z 1/2,0,0) | (3) 2' $1/4,y,0$
(2 _y 1/2,0,0)' | (4) 2' $x,0,0$
(2 _x 0,0,0)' |
| (5) $\bar{1}$ $0,0,0$
($\bar{1}$ 0,0,0)' | (6) a' $(1/2,0,0)$ $x,y,0$
(m _z 1/2,0,0)' | (7) a $(1/2,0,0)$ $x,0,z$
(m _y 1/2,0,0) | (8) m $0,y,z$
(m _x 0,0,0) |
- For (1/2,1/2,0) + set
- | | | | |
|--|--|--|--|
| (1) t' $(1/2,1/2,0)$
(1 1/2,1/2,0)' | (2) 2' $0,1/4,z$
(2 _z 0,1/2,0)' | (3) 2 $(0,1/2,0)$ $0,y,0$
(2 _y 0,1/2,0) | (4) 2 $(1/2,0,0)$ $x,1/4,0$
(2 _x 1/2,1/2,0) |
| (5) $\bar{1}$ $1/4,1/4,0$
($\bar{1}$ 1/2,1/2,0) | (6) b $(0,1/2,0)$ $x,y,0$
(m _z 0,1/2,0) | (7) m' $x,1/4,z$
(m _y 0,1/2,0)' | (8) b' $(0,1/2,0)$ $1/4,y,z$
(m _x 1/2,1/2,0)' |

Generators selected (1); t(1,0,0); t(0,1,0); t(0,0,1); t'(1/2,1/2,0); (2); (3); (5).

Positions

Multiplicity, Wyckoff letter, Site Symmetry.	Coordinates
	(0,0,0) + (1/2,1/2,0) +
16 o 1	(1) x,y,z [u,v,w] (2) $\bar{x}+1/2,\bar{y},z$ [\bar{u},\bar{v},w] (3) $\bar{x}+1/2,y,\bar{z}$ [\bar{u},v,\bar{w}] (4) x,\bar{y},\bar{z} [\bar{u},\bar{v},w] (5) \bar{x},\bar{y},z [\bar{u},\bar{v},w] (6) $x+1/2,y,\bar{z}$ [\bar{u},v,\bar{w}] (7) $x+1/2,\bar{y},z$ [\bar{u},v,\bar{w}] (8) \bar{x},y,z [\bar{u},v,w]
8 n .m'	$x,1/4,z$ [u,0,w] $\bar{x},1/4,z$ [u,0,w] $\bar{x},3/4,\bar{z}$ [$\bar{u},0,\bar{w}$] $x,3/4,\bar{z}$ [$\bar{u},0,w$]
8 m m..	$0,y,z$ [u,0,0] $0,\bar{y}+1/2,z$ [u,0,0] $0,y+1/2,\bar{z}$ [$\bar{u},0,0$] $0,\bar{y},\bar{z}$ [$\bar{u},0,0$]
8 l ..2	$1/4,0,z$ [0,0,w] $3/4,1/2,\bar{z}$ [0,0,w] $3/4,0,\bar{z}$ [0,0,w] $1/4,1/2,z$ [0,0,w]
8 k .2'	$1/4,y,1/4$ [u,0,w] $3/4,\bar{y}+1/2,1/2$ [u,0,w] $3/4,\bar{y},1/2$ [$\bar{u},0,\bar{w}$] $1/4,y+1/2,1/2$ [$\bar{u},0,w$]
8 j .2'	$1/4,y,0$ [u,0,w] $3/4,\bar{y}+1/2,0$ [u,0,w] $3/4,\bar{y},0$ [$\bar{u},0,\bar{w}$] $1/4,y+1/2,0$ [$\bar{u},0,w$]
8 i 2'..	$x,0,1/2$ [0,v,w] $\bar{x},1/2,1/2$ [0,v,w] $\bar{x},0,1/2$ [0,v,w] $x,1/2,1/2$ [0,v,w]
8 h 2'..	$x,0,0$ [0,v,w] $\bar{x},1/2,0$ [0,v,w] $\bar{x},0,0$ [0,v,w] $x,1/2,0$ [0,v,w]
4 g mm'2'	$0,1/4,z$ [u,0,0] $0,3/4,\bar{z}$ [$\bar{u},0,0$]
4 f .2'/m'	$1/4,1/4,1/2$ [u,0,w] $3/4,1/4,1/2$ [u,0,w]
4 e .2'/m'	$1/4,1/4,0$ [u,0,w] $3/4,1/4,0$ [u,0,w]
4 d 2'/m..	$0,0,1/2$ [0,0,0] $0,1/2,1/2$ [0,0,0]
4 c 2'/m..	$0,0,0$ [0,0,0] $0,1/2,0$ [0,0,0]
4 b 2'2'2	$1/4,0,1/2$ [0,0,w] $3/4,0,1/2$ [0,0,w]
4 a 2'2'2	$1/4,0,0$ [0,0,w] $3/4,0,0$ [0,0,w]

Symmetry of Special Projections

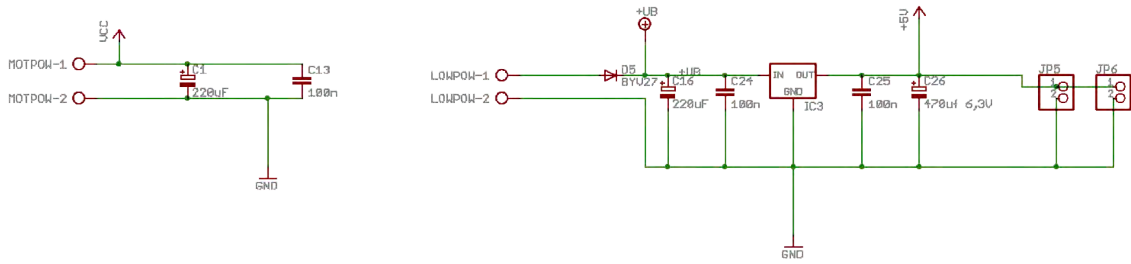
Along [0,0,1] $p_{2a}2mm$ $a^* = -b/2$ $b^* = a/2$ Origin at 0,0,z	Along [1,0,0] $p2mm1'$ $a^* = b/2$ $b^* = c$ Origin at x,0,0	Along [0,1,0] $p_{2a}2mm$ $a^* = -a/2$ $b^* = c$ Origin at 0,y,0
--	--	--

Figure 21.4: Excerpt of the Litvin Tables (colour group C_{Pmma}').

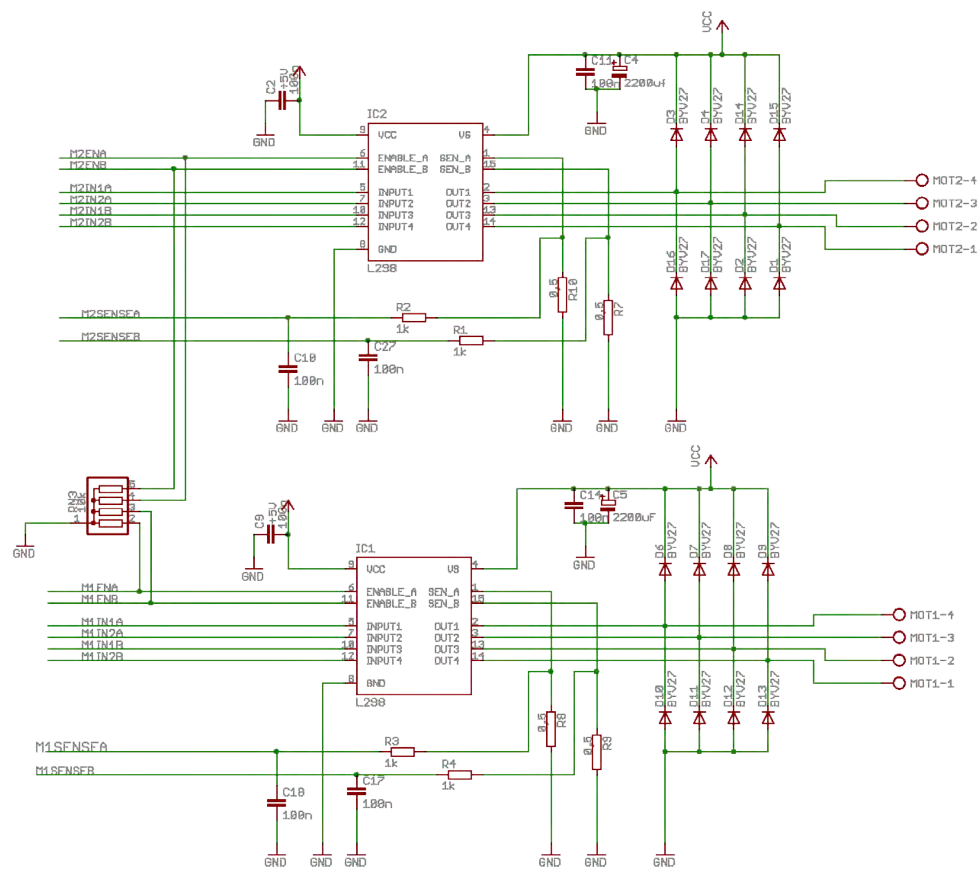
21.6 Susceptometer sample transport circuit and wiring diagrams

This chapter contains the circuit diagrams of the stepper controller and wiring diagram of the QUANTUM DESIGN sample transport for bug fixing purposes. Some figures are courtesy of ROBOTIKHARDWARE.DE.

Voltage stabiliser



Stepping motor end phase



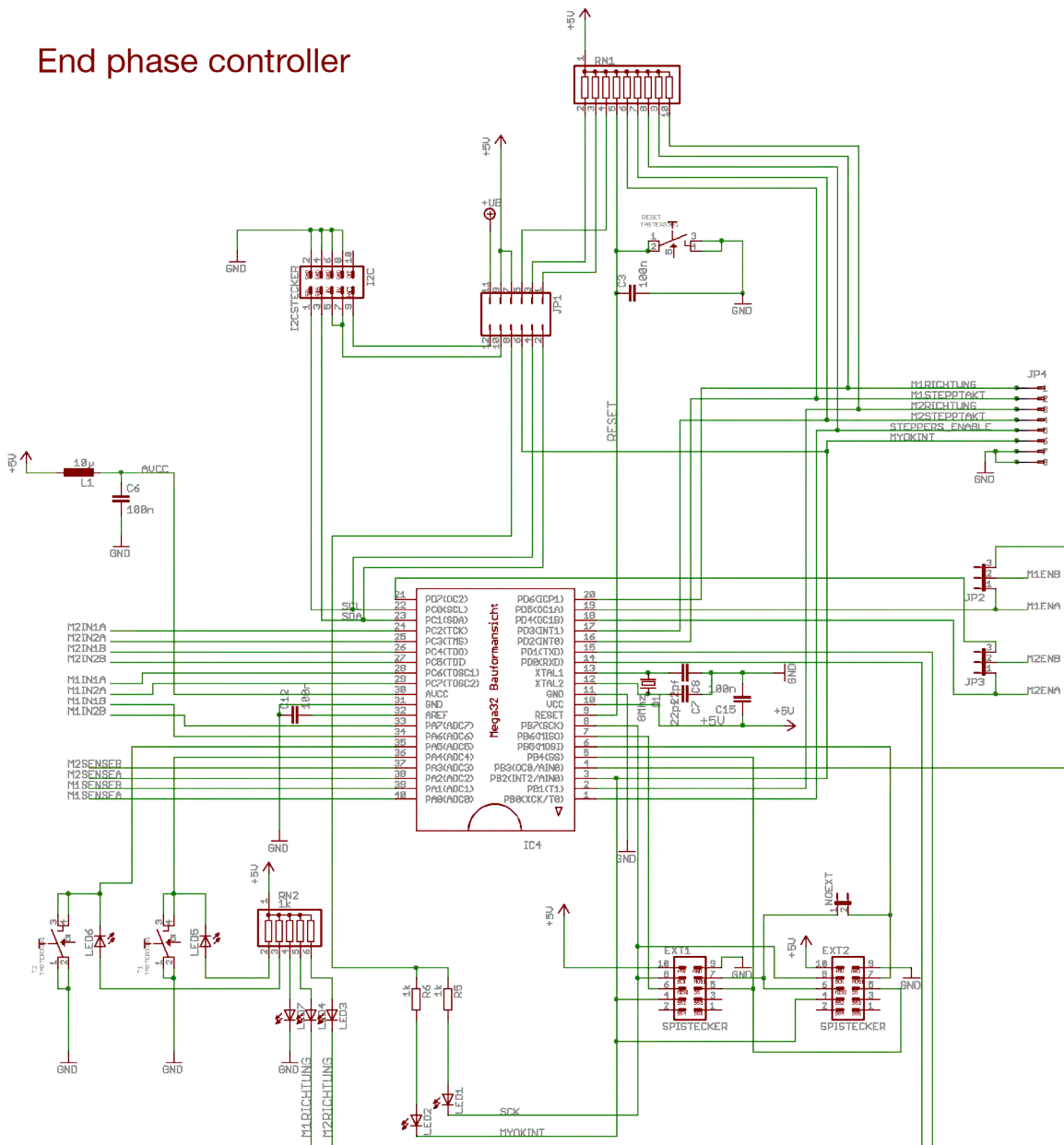
RN-Schrittmotor

Version 1.7
 Images courtesy of
www.robotikhardware.de

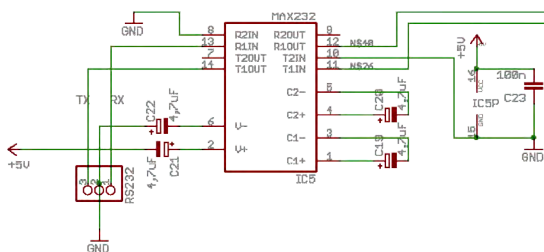
Figure 21.5: Voltage stabiliser (top) and stepping motor end phase (bottom).

RN-Schrittmotor

End phase controller



RS232 level converter



Version 1.7
 Images courtesy of
www.robotikhardware.de

Figure 21.6: End phase controller (top) and RS232 level converter (bottom).

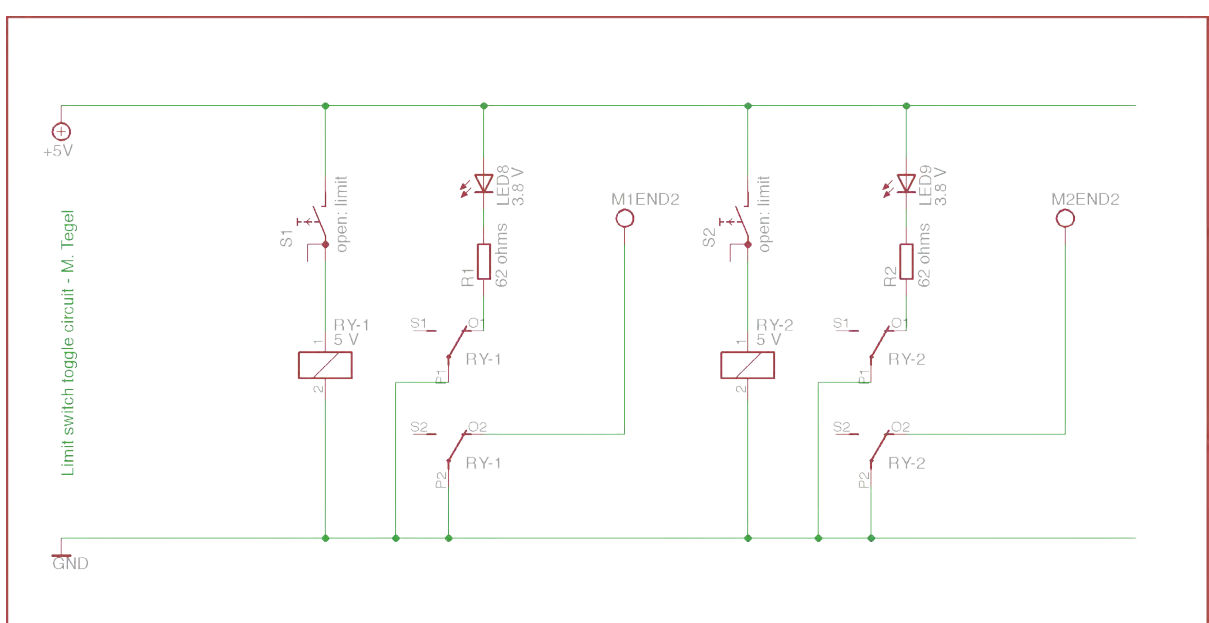


Figure 21.7: Limit switch toggle circuit.

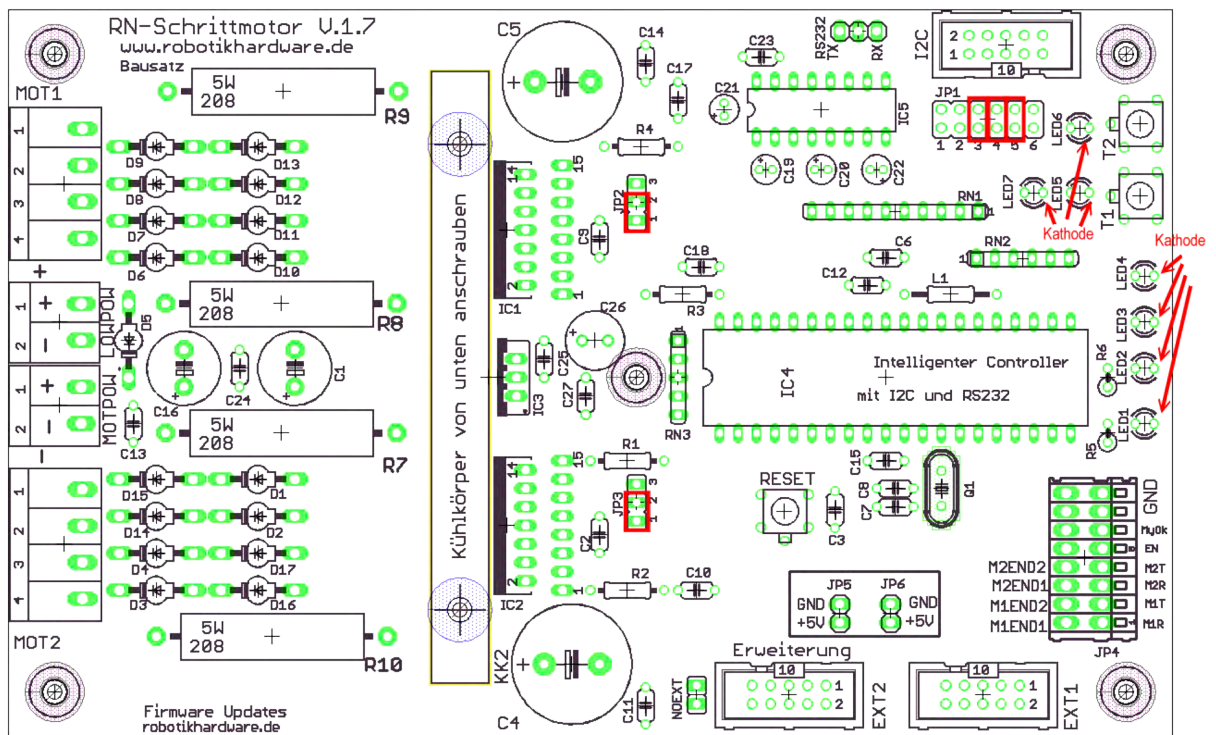
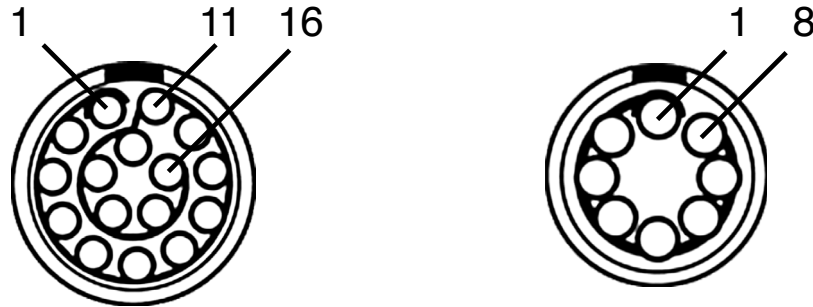


Figure 21.8: Layout of printed circuit board.

QUANTUM Design DC probe head wiring diagram

Rear views (Solder contacts or sockets):



green socket: LEMO EGG.3B.316.CLL yellow socket: LEMO EGG.2B.308.CLL
 connector: LEMO FGG.3B.316.CLAD10

green	yellow	cable wires	#M #P	description
1		green/black	#1 #1	Vertical Stepper Phase A
2		green/brown	#1 #2	Vertical Stepper Phase C
3		–		Vertical Stepper Common A/C
4		–		Vertical Stepper Common B/D
5		brown/yellow	#1 #3	Vertical Stepper Phase B
6		brown/grey	#1 #4	Vertical Stepper Phase D
7		orange		Vertical Limit Switch B (green cable)
8		red		Vertical Limit Switch A (blue cable); (3 = 4)
9	5	yellow		Axial Limit Switch B (black cable)
10	4	green		Axial Limit Switch A
11	1	white/yellow	#2 #1	Axial Stepper Phase A
12	8	white/black	#2 #2	Axial Stepper Phase C
13	2	grey	#2 #4	Axial Stepper Phase D
14	3	blue	#2 #3	Axial Stepper Phase B
15		brown/blue		GND
16		–		unused

Limit switches: limit = switch open; no limit = switch closed
 Stepper movement directions: left corresponds to counterclockwise axially and upwards vertically

Figure 21.9: Wiring diagram and limit switch behaviour of QUANTUM DESIGN sample transport. #M = Motor; #P = Phase. Wire colours are those of the green controller cable.

22. Abbreviations and glossary

22.1 Abbreviations

2D	two-dimensional
3D	three-dimensional
AC	alternating current
APW	augmented plane-wave
ARPES	angle resolved photoemission spectroscopy
arXiv	electronic preprint server of scientific papers freely accessible via http://arxiv.org , hosted by the Cornell University
ASA	atomic-sphere approximation
ASCII	American standard code for information interchange
<i>at%</i>	atomic per cent
au	atomic units
BCS	acronym of Bardeen, Cooper and Schrieffer
BZ	Brillouin zone
CCD	charge coupled device
CGS	centimetre gram second
<i>Ch</i>	chalcogenide
COHP	crystal orbital Hamilton population
CSD	crystal structure database
CW	continuous wave
dB	decibel
DC	direct current
DFT	density functional theory
DOI	digital object identifier (http://dx.doi.org)
DOS	density of states
DSP	digital signal processor
<i>EA</i>	earth alkaline metal
EDX	energy dispersive X-ray spectroscopy
EECE	exact-exchange for correlated electrons

Chapter 22: Abbreviations and glossary

fc	field-cooled (or cooling)
FP	full potential
FR4	'flame-retardant 4' fibreglass-reinforced epoxy laminate printed circuit board
FRM II	Forschungsreaktor München II
FWHM	full width at half maximum
GGA	generalised gradient approximation
gof	goodness of fit
GSAS	general structure analysis system
GUI	graphical user interface
ILL	Institut Laue Langevin
IPDS	imaging plate diffraction system
IUCr	International Union of Crystallography
LAPW	linearised augmented plane-wave
LBJ	Le Bail-Jouanneaux peak width / shape anisotropy correction
LDA	local density approximation
LED	light-emitting diode
LMTO	linear muffin-tin orbital
LMU	Ludwig-Maximilians Universität
<i>Ln</i>	lanthanide
<i>lo</i>	local orbitals
LSDA	local spin density approximation
<i>M</i>	metal
m.w.	molecular weight
MPMS	magnetic property measurement system
NMR	nuclear magnetic resonance
NPLC	number of power line cycles (integration time based on the power line frequency)
<i>o1</i>	origin choice 1
<i>o2</i>	origin choice 2
PCB	printed circuit board
PDF	pair density function

PID	proportional-integral-derivative
PLC	power line cycle(s)
<i>Pn</i>	pnictide / pnicogen
<i>pV</i>	pseudo-Voigt
PVC	polyvinyl chloride
<i>RE</i>	rare earth
RF	radio frequency
RN	RoboterNETZ
RS232	'recommended standard 232' serial interface
SCF	self-consistent field
SDW	spin-density wave
SI	system international d'unités (international system of units)
SIC	self-interaction correction
SODS	second-order Doppler shift
SQUID	superconducting quantum interference device
TB	tight-binding
<i>TM</i>	transition metal
UPS	ultraviolet photoelectron spectroscopy
WHH	acronym of Werthamer, Helfand and Hohenberg
<i>wt%</i>	weight per cent
XY	ASCII file type consisting only of <i>x</i> / <i>y</i> data
YBCO	$\text{YBa}_2\text{Cu}_3\text{O}_{7-x}$
<i>zfc</i>	zero-field-cooled (or cooling)
μSR	muon-spin resonance

22.2 Quantities

Magnetic quantities

' / ''	Real and imaginary part of AC magnetic quantities
$4\pi\chi$	magnetic (e.g. superconducting) volume fraction
<i>B</i>	magnetic flux density
<i>C</i>	Curie constant

Chapter 22: Abbreviations and glossary

H	magnetic field
H_c	thermodynamic critical field
H_{c1}	lower critical field
H_{c2}	upper critical field
M	magnetisation per volume (equivalent to M_V)
M_g	magnetisation per gram
M_m	magnetisation per mole
M_s	magnetisation of the whole sample
N	number of magnetic centres
n_{eff}	number of effective Bohr magnetons (equivalent to μ_{eff}/μ_B)
T_C	Curie temperature
T_N	Néel temperature
Θ	Weiss constant (paramagnetic Curie temperature)
μ/μ_B	permanent atomic magnetic (dipole) moment per magnetic centre or formula unit (in Bohr magnetons)
μ_0	permeability of free space
μ_a	permanent atomic magnetic (dipole) moment
μ_B	Bohr magneton
χ	magnetic susceptibility per volume (equivalent to χ_V)
χ_0	temperature-dependent (positive) contribution of the extended Curie-Weiss law
χ_{dia}	diamagnetic increment
χ_g	magnetic susceptibility per gram
χ_m	magnetic susceptibility per mole
χ_s	magnetic susceptibility of the whole sample

Crystallographic quantities

\dots_o	...orthorhombic
\dots_t	...tetragonal
2θ	diffraction angle
d	interplanar spacing
$d\dots$	interatomic distance

$F...$	structure factor
h, k, l	Miller indices
$I...$	intensity
$m...$	multiplicity
Q	value proportional to reciprocal interplanar spacing
$r...$	radius
$R...$	residual factor
S	inelastic neutron scattering function
T_o	Tetragonal-to-orthorhombic transition temperature
$U...$	thermal displacement parameter(s)
w	weighting scheme
Z	number of empirical formulas per unit cell
η	Lorentzian contribution of the Pseudo-Voigt function
θ	half diffraction angle
λ	wavelength
χ^2	goodness of fit
ω	full width at half maximum of the Pseudo-Voigt function

Other quantities

A	area of one coil loop
B_{hf}	magnetic hyperfine field splitting (Mössbauer spectroscopy)
C_p	specific heat (at constant pressure and external magnetic field)
E	energy
E_F	Fermi energy
E_{vac}	energy level of vacuum
f	frequency
G	Gaussian function
g	gram(s)
$g^{(n)}$	generalised phonon density of states
h	Planck constant
I	electric current
J	magnetic exchange coupling constant

Chapter 22: Abbreviations and glossary

k_B	Boltzmann constant
k_{\max}	maximum reciprocal lattice vectors
l	length of a coil
L	Lorentzian function
M	mole / molar
m_n	mass of a neutron
n	number of atoms (per formula unit)
N	number of turns in a coil
N_A	Avogadro's constant
p	momentum
P	order parameter
P	probability distribution function
R	total resistance
$R...$	residual factor
r_{mt}	muffin-tin radius
S	spin
S	superconducting volume fraction
T	temperature
T_C	critical temperature
T_F	Fermi temperature
T_o	(tetragonal-to-orthorhombic) structural transition temperature
U	<i>Hubbard</i> model correlation energy
U	voltage
v	velocity
V_{zz}	main component of the electric field gradient tensor (Mössbauer spectroscopy)
Z	impedance
β	critical exponent of power law
β	phononic coefficient of specific heat
Γ	experimental line width (Mössbauer spectroscopy)
γ_n	electronic coefficient of specific heat
δ	isomer shift (Mössbauer spectroscopy)

Δ	superconducting energy gap
ΔE_Q	quadrupole splitting parameter (Mössbauer spectroscopy)
θ	angle between B_{hf} and V_{zz} (Mössbauer spectroscopy)
Θ_D	Debye temperature
ν	frequency
ρ	specific electric resistance
σ	standard deviation
χ	goodness of fit

22.3 Glossary

Angle resolved photoemission spectroscopy (ARPES)

ARPES is a technique to experimentally probe the local band structures of solids at the Fermi level. The method is related to other photoelectron spectroscopy methods such as ultraviolet photoelectron spectroscopy (UPS). ARPES however does not only measure the work function of electrons at the Fermi level (i.e. the kinetic energy of photoelectrons) but it is also a momentum-sensitive method, resulting in detailed information on band dispersions and Fermi surfaces. Like UPS, ARPES is a surface-sensitive probe because of relatively short electron mean free paths.

Corner-junction experiment

Also referred to as π -Josephson corner junction experiment. The corner-junction experiment provides a phase-sensitive test of the pairing symmetry in superconductors. The experiment is based on the interference of the quantum-mechanical phases in Josephson tunnel junctions. The first experiment of this kind was carried out on YBCO!^[255] For details, refer to [256].

Half-metal

A half-metal is a true metal with a completely ferromagnetic conduction band.

Isopointal^[211]

According to IUCr, two structures are isopointal if

- (i) they have the same space-group type or belong to a pair of enantiomorphic space-group types
- (ii) the atomic positions, occupied either fully or partially at random, are the same in both structures, i.e. the complete sequence of the occupied Wyckoff positions (including the number of times each Wyckoff position is occupied) is the same for both structures when the structural data have been standardised.

Multigap superconductivity

As a consequence of more than one superconducting order parameter, there are also more than one superconducting energy gaps, which can be observed e.g. by tunnelling spectroscopy or by the course of the electronic contribution of C_p at the superconducting transition.

Nematic ordering

Nematic ordering refers to a spontaneously broken rotational symmetry without the breaking of translational symmetry, i.e. a strong electronic anisotropy.

Optical semiconductor / optical band gap

In the context of this work, the term optical semiconductor denotes a semiconductor with a band gap between ~ 1.6 and 3.3 eV, i.e. in the region, where visible light is absorbed (wavelengths of ~ 780 nm down to ~ 380 nm).

Quantum critical point^[243]

Quantum critical points are special phase transitions at 0 K in solids, which arise from zero temperature quantum fluctuations associated with Heisenberg's uncertainty principle.

Second-order Doppler shift^[215]

The Second-Order Doppler Shift is a temperature-dependent effect on the centre shift of a Mössbauer spectrum. Above 0 K, atoms in a lattice oscillate about their mean position. Although the frequency of this oscillation is such high that the mean displacement during the lifetime of a Mössbauer event is zero, the second term in the Doppler shift depends on v^2 , leading to the mean square displacement being non-zero.

Semi-metal

Semi-metals are true metals, which can formally be derived from indirect semiconductors. The term 'semi-metal' must not be confused with the term 'half-metal', which also denotes a true metal, but with a completely ferromagnetic conduction band.

Spin-density wave (SDW)^[20]

A spin-density wave (SDW) is a periodic modulation of the electron spin with a characteristic spatial periodicity, which mostly is incommensurate with the crystal structure. It often occurs as ground state in materials of low dimensionality, metals with a high DOS at E_F or because of the existence of Fermi surface nesting vectors as it is the case in the iron pnictides. Similar to superconductivity, the occurrence of a SDW causes the formation of an energy gap that lowers the system's total energy.

Superconducting order parameter

The superconducting order parameter is the quantum mechanical description of the electron pairing in the superconducting state. For details, refer to Chapter 1.1.2.

23. Publications and talks

23.1 Publications in peer-reviewed journals

Many results of this dissertation already have been published in peer-reviewed journals. As these publications are not necessarily cited in the corresponding chapters of this dissertation, this chapter contains a full list of papers, which have been published within or beyond this dissertation (in reverse order). Papers beyond this thesis (collaborations or earlier works) are marked with an asterisk.

21. Tegel, Marcus; Schmid, Tanja; Stürzer, Tobias; Egawa, Masamitsu; Su, Yixi; Senyshyn, Anatoliy; Johrendt, Dirk; “Suppression of superconductivity by V-doping and possible magnetic order in $\text{Sr}_2\text{VO}_3\text{FeAs}$ ” *ArXiv.org, Condensed Matter*: [1008.2687](#), *Phys. Rev. B* **2010**, 82, 140507(R).
- 20.* Rybak Jens-Christoph; Tegel, Marcus; Johrendt, Dirk; Müller-Buschbaum, Klaus; “Polymorphism of Isotypic Series of Homoleptic 1,2,3-Triazolate MOFs $[\text{Ln}(\text{Tz}^*)_3]$ Containing the Heavy Lanthanides Gd-Lu: From Open to Dense Frameworks of Varying Dimensionality”, *Z. Kristallogr.* **2010**, 225, 187.
19. Tegel, Marcus; Löhnert, Catrin; Johrendt, Dirk; “The crystal structure of $\text{FeSe}_{0.44}\text{Te}_{0.56}$ ” *ArXiv.org, Condensed Matter*: [0912.3706](#), *Solid State Comm.* **2010**, 150, 383.
18. Tegel, Marcus; Hummel, Franziska; Su, Yixi; Chatterji, Tapan; Brunelli, Michela; Johrendt, Dirk; „Non-stoichiometry and the magnetic structure of $\text{Sr}_2\text{CrO}_3\text{FeAs}$ “ *ArXiv.org, Condensed Matter*: [0911.0450](#), *Europhys. Lett.* **2010**, 89, 37006.
17. Tegel, Marcus; Schellenberg, Inga; Hummel, Franziska; Pöttgen, Rainer; Johrendt, Dirk; “Low-Temperature Crystal Structure and ^{57}Fe Mössbauer Spectroscopy of $\text{Sr}_3\text{Sc}_2\text{O}_5\text{Fe}_2\text{As}_2$ ” *ArXiv.org, Condensed Matter*: [0905.0337](#), *Z. Naturforsch. B* **2009**, 64b, 815.
16. Tegel, Marcus; Hummel, Franziska; Lackner, Sebastian; Schellenberg, Inga; Pöttgen, Rainer; Johrendt, Dirk; “The layered iron arsenides $\text{Sr}_2\text{CrO}_3\text{FeAs}$ and $\text{Ba}_2\text{ScO}_3\text{FeAs}$ ” *ArXiv.org, Condensed Matter*: [0904.0479](#), *Z. Anorg. Allg. Chem.* **2009**, 635, 2242.
- 15.* Mittal, Ranjan; Rols, Stéphane; Zbiri, Mohamed; Su, Yixi; Schober, Helmut; Chaplot, S. L.; Johnson, Mark; Tegel, Marcus; Chatterji, Tapan; Matsuishi,

-
- Satoru; Hosono, Hideo; Johrendt, Dirk; Brückel, Thomas; "Phonon spectra in CaFe_2As_2 and $\text{Ca}_{0.6}\text{Na}_{0.4}\text{Fe}_2\text{As}_2$: Measurement of the pressure and temperature dependence and comparison with ab-initio and shell model calculations" *ArXiv.org, Condensed Matter*: [0902.4590](https://arxiv.org/abs/0902.4590), *Phys. Rev. B* **2009**, 79, 144516.
14. Rotter, Marianne; Tegel, Marcus; Schellenberg, Inga; Schappacher, Falko M.; Pöttgen, Rainer; Deisenhofer, Joachim; Günther, Axel; Schrettle, Florian; Loidl, Alois; Johrendt, Dirk; "Competition of magnetism and superconductivity in underdoped $(\text{Ba}_{1-x}\text{K}_x)\text{Fe}_2\text{As}_2$ " *ArXiv.org, Condensed Matter*: [0812.2827](https://arxiv.org/abs/0812.2827), *New J. Phys.* **2009**, 11, 025014.
 13. Mittal, Ranjan; Su, Yixi; Rols, Stéphane; Tegel, Marcus; Chaplot, S. L.; Schöber, Helmut; Chatterji, Tapan; Johrendt, Dirk; Brückel, Thomas; "Phonon dynamics in $\text{Sr}_{0.6}\text{K}_{0.4}\text{Fe}_2\text{As}_2$ and $\text{Ca}_{0.6}\text{Na}_{0.4}\text{Fe}_2\text{As}_2$ " *ArXiv.org, Condensed Matter*: [0810.4498](https://arxiv.org/abs/0810.4498), *Phys. Rev. B* **2008**, 78, 224518.
 12. Tegel, Marcus; Johansson, Sebastian; Weiß, Veronika; Schellenberg, Inga; Hermes, Wilfried; Pöttgen, Rainer; Johrendt, Dirk; "Synthesis, crystal structure and spin-density wave anomaly of the iron arsenide-fluoride SrFeAsF " *ArXiv.org, Condensed Matter*: [0810.2120](https://arxiv.org/abs/0810.2120), *Europhys. Lett.* **2008**, 84, 67007.
 11. Tegel, Marcus; Welzmler, Simon; Johrendt, Dirk; "Synthesis, Crystal Structure and Magnetism of EuMnPF "; *Z. Anorg. Allg. Chem.* **2008**, 634, 2085.
 10. Rotter, Marianne; Pangerl, Michael; Tegel, Marcus; Johrendt, Dirk; "Superconductivity and Crystal Structures of $(\text{Ba}_{1-x}\text{K}_x)\text{Fe}_2\text{As}_2$ ($x = 0 - 1$)" *ArXiv.org, Condensed Matter*: [0807.4096](https://arxiv.org/abs/0807.4096); *Angew. Chem. Int. Ed.* **2008**, 47, 7949 ([Link](#)); *Angew. Chem.* **2008**, 120, 8067.
 9. Tegel, Marcus; Rotter, Marianne; Weiß, Veronika; Schappacher, Falko M.; Pöttgen, Rainer; Johrendt, Dirk; "Structural and magnetic phase transitions in the ternary iron arsenides SrFe_2As_2 and EuFe_2As_2 " *ArXiv.org, Condensed Matter*: [0806.4782](https://arxiv.org/abs/0806.4782), *J. Phys. Cond. Mat.* **2008**, 20, 452201.
 8. Rotter, Marianne; Tegel, Marcus; Johrendt, Dirk; "Superconductivity at 38 K in the iron arsenide $(\text{Ba}_{1-x}\text{K}_x)\text{Fe}_2\text{As}_2$ " *ArXiv.org, Condensed Matter*: [0805.4630](https://arxiv.org/abs/0805.4630), *Phys. Rev. Letters* **2008**, 101, 107006.
 7. Rotter, Marianne; Tegel, Marcus; Schellenberg, Inga; Hermes, Wilfried; Pöttgen, Rainer; Johrendt, Dirk; "Spin-density wave anomaly at 140 K in the ternary iron arsenide BaFe_2As_2 " *ArXiv.org, Condensed Matter*: [0805.4021](https://arxiv.org/abs/0805.4021), *Phys. Rev. B* **2008**, 78, 020503(R).
-

-
6. Tegel, Marcus; Schellenberg, Inga; Pöttgen, Rainer; Johrendt, Dirk; "A ^{57}Fe Mössbauer Spectroscopy Study of the 7 K Superconductor LaFePO ." *ArXiv.org, Condensed Matter: 0805.1208*, *Z. Naturforsch. B* **2008**, 63b, 1057–1061.
 5. Lincke, Hannes; Glaum, Robert; Dittrich, Volker; Tegel, Marcus; Johrendt, Dirk; Hermes, Wilfried; Möller, Manfred H.; Nilges, Tom; Pöttgen, Rainer; "Magnetic, Optical and Electronic Properties of the Phosphide Oxides REZnPO ($\text{RE} = \text{Y}, \text{La-Nd}, \text{Sm}, \text{Gd}, \text{Dy}, \text{Ho}$)"; *Z. Anorg. Allg. Chem.*, **2008**, 634, 1339–1348.
 - 4.* Tegel, Marcus; Bichler, Daniel; Johrendt, Dirk; "Synthesis, crystal structure and superconductivity of LaNiPO "; *Solid State Sciences*, **2008**, 10, 193–197.
 - 3.* Farrugia, Louis J.; Evans, Cameron; Tegel, Marcus; "Chemical Bonds without 'Chemical Bonding'? A Combined Experimental and Theoretical Charge Density Study on an Iron Trimethylenemethane Complex"; *Journal of Physical Chemistry A*, **2006**, 110(25), 7952–7961.
 - 2.* Evans, Cameron; Farrugia, Louis J.; Tegel, Marcus; "Bis(*tert*-butyl isocyanide)- $1\mu^2\text{C}$ -di- μ -carbonyl- $2:3\mu^4\text{C}$ -octacarbonyl- $1\mu^2\text{C}, 2\mu^3\text{C}, 3\mu^3\text{C}$ -triangulo-diironosmium"; *Acta Crystallographica, Section E: Structure Reports Online*, **2006**, E62(3), m478–m479.
 - 1.* Evans, Cameron; Farrugia, Louis J.; Tegel, Marcus; "*tert*-Butyl isocyanide- $1\mu\text{C}$ -di- μ -carbonyl- $2:3\mu^4\text{C}$ -nonacarbonyl- $1\mu^3\text{C}, 2\mu^3\text{C}, 3\mu^3\text{C}$ -triangulo-diironosmium"; *Acta Crystallographica, Section E: Structure Reports Online*, **2006**, E62(3), m475–m477.

23.2 Conference contributions

This chapter contains a list of conference contributions (talks and posters) with download links for the slides or posters, respectively (in reverse order). Contributions beyond this dissertation (collaborations) are marked with an asterisk.

9. Tegel, Marcus; Hummel, Franziska; Schmid, Tanja; Stürzer, Tobias; Egawa, Masamitsu; Su, Yixi; Senyshyn, Anatoliy; Johrendt, Dirk; "The Role of Stoichiometry and Magnetism in the Superconductor $\text{Sr}_2\text{VO}_3\text{FeAs}$ and Related Compounds", International Workshop on Novel Superconductors and Super Materials (NS_{2011}^2), Tokyo, Japan, **March 2011**.^[257]

-
8. Tegel, Marcus; "Supraleiter mit Arsen vergiften", Hemdsärmelkolloquium, Stuttgart, **March 2010**.^[258]
 7. Tegel, Marcus; Welzmler, Simon; Johrendt, Dirk; "Crystal structures, superconductivity and magnetism of the cobalt-doped iron phosphide oxides $\text{La}(\text{Co}_x\text{Fe}_{1-x})\text{PO}$ ($x = 0 - 1$)", ECSSC XII European Conference on Solid State Chemistry, Münster, **September 2009**.^[259]
 - 6.* Rybak, J. C.; Tegel, M.; Johrendt, D.; Müller-Buschbaum, K. „Structure Solution of a Metal-Organic-Framework from X-ray-Powder-Data High- and Low-Temperature Modifications of Terbium-1,2,3-Triazolate“, ECSSC XII European Conference on Solid State Chemistry, Münster, **September 2009**.
 5. Tegel, Marcus; "Eisenarsenide mit großem Schichtabstand", Hirschegg-Seminar, Hirschegg, **June 2009**.^[260]
 4. Tegel, Marcus; Rotter, Marianne; Schellenberg, Inga; Pöttgen, Rainer; Johrendt, Dirk; "Boundless variety – Superconducting", Max-Planck-Gesellschaft, "Science Express Expedition Zukunft 2009", Carriage 6: "Innovative materials and the factory of the future", Germany, **April to November 2009**.^[261]
 3. Tegel, Marcus; "Das eine hat's, das andere nicht! * Zwei neue Eisenarsenide", Hemdsärmelkolloquium, Marburg, **March 2009**.^[262]
 2. Tegel, Marcus; Welzmler, Simon; Weiß, Veronika; Johansson, Sebastian; Johrendt, Dirk; "Synthesis, structure, magnetism of EuMnPF and the new iron arsenide fluoride SrFeAsF ", GDCh-Festkörpertagung, Bayreuth, **September 2008**.^[263]
 1. Tegel, Marcus; "Supraleitung quaternärer Pnictidoxide - auf dem Weg zu neuen Hochtemperatursupraleitern", Hirschegg-Seminar, Hirschegg, **May 2008**.^[264]

23.3 LMU talks and methodology seminars

Also several LMU internal talks and methodology seminars were given. A list with download links can be found here.

7. Tegel, Marcus; "Research Report 2007-2010", Ludwig-Maximilians-Universität, München, **December 2010**.^[265]

Chapter 23: Publication and talks

6. Tegel, Marcus; „Adobe CS4 for scientists“, Ludwig-Maximilians-Universität, München, **March 2010**.
5. Tegel, Marcus; "Research Report 2009", Ludwig-Maximilians-Universität, München, **November 2009**.^[266]
4. Tegel, Marcus; "Rietveld methodology seminar 2009 - An introduction to TOPAS Academic", Ludwig-Maximilians-Universität, München, **February 2009**.^[68]
3. Tegel, Marcus; "Research Report 2008", Ludwig-Maximilians-Universität, München, **November 2008**.^[267]
2. Tegel, Marcus; "Rietveld methodology seminar 2008 - An introduction to the Rietveld method and GSAS", Ludwig-Maximilians-Universität, München, **May 2008**.^[268]
1. Tegel, Marcus; "Research Report 2007", Ludwig-Maximilians-Universität, München, **November 2007**.^[269]

24. Curriculum Vitae

Personal information

Name	Marcus Christian Tegel
Date of Birth	27/12/1979
Place of Birth	Backnang (Baden-Württemberg)
Nationality	German
Marital status	single

Education

since 10/2007	Ph.D. studies in the group of Prof. Dr. Dirk Johrendt at the Ludwig-Maximilians-Universität, München. Ph.D. thesis title: "Iron pnictide superconductors".
10/2000 – 07/2007	Undergraduate studies in Chemistry at the Ludwig-Maximilians-Universität, München. Diploma.
01/2007 – 07/2007	Diploma thesis "Synthese, Struktur und Supraleitung quaternärer Oxidphosphide".
09/2003 – 08/2004	Practical research year in inorganic and physical chemistry, University of Glasgow, United Kingdom.
11/2002	Intermediate diploma.
09/1990 – 06/1999	Gymnasium in der Taus (secondary school), Backnang. Abitur (A-Levels).
09/1986 – 07/1990	Mörike-Grundschule (primary school), Backnang.

Civilian service

09/1999 – 07/2000	Care of physically and mentally challenged adults at the Karlshöhe, Ludwigsburg
-------------------	---

Honours

2009	2009 Lindau Meeting of Nobel Laureates member.
2008	Dr. Klaus Römer award for outstanding achievements in Ph.D. studies.
2008	GDCh Poster prize
2007	Dr. Klaus Römer award for outstanding achievements in diploma studies.
2007	LMU München, book prize for excellent diploma.
1999	FCI Chemistry book prize for best A-Levels in chemistry.

25. Bibliography

Italic citation numbers indicate literal citations and copied figures. Citations at the end of a paragraph often refer to the paragraph as a whole. Due to technical reasons, references could not be made from within footnotes or figure captions, which hence can be found in the text body referring to the corresponding object instead.

- [1] J. G. Bednorz, K. A. Müller, *Zeitschrift für Physik B* **1986**, 64, 189.
- [2] T. Ruf, *Physik in unserer Zeit* **1998**, 29, 160.
- [3] a) Google ngram, <http://ngrams.googlelabs.com/>, **2011**; b) J.-B. Michel, Y. K. Shen, A. P. Aiden, A. Veres, M. K. Gray, T. G. B. Team, J. P. Pickett, D. Hoiberg, D. Clancy, P. Norvig, J. Orwant, S. Pinker, M. A. Nowak, E. L. Aiden, *Science* **2011**, 331, 176.
- [4] R. Flükiger, S. Y. Hariharan, R. Küntzler, H. L. Luo, F. Weiss, T. Wolf, J. Q. Xu, in *Landolt-Börnstein - Group III Condensed Matter - Nb based alloys and compounds, Vol. 21b2*.
- [5] B. T. Matthias, T. H. Geballe, S. Geller, E. Corenzwit, *Physical Review* **1954**, 95, 1435.
- [6] R. Lucio, *Superconductor Science and Technology* **2010**, 23, 034001.
- [7] A. Bhattacharya, *Nature* **2010**, 463, 605.
- [8] M. Bäcker, *Zeitschrift für Kristallographie* **2011**, in press (DOI: 10.1524/zkri.2011.1330).
- [9] a) J. Kellers, *International Water Power & dam construction* **2009**, 8, 28; b) S. S. Kalsi, *Power Engineering Society General Meeting, IEEE* **2004**, 2047.
- [10] W. V. Hassenzahl, *Proceedings of the IEEE* **2004**, 92, 1655.
- [11] a) D. Dilba, *Technology Review (German edition)* **2011**, 1, 68; b) F. N. Werfel, U. Floegel-Delor, T. Riedel, R. Rothfeld, D. Wippich, B. Goebel, G. Reiner, N. Wehlau, *Journal of Physics: Conference Series* **2008**, 97, 012206.
- [12] D. Larbalestier, A. Gurevich, D. M. Feldmann, A. Polyanskii, *Nature* **2001**, 414, 368.

-
- [13] a) B. P. Martins, *Recent Developments in Superconductivity Research*, Nova Science, **2006**; b) S. S. Saxena, P. B. Littlewood, *Nature* **2001**, 412, 290.
- [14] Y. Kamihara, T. Watanabe, M. Hirano, H. Hosono, *Journal of the American Chemical Society* **2008**, 130, 3296.
- [15] Z.-A. Ren, W. Lu, J. Yang, W. Yi, X.-L. Shen, Z.-C. Li, G.-C. Che, X.-L. Dong, L.-L. Sun, F. Zhou, Z.-X. Zhao, *Chinese Physics Letters* **2008**, 25, 2215.
- [16] J. Q. Yan, S. Nandi, J. L. Zarestky, W. Tian, A. Kreyssig, B. Jensen, A. Kracher, K. W. Dennis, R. J. McQueeney, A. I. Goldman, R. W. McCallum, T. A. Lograsso, *Applied Physics Letters* **2009**, 95, 222504.
- [17] a) J. Bardeen, *Physical Review* **1955**, 97, 1724; b) L. N. Cooper, *Physical Review* **1956**, 104, 1189; c) J. Bardeen, L. N. Cooper, J. R. Schrieffer, *Physical Review* **1957**, 106, 162.
- [18] Wikipedia: High-temperature superconductivity, http://en.wikipedia.org/w/index.php?title=High-temperature_superconductivity&oldid=403941451, **2010**.
- [19] A. Schilling, M. Cantoni, J. D. Guo, H. R. Ott, *Nature* **1993**, 363, 56.
- [20] Wikipedia: Spin-density wave, http://en.wikipedia.org/w/index.php?title=Spin_density_wave&oldid=411145348, **2011**.
- [21] W. Tremel, E. W. Finckh, *Chemie in unserer Zeit* **2004**, 38, 326.
- [22] a) R. Juza, K. Langer, *Zeitschrift für Anorganische und Allgemeine Chemie* **1968**, 361, 58; b) P. Quebe, L. J. Terbuchte, W. Jeitschko, *Journal of Alloys and Compounds* **2000**, 302, 70; c) E. A. Owen, E. L. Yates, *Philosophical Magazine* **1933**, 15, 472.
- [23] D. C. Johnston, *Advances in Physics* **2010**, 59, 803 (p. 824).
- [24] A. Y. Liu, I. I. Mazin, J. Kortus, *Physical Review Letters* **2001**, 87, 087005.
- [25] a) A. A. Golubov, I. I. Mazin, *Physical Review B* **1997**, 55, 15146; b) D. F. Agterberg, V. Barzykin, L. P. Gor'kov, *Physical Review B* **1999**, 60, 14868.
- [26] Y. Ohta, T. Tohyama, S. Maekawa, *Physical Review Letters* **1991**, 66, 1228.
- [27] H. A. Kramers, *Physica I* **1934**, 182.
- [28] B. Batlogg, *Physics Today* **1991**, 44, 44.
-

Chapter 25: Bibliography

- [29] A. J. Leggett, *Nature Physics* **2006**, 2, 134.
- [30] P. A. Lee, N. Nagaosa, X.-G. Wen, *Reviews of Modern Physics* **2006**, 78, 17.
- [31] C. d. I. Cruz, Q. Huang, J. W. Lynn, J. Li, W. RatcliffII, J. L. Zarestky, H. A. Mook, G. F. Chen, J. L. Luo, N. L. Wang, P. Dai, *Nature* **2008**, 453, 899.
- [32] a) I. I. Mazin, D. J. Singh, M. D. Johannes, M. H. Du, *Physical Review Letters* **2008**, 101, 057003; b) Y.-R. Zhou, Y.-R. Li, J.-W. Zuo, R.-Y. Liu, S.-K. Su, G. F. Chen, J. L. Lu, N. L. Wang, Y.-P. Wang, **2008**, arXiv:0812.3295; c) K. Nakayama, T. Sato, P. Richard, Y.-M. Xu, Y. Sekiba, S. Souma, G. F. Chen, J. L. Luo, N. L. Wang, H. Ding, T. Takahashi, *Europhysics Letters* **2009**, 85, 67002.
- [33] a) N. Qureshi, Y. Drees, J. Werner, S. Wurmehl, C. Hess, R. Klingeler, B. Büchner, M. T. Fernández-Díaz, M. Braden, *Physical Review B* **2010**, 82, 184521; b) M. A. McGuire, A. D. Christianson, A. S. Sefat, B. C. Sales, M. D. Lumsden, R. Jin, E. A. Payzant, D. Mandrus, *Physical Review B* **2008**, 78, 094517; c) H. F. Li, W. Tian, J. Q. Yan, J. L. Zarestky, R. W. McCallum, T. A. Lograsso, D. Vaknin, *Physical Review B* **2010**, 82, 064409.
- [34] a) T. Park, E. Park, H. Lee, T. Klimczuk, E. D. Bauer, F. Ronning, J. D. Thompson, *Journal of Physics: Condensed Matter* **2008**, 20, 322204; b) P. L. Alireza, Y. T. C. Ko, J. Gillett, C. M. Petrone, J. M. Cole, G. G. Lonzarich, S. E. Sebastian, *Journal of Physics: Condensed Matter* **2009**, 21, 012208.
- [35] L. Boeri, O. V. Dolgov, A. A. Golubov, *Physical Review Letters* **2008**, 101, 026403.
- [36] D. J. Scalapino, *Journal of Low Temperature Physics* **1999**, 117, 179.
- [37] D. J. Scalapino, *Physics Reports* **1995**, 250, 329.
- [38] O. K. Andersen, O. Jepsen, *Stuttgart Tight-Binding LMTO-ASA program*, v. 4.7c, Max-Planck-Institut für Festkörperforschung, Stuttgart, **1998**.
- [39] P. Blaha, K. Schwarz, G. K. H. Madsen, D. Kvasnicka, J. Luitz, *WIEN2k - An Augmented Plane Wave + Local Orbitals Program for Calculating Crystal Properties*, v. 09.1, TU Wien, **2009**.
- [40] J. P. Perdew, K. Burke, M. Ernzerhof, *Physical Review Letters* **1997**, 77, 3865.
- [41] R. Dronskowski, P. E. Blöchl, *Journal of Physical Chemistry* **1993**, 97, 8617.
- [42] E. Sjöstedt, L. Nordström, D. J. Singh, *Solid State Communications* **2000**, 114, 15.
-

-
- [43] G. K. H. Madsen, P. Blaha, K. Schwarz, E. Sjöstedt, L. Nordström, *Physical Review B* **2001**, 64, 195134/1.
- [44] D. J. Singh, L. Nordström, *Planewaves, Pseudopotentials and the LAPW Method*, Springer, New York, **2006**.
- [45] V. I. Anisimov, F. Aryasetiawan, A. I. Lichtenstein, *Journal of Physics: Condensed Matter* **1997**, 9, 767.
- [46] V. I. Anisimov, I. V. Solovyev, M. A. Korotin, M. T. Czyzyk, G. A. Sawatzky, *Physical Review B* **1993**, 48, 16929.
- [47] P. Novak, J. Kunes, L. Chaput, W. E. Pickett, *Physica Status Solidi B* **2006**, 243, 563.
- [48] A. Kokalj, *XCrySDen*, v. 1.5.17, **2004**.
- [49] *Maple*, v. 11.02, Maplesoft, **2007**.
- [50] M. Tegel, DFT volume optimisation 2D-Taylor fit example worksheet, http://mtegel.eu/intern/volume_optimisation.mw, user name / password : intern / arsenig, **2010**.
- [51] M. Tegel, *HConvert*, v. 0.7, Ludwig-Maximilians-Universität, München, http://mtegel.eu/downloads_en/downloads_en.html, **2010**.
- [52] WINXPOW, 2.21, STOE & Cie GmbH, Darmstadt, **2007**.
- [53] JCPDS, *PCPDFWin*, v. 2.2, International Center for Diffraction Data, Swathmore, USA, **2001**.
- [54] JCPDS, *DDView+*, v. 4.9.0.5, **2009**.
- [55] a) JCPDS, PDF 2, International Center for Diffraction Data, Swathmore, USA, **2001**; b) JCPDS, PDF 4+, International Center for Diffraction Data, Swathmore, USA, **2009**.
- [56] A. Coelho, *TOPAS-Academic*, v. 4.1, Coelho Software, Brisbane, **2007**.
- [57] B. H. Toby, *Journal of Applied Crystallography* **2005**, 38, 1040.
- [58] D. Louër, A. Boultif, *DICVOL*, v. 06, **2006**.
- [59] O. Schärpf, H. Capellmann, *Physica Status Solidi A* **1993**, 135, 359.
- [60] *CrystalDiffract*, v. 5.1.9 (Mac), CrystalMaker Ltd., **2009**.
- [61] *CrystalMaker*, v. 8.3.0 (Mac), CrystalMaker Ltd., **2010**.
-

Chapter 25: Bibliography

- [62] H. M. Rietveld, *Journal of Applied Crystallography* **1969**, 2, 65.
- [63] a) A. C. Larson, R. B. Von Dreele, *General Structure Analysis System (GSAS)*, v. **2004**; b) B. H. Toby, *Journal of Applied Crystallography* **2001**, 34, 210.
- [64] P. Thompson, D. E. Cox, J. B. Hastings, *Journal of Applied Crystallography* **1987**, 20, 79.
- [65] L. W. Finger, D. E. Cox, A. P. Jephcoat, *Journal of Applied Crystallography* **1992**, 27, 79.
- [66] A. Le Bail, A. Jouanneaux, *Journal of Applied Crystallography* **1997**, 30, 265.
- [67] a) A. March, *Zeitschrift für Kristallographie* **1932**, 81, 285; b) W. A. Dollase, *Journal of Applied Crystallography* **1986**, 19, 267.
- [68] M. Tegel, TOPAS launch mode .inp templates, http://mtegel.eu/topas_en/topas_en.html, user name / password: LMU / phosphorig, **2010**.
- [69] A. Coelho, TOPAS-Academic Technical Reference, 4.1, **2007**.
- [70] M. Baier, *Aufbau und Charakterisierung eines Guinier-Diffraktometers*, diploma thesis, Friedrich-Alexander-Universität (Erlangen), **2001**.
- [71] W. I. F. David, *Journal of Applied Crystallography* **2001**, 34, 691.
- [72] K. H. Stone, S. H. Lapidus, P. W. Stephens, *Journal of Applied Crystallography* **2009**, 42, 385.
- [73] *FACEIT Video System*, v. 1.35b, STOE & Cie GmbH, Darmstadt, **2000**.
- [74] *X-RED 32*, v. 1.03, STOE & Cie GmbH, Darmstadt, **2002**.
- [75] *X-Shape*, v. 2.01, STOE & Cie GmbH, Darmstadt, **2001**.
- [76] *XPREP - Data Preparation & Reciprocal Space Exploration*, v. 6.12, Bruker-AXS, **2001**.
- [77] A. L. Spek, *Journal of Applied Crystallography* **2003**, 36, 7.
- [78] M. C. Burla, R. Caliendo, M. Camalli, B. Carrozzini, G. L. Cascarano, L. D. Caro, C. Giacovazzo, G. Polidori, D. Siliqi, R. Spagna, *Journal of Applied Crystallography* **2007**, 40, 609.
- [79] G. M. Sheldrick, *Acta Crystallographica Section A* **2008**, A64, 112.
-

-
- [80] a) *TextMate*, v. 1.5.9, Macromates, **2009**; b) M. Tegel, <http://mtegel.eu/da/SHELX.tmbundle.zip>, **2007**.
- [81] T. Chatterji, *Neutron scattering from magnetic materials*, First ed., Elsevier (Amsterdam), **2006**.
- [82] a) G. Cicognani, H. Mutka, F. Sacchetti, *Physica B* **2000**, 276-278, 83; b) Y. Blanc, *Le Spectrometre a temps de vol IN6*, Insitutit Laue-Langevin, Grenoble, **1983**, p. Report 83BL21G.
- [83] R. Mittal, Y. Su, S. Rols, M. Tegel, S. L. Chaplot, H. Schober, T. Chatterji, D. Johrendt, T. Brückel, *Physical Review B* **2008**, 78, 224518.
- [84] R. Mittal, S. Rols, M. Zbiri, Y. Su, H. Schober, S. L. Chaplot, M. Johnson, M. Tegel, T. Chatterji, S. Matsuishi, H. Hosono, D. Johrendt, T. Brueckel, *Physical Review B* **2009**, 79, 144516.
- [85] *INCA*, v. 4.02, Oxford Instruments Analytical LTD, **2002**.
- [86] M. Tegel, *Synthese, Struktur und Supraleitung quaternärer Phosphidoxide*, diploma thesis, Ludwig-Maximilians-Universität (München), **2007**.
- [87] D. Bichler, *Magnetismus und strukturelle Phasenumwandlungen von Verbindungen mit tetraedrischen Metallclustern*, Ph.D. thesis, Ludwig-Maximilians-Universität (München), **2010**.
- [88] a) M. McElfresh, *Fundamentals of Magnetism and Magnetic Measurements featuring Quantum Design's Magnetic Property Measurement System*, Purdue University, **1994**; b) *Magnetic Property Measurement System MPMS XL, Hardware Reference Manual*, Quantum Design, San Diego, **2005**.
- [89] *MPMS MultiVu*, v. 1.56 Build 72 (EEPROM 1802: v. 3.21; EEPROM 1822: v. 3.25), Quantum Design Inc., **2005**.
- [90] *Origin*, v. 8.0773, OriginLab Corporation, Northampton, **2007**.
- [91] M. Tegel, *SQUID Processor*, v. 0.2 (Mac/Windows), Ludwig-Maximilians-Universität, München, http://mtegel.eu/downloads_en/downloads_en.html, **2010**.
- [92] M. Tegel, *AC susceptometer control*, v. 1.67 rc, Ludwig-Maximilians-Universität, München, **2010**.
- [93] L. J. van-der-Pauw, *Philips Research Reports* **1958**, 13, 1.
- [94] C. Kranenberg, *LEITMESS*, v. 2.5, Heinrich-Heine-Universität, Düsseldorf, **1998**.
-

Chapter 25: Bibliography

- [95] M. Tegel, *Conductivity control*, v. 0.2, Ludwig-Maximilians-Universität, München, **2010**.
- [96] R. A. Brand, *Normos Mössbauer Fitting Program*, v. Universität Duisburg, **2002**.
- [97] C. Enss, S. Hunklinger, in *Low-Temperature Physics*, Springer-Verlag Berlin Heidelberg, **2005**, pp. 391.
- [98] Y. Kamihara, H. Hiramatsu, M. Hirano, R. Kawamura, H. Yanagi, T. Kamiya, H. Hosono, *Journal of the American Chemical Society* **2006**, *128*, 10012.
- [99] S. Lebègue, *Physical Review B* **2007**, *75*, 035110/1.
- [100] a) M. Tegel, D. Bichler, D. Johrendt, *Solid State Sciences* **2008**, *10*, 193; b) T. Watanabe, H. Yanagi, T. Kamiya, Y. Kamihara, H. Hiramatsu, M. Hirano, H. Hosono, *Inorganic Chemistry* **2007**, *46*, 7719.
- [101] C. Wang, Y. K. Li, Z. W. Zhu, S. Jiang, X. Lin, Y. K. Luo, S. Chi, L. J. Li, Z. Ren, M. He, H. Chen, Y. T. Wang, Q. Tao, G. H. Cao, Z. A. Xu, *Physical Review B* **2009**, *79*, 054521.
- [102] a) S. Kitao, Y. Kobayashi, S. Higashitanguchi, M. Saito, Y. Kamihara, M. Hirano, T. Mitsui, H. Hosono, M. Seto, *Journal of the Physical Society of Japan* **2008**, *77*, 103706; b) H.-H. Klauss, H. Luetkens, R. Klingeler, C. Hess, F. J. Litterst, M. Kraken, M. M. Korshunov, I. Eremin, S.-L. Drechsler, R. Khasanov, A. Amato, J. Hamann-Borrero, N. Leps, A. Kondrat, G. Behr, J. Werner, B. Büchner, *Physical Review Letters* **2008**, *101*, 077005.
- [103] L. Häggström, T. Ericsson, R. Wäppling, *Physica Scripta* **1975**, *11*, 94.
- [104] a) R. Wäppling, L. Häggström, S. Rundqvist, E. Karlsson, *Journal of Solid State Chemistry* **1971**, *3*, 276; b) R. Wäppling, L. Häggström, T. Ericsson, S. Devanarayanan, E. Karlsson, B. Carlsson, S. Rundqvist, *Journal of Solid State Chemistry* **1975**, *13*, 258.
- [105] a) E. M. Baggio-Saitovitch, D. R. Sánchez, M. B. Fontes, S. N. Medeiros, E. Passamani, H. Micklitz, *Hyperfine Interactions* **2002**, *144/145*, 161; b) D. R. Sánchez, H. Micklitz, M. B. Fontes, E. Baggio-Saitovitch, *Journal of Physics: Condensed Matter* **1997**, *9*, L299.
- [106] M. M. Qazilbash, J. J. Hamlin, R. E. Baumbach, L. Zhang, D. J. Singh, M. B. Maple, D. N. Basov, *Nature Physics* **2009**, *5*, 647.
- [107] W. L. Yang, A. P. Sorini, C. C. Chen, B. Moritz, W. S. Lee, F. Vernay, P. Olalde-Velasco, J. D. Denlinger, B. Delley, J. H. Chu, J. G. Analytis, I. R.
-

-
- Fisher, Z. A. Ren, J. Yang, W. Lu, Z. X. Zhao, J. van den Brink, Z. Hussain, Z. X. Shen, T. P. Devereaux, *Physical Review B* **2009**, *80*, 014508.
- [108] Z. P. Yin, K. Haule, G. Kotliar, *arXiv:1007.2867* **2010**.
- [109] M. Tegel, I. Schellenberg, R. Pöttgen, D. Johrendt, *Zeitschrift für Naturforschung B* **2008**, *63*, 1057.
- [110] A. S. Sefat, A. Huq, M. A. McGuire, R. Y. Jin, B. C. Sales, D. Mandrus, L. M. D. Cranswick, P. W. Stephens, K. H. Stone, *Physical Review B* **2008**, *78*, 104505.
- [111] M. Tegel, S. Johansson, V. Weiß, I. Schellenberg, W. Hermes, R. Pöttgen, D. Johrendt, *Europhysics Letters* **2008**, *84*, 67007.
- [112] I. Nowik, I. Felner, V. P. S. Awana, A. Vajpayee, H. Kishan, *Journal of Physics: Condensed Matter* **2008**, *20*, 292201.
- [113] C. Wivel, S. Mørup, *Journal of Physics E* **1981**, *14*, 605.
- [114] T. Nomura, S. W. Kim, Y. Kamihara, M. Hirano, P. V. Sushko, K. Kato, M. Takata, A. L. Shluger, H. Hosono, *Superconductor Science and Technology* **2008**, *21*, 125028.
- [115] Y. Xiao, Y. Su, R. Mittal, T. Chatterji, T. Hansen, S. Price, C. M. N. Kumar, J. Persson, S. Matsuishi, Y. Inoue, H. Hosono, T. Brueckel, *Physical Review B* **2010**, *81*, 094523.
- [116] R. M. Fernandes, L. H. VanBebber, S. Bhattacharya, P. Chandra, V. Keppens, D. Mandrus, M. A. McGuire, B. C. Sales, A. S. Sefat, J. Schmalian, *Physical Review Letters* **2010**, *105*, 157003.
- [117] J.-H. Chu, J. G. Analytis, K. De Greve, P. L. McMahon, Z. Islam, Y. Yamamoto, I. R. Fisher, *Science* **2010**, *329*, 824.
- [118] J. Dong, H. J. Zhang, G. Xu, Z. Li, G. Li, W. Z. Hu, D. Wu, G. F. Chen, X. Dai, J. L. Luo, Z. Fang, N. L. Wang, *Europhysics Letters* **2008**, *83*, 27006.
- [119] W. Lv, J. Wu, P. Phillips, *Physical Review B* **2009**, *80*, 224506.
- [120] G. M. Zhang, Y. H. Su, Z. Y. Lu, Z. Y. Weng, D. H. Lee, T. Xiang, *Europhysics Letters* **2009**, *86*, 37006.
- [121] D. C. Johnston, *Advances in Physics* **2010**, *59*, 803 (p. 861).
-

Chapter 25: Bibliography

- [122] S. Johansson, *Neue quaternäre Eisenarsenide und inelastische Neutronenstreuung an Eisenarsenidsupraleitern*, Bachelor thesis, Ludwig-Maximilians-Universität (München), **2008**.
- [123] G. Wu, Y. L. Xie, H. Chen, M. Zhong, R. H. Liu, B. C. Shi, Q. J. Li, X. F. Wang, T. Wu, Y. J. Yan, J. J. Ying, X. H. Chen, *Chinese Science Bulletin* **2009**, *54*, 1872.
- [124] X. Y. Zhu, F. Han, P. Cheng, G. Mu, B. Shen, H. H. Wen, *Europhysics Letters* **2009**, *85*, 17011.
- [125] G. Wu, Y. L. Xie, H. Chen, M. Zhong, R. H. Liu, B. C. Shi, Q. J. Li, X. F. Wang, T. Wu, Y. J. Yan, J. J. Ying, X. H. Chen, *Journal of Physics: Condensed Matter* **2009**, *21*, 142203.
- [126] S. V. Chong, S. Hashimoto, H. Yamaguchi, K. Kadowaki, *Journal of Superconductivity and Novel Magnetism* **2010**, *23*, 1479.
- [127] S. Matsuishi, Y. Inoue, T. Nomura, H. Yanagi, M. Hirano, H. Hosono, *Journal of the American Chemical Society* **2008**, *130*, 14428.
- [128] A. C. Payne, A. E. Sprauve, M. M. Olmstead, S. M. Kauzlarich, *Journal of Solid State Chemistry* **2002**, *163*, 498.
- [129] S. L. Brock, J. E. Greedan, S. M. Kauzlarich, *Journal of Solid State Chemistry* **1994**, *113*, 303.
- [130] H. Yanagi, T. Watanabe, K. Kodama, S. Iikubo, S.-i. Shamoto, T. Kamiya, M. Hirano, H. Hosono, *Journal of Applied Physics* **2009**, *105*, 093916.
- [131] H. Lincke, T. Nilges, R. Pöttgen, *Zeitschrift für Anorganische und Allgemeine Chemie* **2006**, *632*, 1804.
- [132] A. Mewis, *Zeitschrift für Naturforschung B* **1980**, *35b*, 141.
- [133] M. Pfisterer, G. Nagorsen, *Zeitschrift für Naturforschung B* **1980**, *35b*, 703.
- [134] P. Klüfers, A. Mewis, *Zeitschrift für Naturforschung B* **1978**, *33*, 151.
- [135] V. Johnson, W. Jeitschko, *Journal of Solid State Chemistry* **1974**, *11*, 161.
- [136] R. N. Shelton, H. F. Braun, E. Musick, *Solid State Communications* **1984**, *52*, 797.
- [137] a) M. François, G. Venturini, J. F. Marêché, B. Malaman, B. Roques, *Journal of the Less Common Metals* **1985**, *113*, 231; b) W. Jeitschko, R. Glaum, L. Boonk, *Journal of Solid State Chemistry* **1987**, *69*, 93; c) M. Hirjak, P. Lejay,
-

-
- B. Chevalier, J. Etourneau, P. Hagenmüller, *Journal of the Less Common Metals* **1985**, 105, 139; d) T. Mine, H. Yanagi, T. Kamiya, Y. Kamihara, M. Hirano, H. Hosono, *Solid State Communications* **2008**, 147, 111.
- [138] M. Pfisterer, G. Nagorsen, *Zeitschrift für Naturforschung B* **1983**, 38b, 811.
- [139] M. Rotter, Ph.D. thesis, Ludwig-Maximilians-Universität (München), **2010**.
- [140] a) W. Lu, X.-L. Shen, J. Yang, Z.-C. Li, W. Yi, Z.-A. Ren, X.-L. Dong, G.-C. Che, L.-L. Sun, F. Zhou, Z.-X. Zhao, *Solid State Communications* **2008**, 148, 168; b) H.-H. Wen, G. Mu, L. Fang, H. Yang, X. Zhu, *Europhysics Letters* **2008**, 82, 17009.
- [141] I. Nowik, I. Felner, *Journal of Superconductivity and Novel Magnetism* **2008**, 21, 297.
- [142] S. Rozsa, H. U. Schuster, *Zeitschrift für Naturforschung B* **1981**, 36B, 1668.
- [143] M. Rotter, M. Tegel, D. Johrendt, *Physical Review Letters* **2008**, 101, 107006.
- [144] K. Selte, A. Kjekshus, A. F. Andresen, *Acta Chemica Scandinavica* **1972**, 26, 3101.
- [145] K. Togano, A. Matsumoto, H. Kumakura, *Superconductor Science and Technology* **2010**, 23, 045009.
- [146] N. R. Werthamer, E. Helfand, P. C. Hohenberg, *Physical Review* **1966**, 147, 295.
- [147] a) M. M. Altarawneh, K. Collar, C. H. Mielke, *Physical Review B* **2008**, 78, 220505(R); b) H. Q. Yuan, J. Singleton, F. F. Balakirev, S. A. Baily, G. F. Chen, J. L. Luo, N. L. Wang, *Nature* **2009**, 457, 565; c) M. Putti, I. Pallecchi, E. Bellingeri, M. R. Cimberle, M. Tropeano, C. Ferdeghini, A. Palenzona, C. Tarantini, A. Yamamoto, J. Jiang, J. Jaroszynski, F. Kametani, D. Abraimov, A. Polyanskii, J. D. Weiss, E. E. Hellstrom, A. Gurevich, D. C. Larbalestier, R. Jin, B. C. Sales, A. S. Sefat, M. A. McGuire, D. Mandrus, P. Cheng, Y. Jia, H.-H. Wen, S. Lee, C. B. Eom, *Superconductor Science and Technology* **2010**, 23, 034003.
- [148] L. Jiao, J. L. Zhang, F. F. Balakirev, G. F. Chen, J. L. Luo, N. L. Wang, H. Q. Yuan, *Journal of Physics and Chemistry of Solids* **2011**, in press (DOI: 10.1016/j.jpccs.2010.10.070).
- [149] a) P. M. Aswathy, J. B. Anooja, P. M. Sarun, U. Syamaprasad, *Superconductor Science and Technology* **2010**, 23, 073001 (p. 8); b) J. Guo,
-

Chapter 25: Bibliography

- S. Jin, G. Wang, S. Wang, K. Zhu, T. Zhou, M. He, X. Chen, *Physical Review B* **2010**, 82, 180520.
- [150] Z.-A. Ren, G.-C. Che, X.-L. Dong, J. Yang, W. Lu, W. Yi, X.-L. Shen, Z.-C. Li, L.-L. Sun, F. Zhou, Z.-X. Zhao, *Europhysics Letters* **2008**, 83, 17002.
- [151] G. Mu, L. Fang, H. Yang, X. Zhu, P. Cheng, H.-H. Wen, *Journal of the Physical Society of Japan* **2008**, 77, 15.
- [152] M. Rotter, M. Pangerl, M. Tegel, D. Johrendt, *Angewandte Chemie, International Edition* **2008**, 47, 7949.
- [153] H. Luetkens, H. H. Klauss, M. Kraken, F. J. Litterst, T. Dellmann, R. Klingeler, C. Hess, R. Khasanov, A. Amato, C. Baines, M. Kosmala, O. J. Schumann, M. Braden, J. Hamann-Borrero, N. Leps, A. Kondrat, G. Behr, J. Werner, B. Buchner, *Nature Materials* **2009**, 8, 305.
- [154] Q. Huang, J. Zhao, J. W. Lynn, G. F. Chen, J. L. Luo, N. L. Wang, P.-C. Dai, *Physical Review B* **2008**, 78, 054529.
- [155] a) J. Zhao, Q. Huang, C. de la Cruz, S. L. Li, J. W. Lynn, Y. Chen, M. A. Green, G. F. Chen, G. Li, Z. Li, J. L. Luo, N. L. Wang, P. C. Dai, *Nature Materials* **2008**, 7, 953; b) A. J. Drew, C. Niedermayer, P. J. Baker, F. L. Pratt, S. J. Blundell, T. Lancaster, R. H. Liu, G. Wu, X. H. Chen, I. Watanabe, V. K. Malik, A. Dubroka, M. Rossle, K. W. Kim, C. Baines, C. Bernhard, *Nature Materials* **2009**, 8, 310; c) S. Margadonna, Y. Takabayashi, M. T. McDonald, M. Brunelli, G. Wu, R. H. Liu, X. H. Chen, K. Prassides, *Physical Review B* **2009**, 79, 014503.
- [156] B. Keimer, N. Belk, R. J. Birgeneau, A. Cassanho, C. Y. Chen, M. Greven, M. A. Kastner, A. Aharony, Y. Endoh, R. W. Erwin, G. Shirane, *Physical Review B* **1992**, 46, 14034.
- [157] H. Chen, Y. Ren, Y. Qiu, W. Bao, R. H. Liu, G. Wu, T. Wu, Y. L. Xie, X. F. Wang, Q. Huang, X. H. Chen, *Europhysics Letters* **2009**, 85, 17006.
- [158] M. Rotter, M. Tegel, I. Schellenberg, F. M. Schappacher, R. Pöttgen, J. Deisenhofer, A. Günther, F. Schrettle, A. Loidl, D. Johrendt, *New Journal of Physics* **2009**, 11, 025014.
- [159] a) A. A. Aczel, E. Baggio-Saitovitch, S. L. Budko, P. C. Canfield, J. P. Carlo, G. F. Chen, P. C. Dai, T. Goko, W. Z. Hu, G. M. Luke, J. L. Luo, N. Ni, D. R. Sanchez-Candela, F. F. Tafti, N. L. Wang, T. J. Williams, W. Yu, Y. J. Uemura, *Physical Review B* **2008**, 78, 214503; b) T. Goko, A. A. Aczel, E. Baggio-Saitovitch, S. L. Bud'ko, P. C. Canfield, J. P. Carlo, G. F. Chen, P. C. Dai, A. C. Hamann, W. Z. Hu, H. Kageyama, G. M. Luke, J. L. Luo, B.
-

-
- Nachumi, N. Ni, D. Reznik, D. R. Sanchez-Candela, A. T. Savici, K. J. Sikes, N. L. Wang, C. R. Wiebe, T. J. Williams, T. Yamamoto, W. Yu, Y. J. Uemura, *Physical Review B* **2009**, *80*, 024508; c) J. T. Park, D. S. Inosov, C. Niedermayer, G. L. Sun, D. Haug, N. B. Christensen, R. Dinnebier, A. V. Boris, A. J. Drew, L. Schulz, T. Shapoval, U. Wolff, V. Neu, X. P. Yang, C. T. Lin, B. Keimer, V. Hinkov, *Physical Review Letters* **2009**, *102*, 117006.
- [160] S. Nandi, M. G. Kim, A. Kreyssig, R. M. Fernandes, D. K. Pratt, A. Thaler, N. Ni, S. L. Bud'ko, P. C. Canfield, J. Schmalian, R. J. McQueeney, A. I. Goldman, *Physical Review Letters* **2010**, *104*, 057006.
- [161] E. Wiesenmayer, *Synthese von $Ba_{1-x}K_xFe_2As_2$ ($x = 0.2 - 0.3$) und strukturelle Charakterisierung bei tiefen Temperaturen*, Master thesis, Ludwig-Maximilians-Universität (München), **2010**.
- [162] J.-Q. Yan, A. Kreyssig, S. Nandi, N. Ni, S. L. Bud'ko, A. Kracher, R. J. McQueeney, R. W. McCallum, T. A. Lograsso, A. I. Goldman, P. C. Canfield, *Physical Review B* **2008**, *78*, 024516.
- [163] A. Hellmann, A. Löhken, A. Würth, A. Mewis, *Zeitschrift für Naturforschung B* **2007**, *62*, 155.
- [164] C. Krellner, N. Caroca-Canales, A. Jesche, H. Rosner, A. Ormeci, C. Geibel, *Physical Review B* **2008**, *78*, 100504(R).
- [165] a) C. Hermann, *Zeitschrift für Kristallographie* **1929**, *69*, 533; b) S. Deonarine, J. L. Birman, *Physical Review B* **1983**, *27*, 4261.
- [166] Q. Huang, Y. Qiu, W. Bao, J. W. Lynn, M. A. Green, Y. Chen, T. Wu, G. Wu, X. H. Chen, *Physical Review Letters* **2008**, *101*, 257003.
- [167] a) M. E. Lines, A. M. Glass, *Principles and Applications of Ferroelectrics and Related Materials*, Oxford: Clarendon, **1977**; b) H. E. Stanley, *Introduction to Phase Transitions and Critical Phenomena*, Oxford: Clarendon, **1971**.
- [168] H. Raffius, E. Mörsen, B. D. Mosel, W. Müller-Warmuth, W. Jeitschko, L. Terbüchte, T. Vomhof, *Journal of Physics and Chemistry of Solids* **1993**, *54*, 135.
- [169] a) K. Matan, R. Morinaga, K. Iida, T. J. Sato, *Physical Review B* **2009**, *79*, 054526; b) J. Zhao, W. Ratcliff, J. W. Lynn, G. F. Chen, J. L. Luo, N. L. Wang, J. Hu, P. Dai, *Physical Review B* **2008**, *78*, 140504; c) Y. Xiao, Y. Su, M. Meven, R. Mittal, C. M. N. Kumar, T. Chatterji, S. Price, J. Persson, N. Kumar, S. K. Dhar, A. Thamizhavel, T. Brueckel, *Physical Review B* **2009**, *80*, 174424.
-

Chapter 25: Bibliography

-
- [170] S. D. Wilson, Z. Yamani, C. R. Rotundu, B. Freelon, E. Bourret-Courchesne, R. J. Birgeneau, *Physical Review B* **2009**, 79, 184519.
- [171] C. R. Rotundu, B. Freelon, T. R. Forrest, S. D. Wilson, P. N. Valdivia, G. Pinuellas, A. Kim, J. W. Kim, Z. Islam, E. Bourret-Courchesne, N. E. Phillips, R. J. Birgeneau, *Physical Review B* **2010**, 82, 144525.
- [172] R. A. Ewings, T. G. Perring, R. I. Bewley, T. Guidi, M. J. Pitcher, D. R. Parker, S. J. Clarke, A. T. Boothroyd, *Physical Review B* **2008**, 78, 220501.
- [173] A. D. Christianson, E. A. Goremychkin, R. Osborn, S. Rosenkranz, M. D. Lumsden, C. D. Malliakas, I. S. Todorov, H. Claus, D. Y. Chung, M. G. Kanatzidis, R. I. Bewley, T. Guidi, *Nature* **2008**, 456, 930.
- [174] M. Zbiri, H. Schober, M. R. Johnson, S. Rols, R. Mittal, Y. Su, M. Rotter, D. Johrendt, *Physical Review B* **2009**, 79, 064511.
- [175] R. I. Bewley, R. S. Eccleston, K. A. McEwen, S. M. Hayden, M. T. Dove, S. M. Bennington, J. R. Treadgold, R. L. S. Coleman, *Physica B* **2006**, 385-386, 1029.
- [176] F. Gompf, W. Reichardt, H. Schober, B. Renker, M. Buchgeister, *Physical Review B* **1997**, 55, 9058.
- [177] R. H. Liu, T. Wu, G. Wu, H. Chen, X. F. Wang, Y. L. Xie, J. J. Ying, Y. J. Yan, Q. J. Li, B. C. Shi, W. S. Chu, Z. Y. Wu, X. H. Chen, *Nature* **2009**, 459, 64.
- [178] a) G. Hägg, A. L. Kindström, *Zeitschrift für Physikalische Chemie B* **1933**, 22, 453; b) H. Okamoto, *Journal of Phase Equilibria* **1991**, 12, 383.
- [179] X. C. Wang, Q. Q. Liu, Y. X. Lv, W. B. Gao, L. X. Yang, R. C. Yu, F. Y. Li, C. Q. Jin, *Solid State Communications* **2008**, 148, 538.
- [180] F.-C. Hsu, J.-Y. Luo, K.-W. Yeh, T.-K. Chen, T.-W. Huang, P. M. Wu, Y.-C. Lee, Y.-L. Huang, Y.-Y. Chu, D.-C. Yan, M.-K. Wu, *Proceedings of the National Academy of Sciences* **2008**, 105, 14262.
- [181] a) A. J. Williams, T. M. McQueen, R. J. Cava, *Solid State Communications* **2009**, 149, 1507; b) T. M. McQueen, Q. Huang, V. Ksenofontov, C. Felser, Q. Xu, H. Zandbergen, Y. S. Hor, J. Allred, A. J. Williams, D. Qu, J. Checkelsky, N. P. Ong, R. J. Cava, *Physical Review B* **2009**, 79, 014522.
- [182] a) Y. Mizuguchi, F. Tomioka, S. Tsuda, T. Yamaguchi, Y. Takano, *Applied Physics Letters* **2008**, 93, 152505; b) S. Medvedev, T. M. McQueen, I. A. Troyan, T. Palasyuk, M. I. Eremets, R. J. Cava, S. Naghavi, F. Casper, V. Ksenofontov, G. Wortmann, C. Felser, *Nature Materials* **2009**, 8, 630.
-

-
- [183] T. M. McQueen, A. J. Williams, P. W. Stephens, J. Tao, Y. Zhu, V. Ksenofontov, F. Casper, C. Felser, R. J. Cava, *Physical Review Letters* **2009**, *103*, 057002.
- [184] J. Leciejewicz, *Acta Chemica Scandinavica* **1963**, *17*, 2593.
- [185] Y. Mizuguchi, F. Tomioka, S. Tsuda, T. Yamaguchi, Y. Takano, *Physica C* **2009**, *469*, 1027.
- [186] M. J. Han, S. Y. Savrasov, *Physical Review Letters* **2009**, *103*, 067001.
- [187] K.-W. Yeh, T.-W. Huang, Y.-I. Huang, T.-K. Chen, F.-C. Hsu, P. M. Wu, Y.-C. Lee, Y.-Y. Chu, C.-L. Chen, J.-Y. Luo, D.-C. Yan, M.-K. Wu, *Europhysics Letters* **2008**, *84*, 37002.
- [188] C.-Y. Moon, H. J. Choi, *Physical Review Letters* **2010**, *104*, 057003.
- [189] S. Lebègue, Z. P. Yin, W. E. Pickett, *New Journal of Physics* **2009**, *11*, 025004.
- [190] N. C. Gresty, Y. Takabayashi, A. Y. Ganin, M. T. McDonald, J. B. Claridge, D. Giap, Y. Mizuguchi, Y. Takano, T. Kagayama, Y. Ohishi, M. Takata, M. J. Rosseinsky, S. Margadonna, K. Prassides, *Journal of the American Chemical Society* **2009**, *131*, 16944.
- [191] R. D. Shannon, C. T. Prewitt, *Acta Crystallographica Section B* **1969**, *25*, 925.
- [192] M. C. Lehman, D. Louca, K. Horigane, A. Llobet, R. Arita, S. Ji, N. Katayama, S. Konbu, K. Nakamura, P. Tong, T.-Y. Koo, K. Yamada, *arXiv:0909.0480* **2009**.
- [193] M. Tegel, C. Löhnert, D. Johrendt, *Solid State Communications* **2010**, *150*, 383.
- [194] M. H. Fang, H. M. Pham, B. Qian, T. J. Liu, E. K. Vehstedt, Y. Liu, L. Spinu, Z. Q. Mao, *Physical Review B* **2008**, *78*, 224503.
- [195] V. Petricek, M. Dusek, L. Palatinus, *Jana2006 structure determination software programs*, v. 2006, Institute of Physics, Prague, **2009**.
- [196] C.-H. Lee, A. Iyo, H. Eisaki, H. Kito, M. T. Fernandez-Diaz, T. Ito, K. Kihou, H. Matsuhata, M. Braden, K. Yamada, *Journal of the Physical Society of Japan* **2008**, *77*, 083704.
- [197] A. Subedi, L. Zhang, D. J. Singh, M. H. Du, *Physical Review B* **2008**, *78*, 134514.
-

Chapter 25: Bibliography

- [198] T. Yildirim, *Physical Review Letters* **2009**, *102*, 037003.
- [199] W. Bao, Y. Qiu, Q. Huang, M. A. Green, P. Zajdel, M. R. Fitzsimmons, M. Zhernenkov, S. Chang, M. Fang, B. Qian, E. K. Vehstedt, J. Yang, H. M. Pham, L. Spinu, Z. Q. Mao, *Physical Review Letters* **2009**, *102*, 247001.
- [200] S. Onari, H. Kontani, *Physical Review Letters* **2009**, *103*, 177001.
- [201] P. Cheng, B. Shen, G. Mu, X. Zhu, F. Han, B. Zeng, H.-H. Wen, *Europhysics Letters* **2009**, *85*, 67003.
- [202] J. H. Tapp, Z. Tang, B. Lv, K. Sasmal, B. Lorenz, P. C. W. Chu, A. M. Guloy, *Physical Review B* **2008**, *78*, 060505.
- [203] a) W. J. Zhu, P. H. Hor, *Journal of Solid State Chemistry* **1997**, *134*, 128; b) W. J. Zhu, P. H. Hor, *Inorganic Chemistry* **1997**, *36*, 3576.
- [204] a) X. Zhu, F. Han, G. Mu, B. Zeng, P. Cheng, B. Shen, H.-H. Wen, *Physical Review B* **2009**, *79*, 024516; b) H. Ogino, Y. Katsura, S. Horii, K. Kishio, J.-I. Shimoyama, *Superconductor Science and Technology* **2009**, *22*, 085001.
- [205] H. Ogino, Y. Matsumura, Y. Katsura, K. Ushiyama, S. Horii, K. Kishio, J.-I. Shimoyama, *Superconductor Science and Technology* **2009**, *22*, 075008.
- [206] X. Zhu, F. Han, G. Mu, P. Cheng, B. Shen, B. Zeng, H.-H. Wen, *Physical Review B* **2009**, *79*, 220512.
- [207] E. Makovicky, Z. Johan, S. Karup-Møller, *Neues Jahrbuch für Mineralogie (Abhandlungen)* **1980**, *138*, 122.
- [208] O. Y. Mruz, V. K. Pecharsky, A. N. Sobolev, O. I. Bodak, *Kristallografiya* **1990**, *35*, 202.
- [209] R. Pöttgen, B. Chevalier, P. Gravereau, B. Darriet, W. Jeitschko, J. Etourneau, *Journal of Solid State Chemistry* **1995**, *115*, 247.
- [210] a) E. Parthé, L. M. Gelato, *Acta Crystallographica Section A* **1984**, *40*, 169; b) L. M. Gelato, E. Parthe, *Journal of Applied Crystallography* **1987**, *20*, 139.
- [211] J. Lima-de-Faria, E. Hellner, F. Liebau, E. Makovicky, E. Parthé, *Acta Crystallographica Section A* **1990**, *A46*, 1.
- [212] W. J. Zhu, P. H. Hor, *Journal of Solid State Chemistry* **1997**, *130*, 319.
- [213] K. Otschi, H. Ogino, J.-I. Shimoyama, K. Kishio, *Journal of Low Temperature Physics* **1999**, *117*, 729.
-

-
- [214] C. Lux, G. Wenski, A. Mewis, *Zeitschrift für Naturforschung B* **1991**, 46b, 1035.
- [215] J. Bland, *A Mössbauer Spectroscopy and Magnetometry Study of Magnetic Multilayers and Oxides*, PhD thesis, University of Liverpool **2002**.
- [216] a) D. J. Singh, M. H. Du, *Physical Review Letters* **2008**, 100, 237003; b) K. Haule, J. H. Shim, G. Kotliar, *Physical Review Letters* **2008**, 100, 226402; c) G. Xu, H. Zhang, X. Dai, Z. Fang, *Europhysics Letters* **2008**, 84, 67015; d) D. J. Singh, *Physical Review B* **2008**, 78, 094511; e) I. Nekrasov, Z. Pchelkina, M. Sadovskii, *Journal of Experimental and Theoretical Physics Letters* **2008**, 88, 144.
- [217] V. B. Zabolotnyy, D. S. Inosov, D. V. Evtushinsky, A. Koitzsch, A. A. Kordyuk, G. L. Sun, J. T. Park, D. Haug, V. Hinkov, A. V. Boris, C. T. Lin, M. Knupfer, A. N. Yaresko, B. Büchner, A. Varykhalov, R. Follath, S. V. Borisenko, *Nature* **2009**, 457, 569.
- [218] a) I. R. Shein, A. L. Ivanovskii, *arXiv:0903.4038* **2009**; b) I. Shein, A. Ivanovskii, *Journal of Experimental and Theoretical Physics Letters* **2009**, 89, 41; c) I. Shein, A. Ivanovskii, *Central European Journal of Physics* **2010**, 8, 432.
- [219] H. Ogino, S. Sato, K. Kishio, J.-I. Shimoyama, T. Tohei, Y. Ikuhara, *Applied Physics Letters* **2010**, 97, 072506.
- [220] J. Munevar, D. R. Sanchez, M. Alzamora, E. Baggio-Saitovitch, J. P. Carlo, T. Goko, A. A. Aczel, T. J. Williams, G. M. Luke, H.-H. Wen, X. Zhu, F. Han, Y. J. Uemura, *arXiv:1011.1894* **2010**.
- [221] S. Sato, H. Ogino, N. Kawaguchi, Y. Katsura, K. Kishio, J.-I. Shimoyama, H. Kotegawa, H. Tou, *Superconductor Science and Technology* **2010**, 23, 045001.
- [222] A. S. Sefat, D. J. Singh, L. H. VanBebber, Y. Mozharivskyj, M. A. McGuire, R. Jin, B. C. Sales, V. Keppens, D. Mandrus, *Physical Review B* **2009**, 79, 224524.
- [223] F. Han, X. Y. Zhu, G. Mu, P. Cheng, B. Shen, B. Zeng, H. H. Wen, *Science China-Physics Mechanics & Astronomy* **2010**, 53, 1202.
- [224] D. B. Litvin, *Acta Crystallographica Section A* **2008**, 64, 419.
- [225] I. I. Mazin, M. D. Johannes, *Nature Physics* **2009**, 5, 141.
-

Chapter 25: Bibliography

-
- [226] D. R. Parker, M. J. Pitcher, P. J. Baker, I. Franke, T. Lancaster, S. J. Blundell, S. J. Clarke, *Chemical Communications* **2009**, 2189.
- [227] K. W. Lee, W. E. Pickett, *Europhysics Letters* **2010**, 89, 57008.
- [228] Mazin, II, *Physical Review B* **2010**, 81, 020507.
- [229] G. Cao, Z. Ma, C. Wang, Y. Sun, J. Bao, S. Jiang, Y. Luo, C. Feng, Y. Zhou, Z. Xie, F. Hu, S. Wei, I. Nowik, I. Felner, L. Zhang, Z. Xu, F. Zhang, *Physical Review B* **2010**, 82, 104518.
- [230] A. Pal, A. Vajpayee, R. S. Meena, H. Kishan, V. P. S. Awana, *Journal of Superconductivity and Novel Magnetism* **2009**, 22, 619.
- [231] T. Qian, N. Xu, Y.-B. Shi, K. Nakayama, P. Richard, T. Kawahara, T. Sato, T. Takahashi, M. Neupane, Y.-M. Xu, X.-P. Wang, G. Xu, X. Dai, Z. Fang, P. Cheng, H.-H. Wen, H. Ding, *arXiv:1008.4905* **2010**.
- [232] a) Z. Gao, L. Wang, Y. Qi, D. Wang, X. Zhang, Y. Ma, *Superconductor Science and Technology* **2008**, 21, 105024; b) L. Wang, Y. Qi, D. Wang, Z. Gao, X. Zhang, Z. Zhang, C. Wang, Y. Ma, *Superconductor Science and Technology* **2010**, 23, 075005.
- [233] a) Y. Mizuguchi, K. Deguchi, S. Tsuda, T. Yamaguchi, H. Takeya, H. Kumakura, Y. Takano, *Applied Physics Express* **2009**, 2, 083004; b) T. Ozaki, K. Deguchi, Y. Mizuguchi, H. Kumakura, Y. Takano, *arxiv:1008.1447* **2010**.
- [234] a) Y. Qi, X. Zhang, Z. Gao, Z. Zhang, L. Wang, D. Wang, Y. Ma, *Physica C* **2009**, 469, 717; b) L. Wang, Y. Qi, D. Wang, X. Zhang, Z. Gao, Z. Zhang, Y. Ma, S. Awaji, G. Nishijima, K. Watanabe, *Physica C* **2010**, 470, 183.
- [235] a) T. Katase, H. Hiramatsu, H. Yanagi, T. Kamiya, M. Hirano, H. Hosono, *Solid State Communications* **2009**, 149, 2121; b) T. Thersleff, K. Iida, S. Haindl, M. Kizszun, D. Pohl, A. Hartmann, F. Kurth, J. Hanisch, R. Huhne, B. Rellinghaus, L. Schultz, B. Holzapfel, *Applied Physics Letters* **2010**, 97, 022506.
- [236] T. Katase, Y. Ishimaru, A. Tsukamoto, H. Hiramatsu, T. Kamiya, K. Tanabe, H. Hosono, *arXiv:1011.5721* **2010**.
- [237] a) D. H. Lu, M. Yi, S. K. Mo, A. S. Erickson, J. Analytis, J. H. Chu, D. J. Singh, Z. Hussain, T. H. Geballe, I. R. Fisher, Z. X. Shen, *Nature* **2008**, 455, 81; b) T. Kondo, A. F. Santander-Syro, O. Copie, C. Liu, M. E. Tillman, E. D. Mun, J. Schmalian, S. L. Bud'ko, M. A. Tanatar, P. C. Canfield, A. Kaminski, *Physical Review Letters* **2008**, 101, 147003; c) H. Ding, P. Richard, K. Nakayama, K. Sugawara, T. Arakane, Y. Sekiba, A. Takayama, S. Souma, T.
-

-
- Sato, T. Takahashi, Z. Wang, X. Dai, Z. Fang, G. F. Chen, J. L. Luo, N. L. Wang, *Europhysics Letters* **2008**, 83, 47001.
- [238] D. J. Singh, *Physica C* **2009**, 469, 418.
- [239] J. Paglione, R. L. Greene, *Nature Physics* **2010**, 6, 645.
- [240] M. Gooch, B. Lv, K. Sasmal, J. H. Tapp, Z. J. Tang, A. M. Guloy, B. Lorenz, C. W. Chu, *Physica C* **2010**, 470, S276.
- [241] a) L. Boeri, M. Calandra, I. I. Mazin, O. V. Dolgov, F. Mauri, *Physical Review B* **2010**, 82, 020506(R); b) P. M. Shirage, K. Miyazawa, K. Kihou, H. Kito, Y. Yoshida, Y. Tanaka, H. Eisaki, A. Iyo, *Physical Review Letters* **2010**, 105, 037004.
- [242] a) F. L. Ning, K. Ahilan, T. Imai, A. S. Sefat, M. A. McGuire, B. C. Sales, D. Mandrus, P. Cheng, B. Shen, H. H. Wen, *Physical Review Letters* **2010**, 104, 037001; b) J. Dai, Q. Si, J.-X. Zhu, E. Abrahams, *Proceedings of the National Academy of Sciences* **2009**, 106, 4118.
- [243] Wikipedia: Quantum critical point, http://en.wikipedia.org/w/index.php?title=Quantum_critical_point&oldid=420688225, **2011**.
- [244] R. Thomale, C. Platt, W. Hanke, J. Hu, B. A. Bernevig, *arXiv:1101.3593* **2011**.
- [245] M. Nikolo, *American Journal of Physics* **1995**, 63, 57.
- [246] <http://www.omega.com/temperature/z/pdf/z115-117.pdf>, **2006**.
- [247] M. Tegel, Primary coil calculation sheet, http://mtegel.eu/intern/primary_coil.mw, user name / password : intern / arsenig, **2010**.
- [248] *LabVIEW*, v. 8.6.1, National Instruments, <http://www.ni.com/labview/>, **2009**.
- [249] M. Tegel, AC Susceptometer Control (source code), <http://mtegel.eu/intern/susceptometer.zip>, user name / password : intern / arsenig, **2010**.
- [250] M. Tegel, Conductivity Control (source code), <http://mtegel.eu/intern/conductivity.zip>, user name / password : intern / arsenig, **2010**.
- [251] M. Tegel, HConvert (source code), <http://mtegel.eu/intern/hconvert.zip>, user name / password : intern / arsenig, **2010**.
-

Chapter 25: Bibliography

- [252] H. Lueken, *Magnetochemie*, Teubner, Stuttgart, Leipzig, **1999**.
- [253] M. Tegel, *Molar Weight Calculator*, v. 0.2 (Mac/Windows), Ludwig-Maximilians-Universität, München, http://mtegel.eu/downloads_en/downloads_en.html, **2010**.
- [254] I. I. Mazin, *Nature* **2010**, 464, 183.
- [255] D. J. Van Harlingen, *Reviews of Modern Physics* **1995**, 67, 515.
- [256] Wikipedia: Pi Josephson junction, http://en.wikipedia.org/w/index.php?title=Pi_Josephson_junction&oldid=377104370, **2010**.
- [257] M. Tegel, F. Hummel, T. Schmid, T. Stürzer, M. Egawa, Y. Su, A. Senyshyn, D. Johrendt, The Role of Stoichiometry and Magnetism in the Superconductor $\text{Sr}_2\text{VO}_3\text{FeAs}$ and Related Compounds, http://mtegel.eu/schriften/tokyo_1103.pdf, user name / password : LMU / phosphorig, **2011**.
- [258] M. Tegel, Supraleiter mit Arsen vergiften, http://mtegel.eu/schriften/HAEKO_1003.pdf, user name / password : LMU / phosphorig, **2010**.
- [259] M. Tegel, S. Welzmler, D. Johrendt, Crystal structures, superconductivity and magnetism of the cobalt-doped iron phosphide oxides $\text{La}(\text{Co}_x\text{Fe}_{1-x})\text{PO}$ ($x = 0 - 1$), http://mtegel.eu/schriften/muenster_0909.pdf, user name / password : LMU / phosphorig, **2009**.
- [260] M. Tegel, Eisenarsenide mit großem Schichtabstand, http://mtegel.eu/schriften/hirschegg_0906.pdf, user name / password : LMU / phosphorig, **2009**.
- [261] <http://expedition-zukunft.org/>, **2009**.
- [262] M. Tegel, Das eine hat's, das andere nicht! * Zwei neue Eisenarsenide, http://mtegel.eu/schriften/HAEKO_0903.pdf, user name / password : LMU / phosphorig, **2009**.
- [263] M. Tegel, S. Welzmler, V. Weiß, S. Johansson, D. Johrendt, Synthesis, structure, magnetism of EuMnPF and the new iron arsenide fluoride SrFeAsF , http://mtegel.eu/schriften/bayreuth_0809.pdf, user name / password : LMU / phosphorig, **2008**.
- [264] M. Tegel, Supraleitung quaternärer Pnictidoxide - auf dem Weg zu neuen Hochtemperatursupraleitern, http://mtegel.eu/schriften/hirschegg_0805.pdf, user name / password : LMU / phosphorig, **2008**.
-

-
- [265] M. Tegel, Research Report 2007-2010,
http://mtegel.eu/intern/presentation_1012.pdf, user name / password : intern
/ arsenig, **2010**.
- [266] M. Tegel, Research Report 2009,
http://mtegel.eu/intern/presentation_0911.pdf, user name / password : intern
/ arsenig, **2009**.
- [267] M. Tegel, Research Report 2008,
http://mtegel.eu/intern/presentation_0811.pdf, user name / password : intern
/ arsenig, **2008**.
- [268] M. Tegel, Rietveld methodology seminar 2008 - An introduction to the
Rietveld method and GSAS, http://mtegel.eu/intern/rietveld_0805.zip, user
name / password : intern / arsenig, **2008**.
- [269] M. Tegel, Research Report 2007,
http://mtegel.eu/intern/presentation_0711.pdf, user name / password : intern
/ arsenig, **2007**.